



## Durham E-Theses

---

# *Paper-based Screen-printed Passive Electronic Components*

SHENTON, SAMANTHA,ANN

### How to cite:

---

SHENTON, SAMANTHA,ANN (2018) *Paper-based Screen-printed Passive Electronic Components*, Durham theses, Durham University. Available at Durham E-Theses Online:  
<http://etheses.dur.ac.uk/12675/>

### Use policy

---

The full-text may be used and/or reproduced, and given to third parties in any format or medium, without prior permission or charge, for personal research or study, educational, or not-for-profit purposes provided that:

- a full bibliographic reference is made to the original source
- a [link](#) is made to the metadata record in Durham E-Theses
- the full-text is not changed in any way

The full-text must not be sold in any format or medium without the formal permission of the copyright holders.

Please consult the [full Durham E-Theses policy](#) for further details.

---

Academic Support Office, Durham University, University Office, Old Elvet, Durham DH1 3HP  
e-mail: [e-theses.admin@dur.ac.uk](mailto:e-theses.admin@dur.ac.uk) Tel: +44 0191 334 6107  
<http://etheses.dur.ac.uk>



# Paper-based Screen-printed Passive Electronic Components

**Samantha Ann Shenton**

Thesis presented for the degree of  
Doctor of Philosophy



Department of Engineering  
University of Durham, UK  
2018

# Dedicated to

Pops and AC, always thinking of you x

# Abstract

This thesis investigates paper-based electronics in terms of various substrates, fabrication methods and example devices, including touch sensors and microwave resonators. The term ‘paper’ is very broad and covers a wide range of substrates. A decision matrix has been created to determine the optimum paper for an application, based on a range of properties. Thermal evaporation and screen printing are compared for their use as fabrication methods for paper-based electronics and a second decision matrix has been compiled. Based on these decision matrices, screen printing onto a thicker matt paper was determined to be optimal. The printing process was further optimised to achieve the best results from the in-house process.

Using this well-developed screen-printing method, passive components (including inductors and interdigitated capacitive touch sensors) were fabricated and found to be comparable with state-of-the-art results reported in the literature. Measurements from the touch pads were compared to modelling, with little variation between the two, and were confirmed to work under a wide range of conditions, showing that they are compatible with any user.

The microwave characteristics, up to 3 GHz, of both the chosen substrate and silver-flake ink were investigated through production of screen-printed transmission lines. These characteristics were then used to create microwave resonators. The frequency range is important for applications as the industrial, scientific and medical radio band (ISM band) lies between 2.45 and 2.55 GHz which includes Wi-Fi and Bluetooth. Initially, stub resonators were considered to determine the cause of differences between theoretical and measured results. Then spiral defected ground structures were made, with multiple resonances, and sensitivity to touch and humidity demonstrated.

As paper is hygroscopic, the effect of humidity on paper-based electronics is of key importance. This has been considered for all the devices fabricated in this work and it has been determined that the change in permittivity of the substrate, as a result of absorbed water within paper, is the most dominant factor.

# Declaration

I hereby declare that the work carried out in this thesis has not been previously submitted for any degree and is not currently being submitted in candidature for any other degree.

**Copyright ©2018 Samantha Shenton**

The copyright of this thesis rests with the author. No quotation from it should be published without the author's prior written consent and information derived from it should be acknowledged.

# List of Publications

- S. Shenton, M. Cooke, Z. Racz, C. Balocco and D. Wood, “The effect of humidity on microwave characteristics of screen printed paper-based electronics”, *Physica status solidi a* - in press.
- S. Shenton, D. Wood, “Paper-based electronics: The facts versus the fiction”, *MicroMatters*, Spring 2016.
  
- **Conference Attended (Oral Presentation):** European Materials Research Society, “Optimum fabrication methods and substrates for paper-based electronics”, Lille, May 2015.
  
- **Other Work:** L. Dodd, S. Shenton, A. Gallant and D. Wood, “Improving metal-oxide-metal (MOM) diode performance via the optimization of the oxide layer”, *Journal of Electronics Materials*, Vol. 44, No. 5, p. 1361, 2015.

# Acknowledgements

Firstly, I would like to thank those who helped produce the images within the thesis. Cyril Bourgenot from Netpark took all the Zygo white light interferometer images, the talysurf images and the talystep images for assessing the topography of paper. Leon Bowen took the FIB images and was a great help with the SEM images. Richard Walshaw undertook the environmental SEM imaging. Polly, who drew the anatomical drawing of a finger, you are indeed a great artist, thank you.

I would like to thank all my friends and family for their continued support and patience throughout the last four years especially those who have been through the same and have lightened the time with cards and more enjoyable activities. Thank you Andreas for always keeping me well fed, thanks Carlo for the many pick-me-up chats and a huge thanks to Matty who is king of LaTeX! Sarah, you've always been there with food and wine even though you've been going through the same thing, you're one of the most kind people I know and I hope I can return it over the next year and support you in the same way. A special thank you to Dinah for taking the time to proof read.

A massive thank you to Alex who has put up with me for the last four years and made it that little bit more bearable. We've both spent a long time now working towards the next step in our lives and I can't wait to be able to relax and spend it in a more pleasant place.

Finally, I could not have done this without the help of my supervisors: Prof. David Wood, Dr Claudio Balocco, Dr Zoltan Racz and Dr Mike Cooke. Mike, you were always there to talk to and provide advice and feedback, thank you. David, you've always believed I could get to this point even when I didn't believe it myself. You've been a great support and I still can't believe I'm here! Claudio, you turned up at the right time and you've not managed to get rid of me since. I cannot thank you enough for the time you have dedicated to me.

# Contents

<b>1</b>	<b>Introduction</b>	<b>1</b>
1.1	Types of Paper . . . . .	3
1.2	Fabrication Methods for Paper Electronics . . . . .	4
1.3	Paper-based Electronic Devices . . . . .	6
1.4	Effect of Humidity on Paper . . . . .	9
1.5	Structure of the Thesis . . . . .	11
<b>2</b>	<b>Experimental Techniques</b>	<b>21</b>
2.1	Introduction . . . . .	21
2.2	Fabrication Methods for Paper Electronics . . . . .	21
2.2.1	Thermal Evaporation . . . . .	22
2.2.2	Screen Printing . . . . .	23
2.3	Analysis of Surface Morphology . . . . .	25
2.3.1	Surface Roughness Characterisation Techniques . . . . .	25
2.3.2	Dektak Surface Profiler . . . . .	28
2.3.3	Scanning Electron Microscopy . . . . .	29
2.3.4	Focused Ion-Beam Milling . . . . .	31
2.4	Electrical Measurement Techniques . . . . .	32
2.4.1	Four-Point Probe . . . . .	32
2.4.2	Vector Network Analyser . . . . .	33
2.5	Simulation Packages . . . . .	36
2.5.1	COMSOL Multiphysics . . . . .	36
2.5.2	Advanced Design System (ADS) . . . . .	36
2.6	Conclusion . . . . .	37
<b>3</b>	<b>Paper and Process Selection</b>	<b>39</b>
3.1	Introduction . . . . .	39
3.2	Paper Structure . . . . .	40
3.2.1	Matt Papers . . . . .	40
3.2.2	Coated Papers . . . . .	41
3.2.3	Stone Papers . . . . .	44
3.3	Comparison of Paper-based Substrates . . . . .	44
3.3.1	Surface Roughness . . . . .	45
3.3.2	Thermal Resilience . . . . .	49

3.3.3	Water Resilience . . . . .	50
3.3.4	Flexibility . . . . .	52
3.3.5	Cost . . . . .	53
3.3.6	Weight/Thickness . . . . .	53
3.4	Comparison of Thermal Evaporation and Screen Printing . . . . .	53
3.4.1	Thermal Evaporation . . . . .	54
3.4.2	Screen Printing . . . . .	56
3.4.3	Sheet Resistance . . . . .	58
3.4.4	Surface Roughness and Sheet Resistance . . . . .	60
3.4.5	Adhesion . . . . .	62
3.5	Decision Matrices for Paper and Fabrication Method . . . . .	63
3.5.1	Determining an Optimum Paper and Fabrication Method . . . . .	66
3.6	Comparison of Paper with Established Substrate Materials . . . . .	67
3.7	Conclusion . . . . .	69
<b>4</b>	<b>Screen Printing Optimisation</b>	<b>71</b>
4.1	Introduction . . . . .	71
4.2	The Screen . . . . .	72
4.3	The Printing Process . . . . .	77
4.4	Curing of the Ink . . . . .	81
4.5	Ink/Paper Interface . . . . .	85
4.6	Screen-printed Passive Components . . . . .	87
4.6.1	Resistors . . . . .	87
4.6.2	Capacitors . . . . .	87
4.6.3	Inductors . . . . .	89
4.7	Conclusion . . . . .	91
<b>5</b>	<b>Fabrication and Characterisation of Interdigitated Touch Sensors</b>	<b>93</b>
5.1	Introduction . . . . .	93
5.2	Interdigitated Capacitive Sensor Geometries . . . . .	97
5.3	Theoretical Analysis of the Interdigitated Sensors . . . . .	99
5.3.1	Analytical Expression for the Sensor Capacitance . . . . .	99
5.3.2	COMSOL Modelling of the Sensors . . . . .	100
5.4	Impedance Measurement of the Interdigitated Sensors . . . . .	106
5.5	Measurement of the Sensors using an Embedded System . . . . .	110
5.5.1	Repeatability of the Fabrication Method . . . . .	112
5.5.2	Comparing Touch of the Printed and Non-printed Sides of the Sensor . . . . .	113
5.5.3	Comparing Touch of the Sensor Using Different Parts of the Hand . . . . .	115
5.5.4	Untouched and Touched Capacitance of the Sensors . . . . .	117
5.5.5	Varying the Touching Pressure . . . . .	118
5.5.6	Varying the Contact Area Between the Finger and Sensor . . . . .	120
5.5.7	Varying the Position of the Finger on the Sensor . . . . .	122
5.5.8	Varying the Proximity of the Finger to the Sensor . . . . .	124



5.6	Effect of Humidity on the Sensors . . . . .	124
5.7	Conclusion . . . . .	127
<b>6</b>	<b>Paper-based Microwave Transmission Lines</b>	<b>130</b>
6.1	Introduction . . . . .	130
6.2	Transmission Line Theory . . . . .	131
6.2.1	Lossless Transmission Line . . . . .	131
6.2.2	Characteristic Impedance . . . . .	133
6.2.3	Transmission Lines with Losses . . . . .	134
6.3	Transmission Line Parameter Extraction from Measured Scattering Parameters . . . . .	135
6.4	Effect of Changing Transmission Line Parameters on the Transmission Line Response	140
6.5	Effect of Humidity at Microwave Frequencies . . . . .	151
6.5.1	Scattering Parameters and Line Parameters . . . . .	151
6.5.2	Effect of Humidity on the Ink . . . . .	156
6.5.3	Water Absorption of Paper . . . . .	161
6.6	Conclusion . . . . .	167
<b>7</b>	<b>Paper-based Microwave Resonators</b>	<b>170</b>
7.1	Introduction . . . . .	170
7.2	Theory . . . . .	170
7.3	Transmission Line Stubs . . . . .	175
7.3.1	Analytical Modelling of Transmission Line Stubs . . . . .	176
7.3.2	Screen-printed Transmission Line Stubs . . . . .	179
7.3.3	Simulations of Transmission Line Stubs . . . . .	190
7.4	Defected Ground Structure Resonators . . . . .	191
7.4.1	Design of Spiral Defected Ground Structure Resonators . . . . .	193
7.4.2	Measurement of Spiral Defected Ground Structure Resonators . . . . .	196
7.4.3	Effect of Humidity on Spiral Defected Ground Structure Resonators . . . . .	203
7.4.4	Spiral Defected Ground Structure Resonators as Touch Pads . . . . .	206
7.5	Conclusion . . . . .	207
<b>8</b>	<b>Conclusions and Outlook</b>	<b>209</b>
8.1	Suggestions for Further Work . . . . .	211

# List of Figures

2.1	Diagram of a thermal evaporator. . . . .	22
2.2	Image of an example screen made in house for printing transmission line stubs (detailed in Chapter 6). . . . .	24
2.3	The process of screen printing. (a) The screen is flooded with ink. (b) The screen is placed above the substrate and the squeegee is used to push the ink through the screen onto the substrate. (c) The screen is removed, showing the resulting print. . . . .	24
2.4	Diagram of an atomic force microscope. . . . .	25
2.5	Diagram of a white light interferometer. . . . .	27
2.6	Features of the Diative DH-7 stylus profilometer. (a) The whole system including the stylus, traversing unit, computation and output equipment, example sample of matt paper and the corresponding example trace. (b) Close-up of the tracer and diamond stylus. . . . .	28
2.7	Annotated photograph of the Dektak 3ST. . . . .	29
2.8	Diagram of a scanning electron microscope. . . . .	30
2.9	Diagram of a dual beam system with an FIB and SEM. . . . .	31
2.10	The principles of four-point probe measurements. . . . .	33
2.11	Diagram of a vector network analyser. . . . .	34
2.12	Images of the vector network analyser and devices used in this work. (a) An illustration of the reference and reflected signals from port 1 and 2. (b) A photograph of the experimental setup including the vector network analyser and a transmission line under test. (c) The connectors used in this work. . . . .	35
3.1	SEM images of Office Depot 80 gsm printer paper. The image on the right highlights the calcium carbonate (red) and cellulose fibres (blue) within the paper structure. . .	40
3.2	SEM image of 85.5 gsm Berkshire BCR bond cleanroom paper. . . . .	41
3.3	SEM image of 199 gsm Neenah paper. . . . .	41
3.4	SEM images of 225 gsm Epson glossy photo paper. . . . .	42
3.5	SEM images of 250 gsm Felix Schoeller gloss/gloss photo paper. . . . .	42
3.6	SEM image of 250 gsm Felix Schoeller gloss/gloss photo paper cross-section and a pictorial representation, illustrating the various layers within the paper. . . . .	43
3.7	SEM images of Powercoat HD 95 paper. . . . .	43
3.8	SEM images of Morrison's baking paper. . . . .	44
3.9	SEM images of 192 gsm Parax stone paper. . . . .	44

3.10	An AFM image of the top surface of 250 gsm Felix Schoeller gloss/gloss photo paper illustrating the nanometer grain structure of the coating. . . . .	46
3.11	Data taken from the Zygo software showing Powercoat HD 95 paper. (a) A two-dimensional representation of a $2.81 \times 2.11$ mm section. (b) A three-dimensional surface profile of the same section and (c) A one-dimensional plot along the line shown (a). . .	47
3.12	Data taken from the Talysurf software showing a 10 mm line profile of printer paper. .	48
3.13	Examples of papers after heat treatment. From top left going clockwise: Parax paper removed from the oven at $100^\circ\text{C}$ due to excessive curling; gloss photo paper removed at $175^\circ\text{C}$ due to excessive yellowing; baking paper and matt paper removed at $200^\circ\text{C}$ but both could have withstood higher temperatures. All samples were $4 \times 7.5$ cm before being placed in the oven. . . . .	49
3.14	Images illustrating flexibility testing on paper samples. (a) Shows folding of the sample, (b) shows rolling of the sample, (c) and (d) show matt paper before and after rolling respectively and (e) shows photo paper where the coating cracked during folding. . . .	52
3.15	Examples of thermally evaporated samples. The left-hand samples show features down to $200\ \mu\text{m}$ and highlight the rounding of corners due to a suboptimal shadow mask. The right-hand, larger samples highlight the issue of the shadow mask moving during deposition. . . . .	55
3.16	Plot of sheet resistance of thermally evaporated layers on various papers listed in order of surface roughness. 180 Gloss has a roughness ( $R_a$ ) of $0.098\ \text{nm}$ and cleanroom paper has a roughness ( $R_a$ ) of $3.67\ \text{nm}$ . Rougher papers were found to have higher sheet resistance values due to the thin layers deposited. . . . .	56
3.17	SEM image of screen-printed 1 mm lines using silver ink on 199 gsm matt paper. . . .	57
3.18	Image illustrating shorting between two screen-printed lines due to insufficient tension in the mesh. . . . .	57
3.19	Adapted SEM images illustrating the difference in theoretical metal layers (shown in red) deposited on matt (top) and coated papers (bottom). . . . .	59
3.20	Illustration to show the difference between screen-printed layers on smooth and rough papers. . . . .	59
3.21	Sheet resistance for thermally evaporated and screen-printed metal layers on various paper samples. The substrates are listed in order of surface roughness with silicon being the smoothest (with a surface roughness of $0.016\ \mu\text{m}$ ) and chromatography paper being the roughest (with a surface roughness of $6.15\ \mu\text{m}$ ). . . . .	61
3.22	Illustration of ISO Standard for adhesion testing. Classification is taken to be 0 for no metal removed and 5 for more than 65% of the metal removed. The white regions are the deposited metal layer and the black regions are the paper substrate where the metal has been removed. . . . .	62
4.1	Images illustrating the difference in print quality when using different screens. (a) Preliminary printing with a 90T mesh screen made in-house, (b) and (c) printing with a 32T mesh screen made by a framing shop, d) printing with an 90T mesh screen made by a framing shop and after optimisation. All images are the same scale. . . . .	72

4.2	Comparison of a screen with 32T mesh (left) and a screen with a 120T mesh (right), highlighting the larger, more visible threads in the 32T mesh and the poorer definition in features. . . . .	73
4.3	Comparison of feature sizes of acetate masks produced commercially (left) and in house (right), highlighting the poorer quality for those produced in house. . . . .	73
4.4	Comparison of feature sizes and gaps between features on the screen for various mesh thread counts. The whiskers of the box plots show the maximum and minimum values measured. . . . .	74
4.5	Comparison of feature sizes and gaps between features for printed structures printed using meshes with various thread counts. The whiskers of the box plots show the maximum and minimum values. . . . .	75
4.6	Comparison of thicknesses of printed structures using meshes with various thread counts. Measurements were taken using a Dektak profilometer. The whiskers of the box plots show the maximum and minimum values. . . . .	76
4.7	Comparison of sheet resistance values for squares printed using meshes with various thread counts. The whiskers of the box plots show the maximum and minimum values. . . . .	76
4.8	Comparison of printed features using a round-edged squeegee (left) and a square-edged squeegee (right). . . . .	77
4.9	Illustration of the side profile of a square-edged squeegee (left) and a round-edged squeegee (right). . . . .	78
4.10	Comparison of printed features using different forces applied to the squeegee. Equivalent mass values are shown for each print. . . . .	79
4.11	Comparison of printed features using different squeegee angles while printing. . . . .	79
4.12	Comparison of printed features when printing took place over different speeds. . . . .	80
4.13	Comparison of printed features when different number of passes with the squeegee has taken place. . . . .	81
4.14	Sheet resistance values of printed squares over time with different curing temperatures. . . . .	82
4.15	Image of samples after being cured at 75, 125 and 175 °C for 30 minutes. . . . .	83
4.16	SEM images of screen-printed samples prior to curing (top) and samples which have been cured for three hours at 125 °C (bottom). . . . .	83
4.17	Curing of screen-printed silver ink on glass, cured at 500 °C for 30 minutes. . . . .	84
4.18	Sheet resistance values of screen-printed samples which have been air dried for over 70 days at room temperature. . . . .	85
4.19	SEM image of a focused ion-beam milled section of screen-printed silver ink on paper. . . . .	85
4.20	SEM image of a focused ion-beam milled section of screen-printed silver ink on paper with thickness values added. . . . .	86
4.21	SEM image of a focused ion-beam milled section of the edge of screen-printed silver ink on paper with thickness values added. . . . .	86
4.22	Examples of screen-printed parallel plate (left) and interdigitated capacitors (right) with their respective capacitance values. . . . .	88
4.23	Capacitance and phase against frequency for the parallel plate capacitor shown in Figure 4.22. . . . .	89

4.24	Example of a screen-printed inductor with 1 mm track width and spacing, an outer diameter of 76 mm and 14 turns. . . . .	89
4.25	Model of paper-based spiral inductors for a.c. analysis. . . . .	91
4.26	Typical plot of impedance with frequency for inductors on paper, comparing theory with measurements. . . . .	91
5.1	Capacitance buttons fabricated on metallised paper, highlighting the greater increase in capacitance when using an interdigitated structure. Adapted from [4]. . . . .	95
5.2	The electric field patterns for both the un-touched and touched states of the interdigitated touch pad design. . . . .	96
5.3	Illustration of an interdigitated capacitive sensor with key dimensions added. . . . .	97
5.4	Four designs of interdigitated capacitive touch pads considered in this work. . . . .	98
5.5	Example of Design 1 touch sensor created in COMSOL. All units are in mm. . . . .	100
5.6	Cross-sectional view to show the electric field for sensor design 1 as modelled by COMSOL when one set of electrodes are set to 1V and the other to 0V. The electrodes are situated on top of the paper substrate. . . . .	102
5.7	Anatomical and COMSOL model of the human finger with skin, fat and bone labelled. The anatomical drawing has been adapted from [43]. . . . .	104
5.8	Example of the electric field for Design 1 touch sensor in contact with the finger as calculated by COMSOL. . . . .	105
5.9	Change in capacitance as the thickness of the skin layer is varied between 0.05 and 1.5 mm in the COMSOL model. . . . .	106
5.10	Capacitance data taken from an impedance analyser for a Design 1 touch sensor in the touched and untouched states. . . . .	107
5.11	A schematic of the equivalent model for the touch sensors used in this work. The ends of the circuit are equivalent to the ‘legs’ on the sensors. . . . .	108
5.12	Comparison of impedance data taken from the impedance analyser and RC modelling technique. . . . .	109
5.13	Comparison of the corresponding phase data taken from the impedance analyser and RC modelling technique. . . . .	109
5.14	The custom-built measurement system for the touch sensors consisting of an Arduino MEGA, a PCB with FDC 2214 chip and RLC components and an example of a Design 2 interdigitated sensor. . . . .	110
5.15	Schematic of the PCB and Arduino system, taken from [48]. . . . .	111
5.16	Repeatability of the fabrication method for the interdigitated touch pads. . . . .	113
5.17	Comparison of capacitance values for touching the touch pad in different ways. Touching the front, touching the back, touching the front of the touch pad with gloves on and touching the front when it had been covered in a layer of tape. . . . .	114
5.18	Example data for various users touching the front and back of a touch pad. . . . .	115
5.19	Various parts of the hand used to compare the difference in capacitance when each part is used to touch the sensors. In reality, the sensor was touched on the back, however the front has been shown for clarity. . . . .	116

5.20	Measured capacitance values when different parts of the hand are used to touch the touch pad. . . . .	117
5.21	Measured capacitance values when different forces were applied to a touch pad with a paper substrate. . . . .	119
5.22	Measured capacitance values when different forces were applied to a touch pad with a glass substrate. . . . .	120
5.23	Comparison of measured and simulated capacitance values when the contact area between the finger and touch pad was varied. . . . .	121
5.24	Illustration of the smallest and largest contact area between the finger and touch pad when using the COMSOL modelling. . . . .	122
5.25	Illustration of the various positions of the finger in the COMSOL model to determine any change in capacitance with position. . . . .	123
5.26	Simulated capacitance values for a finger touching the touch pad in different positions.	123
5.27	Simulated capacitance values when the proximity of the finger and the touch pad was varied between 0 and 1 mm. . . . .	124
5.28	Set-up for humidity measurements showing an example device under test. An environmental chamber and the custom measurement system were used to vary the relative humidity and simultaneously measure the capacitance of the touch pads. . . . .	125
5.29	Measured capacitance values for the four touch sensor designs when the relative humidity is varied from 40 to 90% and returned again to 40%. . . . .	126
6.1	Simple model for an ideal transmission line. Two parallel, lossless wires of infinite length were split into sections made up of series inductance $L$ and parallel capacitance $C$ per unit length. . . . .	131
6.2	Simple model for an ideal transmission line terminated with a load impedance $Z_L$ . .	133
6.3	Simple model for a real transmission line. Two parallel wires of infinite length are split into sections made up of series inductance $L$ , resistance $R$ , parallel capacitance $C$ and conductance $G$ per unit length. . . . .	134
6.4	Example transmission line geometry using the coplanar waveguide structure which includes a signal track and two ground planes all printed on one side of a paper substrate. This example is 17 cm long with 2 mm and 15 mm signal and ground track widths respectively. . . . .	135
6.5	Illustration for transmitted and reflected signals for a two port microwave device, used to calculate the scattering parameters. This should be considered in conjunction with Equation (6.17). . . . .	136
6.6	Illustration for the transmission (ABCD) matrix in terms of port 1 and 2 voltages and currents. This should be considered in conjunction with Equation (6.17). . . . .	136
6.7	Comparison of measured and fitted scattering parameters for a 17 cm long transmission line with a 2 mm wide signal track. The fitted scattering parameters have been constructed by taking an initial guess of the line parameters and calculating the ABCD matrix. From this, the s-parameters could be extracted and the error between these and the measured values limited. . . . .	138

6.8	Corresponding losses, propagation velocity and magnitude/phase of the characteristic impedance for the same transmission line as the results shown in Figure 6.7. These line parameters were constructed by the fitting algorithm detailed in the text. . . . .	139
6.9	Line parameters of ten transmission lines with identical geometry to show repeatability of the devices. The maximum deviation is $3\sigma$ from the magnitude of the characteristic impedance. . . . .	141
6.10	Line parameters of a transmission line with length varied between 17 and 5 cm in 2 cm steps. Results show a maximum deviation of $2\sigma$ from the magnitude of the characteristic impedance. . . . .	142
6.11	Scattering parameters of transmission line with ground plane width varied between 30 and 2 mm. . . . .	143
6.12	Line parameters of transmission lines with signal track widths of 1, 2, 3, 5 and 6 mm. .	144
6.13	Line parameters of transmission lines with a gap between signal and ground of 1, 2 and 4 mm. . . . .	145
6.14	Comparison of measured and simulated scattering parameters for a transmission line that is 17 cm long with 2 mm signal track width and 15 mm ground track width. . . .	146
6.15	Simulated line parameters of transmission lines of substrate thickness varying between 100 and 500 $\mu\text{m}$ . Scattering parameters were simulated using ADS software and line parameters extracted. . . . .	147
6.16	Simulated line parameters of transmission lines varying the substrate permittivity between 1 and 10. Scattering parameters were simulated using ADS software and line parameters extracted. . . . .	148
6.17	Simulated line parameters of transmission lines varying the metal conductivity between $1 \times 10^6$ and $1 \times 10^7$ S/m. Scattering parameters were simulated using ADS software and line parameters extracted. . . . .	149
6.18	Simulated line parameters of transmission lines varying the metal thickness between 1 and 50 $\mu\text{m}$ . Scattering parameters were simulated using ADS software and line parameters extracted. . . . .	150
6.19	Measured scattering parameters for a transmission line 17 cm long with 2 and 15 mm signal and ground track width respectively as the relative humidity was varied between 40 - 90% in 10% steps. . . . .	152
6.20	Measured scattering parameter $s_{11}$ for a transmission line 17 cm long with 2 and 15 mm signal and ground track width respectively as the relative humidity was varied between 40 - 90% in 10% steps and then returned to 40%. . . . .	153
6.21	Measured scattering parameters for a transmission line 17 cm long with 2 and 15 mm signal and ground track width respectively as the relative humidity was varied between 40 - 50% and left for one week. . . . .	154
6.22	Measured line parameters for a transmission line 17 cm long with 2 and 15 mm signal and ground track width respectively as the relative humidity was varied between 40 - 90% in 10% steps. . . . .	155

6.23	Measured scattering parameters for a transmission line printed on glass as the relative humidity was varied between 40 - 90% in 10% steps. The transmission line was 17 cm long with 2 and 15 mm signal and ground track width respectively. . . . .	157
6.24	Variation in measured sheet resistance for screen-printed silver ink on glass and paper substrates as the relative humidity was varied. Measurements were taken using a four point probe method. . . . .	158
6.25	An ESEM image of silver flake ink on paper at a temperature of 3 °C and a pressure of 7.1 Torr showing the saturation of the sample with water and evident water on the sample surface. This combination of temperature and pressure results in a relative humidity past the point of 100%. The water droplets are the darker regions on the sample surface. . . . .	161
6.26	Simulations for a 5% increase in x and y dimensions of the transmission line due to water intake of the paper. The substrate thickness was kept constant as the effect of this has been shown previously. . . . .	162
6.27	Total water content of paper when relative humidity was varied between 30 and 90%. The blue line represents data taken from [21], the red line represents measurements from this work. . . . .	163
6.28	Illustration of tightly and loosely bound water mechanisms in water-paper mixtures. .	163
6.29	Calculated real and imaginary parts of the relative permittivity of pure water between 300 kHz and 3 GHz using the Debye equation and values from [26]. . . . .	165
6.30	Theoretical values of the effective permittivity of a paper-based substrate with increasing relative humidity based on Equation (6.24) and values in Table 6.3. . . . .	166
7.1	Example series RLC resonator where R is the resistance, L is the inductance, C is the capacitance, V is the voltage and I is the current. . . . .	171
7.2	Impedance plots for two example resonators with quality factors of 10 and 50. . . . .	172
7.3	Impedance plots for two example resonators with different quality factors, highlighting the bandwidth for each. . . . .	173
7.4	An example of a coplanar waveguide microwave resonator. This example is a transmission line with an altered signal track to create a resonance. . . . .	174
7.5	Examples of resonances created by systems which are critically coupled, under coupled and over coupled. . . . .	175
7.6	Example of a screen-printed design 4 stub. The stub length and stub width are highlighted. . . . .	176
7.7	Illustration of a stub in parallel with the transmission line and the equivalent circuit. .	176
7.8	Simple model for the stub where $Z_s$ is the equivalent impedance of the stub looking from the end it is connected to the transmission line, $Z_L$ is the load impedance determined by the end of the stub and $d$ is the stub length. . . . .	177
7.9	Scattering parameters generated by analytical modelling for a design 2 stub. . . . .	179
7.10	Measured scattering parameters for stubs with four different geometries. . . . .	181
7.11	Comparison between the measured scattering parameters and those generated by analytical modelling for a design 2 stub. . . . .	182



7.12	Measured scattering parameters for stub 2 design compared to measured scattering parameters for which the impedance mismatch of the ports and transmission lines is removed. . . . .	183
7.13	Measured scattering parameters for stub 2 design compared to scattering parameters calculated analytically (theoretical) and scattering parameters calculated analytically with the effect of the transmission lines (txl) removed. . . . .	184
7.14	Illustration of the minimum and maximum stub length dimensions. . . . .	186
7.15	Comparison of measured scattering parameters for stub 2 design with those calculated analytically using the minimum stub length and the maximum stub length with the effect of fringing also accounted for. . . . .	187
7.16	Examples of air-bridges created using copper tape, made to counteract the effect of discontinuities along the transmission line. . . . .	188
7.17	Measured scattering parameters for stub 2 design with: no air-bridge; a large air-bridge where the discontinuity is fully covered; and a small air-bridge where the ground planes were connected with minimal copper tape. . . . .	189
7.18	Measured and simulated scattering parameters for stub designs 1 and 2. . . . .	190
7.19	Measured and simulated scattering parameters for stub designs 3 and 4. . . . .	191
7.20	The first example of defected ground structure, taken from [22]. . . . .	192
7.21	Example spiral defected ground structure resonators fabricated using screen printing on paper. . . . .	193
7.22	Schematic diagram of an example spiral defected ground structure resonator. Units for all dimensions are in mm. . . . .	194
7.23	Simulated scattering parameters for spiral defected ground structure resonators with varying dimensions with the largest spiral edge ranging from 6 mm to 20 mm. . . . .	195
7.24	Measured scattering parameters for spiral defected ground structure resonators with varying dimensions with the largest spiral edge ranging from 7 mm to 11 mm. . . . .	197
7.25	Measured and simulated scattering parameter $s_{12}$ for an example spiral defected ground structure resonator with 15 (left) and 30 mm (right) transmission lines on either side of the resonator to determine the effect of transmission line length. . . . .	199
7.26	Measured scattering parameter $s_{12}$ for three spiral resonators. One with two identical 9 mm spirals on either side of the transmission line, one with two identical 10 mm spirals on either side of the transmission line and a third with two different spirals on either side of the transmission line, one of 9 mm and one of 10 mm. . . . .	200
7.27	Measured scattering parameter $s_{12}$ for five devices. Four with one identical spiral on either side of the transmission line of sizes 7, 9, 10 and 11 mm and another device with four different pairs of spirals connected along one transmission line. . . . .	201
7.28	Simulated scattering parameters for two pairs of identical spirals, one with a longest length of 8 mm and one with a longest length of 10 mm, when the spacing between them was increased from 1 mm to 25 mm. . . . .	202
7.29	Measured scattering parameters $s_{21}$ and $s_{22}$ for an example 9 mm spiral resonator with humidity increased from 40% to 90% and then returned to 40%. . . . .	203

7.30	Measured scattering parameters $s_{21}$ and $s_{22}$ for an example 10 mm spiral resonator with humidity increased from 40% to 90% and then returned to 40%. . . . .	204
7.31	Measured scattering parameters $s_{21}$ and $s_{22}$ for an example 11 mm spiral resonator with humidity increased from 40% to 90% and then returned to 40%. . . . .	205
7.32	Measured scattering parameters for a spiral resonator with a 8 mm spiral and a 11 mm spiral when it is not touched, and when the spirals are touched independently on the printed and non-printed side of the device. . . . .	206

# List of Tables

3.1	Surface roughness values for Powercoat HD 95 paper with various scan areas taken using a Zygo white light interferometer. . . . .	47
3.2	Comparison of surface roughness measurements for Diavite DH-7 and Talysurf PGI 1250 profilometers. . . . .	48
3.3	Comparison of contact angle measurements for a range of papers. . . . .	51
3.4	Comparison of sheet resistance values obtained for thermally evaporated and screen-printed layers on various papers. . . . .	58
3.5	Examples of adhesion testing, including the ISO standard rating and images of the samples after testing. . . . .	63
3.6	Key papers and their relative properties. . . . .	64
3.7	Fabrication methods and their relative properties as determined in this work. . . . .	66
3.8	Comparison of paper samples with silicon, glass and PET . . . . .	68
4.1	Details on mesh properties of polyester meshes with different thread counts. . . . .	73
4.2	Example dimensions for screen-printed resistors using differing metal inks. . . . .	87
4.3	Screen-printed inductors, comparing measured values of inductance and resistance with theoretical calculations. . . . .	90
5.1	Dimensions of interdigitated touch sensor designs. . . . .	98
5.2	Parameters and dimensions used in the COMSOL modelling of the touch sensors. . . . .	101
5.3	Comparison of the original three finger models trialled in COMSOL. In reality, touch pads are touched on the back, the front is shown here for clarity. . . . .	102
5.4	Comparison of capacitance values for the touch pad designs calculated by Equation (5.1), COMSOL modelling, measured by the impedance analyser and the oscillator-based system. . . . .	112
5.5	Capacitance values for the various designs in touched and untouched states measured using the custom set-up. All values represent the maximum and minimum data. . . . .	117
5.6	Comparison of capacitance values for untouched and touched sensors for work by different groups. . . . .	118
6.1	The effect of changing various transmission line parameters on $\alpha$ , $v$ and $Z$ . . . . .	151
6.2	Environmental Scanning Electron Microscope (ESEM) images of silver flake ink on matt paper at relative humidities between 10 and 90%. . . . .	160

6.3	Percentages and permittivity values for non-freezing water (tightly bound water), freeze-bound water (slightly bound water), freezing-unbound water (free water) and paper at 30, 50, 70 and 90% relative humidity. Percentages have been taken from [21] for uncoated paper, permittivity of free water taken from [28] and permittivity of loosely bound water from [27]. . . . .	166
7.1	Analytical, simulated and measured resonant frequencies for the stub designs. . . . .	179
7.2	Measured resonant frequencies ( $f_r$ ) for four stub geometries compared to analytically calculated resonant frequencies for the same stubs with the effect of fringing accounted for. . . . .	185
7.3	Measured resonant frequencies for four spiral DGS resonators and their respective bandwidth and quality factors. . . . .	198

# Chapter 1

## Introduction

Paper is one of the most versatile and flexible surfaces ever created by mankind. Invented over 2000 years ago in China, and further developed by Cai Lun [1], it is inexpensive, lightweight, mechanically flexible and, most importantly, easily recyclable. Thanks to its properties, it has now become one of the most common materials found in everyday life, such as printing paper, packaging, newspapers, magazines, bags, artworks, etc. It is not surprising therefore that its use in electronic technology is currently being heavily investigated, both commercially and in academia.

Paper-based electronics refers to electronic devices and circuits where either the substrate or part of the device itself consists of paper. While paper is not a direct competitor to silicon for high-performance electronics, as it cannot rival the extremely low surface roughness or easily sustain nanometre-scale features, it can be considered alongside silicon and other substrates for applications where cost and ease of fabrication are more important than performance.

The fast production of paper and its ability to be recycled means it is highly suited for disposable devices [2–4]. A key advantage of paper over plastic is the lack of un-recyclable waste. The UK government is highly concerned over the amount of single-use plastic waste, and several policies are now in place to monitor and reduce the amount of plastic used in packaging [5–7]. Currently, 81.9% of paper and cardboard is recovered and recycled, compared to 44.9% of plastic [8]. The amount of mismanaged plastic waste generated by the coastal population of a single country ranges from 1.1 to 8.8 million tonnes [9]. Paper can simply be burnt (Wang et al. have shown an example of an antenna on paper being burnt which can be important for military applications [10]). Work has also been done to ensure that silver ink can be removed from paper as part of the recycling process [11].

Paper has several properties which can be considered as both advantages and disadvantages depending on the application. For example, the high surface roughness of paper in comparison to

glass can be considered a disadvantage as it will increase the sheet resistance of deposited metal layers. However, in paper-based batteries, high surface roughness leads to a high surface area for reactants to be stored which makes the batteries more efficient [12].

One of the main advantages of paper over other substrates is the fact it is foldable [13]. This is of great interest as it can be used to improve the performance of devices. For example, Liu et al. have produced a piezoresistive cantilever strain sensor which, when the cantilever is folded, increases in stiffness and sensitivity [14]. A carbon resistor is placed at the end of a paper cantilever and connected to silver contact pads. The paper cantilever is much longer than the carbon and so the conductive sections are not folded, only the paper. Groups have incorporated folding into batteries in order to increase the areal energy but keep the surface area minimised when folded [15, 16]. Siegel et al. have produced various foldable printed circuit boards from paper including a crane with LEDs and an anti-tamper envelope [17]. Nogi et al. have investigated foldable antennas from silver nanowires on nanopaper; when the antenna is folded, the resonant frequency shifts [18]. Lin et al. recently demonstrated deformable photodetector arrays on paper [19]. While Lee et al. showed the potential for folding memory [20].

Paper is thousands of times cheaper than silicon or glass. Printer paper is also lower in price than plastics, making it the most cost-effective substrate for electronics. This low cost makes paper-based devices disposable which may be required in smart packaging applications and biological assays. It also paves the way for a new generation of low-cost, flexible gadgets on paper [21].

Technology is now moving towards ‘The Internet of Things’, this is the idea that everything will eventually be connected in a ‘smart’ environment where day-to-day objects will communicate with each other and to centralised control systems. A typical example of this is a refrigerator which automatically stock audits then creates an order with the supermarket. It could also provide alerts for items which are nearing their use-by date and potential recipes which include these items. This also means that an object can be monitored from cradle to grave. The benefits of paper mean it can be easily utilised, at a low cost, in this area. The possibility of home fabrication of printed paper-based electronics has also been demonstrated [22].

An extensive review of existing fabrication methods and devices has been compiled by Tobjörk and Österbacka [23].

## 1.1 Types of Paper

There are many types of paper available, including those that can be bought off the high street, speciality papers, and those that are created for a specific application. Devices have been created on several standard papers including tracing paper [24], tissue paper [25] and card [26, 27]. Groups have compared several papers throughout their work to determine the optimum paper for a certain application. Ref. [28] looks into using thermoplastic electrically conductive adhesives on various papers and also comparing them to PET film. Ohlund et al. compared readily available papers in terms of their properties affecting conductivity of inkjet printed films, including absorption, porosity and surface roughness [29]. Similarly, reference [30] studied the effect of conductivity with various paper properties and reference [31] compared a smooth paper and a rough, porous paper for their compatibility with screen printing.

In addition to commercially available papers, paper can also be fabricated for a specific purpose or application from cellulose fibres or a standard paper can be adapted. For example, reference [32] investigated the effect of altering the coating materials and manufacturing processes of paper, to change its reaction with applied functional polymers such as PEDOT:PSS. In a similar way, Andersson et al. studied the process of dip-coating paper in NaCl for use as humidity sensors; although this increased resistance, it also increased humidity sensitivity [33]. Wang et al. used Teslin paper, which does not deform in water, to demonstrate its ability to be folded and create three-dimensional devices [10].

Several groups have studied nano-cellulose paper, where only the smaller cellulose fibres are used, reducing surface roughness but still producing a ‘green’ material [3, 18, 34–37]. The result of this can be a transparent substrate which has been used for solar cells and transistors [38, 39]. Nanopaper has also been used for a substrate on which to produce antennas [18], a specific example of this takes advantage of the high dielectric constant in order to create miniaturised antennas [40].

In addition to nano-cellulose fibre paper, paper can be easily treated, for example with chemicals or metal compounds, to make it conductive [41, 42]. Reference [41] presents the use of iongels to coat raw cellulose pulp which increases the conductivity of the paper and reference [42] presents the use of silica coating of paper to aid in the sintering of silver inks. Gullapalli et al. embedded piezoelectric zinc oxide in a stable paper matrix to create a nano-composite strain sensor [43], Lessing et al. have produced an omniphobic ‘fluoroalkylated paper’ for high resolution patterns [44] and Thiemann et al. have produced a cellulose based ion-gel for use as a high capacitance gate dielectric. Bioactive papers have been created for use as a material in bioassays [45–47].

## 1.2 Fabrication Methods for Paper Electronics

Traditionally, common fabrication methods for substrates used in the electronics industry, such as silicon or glass, require a cleanroom environment to reduce the chance of defective devices, for example photolithography. These processes are time-consuming and expensive, contrasting with the simple and cost-effective properties of paper substrates [2]. Paper is compatible with both cleanroom processes and also other, well-established, high-volume manufacturing methods. An example of this is newspapers, which have been printed in volume for the last century. Paper-based electronic devices have been produced using a number of large-scale printing methods including gravure printing [48, 49], flexographic printing [50], screen printing [31, 51–58], electrohydrodynamic jet printing [59] and inkjet printing [60–71].

A wide variety of non-printing fabrication methods have been used to create devices on paper substrates including physical vapour deposition [72], soap film coating [73], filtration [74, 75], electroplating [76], spray coating [77, 78], photolithography [79] and direct writing [34, 80–86]. The dry transfer of silver nanowires was investigated by Kim et al. using a dry film photoresist and PET by hot pressing [87].

Direct writing covers a wide range of methods which are often low cost and simple. Using a pencil is a form of direct writing and is the easiest method of producing a conductive layer on paper. Pencils have been used to create simple passive components as well as the active layer in field effect transistors [88–90]. They have also been used to create strain gauges for use as weighing scales [91], gas sensors [92] and chemiresistors [93]. Graphene itself can also be deposited on paper substrates by filtration; although this is a more complex process, it often yields far better results than using a pencil [74, 75, 94]. Huang et al. produced an antenna using a highly conductive graphene laminate that had been compressed with rolling, improving the conductivity by more than 50 times [95].

Another simple example of direct writing is a roller-ball pen filled with liquid-metal ink [81, 83, 84]. Russo et al. have produced a colloidal silver ink which is used in a roller-ball pen to create simple circuits to light up LEDs and a 3D antenna [84]. Li et al. use a similar ‘pen’ method to deposit a thermocouple made from gallium/gallium oxide [80]. Using the same principles as a roller-ball pen, Zheng et al. have produced a method using a static set-up in tapping mode; again, this utilises a liquid metal ink [82]. Zheng et al. also use a roller-ball pen with a moving stage for mounting and moving the substrate [34]. Conductive patterns can be produced in a similar way using a fixed syringe rather than a rollerball pen [85, 86]. Anagnostou et al. used this technique to print antennas for use



in flexible displays [86].

Printing techniques for paper-based electronics include inkjet printing, screen printing, gravure printing and flexographic printing. These techniques are all well-established and have been used for non-conductive ink printing for many years. Inkjet printing is commonly used for paper-based electronics so there is a lot of literature presented here, however it is not scalable in the same way as the other methods and so has not been considered for this work. Gravure printing uses a cylinder with recessed cells which is coated in ink using a blade and then rolled over the substrate so that the recessed pattern is transferred. Gravure printing can achieve a print resolution between 20 - 75  $\mu\text{m}$  and print speeds of 20 - 1000 m/min. Flexographic printing is similar to gravure printing however the pattern is raised on the cylinder rather than recessed and the cylinder is made from a flexible material. Flexographic printing can achieve a print resolution between 30 - 75  $\mu\text{m}$  and print speeds of 50 - 500 m/min. Screen printing will be described in detail in Chapter 2 but in short uses a screen which consists of a frame and patterned mesh through which ink is forced onto a substrate using a squeegee. Screen printing can achieve a print resolution between 50 - 100  $\mu\text{m}$  and print speeds of 10 - 100 m/min. Screen printing was chosen for this work due to the ease of initial set up, its scalability and low cost. The values quoted here for print features and print speeds are taken from the review by Tobjörk and Österbacka [23].

Inkjet printing is one of the most common fabrication methods for flexible electronics and can be used to print both conductive and dielectric materials [60–71, 96–103]. Fukuda et al. studied the profile control of silver electrodes which can be altered by varying the relative humidity and the jetting properties [62]. Andersson et al. have used inkjet printing to produce hybrid electronics in which double-sided paper circuit boards consist of printed and standard components affixed to the board [63]. Sanchez et al. detail the use of inkjet printing to produce skin mountable tattoo paper tags which can be used for monitoring [60].

Several groups have studied the manufacturing of radio frequency identification (RFID) Tags and radio frequency (RF) structures on paper [60, 61, 64, 67–71, 104]. Tentzeris's group at the Georgia Institute of Technology is one of the main groups working on inkjet-printed RF devices, looking into reducing the cost and complexity [61, 64, 69–71, 105–110]. Reference [64] details their work investigating printing only the outline of antenna structures in order to speed up the fabrication process and reduce costs. Reference [71] details work towards RF devices for use in wireless devices including a temperature sensor, a battery-less solar-powered tag and a running shoe with an incorporated piezo-scavenging tag.

Curing and sintering of conductive inks has been widely investigated to optimise printing methods. Groups have addressed the transient variation of an area of inkjet-printed silver nanoparticle ink during furnace sintering [111]. Ultraviolet (UV) curable inks have been formulated to avoid the use of heat which can degrade paper-based substrates [112–114]. Microwave sintering has been considered for its speed [115]. Allen et al. presented work on substrate facilitated nanoparticle sintering at room temperature [116]. The sintering mechanism is based on the chemical removal of the nanoparticle stabilising ligand and is shown to provide conductivity above a quarter that of bulk silver.

Screen printing is compatible with production line processing meaning that fast fabrication of screen-printed devices is possible. It also has low capital costs and can be used to print large areas. Bjorninen et al. compared screen printing, gravure printing and copper etching for fabricating RFID tags [117]. The results of the study show that each of the studied fabrication methods can be used to manufacture reliable RFID tags. Shin et al. compare screen-printed RFID antennas with those fabricated by copper etching and these also show similar performance [118].

As with inkjet printing, different materials can be screen printed, including dielectrics [53]. Screen printing is limited in feature size, often to hundreds of microns, but can be further reduced to tens of microns with micro-machined silicon stencils and viscosity-controlled inks [55, 119]. The feature size is limited by the screen, however literature is available to determine the achievable parameters depending on the material and thread size [120, 121].

Other fabrication methods are often limited to certain papers and inks, for example inkjet printing is not compatible with highly viscous inks as they cannot be printed through the small nozzles used. It is also not compatible with matt papers as the low viscosity ink is absorbed into the porous structure. Screen printing is shown in this work to be compatible with all types of paper and therefore can be used to produce highly flexible devices such as capacitors for use in fully printed low-cost passive RFID labels [51]. Screen printing requires higher viscosity inks than inkjet printing, however inks for both printing methods are widely available.

### **1.3 Paper-based Electronic Devices**

Research on paper-based devices is still a relatively new field in comparison to research into devices which use substrates such as silicon or glass. Although it is still in its infancy, paper-based electronics has yielded a number of devices including displays [122–126], transistors [89, 127–131] and photovoltaic cells [132]. One of the aims of research into paper-based electronics is to produce complete systems

on paper, including the inputs and outputs, the power supply and the device itself. Liu et al. have produced a microfluidic device with integral battery and electrochromic read-out [133]. Paper can also be part of larger device, and gold electrodes on paper have been shown as links between other electronic components [134].

The simplest electronics on paper are hybrid devices that are generally aimed for outreach programs and kits which can be used by anyone [135–137]. These kits include simple components like light emitting diodes (LEDs) and conductive ink that can be directly written on paper substrates, acting as connections between the components. For example, carbon-based inks have been used in order to create LED circuits integrated with artwork or more complex circuits that can be used for pop-up books [138] and also ‘paper robots’ [139, 140]. Karagozler et al. have created paper-based circuits which use different gestures to harvest energy, which can be integrated into pop-up books so no external power supply is required [141].

Another use for paper which is of great interest is in microfluidic devices which can be used for disposable biological assays [142–150]. Highly porous paper (filter paper) and wax printing can be used to create channels within the paper which guide solutions to combine or into test areas. An origami box approach has been used to produce three-dimensional assays which can perform several tests in parallel [151, 152]. Martinez et al. have produced programmable assays using push buttons which can be activated using a pen or pencil [143]. Microfluidic timers have also been created so that assays with time requirements can be realised [153, 154]. In addition to microfluidic devices, other biosensors have been created with paper, including electrodes for electrocardiogram (ECG) signal acquisition [155], a respiration sensor [156] and electrochemical sensors for detecting human papillomavirus [157].

A large area of interest is ‘electronic skin’ [158–162]; these are electronic/active devices which can be adhered to the skin and monitor various parameters or conditions. These devices may be used for healthcare applications but also as a skin-like sensor which is capable of sensing and visualising various sensations and 3D shapes [163]. This research has been continued by a number of groups and the idea of ‘multi-sensing’ has become of great interest. Many of these skin-like sensors will monitor parameters such as strain, temperature, humidity and even pH. Some will also incorporate transistors, LEDs and power sources.

The foldability of paper in electronic devices has been demonstrated by Siegel et al. who created origami structures with printed electronics including an envelope which could potentially be used for security applications [17]. Foldable touch pads fabricated by incorporating polypyrrole into paper and wax patterning of chromatography paper are presented in [164]. Foldable antennas can be created

for the miniaturisation and tunability of devices, in addition to adapting the shape for a specific application [40, 165]. Cybulski et al. have created a microscope for which the casing of the lenses is created using the principles of origami. This microscope can be produced at a very low cost for use in third world countries [166].

Environmental monitoring has become of great concern in the past decade. Issues regarding air pollution and the need for stable conditions have led to the need for high numbers of sensors in a network to monitor conditions in various locations simultaneously [167]. Temperature sensors [168], humidity sensors [24, 33, 35, 169–171] and gas sensors [168, 172–174] have all been produced on paper to reduce costs so that they can be used on a large scale in a disposable manner. Work by Unander and Nilsson [171] included the characterisation of moisture sensors in packaging monitoring applications, for example along production lines in factories. Several fabrication methods and designs were explored in order to produce an optimum monitoring device using paper as a substrate; the repeatability of the devices and effect of humidity on the paper samples were considered. Nitrogen dioxide and ammonia gas sensors [169, 174–176] have been produced in addition to carbon nano-tube chemiresistive sensors which can identify a number of gases [177]. Kiasari et al. have created carbon dioxide and ultra-violet sensors using zinc oxide ink ‘drawn’ onto paper [92].

As well as biological and chemical sensors, strain sensors have been developed on paper. Khajeh et al. have created a strain sensing paper via micro-inkjet printing of conductive carbon black [178]. Many groups have created weighing systems from paper-based strain sensors [14, 91, 179]. Yang et al. have created origami triboelectric nano-generators and self-powered pressure sensors which have also been used as weighing systems [180]. Another application is using paper-based strain sensors for structural health monitoring [43].

RFID is a technology which allows objects to be identified but it can also be used in conjunction with a sensor; for this reason it is one of the key technologies in wireless sensor networks (WSN). A number of groups work on RFID tags on paper [51, 181–185]. Bhattacharyya et al. [186, 187] have investigated the potential for RFID tags to be used as low-cost sensors by mapping a change in some physical parameter of interest to a controlled change in RFID tag antenna electrical properties. In addition, it has been shown that the antenna can suffer a permanent change when critical thresholds have been surpassed. Similarly, Tenzeris’ group [71, 107] have produced an integrated RFID-enabled wireless sensor network infrastructure using ultra-high frequency/radio frequency (UHF/RF) RFID-enabled sensor nodes by inkjet printing. Their work includes various antenna configurations and sensors for a range of applications.

Many other groups have produced antennas on paper using various conductive materials and fabrication methods. Reference [188] detailed work using water-based isotropically conductive adhesives to fabricate RF antennas on various substrates, including paper. Reference [28] detailed work using thermoplastic electrically conductive adhesives to produce bendable antennas. Simple circuits including an antenna and loudspeaker have been fabricated on paper using carbon nanotube ink [189]. In addition to the methods already covered, antennas have been fabricated using gravure printing [48], inkjet overprinting [190] and direct writing [86]. Three-dimensional antennas have been realised, in addition to those that have been folded [84, 191]. Monti et al. have created a three-dimensional patch UHF reader antenna on a cardboard box which has omnidirectional irradiation and is circularly polarised. Their work included comparisons of various antenna designs tested [192].

In addition to the devices detailed above, several other devices have been produced on paper. Other examples include resistor, inductor and capacitor (RLC) circuits on three different papers using direct writing [193]. Metamaterials on paper have been investigated for terahertz sensing [194]. Lien et al. produced printed paper memory using inkjet and screen printing to create metal-insulator-metal resistive random-access memory (RAM) [195]. Loudspeakers [196], actuators [197], photo-conductive infrared sensors [198] and microplasma-generation devices [199] have also been fabricated on paper. SensorTape is a paper-based tape which has a series of repeated proximity sensing modules which can be cut and rejoined. The placement of the sensor nodes provides information on distances including height which can be used to recreate a shape [200].

As many devices require power, paper-based storage devices and generators have been realised to create complete systems on paper [12, 201–203]. Thom and Chen have studied fluidic batteries for use in microfluidic devices [204] and electrophoretic devices [16] respectively. Cheng et al. have produced foldable lithium ion batteries using origami principles, resulting in higher areal energy with a low actual area [15]. Paper-based supercapacitors [205–208] and nano-generators have also been fabricated [209]. A self-powered system has been created on paper consisting of a paper-based triboelectric/piezoelectric hybrid nanogenerator and a paper-based supercapacitor which are capable of sustaining power for low power portable devices [41].

## 1.4 Effect of Humidity on Paper

The hygroscopic nature of paper means that the relative humidity of the environment can have dramatic effects on the performance or operation of paper-based devices. There is a large body

of literature regarding the effect of relative humidity on the printing processes using paper substrates, and also the changes which occur. Padfield reports on the interaction of water vapour with paper and states that “a single piece of paper will come substantially to equilibrium with the surrounding space within a minute or two” and that the diameter of the cellulose fibres increases more drastically than the length [210]. The *Handbook of Physical Testing of Paper* details the hysteric nature of the process; the water absorbed with high relative humidity is not completely desorbed when the humidity is lowered and that the desorption process is much slower than the absorption one [211]. Above a certain humidity, permanent changes can occur in the structure, for example the paper edges are often longer than the centre dimensions and lead to pages no longer being flat [212].

The chemical interaction between paper and water is detailed later in Chapter 6. However it is known that both the conductive and dielectric properties of a paper substrate can change with relative humidity. The conductivity of bare cellulose fibres was studied by Han et al. with changing humidity [169]. Water dissociation occurs under applied bias, producing  $H^+$  and  $OH^-$  ions, and so a current can flow due to the ionic conduction. Water has a higher permittivity than cellulose and so the addition of water to the paper at higher humidities increases the permittivity of the mixture [213, 214]. It has been shown that the addition of water to the substrate changed both the dielectric and dimensional parameters, the water caused swelling of the cellulose fibres and so their dimensions increased [215–217].

Some groups have utilised the dramatic change in the operation of paper-based devices at varying humidities to create sensors [24, 33, 169, 171, 218–220]. Andersson et al. investigated the effect of humidity on different paper coatings, finding that sodium chloride and silica coatings produce good humidity sensors whereas alumina-only coatings result in poor humidity sensors [33]. Kanaparthi et al. created humidity sensors, as part of a multifunctional sensor array, using an interdigitated capacitive sensor drawn on paper using a 5B pencil [220]. The increase in permittivity of the paper with humidity caused a change in capacitance of the sensor which can be used to measure the humidity.

Although the hygroscopic properties of paper can be utilised to create sensors, in many cases it needs to be overcome. Bollstrom et al. investigated the issues with humidity and the use of curtain printing to manufacture a multilayer coating with sealed barrier layer for improved printability, high barrier properties and paper strength [221]. Dimensional changes in the paper, including a change in surface roughness, with humidity were recorded. Niarchos et al. used ZnO nanoparticles as a passivation layer for their gas sensors to control the effect of humidity on the paper substrate [222].

The effect of humidity on paper-based devices has often been included in lifetime or reliability

testing [221, 223]. Merilampi et al. considered five accelerated tests, including low temperature ( $-40^{\circ}\text{C}$ ), high temperature ( $125$  and  $150^{\circ}\text{C}$ ), slow temperature cycling (between  $-55$  and  $100^{\circ}\text{C}$ ), high temperature/high humidity ( $90^{\circ}\text{C}$  and  $65\%$  RH) and water dipping. The high temperature/humidity was found to have the greatest effect on the RFID tags measured for this work; the humidity changed the impedance and increased the losses [224].

## 1.5 Structure of the Thesis

Throughout the literature on paper-based electronics, groups often compared various papers for a certain application however there was no definitive single source which looked at a wide variety of paper types and applications. This work aimed to fill that void and act as a reference point for all future work on paper-based electronics and was of fundamental importance for the field. The literature showed a gap in the understanding of the changes in paper with humidity; although it was clearly shown to heavily influence the performance of devices, most publications tended to only qualify this effect at best, especially at microwave frequencies. This work provides the first detailed quantitative analysis of this area. Although microwave devices are very well researched, there were minimal examples of paper-based microwave devices in the literature. This work includes the fabrication of screen printed microwave components on paper which have not yet been produced in the literature.

This thesis investigates paper-based electronics with the use of several types of paper and fabrication methods. Touch pads and microwave devices are fabricated using screen printing to illustrate paper-based devices and the effect of humidity is considered. Chapter 2 begins with the description of the experimental techniques used in this work. Chapter 3 presents the investigation of several types of paper, including readily available papers and papers designed for specific applications. Similarly, thermal evaporation and screen printing are compared for their use in paper-based electronics. Depending on the desired application, matrices for both different substrates and fabrication methods can be used to determine the optimum of both. Screen printing is determined as the optimum fabrication method for this work and the process is optimised in Chapter 4.

Chapter 5 presents results for screen-printed interdigitated capacitive touch pads. Measurements are compared with numerical modelling for both the touched and untouched sensors. The effect of contact area, force and placement of the finger are considered and it is shown that for any users and touch conditions, there is a distinct, measurable change in capacitance with touch.

Results of microwave device simulation and fabrication are presented in Chapters 6 and 7. Coplanar

waveguide structures are chosen as printing is only required on one side. Transmission lines with various geometries are used to characterise both the substrate and conductor parameters between 300 kHz and 3 GHz. The effect of humidity is of high importance due to the hygroscopic nature of the paper substrate and is shown in this work to have an effect on the transmission line parameters. The results presented in Chapter 6 regarding the effect of humidity have been published [225].

Transmission line stubs are investigated in Chapter 7 as the simplest form of coplanar waveguide resonators. Detailed investigation of the differences between theoretical and measured resonant frequencies is included. More complex resonant structures are then considered using spiral defected ground structures. Multiple resonances are achieved and the use of the devices as both touch and humidity sensors presented.

## References

- [1] S. O. Thompson, "Paper manufacturing and early books," *Annals of the New York Academy of Sciences*, vol. 314, no. 1, p. 167, 1978.
- [2] J. Liu, C. Yang, H. Wu, Z. Lin, Z. Zhang, R. Wang, B. Li, F. Kang, L. Shi, and C. P. Wong, "Future paper based printed circuit boards for green electronics: Fabrication and life cycle assessment," *Energy and Environmental Science*, vol. 7, no. 11, p. 3674, 2014.
- [3] Y. H. Jung, T.-H. Chang, H. Zhang, C. Yao, Q. Zheng, V. W. Yang, H. Mi, M. Kim, S. J. Cho, D.-W. Park, H. Jiang, J. Lee, Y. Qiu, W. Zhou, Z. Cai, S. Gong, and Z. Ma, "High-performance green flexible electronics based on biodegradable cellulose nanofibril paper," *Nature Communications*, vol. 6, p. 7170, May 2015.
- [4] F. Costa, S. Genovesi, C. Mercier, D. Girbau, F. Costa, and D. Girbau, "D2.4 - Material characterization for green chipless RFID report," 2015.
- [5] HM Government, "A green future: Our 25 year plan to improve the environment," 2018.
- [6] Department for Environment, Food and Rural Affairs, "Consultation on changes to the plastic packaging business targets for 2016-17 and new targets for plastic and glass for 2018-20," 2015.
- [7] House of Commons Environmental Audit Committee, "Plastic bottles: Turning back the plastic tide," 2017.
- [8] Department for Environment, Food and Rural Affairs, "UK statistics on waste," 2018.
- [9] J. R. Jambeck, R. Geyer, C. Wilcox, T. R. Siegler, M. Perryman, A. Andrady, R. Narayan, and K. L. Law, "Plastic waste inputs from land into the ocean," *Science*, vol. 347, no. 6223, p. 768, 2015.
- [10] Y. Wang, H. Guo, J. J. Chen, E. Sowade, Y. Wang, K. Liang, K. Marcus, R. R. Baumann, and Z. S. Feng, "Paper-based inkjet-printed flexible electronic circuits," *ACS Applied Materials and Interfaces*, vol. 8, no. 39, p. 26112, 2016.
- [11] K. Dogome, T. Enomae, and A. Isogai, "Method for controlling surface energies of paper substrates to create paper-based printed electronics," *Chemical Engineering and Processing: Process Intensification*, vol. 68, p. 21, 2013.
- [12] T. H. Nguyen, A. Fraiwan, and S. Choi, "Paper-based batteries: A review," *Biosensors and Bioelectronics*, vol. 54, p. 640, 2014.
- [13] S. Perks, "Flat-pack physics," *Physics World*, December 2015.
- [14] X. Liu, M. Mwangi, X. Li, M. O'Brien, and G. M. Whitesides, "Paper-based piezoresistive MEMS sensors," *Lab on a Chip*, vol. 11, p. 2189, 2011.
- [15] Q. Cheng, Z. Song, T. Ma, B. B. Smith, R. Tang, H. Yu, H. Jiang, and C. K. Chan, "Folding paper-based lithium-ion batteries for higher areal energy densities," *Nano Letters*, vol. 13, no. 10, p. 4969, 2013.
- [16] S.-S. Chen, C.-W. Hu, I.-F. Yu, Y.-C. Liao, and J.-T. Yang, "Origami paper-based fluidic batteries for portable electrophoretic devices," *Lab on a Chip*, vol. 14, no. 12, p. 2124, 2014.
- [17] A. C. Siegel, S. T. Phillips, M. D. Dickey, N. Lu, Z. Suo, and G. M. Whitesides, "Foldable printed circuit boards on paper substrates," *Advanced Functional Materials*, vol. 20, p. 28, 2010.
- [18] M. Nogi, N. Komoda, K. Otsuka, and K. Suganuma, "Foldable nanopaper antennas for origami electronics," *Nanoscale*, vol. 5, no. 10, p. 4395, 2013.
- [19] C.-H. Lin, D.-S. Tsai, T.-C. Wei, D.-H. Lien, J.-J. Ke, C.-H. Su, J.-Y. Sun, Y.-C. Liao, and J.-H. He, "Highly deformable origami paper photodetector arrays," *ACS Nano*, vol. 11, no. 10, 2017.



- [20] B. H. Lee, D. I. Lee, H. Bae, H. Seong, S. B. Jeon, M. L. Seol, J. W. Han, M. Meyyappan, S. G. Im, and Y. K. Choi, "Foldable and disposable memory on paper," *Scientific Reports*, vol. 6, p. 38389, 2016.
- [21] A. J. Steckl, "Electronics on paper," *IEEE Spectrum*, no. 1, 2013.
- [22] P. Rosa, A. Câmara, and C. Gouveia, "The potential of printed electronics and personal fabrication in driving the internet of things," *Open Journal of Internet of Things*, vol. 1, no. 1, p. 16, 2015.
- [23] D. Tobjörk and R. Österbacka, "Paper electronics," *Advanced Materials*, vol. 23, p. 1935, 2011.
- [24] C. Steffens, A. Manzoli, R. T. Paschoalin, L. Tiggemann, J. Steffens, E. Teixeira, and P. S. D. P. Herrmann, "Tracing paper substrate used for development of interdigitated graphite electrode and its application as humidity sensor," *Synthetic Metals*, vol. 183, p. 36, 2013.
- [25] S. B. Fuller, E. J. Wilhelm, and J. M. Jacobson, "Ink-jet printed nanoparticle microelectromechanical systems," *Journal of Microelectromechanical Systems*, vol. 11, no. 1, p. 54, 2002.
- [26] U. Kavčič, L. Pavlovič, M. Pivar, M. Dokić, B. Batagelj, and T. Muck, "Printed electronics on recycled paper and cardboards," *Informacije MIDEM*, vol. 43, no. 1, p. 50, 2013.
- [27] H. He, L. Sydanheimo, J. Virkki, and L. Ukkonen, "Experimental study on inkjet-printed passive UHF RFID tags on versatile paper-based substrates," *International Journal of Antennas and Propagation*, 2016.
- [28] H. Wu, S. W. Chiang, W. Lin, C. Yang, Z. Li, J. Liu, X. Cui, F. Kang, and C. P. Wong, "Towards practical application of paper-based printed circuits: Capillarity effectively enhances conductivity of the thermoplastic electrically conductive adhesives," *Scientific Reports*, vol. 4, p. 6275, 2014.
- [29] T. Öhlund, J. Örtengren, S. Forsberg, and H. E. Nilsson, "Paper surfaces for metal nanoparticle inkjet printing," *Applied Surface Science*, vol. 259, p. 731, 2012.
- [30] L. K. Wood, E. Hrehorova, T. W. Joyce, P. D. Fleming, and M. Joyce, "Paper substrates and inks for printed electronics," *Pira Ink on Paper Symposium*, July 2005.
- [31] M. Žveglič, N. Hauptman, M. Maček, and M. K. Gunde, "Screen-printed electrically conductive functionalities in paper substrates," *Materiali in Tehnologije*, vol. 45, no. 6, p. 627, 2011.
- [32] B. Trnovec, M. Stanel, U. Hahn, A. Hübler, H. Kempa, R. Sangl, and M. Forster, "Coated paper for printed electronics," *Professional Papermaking*, vol. 1, p. 48, 2009.
- [33] H. Andersson, A. Manuilskiy, J. Gao, C. Lidenmark, J. Siden, S. Forsberg, T. Unander, and H. E. Nilsson, "Investigation of humidity sensor effect in silver nanoparticle ink sensors printed on paper," *IEEE Sensors Journal*, vol. 14, no. 3, p. 623, 2014.
- [34] G. Zheng, Y. Cui, E. Karabulut, L. Wågberg, H. Zhu, and L. Hu, "Nanostructured paper for flexible energy and electronic devices," *MRS Bulletin*, vol. 38, no. 4, p. 320, 2013.
- [35] T. Syrový, V. Kumar, M. Toivakka, C. Xu, L. Syrova, J. Reboun, and D. Bousfield, "Fully printed biodegradable nanocellulose-based humidity sensor for SMART label applications," *Iarigai Conference, Helsinki*, 2015.
- [36] S. Thiemann, S. J. Sachnov, F. Pettersson, R. Bollström, R. Österbacka, P. Wasserscheid, and J. Zaumseil, "Cellulose-based ionogels for paper electronics," *Advanced Functional Materials*, vol. 24, no. 5, p. 625, 2014.
- [37] J. Xue, F. Song, X.-W. Yin, X.-L. Wang, and Y.-Z. Wang, "Let It Shine: A transparent and photoluminescent foldable nanocellulose/quantum dot paper," *ACS Applied Materials & Interfaces*, p. 10076, 2015.
- [38] L. Hu, G. Zheng, J. Yao, N. Liu, B. Weil, M. Eskilsson, E. Karabulut, Z. Ruan, S. Fan, J. T. Bloking, M. D. McGehee, L. Wågberg, and Y. Cui, "Transparent and conductive paper from nanocellulose fibers," *Energy & Environmental Science*, vol. 6, p. 513, 2013.
- [39] J. Huang, H. Zhu, Y. Chen, C. Preston, K. Rohrbach, J. Cumings, and L. Hu, "Highly transparent and flexible nanopaper transistors," *ACS Nano*, vol. 7, no. 3, p. 2106, 2013.
- [40] T. Inui, H. Koga, M. Nogi, N. Komoda, and K. Suganuma, "A miniaturized flexible antenna printed on a high dielectric constant nanopaper composite," *Advanced Materials*, vol. 27, no. 6, p. 1112, 2015.
- [41] X. He, Y. Zi, H. Yu, S. L. Zhang, J. Wang, W. Ding, H. Zou, W. Zhang, C. Lu, and Z. L. Wang, "An ultrathin paper-based self-powered system for portable electronics and wireless human-machine interaction," *Nano Energy*, vol. 39, p. 328, June 2017.
- [42] H. Andersson, A. Manuilskiy, C. Lidenmark, J. Gao, T. Öhlund, S. Forsberg, J. Örtengren, W. Schmidt, and H.-E. Nilsson, "The influence of paper coating content on room temperature sintering of silver nanoparticle ink," *Nanotechnology*, vol. 24, no. 45, 2013.
- [43] H. Gullapalli, V. S. M. Vemuru, A. Kumar, A. Botello-Mendez, R. Vajtai, M. Terrones, S. Nagarajah, and P. M. Ajayan, "Flexible piezoelectric zno-paper nanocomposite strain sensor," *Small*, vol. 6, p. 1641, 2010.
- [44] J. Lessing, A. C. Glavan, S. B. Walker, C. Keplinger, J. A. Lewis, and G. M. Whitesides, "Inkjet printing of conductive inks with high lateral resolution on omniphobic 'rF paper' for paper-based electronics and MEMS," *Advanced Materials*, vol. 26, no. 27, p. 4677, 2014.
- [45] G. E. Fridley, C. A. Holstein, S. B. Oza, and P. Yager, "The evolution of nitrocellulose as a material for bioassays," *MRS Bulletin*, vol. 38, no. 4, p. 326330, 2013.

- [46] C. Sicard and J. D. Brennan, "Bioactive paper: Biomolecule immobilization methods and applications in environmental monitoring," *MRS Bulletin*, vol. 38, no. 4, p. 331334, 2013.
- [47] A. N. Aleshin, I. P. Shcherbakov, A. K. Khripunov, A. A. Tkachenko, I. N. Trapeznikova, and V. N. Petrov, "Light-emitting flexible transparent paper based on bacterial cellulose modified with semiconducting polymer MEH:PPV," *Flexible and printed electronics*, vol. 2, no. 3, p. 35004, 2017.
- [48] H. Zhu, B. B. Narakathu, Z. Fang, A. Tausif Aijazi, M. Joyce, M. Atashbar, and L. Hu, "A gravure printed antenna on shape-stable transparent nanopaper," *Nanoscale*, vol. 6, no. 15, p. 9110, 2014.
- [49] H. Kempa, B. Trnovec, M. Stanel, and A. Huebler, "Printed electronics on paper," *Proceedings of Organic Electronics Conference and Exhibition*, 2007.
- [50] J. Olkkonen, K. Lehtinen, and T. Erho, "Flexographically printed fluidic structures in paper," *Analytical Chemistry*, vol. 82, no. 24, p. 10246, 2010.
- [51] J. Reboun, T. Blecha, T. Syrový, A. Hamáček, and A. Shlykevich, "Printed passive components for RFID labels," *Proceedings of the 5th Electronics System-Integration Technology Conference*, 2014.
- [52] J. W. Kim and S. B. Jung, "Electrical characterization of screen-printed conductive circuit with silver nanopaste," *Japanese Journal of Applied Physics*, vol. 48, no. 6, 2009.
- [53] A. Eshkeiti, A. S. G. Reddy, S. Emamian, B. B. Narakathu, M. Joyce, M. Joyce, P. D. Fleming, B. J. Bazuin, and M. Z. Atashbar, "Screen printing of multilayered hybrid printed circuit boards on different substrates," *IEEE Transactions on Components, Packaging and Manufacturing Technology*, vol. 5, no. 3, p. 415, 2015.
- [54] J. Suikkola, T. Björninen, M. Mosallaei, T. Kankkunen, P. Iso-Ketola, L. Ukkonen, J. Vanhala, and M. Mäntysalo, "Screen-printing fabrication and characterization of stretchable electronics," *Scientific Reports*, vol. 6, p. 25784, 2016.
- [55] W. J. Hyun, E. B. Secor, M. C. Hersam, C. D. Frisbie, and L. F. Francis, "High-resolution patterning of graphene by screen printing with a silicon stencil for highly flexible printed electronics," *Advanced Materials*, vol. 27, no. 1, p. 109, 2015.
- [56] X. Cao, H. Chen, X. Gu, B. Liu, W. Wang, Y. Cao, F. Wu, and C. Zhou, "Screen printing as a scalable and low-cost approach for rigid and flexible thin-film transistors using separated carbon nanotubes," *ACS Nano*, vol. 8, no. 12, p. 12769, 2014.
- [57] F. Khan and V. Solanki, "Paper moisture sensor based on microwave resonator," *National Conference on Knowledge, Innovation in Technology and Engineering*, p. 321, April 2015.
- [58] A. E. Ostfeld, I. Deckman, A. M. Gaikwad, C. M. Lochner, and A. C. Arias, "Screen printed passive components for flexible power electronics," *Scientific Reports*, vol. 5, p. 15959, 2015.
- [59] J.-U. Park, M. Hardy, S. J. Kang, K. Barton, K. Adair, D. K. Mukhopadhyay, C. Y. Lee, M. S. Strano, A. G. Alleyne, J. G. Georgiadis, P. M. Ferreira, and J. A. Rogers, "High-resolution electrohydrodynamic jet printing," *Nature Materials*, vol. 6, p. 782, October 2007.
- [60] V. Sanchez-Romaguera, M. A. Ziai, D. Oyeka, S. Barbosa, J. S. R. Wheeler, J. C. Batchelor, E. A. Parker, and S. G. Yeates, "Towards inkjet-printed low cost passive UHF RFID skin mounted tattoo paper tags based on silver nanoparticle inks," *Journal of Materials Chemistry C*, vol. 1, p. 6395, 2013.
- [61] L. Yang, A. Rida, R. Vyas, and M. M. Tentzeris, "RFID tag and RF structures on a paper substrate using inkjet-printing technology," *IEEE Transactions on Microwave Theory and Techniques*, vol. 55, no. 12, p. 2894, 2007.
- [62] K. Fukuda, T. Sekine, D. Kumaki, and S. Tokito, "Profile control of inkjet printed silver electrodes and their application to organic transistors," *ACS applied materials & interfaces*, vol. 5, p. 3916, 2013.
- [63] H. Andersson, A. Manuilskiy, S. Haller, M. Hummelgå, J. Sidén, C. Hummelgå, H. K. Olin, and H.-E. Nilsson, "Assembling surface mounted components on ink-jet printed double sided paper circuit board," *Nanotechnology*, vol. 25, p. 94002, 2014.
- [64] G. Orecchini, F. Alimenti, V. Palazzari, A. Rida, M. Tentzeris, and L. Roselli, "Design and fabrication of ultra-low cost radio frequency identification antennas and tags exploiting paper substrates and inkjet printing technology," *IET Microwaves, Antennas & Propagation*, vol. 5, no. 8, p. 993, 2011.
- [65] E. B. Secor, P. L. Prabhurashi, K. Puntambekar, M. L. Geier, and M. C. Hersam, "Inkjet printing of high conductivity, flexible graphene patterns," *Journal of Physical Chemistry Letters*, vol. 4, no. 8, p. 1347, 2013.
- [66] S. Glatzel, Z. Schnepf, and C. Giordano, "From paper to structured carbon electrodes by inkjet printing," *Angewandte Chemie - International Edition*, vol. 52, p. 2355, 2013.
- [67] J. Virtanen, "Inkjet-Printed UHF RFID Tags on Renewable Materials," *Advances in Internet of Things*, vol. 02, p. 79, October 2012.
- [68] B. S. Cook and A. Shamim, "Inkjet printing of novel wideband and high gain antennas on low-cost paper substrate," *IEEE Transactions on Antennas and Propagation*, vol. 60, no. 9, p. 4148, 2012.
- [69] A. Rida, L. Yang, R. Vyas, and M. M. Tentzeris, "Conductive inkjet-printed antennas on flexible low-cost paper-based substrates for RFID and WSN applications," *IEEE Antennas and Propagation Magazine*, vol. 51, no. 3, p. 13, 2009.
- [70] L. Yang and M. M. Tentzeris, "3D multilayer integration and packaging on organic/paper low-cost substrates for RF and wireless applications," *Conference Proceedings of the International Symposium on Signals, Systems and Electronics*, p. 267, 2007.

- [71] V. Lakafosis, A. Rida, R. Vyas, L. Yang, S. Nikolaou, and M. M. Tentzeris, "Progress towards the first wireless sensor networks consisting of inkjet-printed, paper-based RFID-enabled sensor tags," *Proceedings of the IEEE*, vol. 98, no. 9, p. 1601, 2010.
- [72] C. Ramade, S. Silvestre, F. P. Delannoy, and B. Sorli, "Thin film HF RFID tag deposited on paper by thermal evaporation," *International Journal of Radio Frequency Identification Technology and Applications*, vol. 4, no. 1, p. 49, 2012.
- [73] R. Zhang, H. Andersson, M. Andersson, B. Andres, H. K. Edlund, P. Edström, S. Edvardsson, S. Forsberg, M. Hummelgard, N. Johansson, K. Karlsson, H.-E. Nilsson, M. Norgren, M. Olsen, T. Uesaka, T. Ohlund, and H. K. Olin, "Soap-film coating: High-speed deposition of multilayer nanofilms," *Scientific Reports*, vol. 3, p. 1477, 2013.
- [74] G.-W. Huang, H.-M. Xiao, and S.-Y. Fu, "Paper-based silver-nanowire electronic circuits with outstanding electrical conductivity and extreme bending stability," *Nanoscale*, vol. 6, no. 15, p. 8495, 2014.
- [75] W. J. Hyun, O. O. Park, and B. D. Chin, "Foldable graphene electronic circuits based on paper substrates," *Advanced Materials*, vol. 25, p. 4729, 2013.
- [76] M. Balde, F. Jacquemoud-Collet, A. Vena, and B. Sorli, "Physical wet microelectronic technologies on paper substrate for flexible electronic applications," *Sensors & Actuators: A. Physical*, vol. 240, p. 118, 2016.
- [77] J. Kim, J. H. Jong, and W. S. Kim, "Repeatedly bendable paper touch pad via direct stamping of silver nanoink with pressure-induced low-temperature annealing," *IEEE Transactions on Nanotechnology*, vol. 12, no. 6, p. 1139, 2013.
- [78] L. Wang and J. Liu, "Ink spraying based liquid metal printed electronics for directly making smart home appliances," *ECS Journal of Solid State Science and Technology*, vol. 4, no. 4, p. 3057, 2015.
- [79] M. D. Cooke and D. Wood, "Fabrication of micron scale metallic structures on photo paper substrates by low temperature photolithography for device applications," *Journal of Micromechanics and Microengineering*, vol. 25, no. 11, p. 115017, 2015.
- [80] H. Li, Y. Yang, and J. Liu, "Printable tiny thermocouple by liquid metal gallium and its matching metal," *Applied Physics Letters*, vol. 101, p. 3, 2012.
- [81] Y. Gao, H. Li, and J. Liu, "Direct writing of flexible electronics through room temperature liquid metal ink," *PLoS ONE*, vol. 7, no. 9, p. 45485, 2012.
- [82] Y. Zheng, Z.-Z. He, J. Yang, and J. Liu, "Personal electronics printing via tapping mode composite liquid metal ink delivery and adhesion mechanism," *Scientific Reports*, vol. 4, p. 4588, 2014.
- [83] Y.-L. Tai and Z.-G. Yang, "Fabrication of paper-based conductive patterns for flexible electronics by direct-writing," *Journal of Materials Chemistry*, vol. 21, p. 5938, 2011.
- [84] A. Russo, B. Y. Ahn, J. J. Adams, E. B. Duoss, J. T. Bernhard, and J. A. Lewis, "Pen-on-paper flexible electronics," *Advanced Materials*, vol. 23, 2011.
- [85] B. Y. Ahn, D. Shoji, C. J. Hansen, E. Hong, D. C. Dunand, and J. A. Lewis, "Printed origami structures," *Advanced Materials*, vol. 22, no. 20, p. 2251, 2010.
- [86] D. E. Anagnostou, A. A. Gheethan, A. K. Amert, and K. W. Whites, "A direct-write printed antenna on paper-based organic substrate for flexible displays and WLAN applications," *IEEE/OSA Journal of Display Technology*, vol. 6, no. 11, p. 558, 2010.
- [87] S. Kim, T. Y. Eom, M. Cho, K. Y. Song, C. H. An, H. J. Lee, and B. Hwang, "Simple transfer of Ag nanowires by dry film photoresist for paper-based flexible electronics," *Materials Letters*, vol. 199, p. 196, 2017.
- [88] J. E. Thompson, "Pencil-on-paper capacitors for hand-drawn RC circuits and capacitive sensing," *Journal of Chemistry*, 2017.
- [89] N. Kurra, D. Dutta, and G. U. Kulkarni, "Field effect transistors and RC filters from pencil-trace on paper," *Physical chemistry chemical physics*, vol. 15, p. 8367, 2013.
- [90] N. Kurra and G. U. Kulkarni, "Pencil-on-paper: Electronic devices," *Lab on a Chip*, vol. 13, no. 15, p. 2866, 2013.
- [91] T. L. Ren, H. Tian, D. Xie, and Y. Yang, "Flexible graphite-on-paper piezoresistive sensors," *Sensors (Switzerland)*, vol. 12, no. 5, p. 6685, 2012.
- [92] N. M. Kiasari, S. Soltanian, B. Gholamkhass, and P. Servati, "Sketching functional, ubiquitous ZnO nano-sensors on paper," *RSC Advances*, vol. 4, no. 38, p. 19663, 2014.
- [93] C.-W. Lin, Z. Zhao, J. Kim, and J. Huang, "Pencil drawn strain gauges and chemiresistors on paper," *Scientific Reports*, vol. 4, p. 3812, 2014.
- [94] S. Kanaparthy and S. Badhulika, "Solvent-free fabrication of paper based all-carbon disposable multifunctional sensors and passive electronic circuits," *Royal Society of Chemistry Advances*, vol. 6, no. 98, p. 95574, 2016.
- [95] X. Huang, T. Leng, X. Zhang, J. C. Chen, K. H. Chang, A. K. Geim, K. S. Novoselov, and Z. Hu, "Binder-free highly conductive graphene laminate for low cost printed radio frequency applications," *Applied Physics Letters*, vol. 106, no. 20, p. 203105, 2015.
- [96] S. Magdassi, A. Bassa, Y. Vinetsky, and A. Kamyshny, "Silver nanoparticles as pigments for water-based ink-jet inks," *Chemistry of Materials*, vol. 15, no. 17, p. 2208, 2003.

- [97] M. C. Dang, T. M. Dung Dang, and E. Fribourg-Blanc, "Inkjet printing technology and conductive inks synthesis for microfabrication techniques," *Advances in Natural Sciences: Nanoscience and Nanotechnology*, vol. 4, p. 15009, 2013.
- [98] S. M. Bidoki, J. Nouri, and A. A. Heidari, "Inkjet deposited circuit components," *Journal of Micromechanics and Microengineering*, vol. 20, no. 5, p. 55023, 2010.
- [99] S.-P. Chen, H.-L. Chiu, P.-H. Wang, and Y.-C. Liao, "Inkjet printed conductive tracks for printed electronics," *ECS Journal of Solid State Science and Technology*, vol. 4, no. 4, p. 3026, 2015.
- [100] V. Sanchez-Romaguera, S. Wünscher, B. M. Turki, R. Abbel, S. Barbosa, D. J. Tate, D. Oyeka, J. C. Batchelor, E. A. Parker, U. S. Schubert, and S. G. Yeates, "Inkjet printed paper based frequency selective surfaces and skin mounted RFID tags: The interrelation between silver nanoparticle ink, paper substrate and low temperature sintering technique," *Journal of Materials Chemistry C*, vol. 3, no. 9, p. 2132, 2015.
- [101] G. Cummins, "Inkjet printing of conductive materials: A review," *Circuit World*, vol. 38, no. 4, p. 193, 2012.
- [102] A. Määttänen, P. Ihalainen, P. Pulkkinen, S. Wang, H. Tenhu, and J. Peltonen, "Inkjet-printed gold electrodes on paper: Characterisation and functionalization," *ACS Applied Materials & Interfaces*, vol. 4, p. 955, 2012.
- [103] M. Mengel and I. Nikitin, "Inkjet printed dielectrics for electronic packaging of chip embedding modules," *Microelectronic Engineering*, vol. 87, no. 4, p. 593, 2010.
- [104] D. Redinger, S. Molesca, S. Yin, R. Farschi, and V. Subramanian, "An ink-jet-deposited passive component process for RFID," *IEEE Transactions on Electron Devices*, vol. 51, no. 12, p. 1978, 2004.
- [105] R. Li, G. DeJean, M. Tentzeris, and J. Laskar, "Integrable miniaturized folded antennas for RFID applications," *IEEE Antennas and Propagation Society Symposium*, vol. 2, p. 5, 2004.
- [106] G. Shaker, S. Safavi-Naeini, N. Sangary, and M. M. Tentzeris, "Inkjet printing of ultrawideband (UWB) antennas on paper-based substrates," *IEEE Antennas and Wireless Propagation Letters*, vol. 10, p. 111, 2011.
- [107] R. Vyas, V. Lakafosis, A. Rida, N. Chaisilwattana, S. Travis, J. Pan, and M. M. Tentzeris, "Paper-based RFID-enabled wireless platforms for sensing applications," *IEEE Transactions on Microwave Theory and Techniques*, vol. 57, no. 5, p. 1370, 2009.
- [108] A. Rida, G. Shaker, F. Nasri, T. Reynolds, S. Nikolaou, and M. Tenzeris, "Inkjet printing of dual band conformal antenna for use in Wifi frequency bands," *2010 IEEE Radio and Wireless Symposium*, p. 65, 2010.
- [109] F. Alimenti, M. Virili, G. Orecchini, P. Mezzanotte, V. Palazzari, M. M. Tentzeris, and L. Roselli, "A new contactless assembly method for paper substrate antennas and UHF RFID chips," *IEEE Transactions on Microwave Theory and Techniques*, vol. 59, no. 3, p. 627, 2011.
- [110] M. Marroncelli, D. Trincherio, and M. M. Tentzeris, "Paper-based, inkjet-printed, text-meandered UHF resonant antennas for RFID applications," *30th International Union of Radio Science General Assembly and Scientific Symposium*, 2011.
- [111] D. Kim, I. Lee, Y. Yoo, Y. J. Moon, and S. J. Moon, "Transient variation of a cross-sectional area of inkjet-printed silver nanoparticle ink during furnace sintering," *Applied Surface Science*, vol. 305, p. 453, 2014.
- [112] M. Layani, I. Cooperstein, and S. Magdassi, "UV crosslinkable emulsions with silver nanoparticles for inkjet printing of conductive 3D structures," *Journal of Materials Chemistry C*, vol. 1, no. 19, p. 3244, 2013.
- [113] M. Sangermano, A. Chiolerio, G. Marti, and P. Martino, "UV-cured acrylic conductive inks for microelectronic devices," *Macromolecular Materials and Engineering*, vol. 298, p. 607, 2013.
- [114] D. Zhai, T. Zhang, J. Guo, X. Fang, and J. Wei, "Water-based ultraviolet curable conductive inkjet ink containing silver nano-colloids for flexible electronics," *Colloids and Surfaces A: Physicochemical and Engineering Aspects*, vol. 424, 2013.
- [115] J. Perelaer, B. J. De Gans, and U. S. Schubert, "Ink-jet printing and microwave sintering of conductive silver tracks," *Advanced Materials*, vol. 18, p. 2101, 2006.
- [116] M. Allen, J. Leppäniemi, M. Vilkmann, A. Alastalo, and T. Mattila, "Substrate-facilitated nanoparticle sintering and component interconnection procedure," *Nanotechnology*, vol. 21, no. 47, p. 475204, 2010.
- [117] T. Björninen, S. Merilampi, L. Ukkonen, L. Sydänheimo, and P. Ruuskanen, "The effect of fabrication method on passive UHF RFID tag performance," *International Journal of Antennas and Propagation*, 2009.
- [118] D. Y. Shin, Y. Lee, and C. H. Kim, "Performance characterization of screen printed radio frequency identification antennas with silver nanopaste," *Thin Solid Films*, vol. 517, no. 21, 2009.
- [119] O. J. Arenas, E. L. D. L. Jarrige, and F. Boone, "Creating screen-printed passive components for microwave applications," *Microelectronics International*, vol. 27, no. 2, p. 84, 2010.
- [120] A. Hobby, "Fundamentals of screens for electronics screen printing," *Circuit World*, vol. 16, p. 16, 1990.
- [121] G. C. Dubey, "Screens for screen printing electronic circuits," *Microelectronics and Reliability*, vol. 13, p. 203, 1974.
- [122] A. C. Siegel, S. T. Phillips, B. J. Wiley, and G. M. Whitesides, "Thin, lightweight, foldable thermochromic displays on paper," *Lab on a Chip*, vol. 9, no. 19, p. 2775, 2009.

- [123] P. Andersson, D. Nilsson, P. O. Svensson, M. Chen, A. Malmström, T. Remonen, T. Kugler, and M. Berggren, "Active matrix displays based on all-organic electrochemical smart pixels printed on paper," *Advanced Materials*, vol. 14, no. 20, p. 1460, 2002.
- [124] A. Asadpoordarvish, A. Sandström, C. Larsen, R. Bollström, M. Toivakka, R. Österbacka, and L. Edman, "Light-emitting paper," *Advanced Functional Materials*, vol. 25, no. 21, p. 3238, 2015.
- [125] P. F. Bai, R. A. Hayes, M. L. Jin, L. L. Shui, Z. Chuan Yi, L. Wang, X. Zhang, and G. F. Zhou, "Review of paper-like display technologies," *Progress in Electromagnetic Research Letters*, vol. 147, p. 95, 2014.
- [126] M. Hagedon, S. Yang, A. Russell, and J. Heikenfeld, "Bright e-paper by transport of ink through a white electrofluidic imaging film," *Nature Communications*, vol. 3, p. 1173, 2012.
- [127] I. Cunha, R. Barras, P. Grey, D. Gaspar, E. Fortunato, R. Martins, and L. Pereira, "Reusable cellulose-based hydrogel sticker film applied as gate dielectric in paper electrolyte-gated transistors," *Advanced Functional Materials*, vol. 27, no. 16, p. 1606755, 2017.
- [128] M. Trifunovic, T. Shimoda, and R. Ishihara, "Solution-processed polycrystalline silicon on paper," *Applied Physics Letters*, vol. 106, no. 16, p. 163502, 2015.
- [129] A. T. Zocco, H. You, J. A. Hagen, and A. J. Steckl, "Pentacene organic thin-film transistors on flexible paper and glass substrates," *Nanotechnology*, vol. 25, 2014.
- [130] W. Dou, L. Qiang Zhu, J. Jiang, and Q. Wan, "Flexible protonic/electronic coupled neuron transistors self-assembled on paper substrates for logic applications," *Applied Physics Letters*, vol. 102, no. 2013, p. 93509, 2013.
- [131] Y.-H. Kim and J.-I. Han, "Organic thin-film transistors on flexible substrates," *Journal of the Korean Physical Society*, vol. 48, p. 118, January 2006.
- [132] A. Hübler, B. Trnovec, T. Zillger, M. Ali, N. Wetzold, M. Mingeback, A. Wagenpfahl, C. Deibel, and V. Dyakonov, "Printed paper photovoltaic cells," *Advanced Energy Materials*, vol. 1, p. 1018, 2011.
- [133] H. Liu and R. M. Crooks, "Paper-based electrochemical sensing platform with integral battery and electrochromic read-out," *Analytical Chemistry*, vol. 84, no. 5, p. 2528, 2012.
- [134] A. Bellacicca and P. Milani, "Supersonic cluster beam fabrication of a stretchable keyboard with multilayer electrical interconnects integrated with paper-based flexible devices," *ArXiv e-prints*, 2017.
- [135] L. Buechley and S. Hendrix, "Paints, paper, and programs: First steps toward the computational sketchbook," *Proceedings of the Third International Conference on Tangible and Embedded Interaction*, p. 9, 2009.
- [136] M. Coelho, L. Hall, J. Berzowska, and P. Maes, "Pulp-based computing: A framework for building computers out of paper," *Proceedings of the Annual ACM Conference on Human Factors in Computing Systems*, p. 3527, 2009.
- [137] D. A. Mellis, S. Jacoby, L. Buechley, H. Perner-Wilson, and J. Qi, "Microcontrollers as material," *Proceedings of the 7th International Conference on Tangible, Embedded and Embodied Interaction*, p. 83, 2013.
- [138] J. Qi and L. Buechley, "Electronic Popables: Exploring paper-based computing through an interactive pop-up book," *International Conference on Tangible, Embedded and Embodied Interaction*, p. 121, 2010.
- [139] G. Saul, C. Xu, and M. Gross, "Interactive paper devices: end-user design & fabrication," *Proceedings of the Fourth International Conference on Tangible, Embedded and Embodied Interaction*, p. 205, 2010.
- [140] J. Qi and L. Buechley, "Animating paper using shape memory alloys," *Proceedings of the Annual ACM Conference on Human Factors in Computing Systems*, p. 749, 2012.
- [141] M. E. Karagozler, I. Poupyrev, G. K. Fedder, and Y. Suzuki, "Paper generators: Harvesting energy from touching, rubbing and sliding," *ACM User Interface Software and Technology Conference*, p. 23, 2013.
- [142] L. Luo, X. Li, and R. M. Crooks, "Low-voltage origami-paper-based electrophoretic device for rapid protein separation," *Analytical Chemistry*, vol. 86, p. 12390, 2014.
- [143] A. W. Martinez, S. T. Phillips, Z. Nie, C.-M. Cheng, E. Carrilho, B. J. Wiley, and G. M. Whitesides, "Programmable diagnostic devices made from paper and tape," *Lab on a Chip*, vol. 10, p. 2499, 2010.
- [144] W.-J. Lan, E. J. Maxwell, C. Parolo, D. K. Bwambok, A. B. Subramaniam, and G. M. Whitesides, "Paper-based electroanalytical devices with an integrated, stable reference electrode," *Lab on a Chip*, vol. 13, p. 4103, 2013.
- [145] S. T. Phillips and G. G. Lewis, "Advances in materials that enable quantitative point-of-care assays," *MRS Bulletin*, vol. 38, no. 4, p. 315319, 2013.
- [146] J. P. Rolland and D. A. Mourey, "Paper as a novel material platform for devices," *MRS Bulletin*, vol. 38, no. 4, p. 299305, 2013.
- [147] E. J. Maxwell, A. D. Mazzeo, and G. M. Whitesides, "Paper-based electroanalytical devices for accessible diagnostic testing," *MRS Bulletin*, vol. 38, no. 4, p. 309314, 2013.
- [148] Y. Zha and A. L. Zhang, "A paper-based microfluidic switch activated by surface acoustic waves," *Proceedings of the 2011 Symposium on Piezoelectricity, Acoustic Waves and Device Applications*, p. 142, 2011.
- [149] N. Jankovic and V. Radonic, "A microwave microfluidic sensor based on a dual-mode resonator for dual-sensing applications," *Sensors*, vol. 17, no. 12, p. 2713, 2017.

- [150] B. S. Cook, J. R. Cooper, and M. M. Tentzeris, "An inkjet-printed microfluidic rfid-enabled platform for wireless lab-on-chip applications," *IEEE Transactions on Microwave Theory and Techniques*, vol. 61, no. 12, p. 4714, 2013.
- [151] H. Liu and R. M. Crooks, "Three-dimensional paper microfluidic devices assembled using the principles of origami," *Journal of the American Chemical Society*, vol. 133, p. 17564, 2011.
- [152] A. C. Glavan, D. C. Christodouleas, B. Mosadegh, H. D. Yu, B. S. Smith, J. Lessing, M. T. Ferna, and G. M. Whitesides, "Folding analytical devices for electrochemical ELISA in hydrophobic R<sup>H</sup> paper," *Analytical Chemistry*, vol. 86, p. 11999, 2014.
- [153] H. Noh and S. T. Phillips, "Metering the capillary-driven flow of fluids in paper-based microfluidic devices," *Analytical Chemistry*, vol. 82, no. 10, p. 4181, 2010.
- [154] H. Noh and S. T. Phillips, "Fluidic timers for time-dependent, point-of-care assays on paper," *Analytical Chemistry*, vol. 82, no. 19, p. 8071, 2010.
- [155] A. P. Alves, J. Martins, H. Placido da Silva, A. Lourenco, A. Fred, and H. Ferreria, "Experimental study and evaluation of paper-based inkjet electrodes for ECG signal acquisition," *International Conference on Physiological Computing Systems*, p. 275, 2012.
- [156] F. Güder, A. Ainla, J. Redston, B. Mosadegh, A. Glavan, T. J. Martin, and G. M. Whitesides, "Paper-based electrical respiration sensor," *Angewandte Chemie - International Edition*, vol. 2138, p. 5727, 2016.
- [157] P. Teengam, W. Siangproh, A. Tuantranont, C. S. Henry, T. Vilaivan, and O. Chailapakul, "Electrochemical paper-based peptide nucleic acid biosensor for detecting human papillomavirus," *Analytica Chimica Acta*, vol. 952, p. 32, 2017.
- [158] M. Weigel, T. Lu, G. Bailly, A. Oulasvirta, C. Majidi, and J. Steimle, "iSkin: Flexible, stretchable and visually customizable on-body touch sensors for mobile computing," *Proceedings of the 33rd Annual ACM Conference on Human Factors in Computing Systems*, p. 2991, 2015.
- [159] M. Ogata, Y. Sugiura, and Y. Makino, "SenSkin: Adapting skin as a soft interface," *Proceedings of the ACM Symposium on User Interface Software and Technology*, p. 539, 2013.
- [160] J. M. Nassar, M. D. Cordero, A. T. Kutbee, M. A. Karimi, G. A. T. Sevilla, A. M. Hussain, A. Shamim, and M. M. Hussain, "Paper skin multisensory platform for simultaneous environmental monitoring," *Advanced Materials Technologies*, 2016.
- [161] D. P. J. Cotton, I. M. Graz, and S. P. Lacour, "A multifunctional capacitive sensor for stretchable electronic skins," *IEEE Sensors Journal*, vol. 9, no. 12, 2009.
- [162] V. J. Lumelsky, M. S. Shur, and S. Wagner, "Sensitive skin," *IEEE Sensors Journal*, vol. 1, no. 1, p. 41, 2001.
- [163] T. Xu, W. Wang, X. Bian, X. Wang, X. Wang, J. Luo, and S. Dong, "High resolution skin-like sensor capable of sensing and visualizing various sensations and three dimensional shape," *Scientific Reports*, vol. 5, p. 12997, 2015.
- [164] M. Santhiago, J. Bettini, S. R. Araujo, and C. C. B. Bufon, "Three-dimensional organic conductive networks embedded in paper for flexible and foldable devices," *ACS Applied Materials and Interfaces*, vol. 8, no. 17, p. 10661, 2016.
- [165] C. Yang, H. Gu, W. Lin, M. M. Yuen, C. P. Wong, M. Xiong, and B. Gao, "Silver nanowires: From scalable synthesis to recyclable foldable electronics," *Advanced Materials*, vol. 23, no. 27, p. 3052, 2011.
- [166] J. S. Cybulski, J. Clements, and M. Prakash, "Foldscope: Origami-based paper microscope," *PLoS ONE*, vol. 9, no. 6, p. 98781, 2014.
- [167] D. D. Liana, B. Raguse, J. Justin Gooding, and E. Chow, "Recent advances in paper-based sensors," *Sensors (Switzerland)*, vol. 12, p. 11505, 2012.
- [168] A. Vena, L. Sydneimo, L. Ukkonen, and M. M. Tentzeris, "A fully inkjet-printed chipless RFID gas and temperature sensor on paper," *IEEE RFID Technology and Applications Conference*, vol. 2, p. 115, 2014.
- [169] J.-W. Han, B. Kim, J. Li, and M. Meyyappan, "A carbon nanotube based ammonia sensor on cellulose paper," *RSC Advances*, vol. 4, no. 2, p. 549, 2014.
- [170] E. M. Amin, S. Bhuiyan, N. Karmakar, and B. Winther-Jensen, "A novel em barcode for humidity sensing," *IEEE International Conference on RFID*, p. 82, 2013.
- [171] T. Unander and H. E. Nilsson, "Characterization of printed moisture sensors in packaging surveillance applications," *IEEE Sensors Journal*, vol. 9, no. 8, p. 922, 2009.
- [172] L. Yang, S. Member, R. Zhang, S. Member, and D. Staiculescu, "A novel conformal RFID-enabled module utilizing inkjet-printed antennas and carbon nanotubes for gas-detection applications," *IEEE Antennas and Wireless Propagation Letters*, vol. 8, p. 653, 2009.
- [173] P. Bahoumina and H. Hallil, "Chemical gas sensor based on a novel capacitive microwave flexible transducer and composite polymer carbon nanomaterials," *Symposium on Design, Test, Integration and Packaging of MEMs and MOEMs*, p. 5, 2017.
- [174] H. Liu, M. Li, O. Voznyy, L. Hu, Q. Fu, D. Zhou, Z. Xia, E. H. Sargent, and J. Tang, "Physically flexible, rapid-response gas sensor based on colloidal quantum dot solids," *Advanced Materials*, vol. 26, no. 17, p. 2718, 2014.

- [175] L. Huang, P. Jiang, D. Wang, Y. Luo, M. Li, H. Lee, and R. A. Gerhardt, "A novel paper-based flexible ammonia gas sensor via silver and SWNT-PABS inkjet printing," *Sensors and Actuators, B: Chemical*, vol. 197, p. 308, 2014.
- [176] J. Wang, X. Zhang, X. Huang, S. Wang, Q. Qian, W. Du, and Y. Wang, "Forced assembly of water-dispersible carbon nanotubes trapped in paper for cheap gas sensors," *Small*, vol. 9, no. 22, p. 3759, 2013.
- [177] K. Mirica, J. M. Azzarelli, J. G. Weis, J. M. Schnorr, and T. M. Swager, "Rapid prototyping of carbon-based chemiresistive gas sensors on paper," *Proceedings of the National Academy of Sciences of the United States of America*, vol. 110, p. 3265, 2013.
- [178] E. Khajeh, W. Lou, and B. Stoeber, "Paper-based strain sensing material," *Proceedings of the IEEE International Conference on Micro Electro Mechanical Systems (MEMS)*, p. 473, 2013.
- [179] T. Meiss, "Rapid prototyping of resistive MEMS sensing devices on paper substrates," *IEEE International Conference on Micro Electro Mechanical Systems (MEMS)*, p. 536, 2014.
- [180] P.-K. Yang, Z.-H. Lin, K. C. Pradel, L. Lin, X. Li, X. Wen, J.-H. He, and Z. L. Wang, "Paper-based origami triboelectric nanogenerators and self-powered pressure sensors," *ACS Nano*, vol. 9, no. 1, 2015.
- [181] M. A. Islam and N. C. Karmakar, "A novel compact printable dual-polarized chipless RFID system," *IEEE Transactions on Microwave Theory and Techniques*, vol. 60, no. 7, p. 2142, 2012.
- [182] B. S. Cook, R. Vyas, S. Kim, T. Thai, T. Le, A. Traille, H. Aubert, and M. M. Tentzeris, "RFID-based sensors for zero-power autonomous wireless sensor networks," *IEEE Sensors Journal*, vol. 14, no. 8, p. 2419, 2014.
- [183] S. Y. Y. Leung and D. C. C. Lam, "Performance of printed polymer-based RFID antenna on curvilinear surface," *IEEE Transactions on Electronics Packaging Manufacturing*, vol. 30, no. 3, p. 200, 2007.
- [184] C. Kruesi and M. Tentzeris, "'Magic Cube' Antenna configurations for ultra compact RFID and wireless sensor nodes," *Journal of Chemical Information and Modelling*, vol. 53, no. 9, p. 1689, 2013.
- [185] S. Preradovic, I. Balbin, N. C. Karmakar, and G. F. Swiegers, "Multiresonator-based chipless RFID system for low-cost item tracking," *IEEE Transactions on Microwave Theory and Techniques*, vol. 57, no. 5, p. 1411, 2009.
- [186] B. R. Bhattacharyya, C. Floerkemeier, and S. Sarma, "Low-cost, ubiquitous sensing," *Proceedings of the IEEE*, vol. 98, no. 9, p. 1593, 2010.
- [187] R. Bhattacharyya, C. Floerkemeier, S. Sarma, and D. Deavours, "RFID tag antenna based temperature sensing in the frequency domain," *IEEE International Conference on RFID*, p. 70, 2011.
- [188] C. Yang, W. Lin, Z. Li, R. Zhang, H. Wen, B. Gao, G. Chen, P. Gao, M. M. F. Yuen, and C. P. Wong, "Water-based isotropically conductive adhesives: Towards green and low-cost flexible electronics," *Advanced Functional Materials*, vol. 21, no. 23, p. 4582, 2011.
- [189] M. Dragoman, E. Flahaut, D. Dragoman, M. Al Ahmad, and R. Plana, "Writing simple RF electronic devices on paper with carbon nanotube ink," *Nanotechnology*, vol. 20, p. 375203, 2009.
- [190] N. Komoda, M. Nogi, K. Suganuma, and K. Otsuka, "Highly sensitive antenna using inkjet overprinting with particle-free conductive inks," *ACS Applied Materials and Interfaces*, vol. 4, no. 11, p. 5732, 2012.
- [191] J. J. Adams, E. B. Duoss, T. F. Malkowski, M. J. Motala, B. Y. Ahn, R. G. Nuzzo, J. T. Bernhard, and J. A. Lewis, "Conformal printing of electrically small antennas on three-dimensional surfaces," *Advanced Materials*, vol. 23, p. 1335, 2011.
- [192] G. Monti, L. Catarinucci, C. Vasanelli, and L. Tarricone, "3D patch antenna using a cardboard substrate for RFID reader applications," *Proceedings of the 9th European Radar Conference*, p. 884, 2012.
- [193] Y. Gao, H. Li, and J. Liu, "Directly writing resistor, inductor and capacitor to composite functional circuits: A super-simple way for alternative electronics," *PLoS ONE*, vol. 8, no. 8, p. 69761, 2013.
- [194] H. Tao, L. R. Chieffo, M. A. Brenckle, S. M. Siebert, M. Liu, A. C. Strikwerda, K. Fan, D. L. Kaplan, X. Zhang, R. D. Averitt, and F. G. Omenetto, "Metamaterials on paper as a sensing platform," *Advanced Materials*, vol. 23, no. 28, p. 3197, 2011.
- [195] D.-H. Lien, Z.-K. Kao, T.-H. Huang, Y.-C. Liao, S.-C. Lee, and J.-H. He, "All-printed paper memory," *ACS Nano*, p. 7613, 2014.
- [196] A. C. Hubler, M. Bellmann, G. C. Schmidt, S. Zimmermann, A. Gerlach, and C. Haentjes, "Fully mass printed loudspeakers on paper," *Organic Electronics*, vol. 13, no. 11, p. 2290, 2012.
- [197] J. Kim, C.-S. Song, and S.-R. Yun, "Cellulose based electro-active papers: Performance and environmental effects," *Smart Materials and Structures*, vol. 15, p. 719, 2006.
- [198] A. J. Gimenez, J. M. Yáñez-Limón, and J. M. Seminario, "Paper-based photoconductive infrared sensor," *Journal of Physical Chemistry C*, vol. 115, no. 38, p. 18829, 2011.
- [199] H. Cheng-Che, T. Jheng-Han, Y. Yao-Jhen, L. Ying-Chih, and L. Yen-Wen, "A foldable microplasma-generation device on a paper substrate," *JMEMS Letters*, vol. 21, no. 2, p. 253, 2012.
- [200] A. Dementyev and J. A. Paradiso, "SensorTape: Modular and programmable 3D-aware dense sensor network on a tape," *Proceedings of the 28th Annual ACM Symposium on User Interface Software and Technology*, p. 649, 2015.

- [201] A. M. Gaikwad, D. A. Steingart, T. Nga Ng, D. E. Schwartz, and G. L. Whiting, "A flexible high potential printed battery for powering printed electronics," *Applied Physics Letters*, vol. 102, no. 23, p. 233302, 2013.
- [202] L. Hu, H. Wu, and Y. Cui, "Printed energy storage devices by integration of electrodes and separators into single sheets of paper," *Applied Physics Letters*, vol. 96, p. 183502, 2010.
- [203] H. Lee and S. Choi, "An origami paper-based bacteria-powered battery," *Nano Energy*, vol. 15, p. 549, 2015.
- [204] N. K. Thom, K. Yeung, M. B. Pillion, and S. T. Phillips, "Fluidic batteries as low-cost sources of power in paper-based microfluidic devices," *Lab on a Chip*, vol. 12, no. 1, p. 1768, 2012.
- [205] H. Andersson, A. Britta, A. Manuilskiy, S. Forsberg, M. Hummelgard, J. Backstrom, R. Zhang, and H. Olin, "Contacting paper-based supercapacitors to printed electronics on paper substrates," *Nordic Pulp and Paper Research Journal*, vol. 27, no. 02, p. 476, 2012.
- [206] L. Liu, Z. Niu, L. Zhang, W. Zhou, X. Chen, and S. Xie, "Nanostructured graphene composite papers for highly flexible and foldable supercapacitors," *Advanced Materials*, vol. 26, no. 28, p. 4855, 2014.
- [207] W. Liu, C. Lu, H. Li, R. Y. Tay, L. Sun, X. Wang, W. L. Chow, X. Wang, K. Tay, Z. Chen, J. Yan, K. Feng, G. Lui, R. Tjandra, L. Rasenthiram, G. Chiu, and A. Yu, "Paper-based all-solid-state flexible micro-supercapacitors with ultra-high rate and rapid frequency response capabilities," *Journal of Materials Chemistry A: Materials for energy and sustainability*, vol. 4, p. 3754, 2016.
- [208] S. Wang, N. Liu, J. Tao, C. Yang, W. Liu, Y. Shi, Y. Wang, J. Su, L. Li, and Y. Gao, "Inkjet printing of conductive patterns and supercapacitors using a multi-walled carbon nanotube/Ag nanoparticle based ink," *Journal of Materials Chemistry A*, vol. 3, no. 5, p. 2407, 2015.
- [209] H. Guo, M. H. Yeh, Y. Zi, Z. Wen, J. Chen, G. Liu, C. Hu, and Z. L. Wang, "Ultralight Cut-Paper-Based Self-Charging Power Unit for Self-Powered Portable Electronic and Medical Systems," *ACS Nano*, vol. 11, no. 5, p. 4475, 2017.
- [210] T. Padfield, "The interaction of water vapour with paper," *Conservation Physics*, 2006.
- [211] R. Mark, C. C. Habeger, J. Borch, and M. B. Lyne, *Handbook of physical testing of paper*. CRC Press, 1993.
- [212] "Paper: Moisture and relative humidity," *Glatfelter, Technical Bulletin*, vol. 2, 2005.
- [213] S. Akinli-Kocak, "The influence of fiber swelling on paper wetting," *The University of Maine, Electronic Theses and Dissertations*, 2001.
- [214] C. C. Habeger and G. A. Baum, "The microwave dielectric constants of water-paper mixtures: The role of sheet structure and composition," *Journal of Applied Polymer Science*, vol. 28, no. 3, p. 969, 1983.
- [215] G. M. Dorris and D. G. Gray, "Effect of relative humidity on the external area of paper," *Journal of the Chemical Society, Faraday Transactions 1*, vol. 77, p. 713, 1981.
- [216] C. Hill, A. Norton, and G. Newman, "The water vapour sorption behavior of natural fibers," *Journal of Applied Polymer Science*, vol. 112, p. 1524, 2009.
- [217] J. Berthold, M. Rinaudo, and L. Salmeñ, "Association of water to polar groups; Estimates by an adsorption model for ligno-cellulosic materials," *Colloids and Surfaces A: Physicochemical and Engineering Aspects*, vol. 112, no. 2, p. 117, 1996.
- [218] M. Mraović, T. Muck, M. Pivar, J. Trontelj, and A. Pleteršek, "Humidity sensors printed on recycled paper and cardboard," *Sensors (Basel, Switzerland)*, vol. 14, no. 8, p. 13628, 2014.
- [219] M. Balde, A. Vena, and B. Sorli, "Moisture sensor feasibility on paper-based substrate," *Symposium on Design, Test, Integration and Packaging of MEMs and MOEMs*, 2015.
- [220] S. Kanaparthi and S. Badhulika, "Low cost, flexible and biodegradable touch sensor fabricated by solvent-free processing of graphite on cellulose paper," *Sensors and Actuators B: Chemical*, vol. 242, p. 857, 2016.
- [221] R. Bollström, F. Pettersson, P. Dolietis, J. Preston, R. Osterbacka, and M. Toivakka, "Impact of humidity on functionality of on-paper printed electronics," *Nanotechnology*, vol. 25, p. 94003, 2014.
- [222] G. Niarchos, G. Dubourg, G. Afroudakis, M. Georgopoulos, V. Tsouti, E. Makarona, V. Crnojevic-Bengin, and C. Tsamis, "Humidity sensing properties of paper substrates and their passivation with ZnO nanoparticles for sensor applications," *Sensors*, vol. 17, no. 3, p. 516, 2017.
- [223] L. Zhenzhong, M. Nezhil, X. George, O. Yuu, L. Guocheng, and B. Dayan, "Effects of temperature and humidity on UHF RFID," *Smart Materials, Structures & NDT in Aerospace Conference, Quebec, Canada*, November 2011.
- [224] S. L. Merilampi, J. Virkki, L. Ukkonen, and L. Sydneimo, "Testing the effects of temperature and humidity on printed passive uhf rfid tags on paper substrate," *International Journal of Electronics*, vol. 101, no. 5, pp. 711–730, 2014.
- [225] S. Shenton, M. Cooke, Z. Racz, C. Balocco, and D. Wood, "The effect of humidity on microwave characteristics of screen printed paper-based electronics," *Physica status solidi a*, in press.



## Chapter 2

# Experimental Techniques

### 2.1 Introduction

This chapter introduces fundamentals on the key experimental and numerical techniques used in the work presented in this thesis. Fabrication methods are first discussed: although several approaches for the deposition of conductive films have been investigated, only thermal evaporation and screen printing are considered due their potential scalability.

Surface profiling and imaging are essential for the characterisation of both paper and conductive films. Stylus profilometers, atomic-force microscopy and white-light interferometry have been utilised for topographic analysis, whereas the use of scanning-electron microscopy and focused ion-beam milling enabled high-resolution sample imaging.

The passive devices fabricated on paper were electrically characterised both under quasi-static conditions and at microwave frequencies using a vector network analyser (VNA). A general overview of the VNA operation has been included in this chapter, and further details on the experimental methodology have been included in the relevant chapters.

The experimental results have been supported by numerical simulations. Two commercial packages, COMSOL and Advanced Design System (ADS), have been used for simulating the device operation at low and microwave frequencies. Their key features are briefly detailed at the end of this chapter.

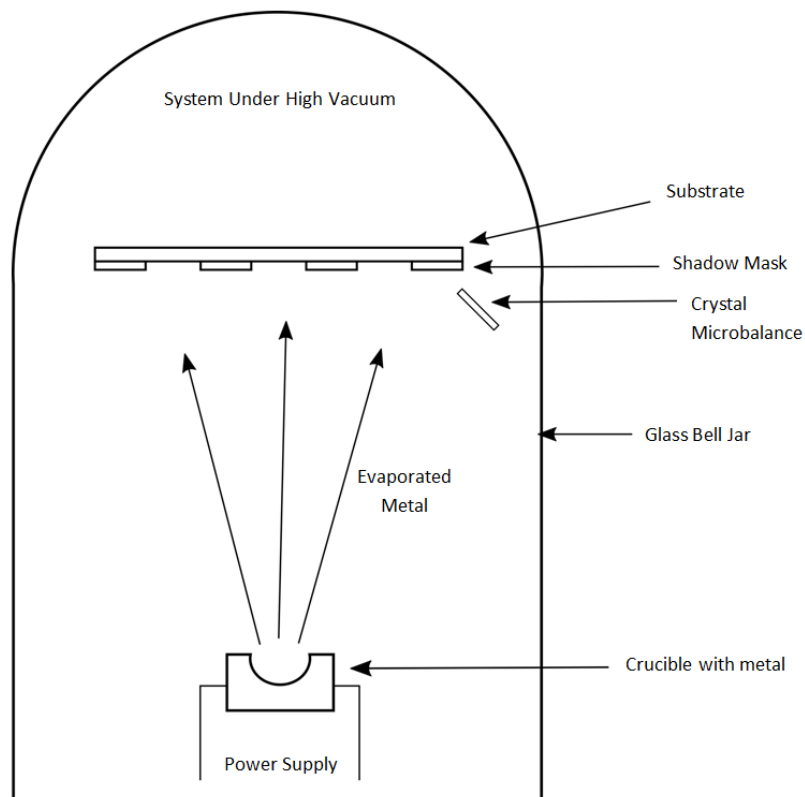
### 2.2 Fabrication Methods for Paper Electronics

Fabrication methods for electronics vary dramatically in their characteristics; for example cost, minimum feature size and thickness. Low cost and simplicity are desired characteristics in fabrication

methods for paper-based electronics; a sheet of A4 paper can cost as little as 0.5 pence and so the fabrication costs for the electronics should also be minimised. In addition to this, paper has a high surface roughness (up to  $10\ \mu\text{m}$ ) and so this should also be considered when determining an optimum fabrication method, as the minimum feature size and thickness of the deposited layer will be limited by the surface topography.

### 2.2.1 Thermal Evaporation

Thermal evaporation is a traditional method for depositing metal films (normally less than 500 nm) on various substrates. During the process, the substrate and source are contained within a high vacuum (less than  $10^{-6}$  mbar), with the substrate suspended above the source as illustrated in Figure 2.1. Metal is added to a crucible or coil which is then connected to a power supply. As the power is increased, the crucible will heat up, melting and then evaporating the metal. The metal will evaporate towards the substrate, where it will condense, as the substrate is at a lower temperature than the metal. A shadow mask can be used to pattern the metal and is positioned in direct contact with the substrate between that and the source.



**Figure 2.1:** Diagram of a thermal evaporator.

This work used an Edwards 306 Thermal Evaporator (Edwards, UK) to deposit aluminium films on various paper substrates. A vacuum of less than  $10^{-6}$  mbar was achieved by an Edwards RV12

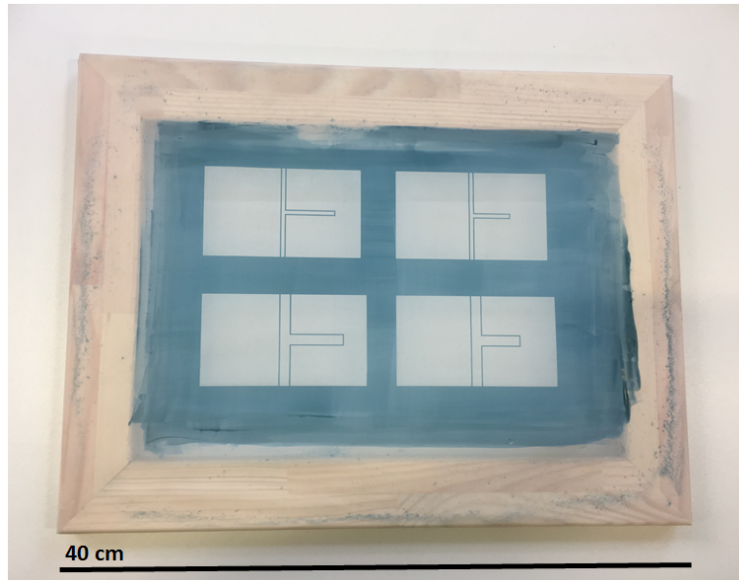
rotary pump backing an Edwards E04K diffusion pump. A liquid nitrogen cooled cryotrap was used to prevent oil vapour from entering the bell jar and contaminating samples. The quartz crystal microbalance was connected to an Edwards FTM7 film thickness monitor which was used to monitor the rate of deposition and final film thickness. Several metals were trialled and it was decided that aluminium was the most suitable for this work due to its low cost and low resistivity. Tungsten coils were used to hold and heat the aluminium with a deposition rate of 0.3 nm/s.

### 2.2.2 Screen Printing

The screen printing process consists of a screen, which refers to the frame and patterned mesh, the required ink and a squeegee. The mesh is patterned so that only certain areas allow the ink to pass through to the substrate. A vast range of frames and meshes are available depending on the application; aluminium and wooden frames are most commonly used and silk, nylon and stainless steel are the most common materials used for the mesh.

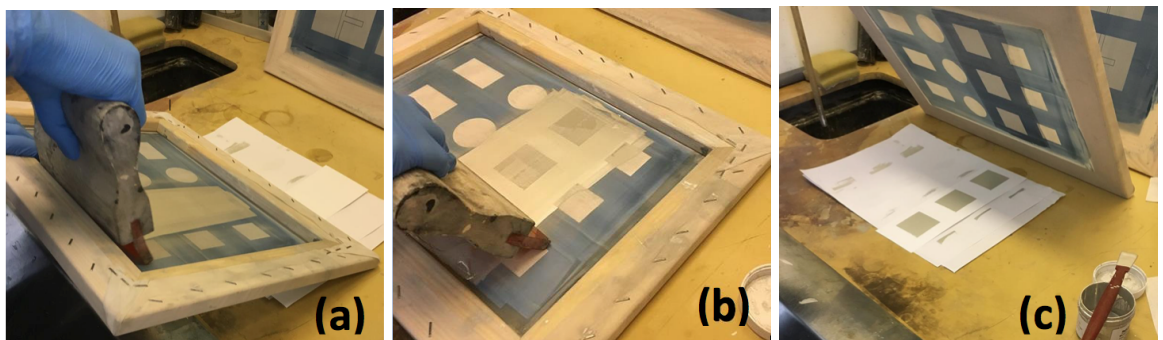
For this work, screens were patterned in house. 90T monofilament silk mesh was fixed to a wooden frame by Seasons Gallery and Framing (Durham, UK) who also produced the frame itself. 90T mesh has a thread diameter of 48  $\mu\text{m}$  and a mesh opening of 63  $\mu\text{m}$ , and was chosen as a suitable compromise between larger thread diameters, which would produce a thicker film, and smaller thread diameters, which can sustain smaller features. To pattern the screens, a Jaquard photo emulsion kit has been used; this contains JS12130 photo emulsion and Diazo Sensitiser which activates the emulsion so it becomes Ultraviolet (UV) sensitive. As per instructions, the sensitiser is mixed with water and then added to the emulsion. This solution was left to settle for an hour and then a layer was added to the screen with a squeegee and left to dry.

To pattern the screen, the photo emulsion is developed/treated as a positive resist, meaning any exposed areas will harden. The emulsion is cross-linked with exposure to UV light and unexposed sections can be washed away with water. A Parker Countess Royale UV source (Parker, UK) was used to expose the screen; an optimum exposure time was determined to be 30 seconds for the thickness of photo emulsion used ( $93 \pm 8 \mu\text{m}$ ). The screen was then washed in water to remove the areas of unexposed emulsion and an example result can be seen in Figure 2.2.



**Figure 2.2:** Image of an example screen made in house for printing transmission line stubs (detailed in Chapter 6).

The printing process is shown in Figure 2.3. When printing, the screen is first held at an angle to avoid contact with the substrate or table and flooded with ink as shown in Figure 2.3(a). The substrate is placed beneath the screen and a 60 durometer square-edged squeegee is then used to apply pressure to the screen. This forces the screen to come in contact with the substrate and the ink to be pushed through the gaps in the screen. This part of the printing process is shown in Figure 2.3(b). An example of the resulting print can be seen in Figure 2.3(c). For this work, all samples were produced by printing Metalon HPS-021LV silver nano-flake ink onto 199 gsm Neenah paper. This paper was chosen as the optimum paper for screen printing as detailed in Chapter 3. All samples were sintered at 125 °C for 30 min in a Medline OV-11 vacuum oven to reduce sheet resistance.



**Figure 2.3:** The process of screen printing. (a) The screen is flooded with ink. (b) The screen is placed above the substrate and the squeegee is used to push the ink through the screen onto the substrate. (c) The screen is removed, showing the resulting print.

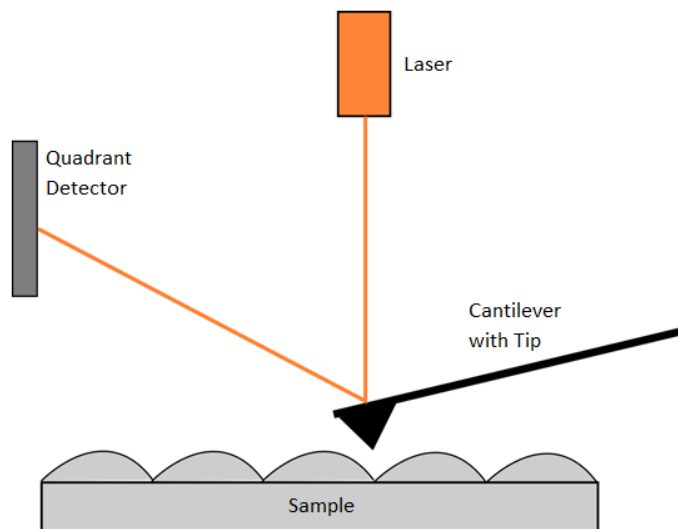
## 2.3 Analysis of Surface Morphology

### 2.3.1 Surface Roughness Characterisation Techniques

Unlike established substrates for electronics, like silicon or glass, paper does not have a smooth surface. In addition to this, different papers have different surface topographies dependent on the manufacturing process used and any coatings added. Glossy photo papers are often coated with a material with a roughness in the scale of nanometres, whereas matt papers are often not coated and so the roughness is directly that of the cellulose fibres, which are often micrometres in size. The surface roughness of the paper is of great importance when depositing metal layers, as the layer thickness can be of the same scale as the roughness of the paper, meaning that the deposited layer can be non-continuous and result in a longer path length than a metal layer deposited on a smoother surface.

#### Atomic Force Microscopy

An atomic force microscope (AFM) was used in this work to investigate the surface properties of paper-based substrates as this is a very high resolution form of scanning probe microscopy. An AFM consists of a cantilever with a sharp tip at the end (a radius of curvature of the order of nanometres), as shown in Figure 2.4. The forces between this tip and the sample's surface determine the vertical measurement of the sample surface.



**Figure 2.4:** Diagram of an atomic force microscope.

The sample is mounted on a three-degree-of-freedom piezoelectric stage. The sample is moved using the stage and the cantilever is deflected by height differences on the sample. A laser is reflected from the cantilever to a quadrant detector. As the cantilever is deflected, the ratio of light intensity

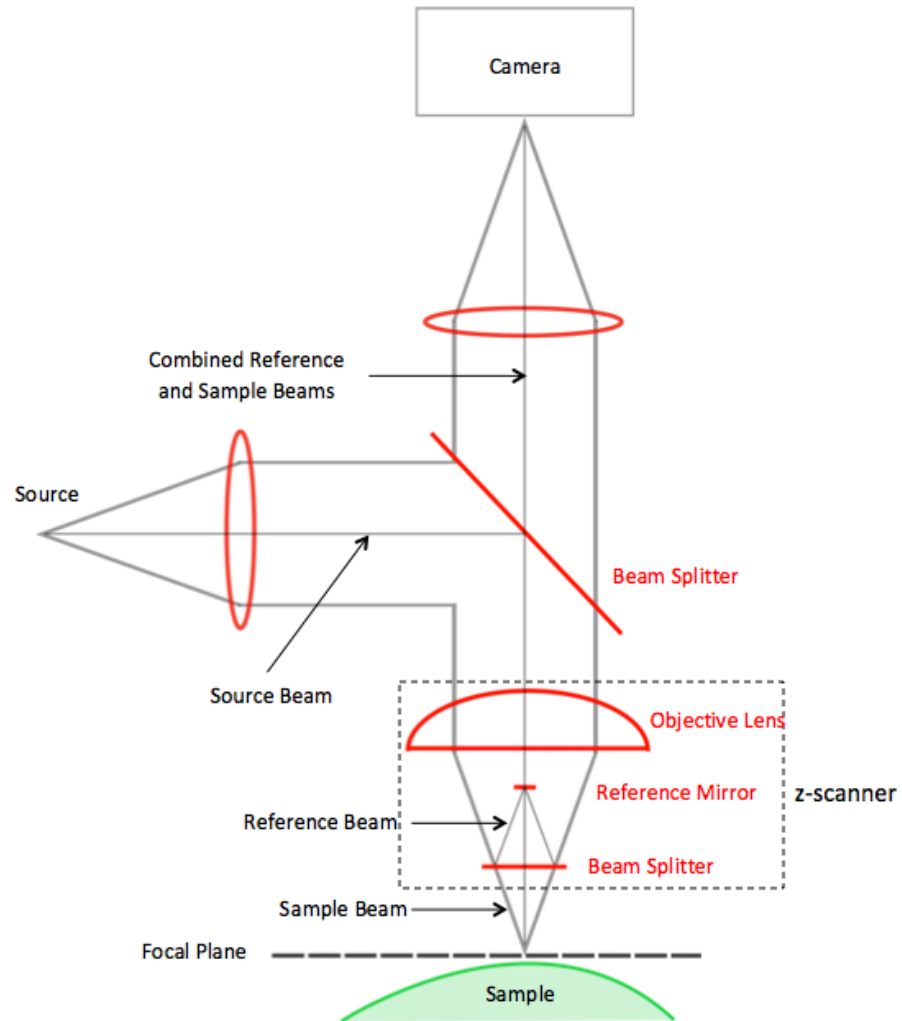
received by the different photodiodes changes, producing an output signal which can be translated into the deflection of the cantilever. The stage is then moved so that the force between the tip and substrate is kept constant. An AFM can be used in contact, tapping or non-contact mode. In tapping mode, the tip oscillates in the repulsive region between the tip and the sample, driven by a piezoelectric element mounted on the tip holder. In non-contact mode, the tip oscillates in the attractive region; this oscillation is affected by the Van der Waals forces, decreasing the frequency of the cantilever [1].

For this work a Veeco NanoMan II (Veeco, New York) has been used in tapping mode. As the maximum range in vertical variation is  $5\ \mu\text{m}$ , only coated papers were imaged by AFM as their roughness was below this limit. Fibres present on the surface of matt and other papers were found to catch on the tip and not provide reasonable data.

### **White Light Interferometry**

White light interferometry is a non-contact optical method for measuring the vertical changes across a sample. Interferometry makes use of the superposition of light waves. When two waves combine and are in phase with each other, constructive interference occurs; conversely when the two waves are out of phase, destructive interference occurs. White light is used as it is the most incoherent light so constructive interference only occurs when the difference in length between two sources is zero.

A white light interferometer has a structure as shown in Figure 2.5. It consists of a white light source, lenses, beam splitters and mirrors. The light source travels along the instrument, through the objective lens and is split in half when it reaches the lower beam splitter. Half of the beam is passed through the focal plane of a microscope objective and is reflected from the test sample, the other half is reflected onto a reference mirror, which remains at a fixed distance from the beam splitter. The beam splitter is located at an equal distance from the focal plane and the reference mirror, meaning that, as the sample beam is moved across the varying surface, the path length of the light is altered and is no longer equal to the distance between the beam splitter and the reference mirror. The z-scanner is then used to change the path length until constructive interference occurs. As white light is the most incoherent, there is a short coherence path and constructive interference only occurs at one point. The camera identifies constructive interference as being lighter than the deconstructive interference and so will obtain a pattern of interference fringes. From this pattern of interference fringes, the height variation along the sample can be determined and the surface reconstructed [2].

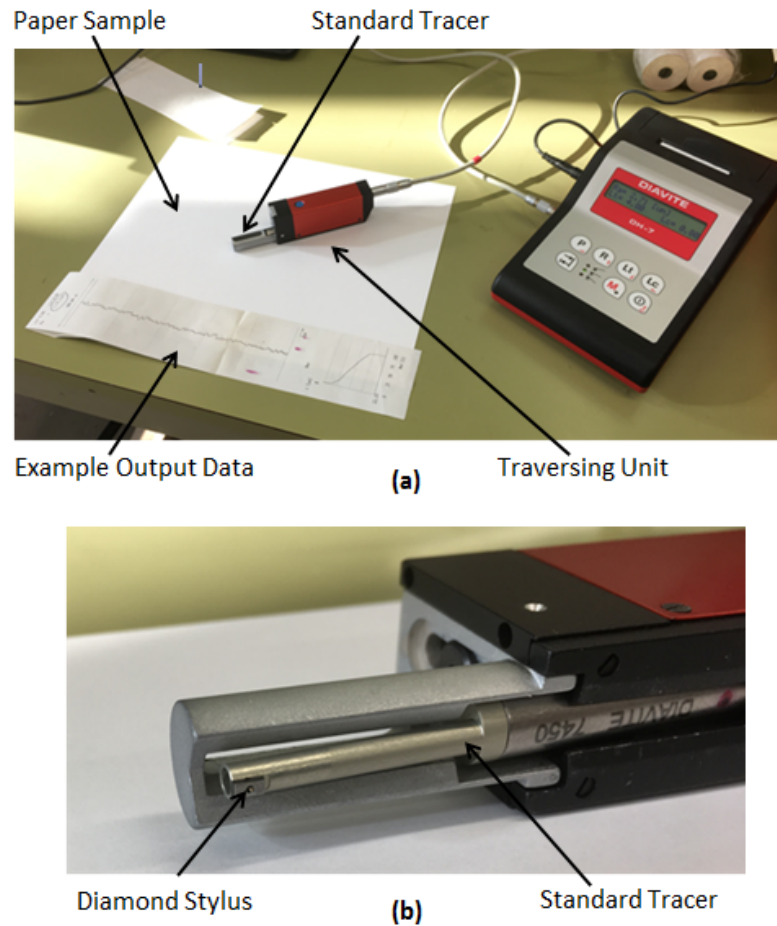


**Figure 2.5:** Diagram of a white light interferometer.

For this work, a Zygo white light interferometer (Zygo, Pennsylvania) has been used. Varying magnifications were used to produce scans of varying areas between  $5 \times 5 \mu\text{m}$  and  $5 \times 5 \text{mm}$ . A cylinder filter was added to the scans to remove any variation caused by the sample not lying flat on the stage. One-, two- and three-dimensional data were taken with the surface roughness ( $R_a$ ) being of key importance. All imaging of the samples in this work has been done by Cyril Bourgenot under the guidance of the author.

### Stylus Profilometers

Stylus profilometers work on the basis of a stylus on the end of a cantilever, an example of which is shown in Figure 2.6, with Figure 2.6(b) highlighting the actual stylus. This stylus physically moves along the surface while a feedback loop monitors the force from the sample pushing up against the stylus. From the forces measured, the changes in vertical distance can be extracted and a single line scan is produced.



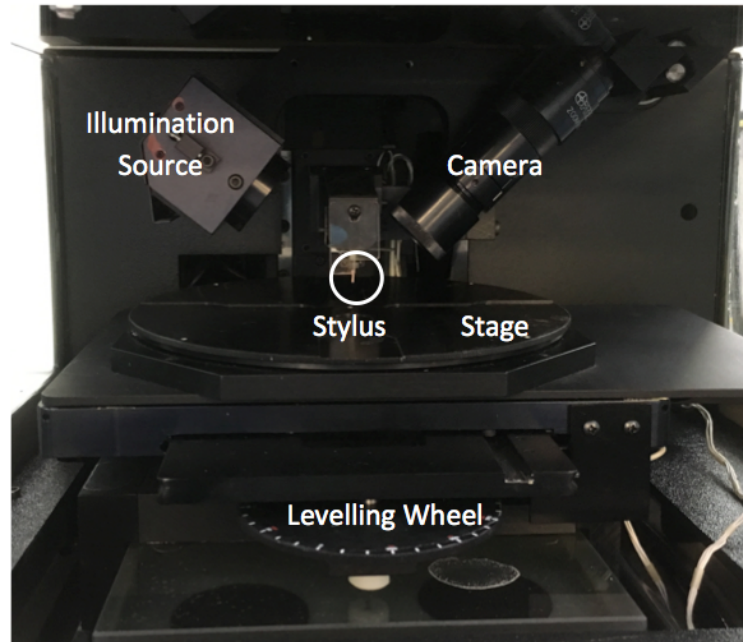
**Figure 2.6:** Features of the Diavite DH-7 stylus profilometer. (a) The whole system including the stylus, traversing unit, computation and output equipment, example sample of matt paper and the corresponding example trace. (b) Close-up of the tracer and diamond stylus.

For this work, two profilometers have been used to determine values for surface roughness for papers; a Diavite DH-7 (Diavite AG, Switzerland) and a Talysurf PGI 1250 (Taylor Hobson, Leicester UK). The maximum line scans of 15 mm and 10 mm were used for the Diavite and the Talysurf scans respectively. The Diavite has a vertical resolution of 10 nm and the Talysurf has a vertical resolution of less than 2 nm.

### 2.3.2 Dektak Surface Profiler

The Dektak surface profiler has a similar operating method to the stylus profilometers detailed above, however is discussed separately as it was used to measure the thickness of deposited layers rather than analyse the surface topography. For this work, a Dektak 3ST has been used and is shown in Figure 2.7.



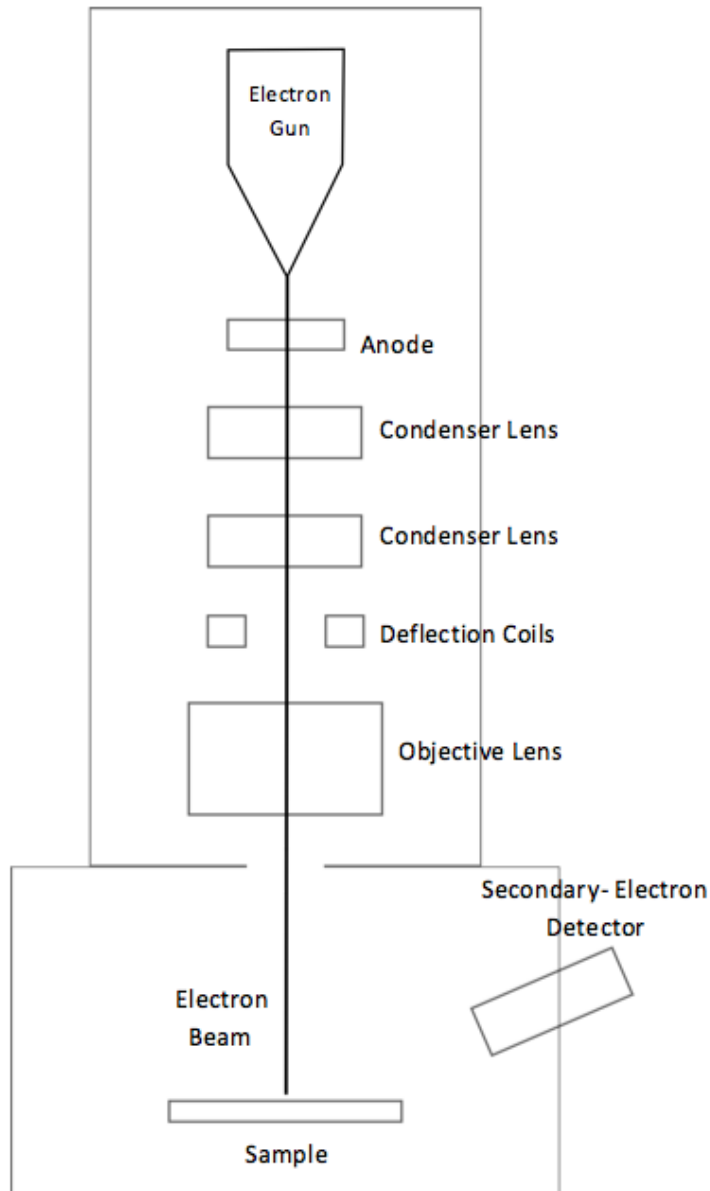


**Figure 2.7:** Annotated photograph of the Dektak 3ST.

This system takes measurements electromechanically by moving a diamond-tipped stylus over the sample. The scan length, speed and stylus force can be determined by the user. In this work, the measurement range was kept at a maximum (1310 nA), the speed and resolution were set to medium (12 second scan) and a scan length of 2000  $\mu\text{m}$  was used. The stylus is linked to a linear variable differential transformer (LVDT) which produces and processes the electrical signals corresponding to surface variations on the sample [3].

### 2.3.3 Scanning Electron Microscopy

Optical microscopes are limited by the wavelength of visible light and can achieve a maximum magnification of approximately 400. Electrons have a smaller wavelength and so have been utilised in Scanning Electron Microscopes (SEMs) to achieve magnifications greater than 100,000. While SEMs vary slightly from model to model, the basic principle for all can be seen in Figure 2.8. An SEM consists of an electron source, anode, condenser lenses, deflection coils, objective lens and electron and x-ray detectors. SEMs are held under vacuum to provide an uninterrupted path for the electrons from source to sample.



**Figure 2.8:** Diagram of a scanning electron microscope.

The electron source provides the electron beam and is typically one of two types; a thermionic gun which heats a filament to remove electrons or a field emission gun which uses a strong electric field to remove electrons. The latter provides much higher resolution. The electrons are then directed and accelerated towards the particle by the anode at different energies to optimise the contrast. The beam is condensed and directed by lenses to increase the precision of the SEM. Once the beam has been focused, the deflection coils (also known as scanning coils) move the beam in the X and Y axes, enabling scanning over the sample.

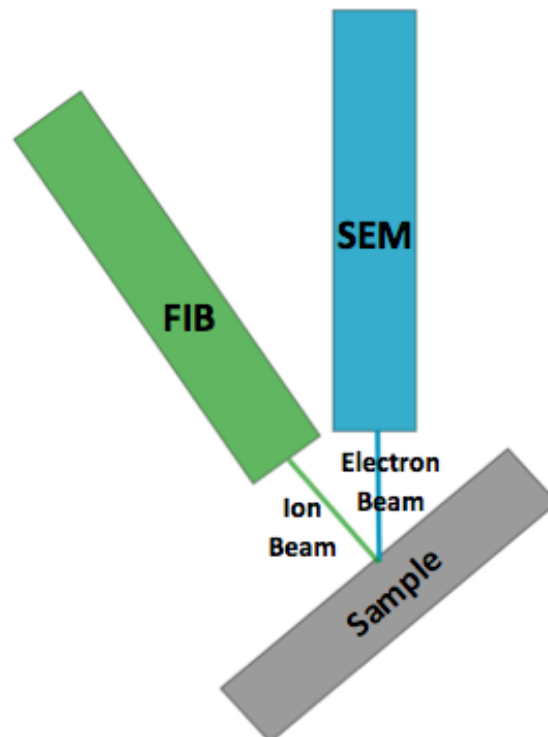
The chamber in which the sample is contained is required to be very stable as only a small amount of vibration can cause blurring of the images. When the beam meets the sample, it penetrates a few microns and will produce secondary-electrons, backscattered electrons and X-rays as the beam and the sample interact. Secondary-electrons are electrons released when the source electrons collide

inelastically with the atoms on the surface of the sample, they have much lower energy than backscattered electrons. Secondary electrons provide information on the topography of the sample with height variations being illustrated in varying brightness. Backscattered electrons are those from the source which collide elastically with the atoms on the surface and change trajectory back towards the source. They can provide elemental compositional information about the sample, as atoms with higher atomic numbers will have electrons which backscatter more efficiently [4].

For this work a Hitachi SU-70 FEG SEM (Hitachi, Tokyo) with a secondary-electron detector has been used to produce images of topography. This particular SEM uses a Schottky field emission gun and has an attainable resolution of a few nanometres. Prior to imaging, samples were sputter coated with 45 nm AuPd to electrically ground the sample and prevent charging from the electron beam.

### 2.3.4 Focused Ion-Beam Milling

A focused ion-beam (FIB) instrument is similar to an SEM using ions rather than electrons as the charged particles. A focused ion-beam instrument can be used to modify or ‘mill’ the surface of a sample by sputtering and can have nanometre precision. This can be used in the fabrication process to produce nanometre features or to remove unwanted material. In some systems, an FIB is used in conjunction with an SEM, as shown in Figure 2.9, to produce real-time microscope images of any milled areas.



**Figure 2.9:** Diagram of a dual beam system with an FIB and SEM.

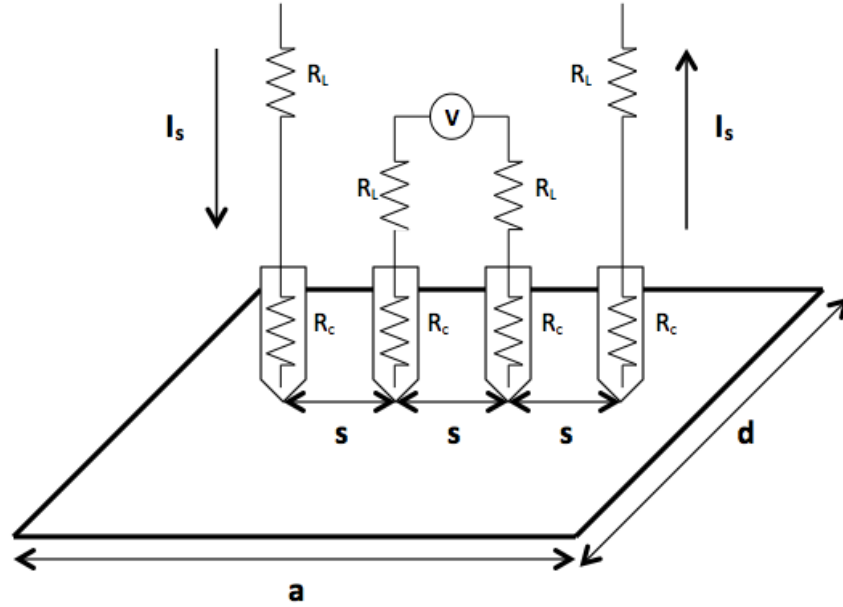
Often gallium is used as the source, with the most common source type for micro machining of samples being the liquid-metal ion source. In a gallium liquid ion source, gallium flows from a reservoir to a needle tip (approximately 10  $\mu\text{m}$ ) where a large potential between that and extraction electrodes causes ionisation and emission of gallium ions. Lenses are used to condense the beam to ensure high precision. Again, a detector is used to determine the interaction with the sample when used for imaging [5, 6].

In this work, an FEI Helios Nanolab 600 Microscope (FEI, Oregon) has been used. This is a dual beam system as shown in Figure 2.9, the gallium ion-column has been used to mill troughs in screen-printed samples which have been imaged using the SEM column. All milling and imaging of the samples in this work has been done by Leon Bowen under the guidance of the author.

## 2.4 Electrical Measurement Techniques

### 2.4.1 Four-Point Probe

To minimise the effect of contact resistance, a four-point probe measurement set up has been used in this work to measure sheet resistance of metal layers deposited on various substrates. A four-point probe measurement uses a constant current and measures the voltage with the set up that is shown in Figure 2.10. The high impedance of the voltmeter means that there is no current through the inner circuit, this removes the effect of contact resistance and resistance of the wires. This lack of contact resistance is the advantage of the four-point probe method, as the sheet resistance values measured in this work are small, the contact resistance can have a large affect on them. The governing equation for this measurement is  $\rho_s = \frac{V}{I}C$ , taken from [7], where  $\rho_s$  is the sheet resistance for the measured layer,  $V$  is the measured voltage,  $I$  is the applied current and  $C$  is the correction factor dependent on the geometry.

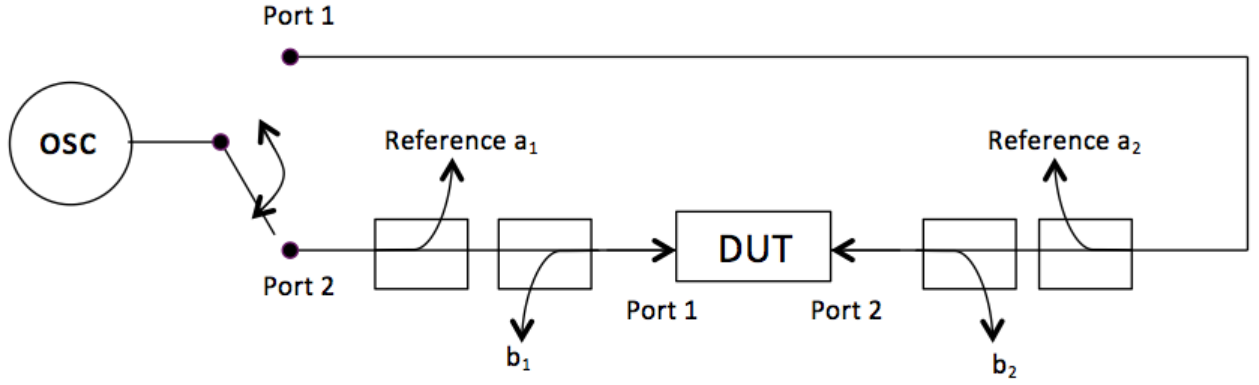


**Figure 2.10:** The principles of four-point probe measurements.

In this work, custom-made probes have been used consisting of spring-loaded pins in order to prevent piercing of sharper probes into the substrate. The current was set to ten different values on a linear scale and the voltage was measured for each current. An average resistance value was calculated ( $R = V/I$ ) for all ten readings and then this was multiplied by the correction factor  $C$  to determine the sheet resistance.  $C$  is dependent on the geometry of the metal layer and the spacing between the probes, for an infinite sheet,  $C = \pi / \ln 2$ . In this work, the spacing between the probes was 3 mm and the metal layers are square, meaning the ratio of dimensions  $a$  and  $d$ , shown in Figure 2.10, is 1. Once the ratio of  $a/d$  is determined, the ratio  $d/s$  must be calculated, for this work this was either 10 or 8.33 for 30 mm and 25 mm dimensions respectively. Using the reference tables in [7],  $C$  is taken to be 4.2209 when  $a$  is equal to 30 mm and 4.1500 when  $a$  is equal to 25 mm.

## 2.4.2 Vector Network Analyser

To investigate structures at microwave frequencies a vector network analyser (VNA) was used. As the reflection and transmission of electrical networks are easy to measure at high frequencies, the scattering parameters (s-parameters) are often measured using a VNA. The principles of how a VNA works are shown in Figure 2.11.



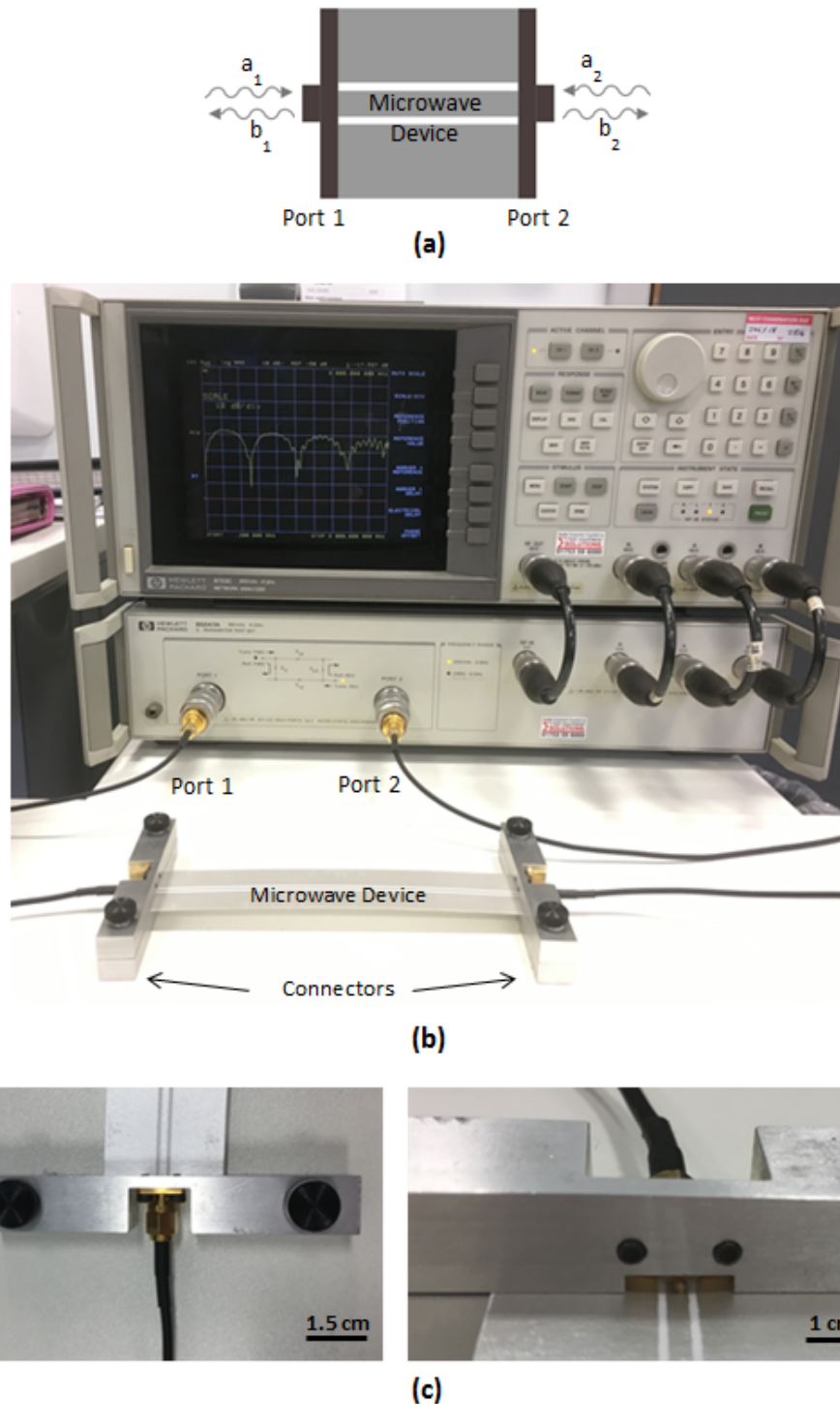
**Figure 2.11:** Diagram of a vector network analyser.

The oscillator alternates between sending signals to port 1 and port 2, parts of these signals are taken as references ( $a_1$  and  $a_2$ ). The reflected signals from port 1 and port 2 ( $b_1$  and  $b_2$ ) are separated from the oscillator signals using directional couplers. The scattering parameters can then be determined from the equation:

$$\begin{pmatrix} b_1 \\ b_2 \end{pmatrix} = (s) \begin{pmatrix} a_1 \\ a_2 \end{pmatrix} \quad (2.1)$$

where  $(s) = \begin{bmatrix} s_{11} & s_{12} \\ s_{21} & s_{22} \end{bmatrix}$ .

This is also illustrated in Figure 2.12(a) where components of  $a$  and  $b$  are the same in both the equation and the images.  $s_{11}$  and  $s_{22}$  are the ratios of reflected signal to the incident signal at port 1 and port 2 respectively.  $s_{12}$  is the ratio of the transmitted signal received at port 1 to the incident signal from port 2, and  $s_{21}$  is the ratio of the transmitted signal received at port 2 to the incident signal from port 1. These four  $s$ -parameters are for a two port network, as used in this work.



**Figure 2.12:** Images of the vector network analyser and devices used in this work. (a) An illustration of the reference and reflected signals from port 1 and 2. (b) A photograph of the experimental setup including the vector network analyser and a transmission line under test. (c) The connectors used in this work.

In this work, a Hewlett Packard 8753C Network Analyser (HP, California), shown in Figure 2.12(b), has been utilised as to measure s-parameters between 300 kHz to 3 GHz with 1601 points and a source power of  $-20$  dBm. Prior to measurements being taken, the VNA was turned on and left to warm up for at least 30 min to ensure reliable and repeatable results. A full two-port calibration was undertaken using a Hewlett Packard 85033C 3.5 mm calibration kit before all sets of measurements. The VNA

was kept at room temperature and humidity and it was found that repeated measurements on several days provided the same results. The data was extracted from the vector network analyser by the Hewlett-Packard Interface Bus (HP-IB) and Matlab code; the s-parameter data was read and the real and imaginary parts were saved to an Excel worksheet.

The paper-based microwave devices were connected to the VNA using custom connectors shown in Figure 2.12(c). Two aluminium blocks were connected together using the black screws on either side to allow for various thicknesses of substrate to be considered. An SMA connector was connected to the top aluminium block such that the signal and ground could be independently put in contact with the microwave device and the ground was common to both sides of the waveguide.

## 2.5 Simulation Packages

### 2.5.1 COMSOL Multiphysics

COMSOL Multiphysics, referred to as COMSOL in the thesis, is a comprehensive software environment capable of simulating different physical mechanisms simultaneously in two and three dimensions. For example, it is possible to couple electromagnetic and mechanical phenomena, a popular approach to micro electromechanical system (MEMS) design. COMSOL is based on the finite-element method (FEM), where the underlying couple partial differential equations are solved. COMSOL is organised in core packages with optional add-on modules for simulating specific phenomena, for example electromagnetics, structural mechanics or chemical reactions [8].

In this work COMSOL AC/DC module has been used to simulate the touch pads in Chapter 5. The ‘Electrostatics interface’ option was used to compute the electric field, electric displacement field and potential distributions in dielectrics under conditions where the electric charge distribution is explicitly prescribed. The physics interface solves Gauss Law for the electric field using the scalar electric potential as the dependent variable.

COMSOL provided capacitance values and images of the electric field distribution for this work. Global parameters were assigned to the geometry and material properties so that they could be varied using parametric sweeps.

### 2.5.2 Advanced Design System (ADS)

Keysight (formerly Agilent) Advanced Design System (ADS) Momentum is an electromagnetic simulator based on the method of moments (MoM) for layered structures, which is optimised for



the microwave simulation of printed circuit board and chip layouts [9]. Following the two-dimensional definition of a layered substrate and the metal layers, the overall layout is simulated in three dimension.

In this work the substrate consisted of a stack of air, paper (modelled as a lossy dielectric), ink (modelled as a metal with finite conductivity) and air again. Open boundary conditions were used on the top and bottom faces. The parameters for the paper and ink were determined either by direct measurement (paper permittivity and thickness, metal conductivity and thickness) or by data fitting (paper loss tangent).

## 2.6 Conclusion

This chapter has given an overview of the experimental and numerical techniques used in this work. Thermal evaporation and screen-printing results are presented in Chapter 3 where both substrates and fabrication methods for paper-based electronics are compared. The surface profiling and imaging techniques are also relevant for Chapter 3 as these have been used to investigate the topography of various papers.

Images of samples which have undergone focused ion-beam milling are presented in Chapter 4 and were used to support thickness measurements taken using the Dektak profilometer. Electrical characterisation is utilised throughout this work, Chapters 3 to 5 present results under quasi-static conditions using the four-point probe method detailed here, whereas Chapters 6 and 7 present results at microwave frequencies for which the vector network analyser has been used.

The numerical analysis of the devices produced in this work is presented in Chapter 5 where COMSOL has been used to support the measurements of the interdigitated capacitive touch pads. Results are also presented in Chapters 6 and 7 where Advanced Design System (ADS) has been used to determine changes in transmission line response when changing parameters of the substrate or ink and has also been used to design resonating structures.

## References

- [1] “Veeco Dimension 3100 Atomic Force Microscope Users Manual,” 2004.
- [2] Zygo Metrology Business Segment, “<https://www.zygo.com/?/met/profilers/opticalprofilersabout.htm>.” Accessed: 2017-10-03.
- [3] R. Ravichandran, “<http://research.engineering.ucdavis.edu/cnm2/wp-content/uploads/sites/11/2016/02/>.” Accessed: 2018-03-12.
- [4] nanoScience Instruments, “<http://www.nanoscience.com/technology/sem-technology/>.” Accessed: 2017-10-03.
- [5] S. Reyntjens and R. Puers, “A review of focused ion beam applications in microsystem technology,” *Journal of Micromechanics and Microengineering*, vol. 11, no. 4, p. 287, 2001.
- [6] C. A. Volkert and A. M. Minor, “Focused ion beam microscopy and micromachining,” *MRS Bulletin*, vol. 32, no. 05, p. 389, 2007.

- [7] F. M. Smits, "Measurement of sheet resistivities with the 4-point probe," *Bell System Technical Journal*, vol. 37, no. 3, p. 711, 1958.
- [8] COMSOL Inc., "<https://www.comsol.com/>." Accessed: 2018-03-12.
- [9] Keysight Technologies, "<https://www.keysight.com/en/pc-1297113/advanced-design-system-ads>." Accessed: 2018-03-12.

## Chapter 3

# Paper and Process Selection

### 3.1 Introduction

Having discussed the novelty of and current work on paper-based electronics, this chapter compares several examples of paper and fabrication methods, with a view to determining an optimum substrate and fabrication method for an end-user defined application. This chapter will start with a brief background on paper manufacturing and will highlight the differences and diversity of the term ‘paper’ by presenting microscopy images of the structures of various papers and comparing their properties.

The work presented in this chapter aims at compiling a review of the most commonly available paper types and their compatibility with metal deposition and patterning processes. The papers selected were simple printer paper, papers coated with different materials (such as baking paper and glossy photopaper) and speciality papers.

Thermal evaporation and screen printing were considered as possible fabrication methods. They were compared in terms of available materials, process repeatability, minimum feature size, thickness range of deposited layer as well as ease of use. Metal films have been deposited onto paper by both methods, and these films were subsequently characterised in terms of sheet resistance and adhesion (using the procedure detailed in the ISO 2409:2013 Cross Cut Test standard).

The key results of this investigation are summarised in the decision matrices compiled for both paper types and fabrication processes. These matrices can be used to determine an optimum paper and metal deposition process for a paper-based electronic device. A comparison with more traditional substrates (glass, silicon and polyethylene terephthalate (PET)) is also included to highlight the benefits of paper as an alternative in applications where cost and environmental impact are of primary concern.

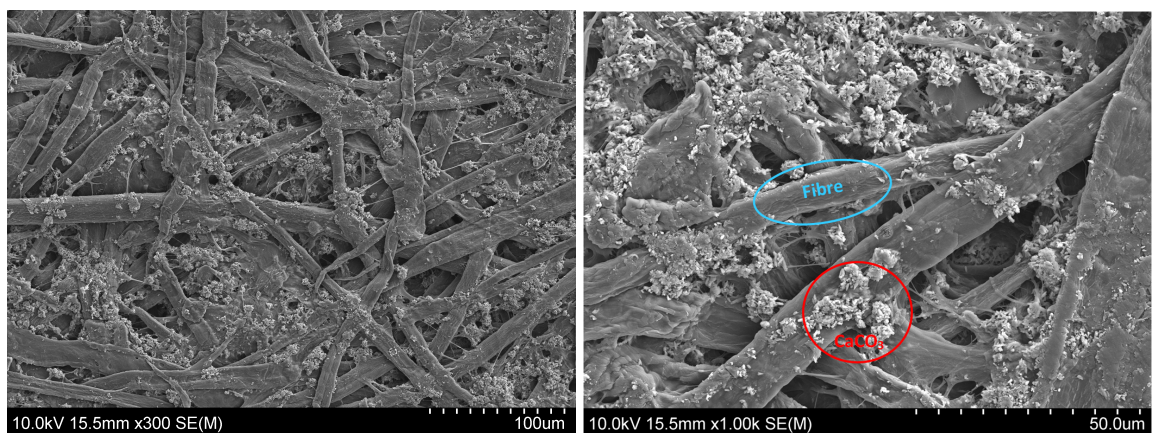
## 3.2 Paper Structure

The structure, and therefore production, of different papers varies depending on the manufacturer. Some papers may contain mainly cellulose with some additives, others may be coated and some actually contain no cellulose at all. Cellulose papers make up 95% of all paper types and so a brief overview is included below of the manufacturing process for this family of substrates.

Trees are cut down into logs, the bark is removed and burned as fuel and pulp is created from the logs by one of several methods, either chemical or mechanical. This pulp contains water, cellulose fibres and lignin; other additives may be added to alter the properties of the paper. Calcium carbonate is often added to provide a smoother, more opaque paper; however it can leave a ‘chalky’ feel to the paper, and so small amounts of sizings (often modified starches) are applied to the surface to counteract this [1, 2]. Once a pulp has been obtained, and the required agents added, the pulp is then sprayed onto a wire mesh to remove the bulk of the water and is subsequently pressed by large, heated rollers to remove the remaining liquid.

### 3.2.1 Matt Papers

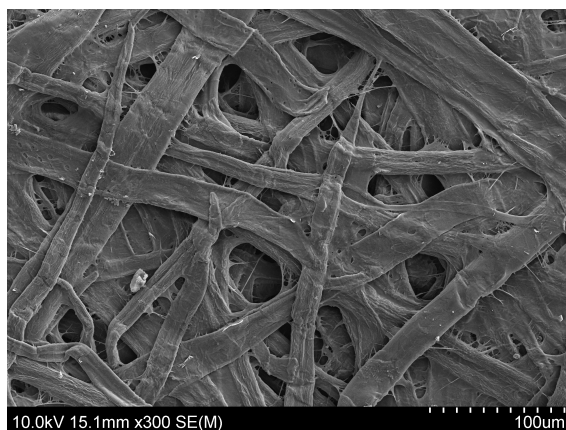
Matt papers are the most common type of paper and include the standard printer paper used in most workplaces and homes. The majority of matt papers are produced using the fabrication method detailed above and no further steps are required. These papers mainly consist of cellulose fibres and calcium carbonate; these components are highlighted in Figure 3.1, a Scanning Electron Microscope (SEM) image of a typical printer paper. This particular paper consists of deinked cellulose pulp (74%), calcium carbonate (18%), small amounts of starch (5%) and other sizings (0.1%) [3].



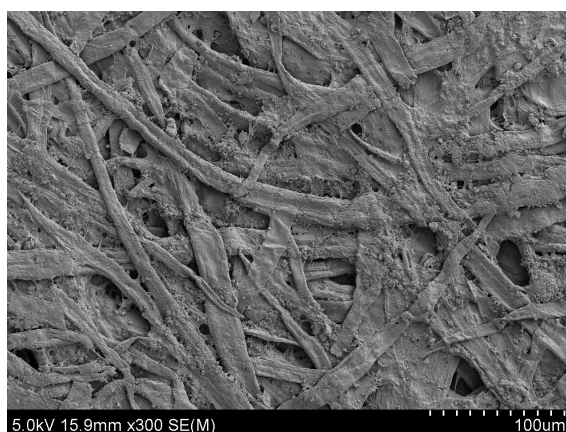
**Figure 3.1:** SEM images of Office Depot 80 gsm printer paper. The image on the right highlights the calcium carbonate (red) and cellulose fibres (blue) within the paper structure.

Cleanroom and Neenah paper are examples of other matt papers investigated in this work and can

be seen in Figures 3.2 and 3.3 respectively. Cleanroom paper is designed to prevent the paper from shedding and contaminating samples or chemicals. The cleanroom paper used in this work consists of pure cellulose fibres with no calcium carbonate and is coated with a synthetic latex [4]. Neenah paper can be seen to have a very similar structure to the basic printer paper as it is made up of cellulose fibres (70-100%), calcium carbonate (1-20%) and starch (1-20%) [5]; it also contains aluminium oxide (1-5%) which is often used for its whitening properties.



**Figure 3.2:** SEM image of 85.5 gsm Berkshire BCR bond cleanroom paper.



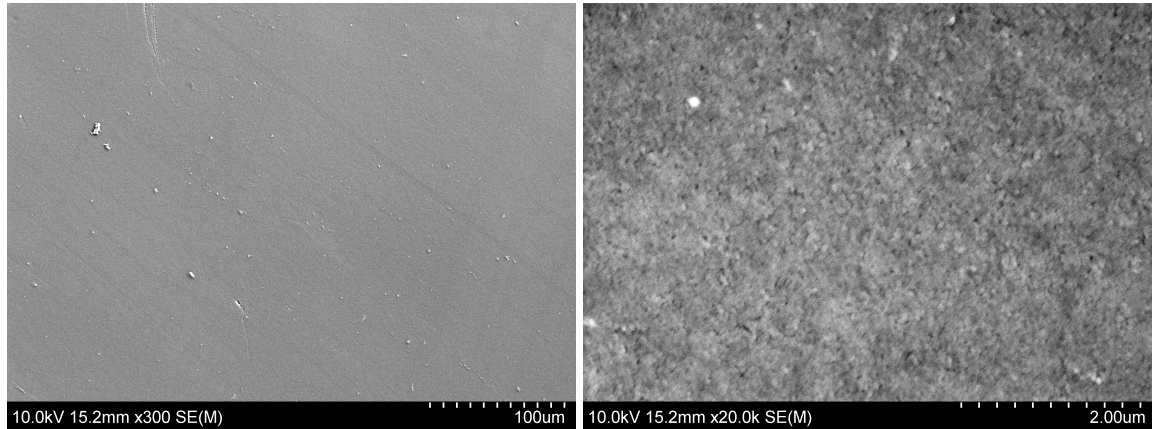
**Figure 3.3:** SEM image of 199 gsm Neenah paper.

### 3.2.2 Coated Papers

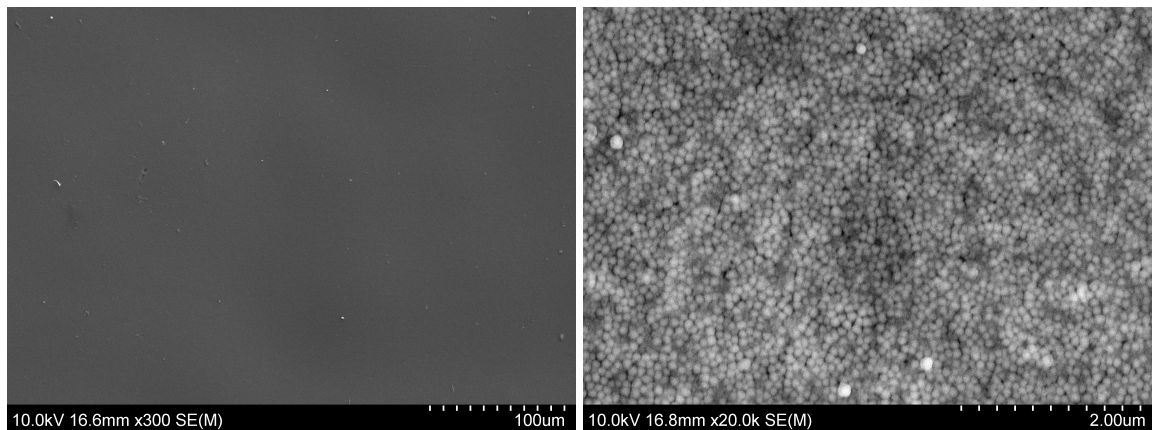
Coated papers are mainly used for applications with colour and images to produce high quality prints. These papers are often cellulose pulp coated on both sides, with one side being more glossy than the other. There are a large number of companies producing coated papers and the chemical structure of these coatings is often commercially confidential and varies depending on the manufacturer.

Two examples of photo papers used in this work are Epson glossy photo paper and Felix Schoeller 250 gsm gloss/gloss photo paper. The surface structures of these papers are shown in Figures 3.4 and 3.5 respectively. It can be seen that both have a much smoother surface than the uncoated

papers with no features of the paper being seen until a much higher magnification is used. It can be seen that these papers are coated in differing grainy structures with sub-micron features. The grain size of the Epson paper is approximately  $0.05\ \mu\text{m}$  which is approximately half the size in the doubled-sided glossy paper, however the grains are less defined in the Epson paper. This is likely due to the use of a different coating method or material.

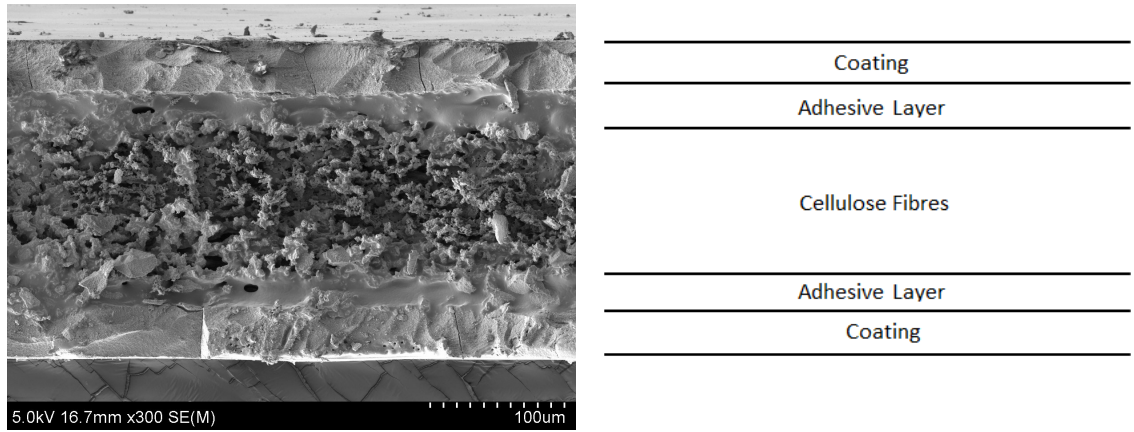


**Figure 3.4:** SEM images of 225 gsm Epson glossy photo paper.



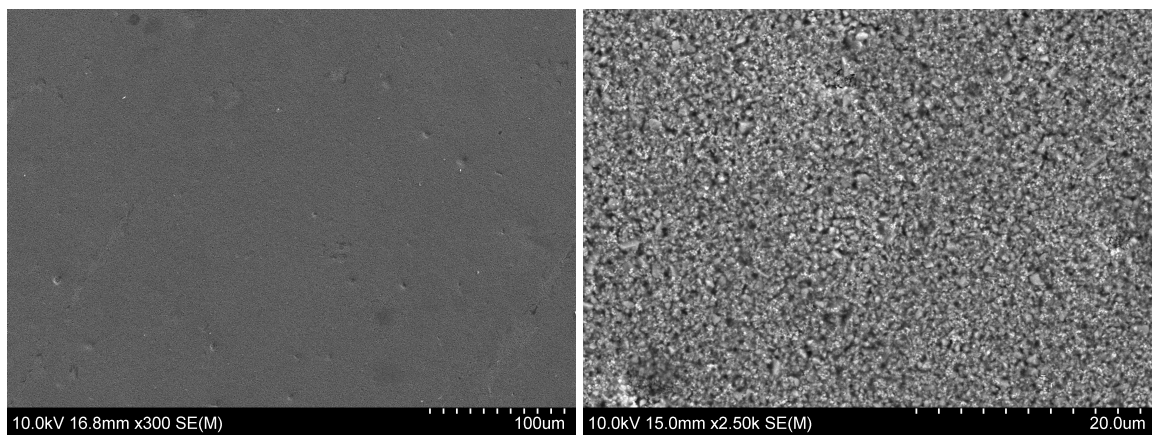
**Figure 3.5:** SEM images of 250 gsm Felix Schoeller gloss/gloss photo paper.

Coated papers often require an adhesion layer to prevent the coating and the cellulose fibres from separating. This is shown in Figure 3.6, the cross-section of a paper which has an identical glossy coating on both sides of the cellulose fibre centre.



**Figure 3.6:** SEM image of 250 gsm Felix Schoeller gloss/gloss photo paper cross-section and a pictorial representation, illustrating the various layers within the paper.

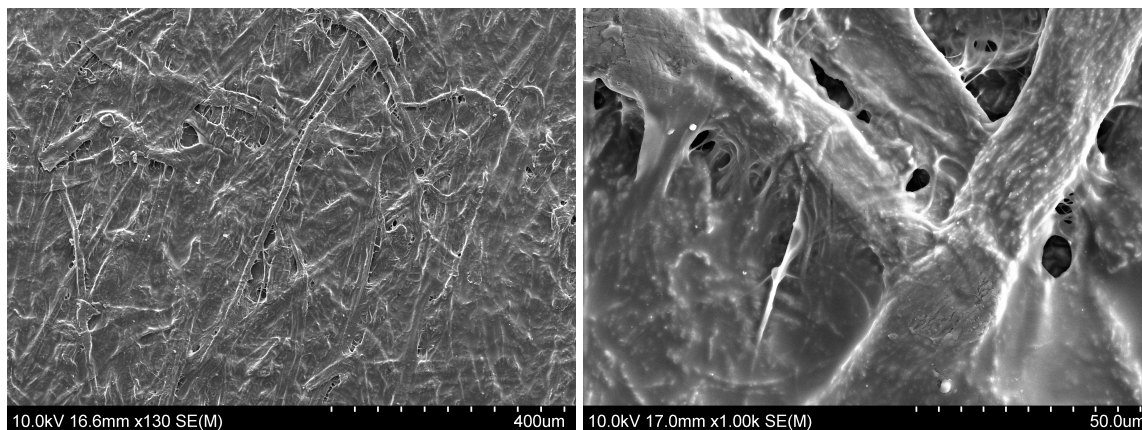
Another example of a coated paper used in this work is Powercoat HD paper, which is specifically designed for printed electronics. The structure of the paper is very similar to that of the other coated papers. However, the grains contained within the coating of the paper are larger (approximately  $1\ \mu\text{m}$ ), as can be seen in Figure 3.7. This paper is coated on both sides with kaolin and calcium carbonate and a further mineral coating is added to one side, producing the glossy finish [6].



**Figure 3.7:** SEM images of Powercoat HD 95 paper.

A final example of a coated paper used in this work is baking paper, which is often used when cooking to prevent foods from sticking to a dish or tray. Many baking papers begin with cellulose pulp which is treated with acid to give high stability and heat resistance, they are then coated with silicone or an oil-based coating to give non-stick properties. As detailed later in this chapter, baking paper is found to have characteristics of both non-coated and coated papers, which can be explained by looking at Figure 3.8 which shows SEM images of Morrison's baking paper. As with matt papers, the cellulose fibres are clearly visible within the structure. However, it is also clear there is some coating on the paper which will lead to characteristics more like the coated papers.



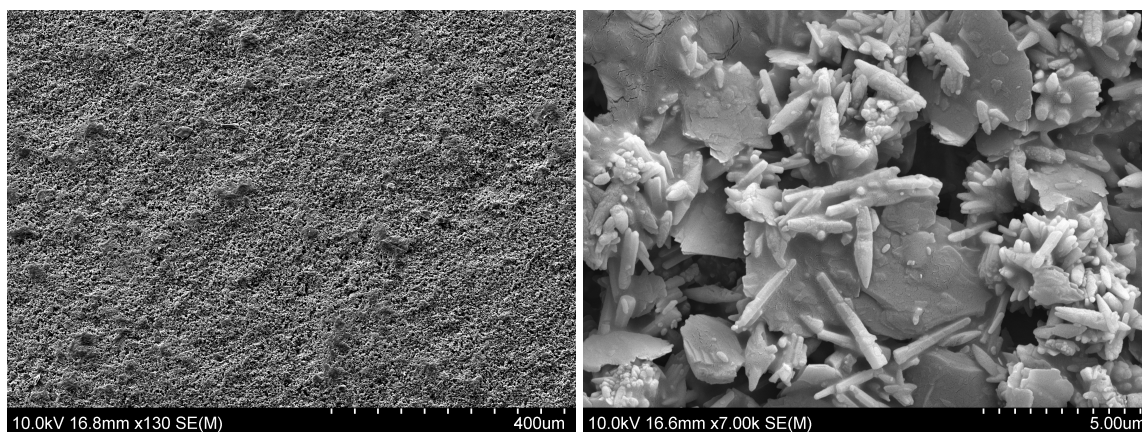


**Figure 3.8:** SEM images of Morrison's baking paper.

### 3.2.3 Stone Papers

Stone papers are paper-like products often made from stone combined with high-density polyethylene or resin, and they often have a higher density than cellulose papers. They are also water resistant and hard to tear. An example of stone paper which has been investigated in this work is Parax paper, which comprises limestone (80%) and non-toxic high-density polyethylene (20%) [7]. Terraskin paper is another example of stone paper, made up of ground up rocks (75%) and resin (25%) [8].

Parax stone paper was found to have a similar surface structure to the coated paper and this is shown in Figure 3.9. This structure is continuous throughout the paper, unlike the coated papers which are not homogeneous.



**Figure 3.9:** SEM images of 192 gsm Parax stone paper.

## 3.3 Comparison of Paper-based Substrates

The diversity of the images and structure of paper described above highlights the fact that 'paper' is a very loose term and can cover many materials with very different structures. The papers investigated in this work have been compared by examining various properties, some of these refer directly to

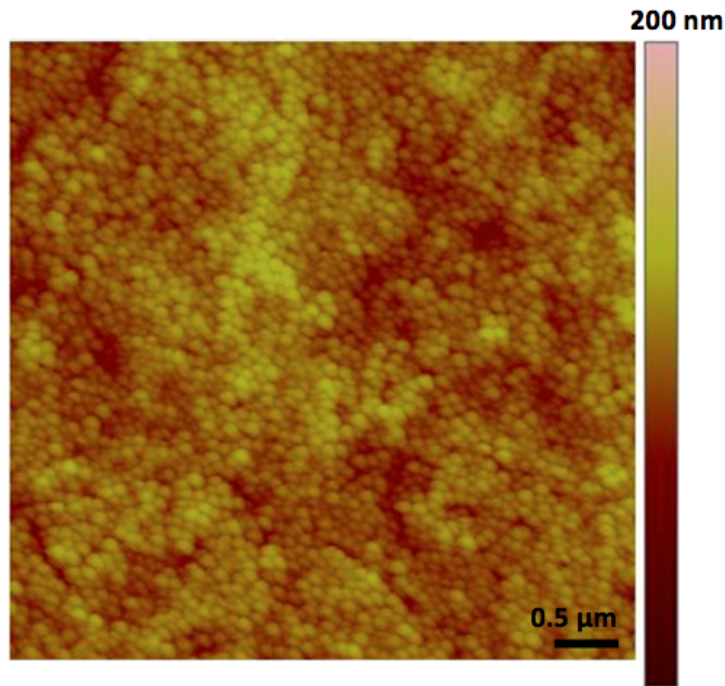


the paper itself, whereas others refer to conductive tracks deposited onto the paper. Table 3.6 is a decision matrix which compiles all of this data and, again, highlights the diversity in papers. The work is presented so that each property is addressed and then all results come together into Table 3.6 towards the end of the chapter.

### 3.3.1 Surface Roughness

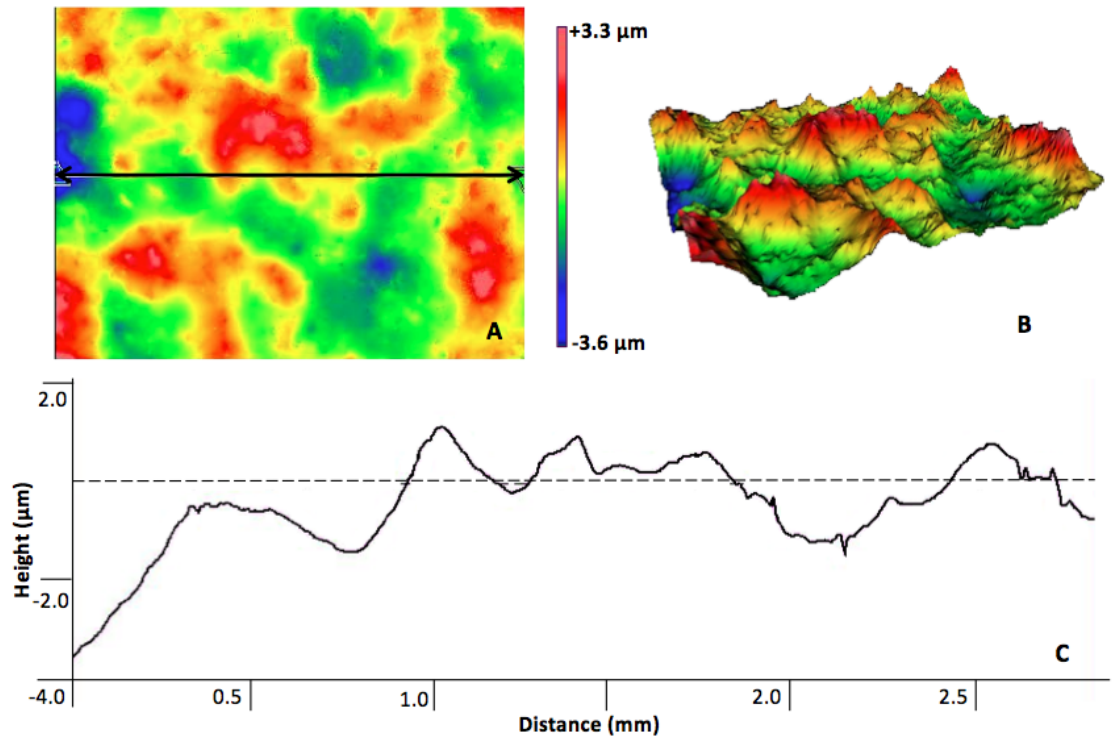
The surface roughness of the papers provides similar information to that in the SEM images. The surface roughness can affect the profile of conductive layers deposited on the paper and so it is important to take into consideration. Several methods were used to determine the surface roughness of the papers in this work: an atomic force microscope (AFM), a Zygo white light interferometer, a Talysurf CLI 2000, a Talysurf PGI 1250 profilometer and a Diavite DH-7. Details on the operation of these instruments has been presented previously in Chapter 2. The AFM, Zygo and the Talysurf CLI collect data from an area of the papers whereas the Talysurf PGI and Diavite only collect data from a line scan. When referring to surface roughness, the arithmetic average of absolute values, Ra, has been used.

The AFM used (NanoMan II scanning probe microscope) is designed for small area measurements (50  $\mu\text{m}$  squares) with small deflections, meaning it is not suitable for matt papers which can have roughness values outside this range. A selection of coated papers were analysed using the AFM and images similar to Figure 3.10 were obtained. This AFM image of gloss/gloss photo paper shows the same structure as in Figure 3.5, with a roughness value of 6.5 nm. The values of roughness obtained for the coated papers tested were all below 10 nm. This is due to the small area scan producing only a local value of roughness rather than a representation of the whole paper.



**Figure 3.10:** An AFM image of the top surface of 250 gsm Felix Schoeller gloss/gloss photo paper illustrating the nanometer grain structure of the coating.

The Zygo white light interferometer can only be used on reflective samples as the white light must be reflected back to the source and so only glossy papers were tested in this way. Figure 3.11 shows example data taken from the Zygo for Powercoat HD paper. The area of the measurement was  $2.11 \times 2.81$  mm and Ra is calculated to be 724.9 nm. Table 3.1 presents surface roughness values for measurements over different sized areas. PV is the peak value measured in the z direction, providing information on the maximum height. It is evident that the larger the area, the higher the surface roughness. The value for lower areas is in keeping with the results obtained by the AFM.



**Figure 3.11:** Data taken from the Zygo software showing Powercoat HD 95 paper. (a) A two-dimensional representation of a  $2.81 \times 2.11$  mm section. (b) A three-dimensional surface profile of the same section and (c) A one-dimensional plot along the line shown (a).

**Table 3.1:** Surface roughness values for Powercoat HD 95 paper with various scan areas taken using a Zygo white light interferometer.

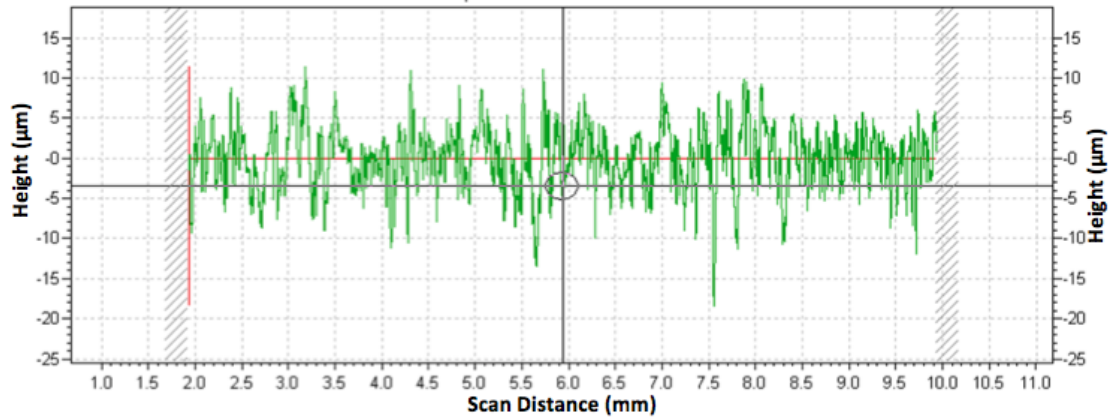
Size of scan (mm)	Peak Value (μm)	Ra (nm)
$0.005 \times 0.005$	0.051	5.0
$1.42 \times 1.06$	7.38	702
$1.79 \times 1.34$	7.64	914
$2.81 \times 2.11$	6.91	725
$3.54 \times 2.65$	7.31	1050

The Talysurf CLI 2000 produces 2D plots similar to those obtained by the Zygo, however it is not restricted to reflective materials. It has a lower resolution and scans take longer, for a  $0.5 \times 0.5$  mm scan with  $501 \times 52$  points it took 11 minutes in comparison to 20 seconds for the Zygo. For a scan of  $0.5 \times 0.5$  mm with  $501 \times 52$  points, the Powercoat HD 95 paper had a roughness value of 116.4 nm which is comparable to 195 nm for a  $0.35 \times 0.27$  mm scan on the Zygo white light interferometer.

Although the results taken using the AFM, Zygo and Talysurf CLI provide detail on an area of the paper, each have proven to have their disadvantages for measuring the surface roughness of several types of paper. The AFM and Zygo are only suited to a small number of papers and the Talysurf CLI takes a long time for scans.

The Talysurf PGI 1250 profilometer and the Diavite DH-7 are both compatible with all papers and take line scans, meaning they are much faster. An example line profile taken from the Talysurf

PGI can be seen in Figure 3.12, which is similar to the printed output of the Diavite.



**Figure 3.12:** Data taken from the Talysurf software showing a 10 mm line profile of printer paper.

Results from both profilometers are shown in Table 3.2 and can be seen to be in agreement with each other. The surface roughness measured for the largest scan with the Zygo for Powercoat paper is found to be  $0.911 \mu\text{m}$ , as shown in Table 3.1. This is in agreement with data from the profilometers which have a longer scan ( $> 1 \text{ cm}$ ) and so are likely to have higher roughness values. Although both are fast and compatible with all papers, it was decided that the Diavite would be used to take readings as it was simple to use and portable.

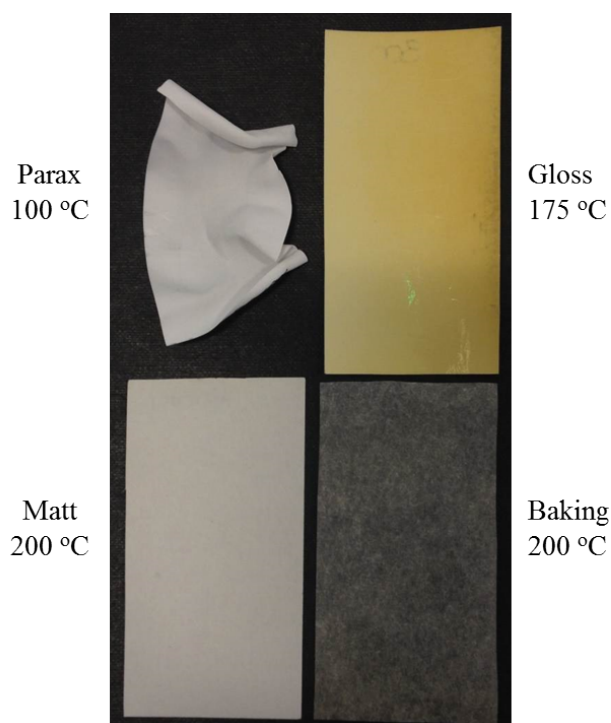
**Table 3.2:** Comparison of surface roughness measurements for Diavite DH-7 and Talysurf PGI 1250 profilometers.

Paper	Surface Roughness ( $\mu\text{m}$ )	
	Diavite DH-7	Talysurf PGI 1250
Epson Photo	0.25	0.286
Gloss/Gloss Photo	0.69	0.659
Powercoat HD 95	1.34	1.28
Parax	1.68	1.29
Printer	3.08	3.21
Baking	3.56	4.00
Cleanroom	3.67	3.84

It is evident that photo papers are less rough than matt papers; this is due to the features of the coating of the paper being much smaller than the cellulose fibres. The SEM images presented earlier show that cellulose fibres are approximately  $200 \mu\text{m}$  wide and hundreds of  $\mu\text{m}$  long and are the main component of matt papers, whereas the grain type structure on many of the coated papers is less than  $0.1 \mu\text{m}$ . Baking paper is found to have a similar roughness to matt papers. Figure 3.8 shows that the fibres inside the baking paper are prominent and so will affect the roughness of the surface rather than be dominated by the coating.

### 3.3.2 Thermal Resilience

For some applications, substrates may have to withstand high temperatures, for example printed temperature sensors. For this investigation, paper samples were put in a Medline OV-11 oven and the temperature was increased between 50 and 200 °C. Changes in their colour and shape were recorded. The temperature was limited below 200 °C to prevent the spontaneous combustion of any samples. The value recorded for each paper shows the temperature at which the sample was removed from the oven due to excessive curling or yellowing. '200+' indicates the sample survived above 200 °C and would have been able to withstand even higher temperatures. Figure 3.13 shows examples of some papers after the heat treatment and notes the temperature at which the sample was removed from the oven.



**Figure 3.13:** Examples of papers after heat treatment. From top left going clockwise: Parax paper removed from the oven at 100 °C due to excessive curling; gloss photo paper removed at 175 °C due to excessive yellowing; baking paper and matt paper removed at 200 °C but both could have withstood higher temperatures. All samples were 4 × 7.5 cm before being placed in the oven.

Many of the matt papers were able to withstand higher temperatures than coated papers which often yellowed and curled at approximately 150 °C. Parax papers and the mineral papers were not able to withstand high temperatures at all and were found to curl and deform at temperatures as low as 50 °C. These samples hardened in the deformed positions once cooled and so were unusable after thermal testing. Powercoat and baking papers were found to withstand temperatures over 200 °C with very little change. Many of these results are explained by the chemical composition of the papers, for example, baking papers are often coated with silicone and Powercoat papers with kaolin, which both

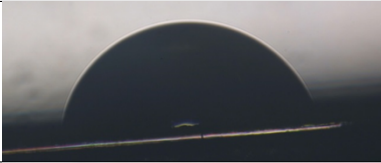
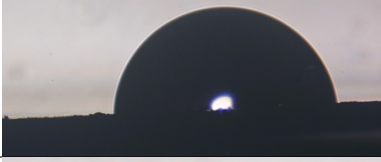

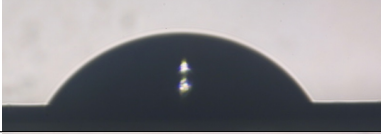



have heat resistant properties. Alternatively, Parax papers and the mineral papers are made with polymers which are unlikely to be heat resistant.

### 3.3.3 Water Resilience

Similarly to heat, some applications may require the papers to be water resistant or waterproof, for example if the device needs to be used outside. This is a subjective measurement that was based on two experiments. In the first experiment, a sample ( $4 \times 6$  cm) of each paper was submerged into a beaker of water and examined after it was removed and left to dry. The second experiment used a sample of the same size, and 2 ml of water from a pipette was dropped onto it, again examining the sample after it was left to dry. ‘Excellent’ was used to indicate that the sample was not affected by the water in both experiments and no visible change had occurred, for example Parax paper. ‘Good’ indicates the sample was unaffected by the water on one side or there was only a slight visible change, for example baking paper. ‘Average’ indicates that there was a change after being submerged, but no visible change from the droplets, for example glossy papers. ‘Poor’ indicates the sample curled and changed shape and there is a significant change after the experiment, for example matt papers. ‘Very Poor’ indicates the paper tore easily when wet, for example cigarette paper.

The contact angle gives further, quantitative information on the surface of the papers and their interaction with water. It was found that, on the whole, matt papers absorbed water whereas glossy papers did not, meaning contact angle measurements could be taken for glossy papers but not for matt samples. Microscope images of a 2  $\mu$ l drop on each paper were taken and the contact angle was calculated manually, with results shown in Table 3.3.

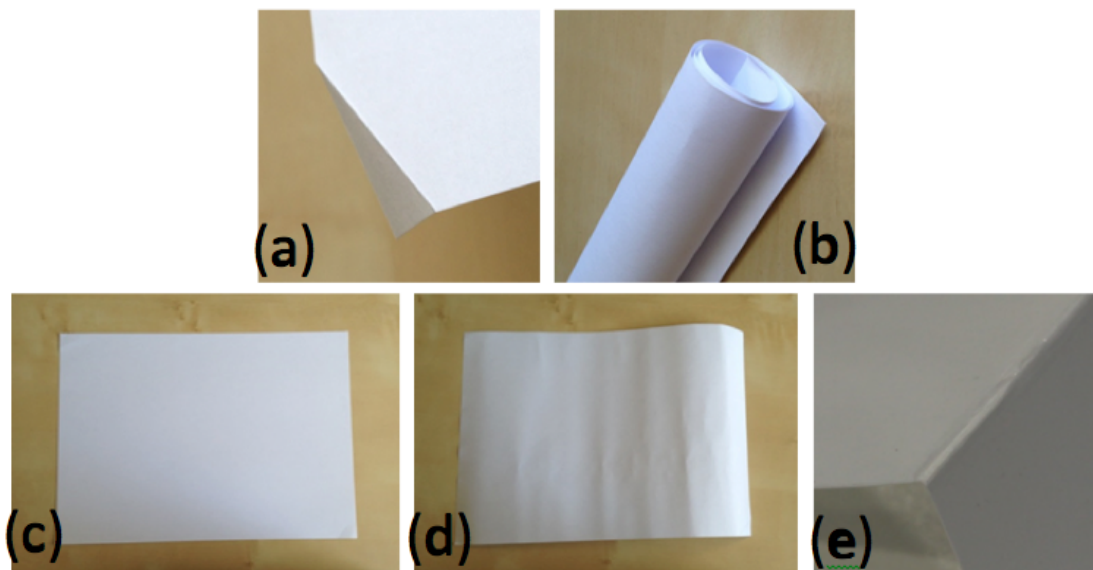
**Table 3.3:** Comparison of contact angle measurements for a range of papers.

Paper	Contact angle measurement image	Average Contact Angle (°)
Powercoat HD 95		71
Parax		84
Epson		52
180 Gloss		58
Gloss/Gloss		32
Baking		115
Photo		68

From all results taken in the water resilience testing, the coated papers are seen to be more water resistant than matt papers. By comparing Figures 3.1 and 3.4, it can be seen that the coating of the Epson paper will prevent water being absorbed into the fibrous structure, whereas the printer paper has no coating and so the water can be easily absorbed into the paper structure. Figure 3.6 shows the cross section of the glossy paper coated on both sides and it can be seen that the pulp within the paper is exposed at the cut edges, meaning that water can be absorbed here and explaining why the results for the submerged test will differ slightly from the contact angle results. Parax paper has a homogeneous structure and is designed to be submerged in the water; although it was rated ‘excellent’ in these results, the contact angle is actually not the highest due to baking paper being coated with silicone which provides a hydrophobic surface.

### 3.3.4 Flexibility

Some applications may require a substrate which can be folded or rolled around something. As with the waterproof test, this is a subjective scale dependent on how easily the paper can be folded and rolled. A4 sheets were used in this experiment, the corners were folded to determine any permanent damage, as in Figure 3.14(a), and the whole sheet was rolled around a 1.5 cm radius, as shown in Figure 3.14(b).



**Figure 3.14:** Images illustrating flexibility testing on paper samples. (a) Shows folding of the sample, (b) shows rolling of the sample, (c) and (d) show matt paper before and after rolling respectively and (e) shows photo paper where the coating cracked during folding.

‘Excellent’ was used to indicate that a paper can be rolled and returns to its original shape and that it can also be folded easily with no damage to the sample. ‘Good’ indicates the paper stays loosely rolled/creased but can be easily folded. This is illustrated in Figure 3.14, where (c) shows the paper before rolling and (d) shows the paper after. ‘Average’ indicates the paper stays loosely rolled/creased and is harder to fold; this applied mainly to thicker matt papers. ‘Poor’ indicates the paper stays rolled and part of the paper tears when folded; this applied mainly to coated papers where the plastic layer cracked during folding, as shown in Figure 3.14(e). ‘Very Poor’ indicates the paper could not be folded or rolled; this is more appropriate for card.

All papers were shown to have some permanent change when rolled and folded, although the coated glossy papers were found to have a more severe change than the matt papers. It can be seen from Figure 3.14(e) that the gloss coating has cracked when folded. Looking again at the SEM images of printer paper and Epson paper (Figures 3.1 and 3.4), it can be seen that with matt papers the fibres are exposed and can easily move over each other, whereas the coating on glossy papers is stiff and



restricts this movement. Some coated papers like baking paper are found to be flexible which is due to the coating being a silicone, which is an elastomer.

### **3.3.5 Cost**

Although all papers are much cheaper than traditional substrates like silicon or glass, there is still a large difference in cost between printer paper and some speciality papers. Printer paper can be bought in bulk for less than half a pence per A4 sheet, whereas some coated papers investigated here were up to 60 pence per sheet. It must also be noted that, due to supply and demand, the price of speciality papers may be reduced if the demand for paper-based electronics increases. Each cost is calculated using a quote from the company who provided the paper for the project. The cost is calculated for an A4 sheet to make comparisons simpler, although some papers may not be directly available in this size. For example Morrison's baking paper is sold per roll (380 mm × 10 m) and Rizla Green cigarette paper comes in small sheets (67 × 35 mm).

Coated papers and speciality papers which have added ingredients and require more complex fabrication methods are more expensive. Simple printer paper that is produced in very large quantities and has a simple structure and manufacturing process is obviously cheaper.

### **3.3.6 Weight/Thickness**

The weight and thickness of a paper are basic properties that may be useful to know if paper is to be used as part of the device. For example, the thickness is key when paper is used as the dielectric in a parallel plate capacitor. Weight consideration may be important in some applications, such as for use in aeroplanes. These values have been obtained using a balance (for weight) and a micrometer (for thickness). The tolerances are  $\pm 0.05$  g and  $\pm 0.005$  mm for weight and thickness measurements respectively. As with cost, simple papers with no coating are likely to weigh less and be thinner than those with a coating and added components. This was found with the papers investigated here.

## **3.4 Comparison of Thermal Evaporation and Screen Printing**

As with substrates for paper-based electronics, fabrication methods can also be compared and the optimum method for a certain application can be determined. This must be considered in parallel with the substrate to ensure they are compatible with each other. Thermal evaporation and screen printing are considered here in terms of the available materials, process repeatability, minimum repeatable

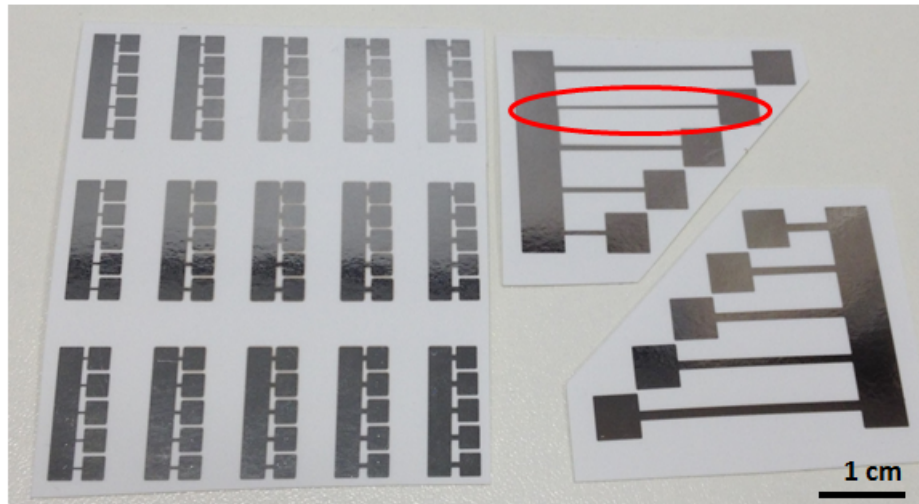
feature size, thickness range of deposited layer, paper compatibility as well as ease of use. The results of these investigations are summarised in a decision matrix, Table 3.7. Both methods are then used to deposit metal layers on various papers which are characterised in terms of sheet resistance and adhesion, with results shown in Table 3.6. As with the investigation into papers, the matrix is presented towards the end of the chapter.

In this work, the term ‘repeatability’ is somewhat subjective and is a combination of the repeatability of both the feature size and the achieved sheet resistance. The rating given is relative to the other method, and was determined by four point probe measurements to calculate the sheet resistance and measurements of dimensions using microscopy and profilometry techniques. Although this is a key factor in choosing an optimum fabrication method, this can also be greatly improved on a larger, industrial scale.

It should be noted that the results are for the equipment available and it could be possible to achieve better results in an industrial environment. The thermal evaporator was existing prior to this work, the screen printing process was developed for this work and details of both processes have been presented in Chapter 2.

### **3.4.1 Thermal Evaporation**

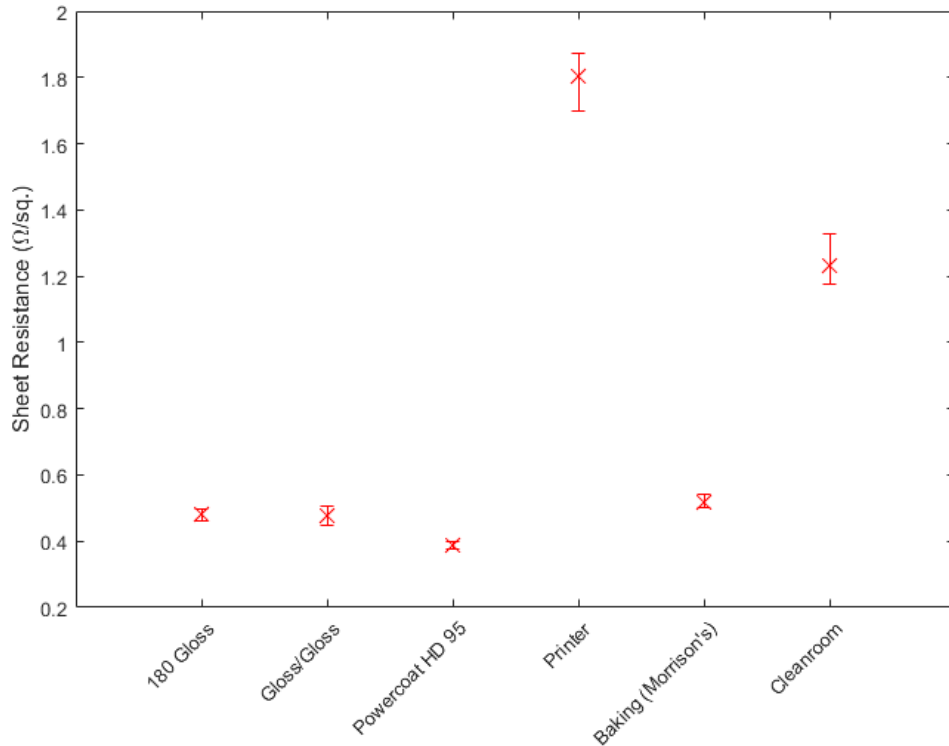
The minimum repeatable feature size when using a shadow mask is limited by both the quality of the mask and the distance between the mask and the substrate. As the shadow mask is moved further out of contact with the substrate, shadowing occurs and so features are larger than intended. When depositing patterns as shown in Figure 3.15, the minimum feature size was found to be 200  $\mu\text{m}$ . It can be seen that the smaller features on the left-hand side do not have sharp corners, however the connections between pads are distinct. The mask used in this work could be better quality leading to higher definition and smaller features. Shadow masks with nanoscale features have been successfully produced in a free-standing silicon nitride membrane which can then produce nanoscale features, although these require long production times [9].



**Figure 3.15:** Examples of thermally evaporated samples. The left-hand samples show features down to 200  $\mu\text{m}$  and highlight the rounding of corners due to a suboptimal shadow mask. The right-hand, larger samples highlight the issue of the shadow mask moving during deposition.

The red circle on the right-hand side of Figure 3.15 highlights a possible issue when using a shadow mask in which there are sections which are secured on only one edge and can be considered as ‘floating’. The mask moved during deposition and so features different to those that have been designed were achieved. This can be avoided by designing the shadow mask so that all sections have two points of contact with others and are not free to move.

The thickness of thermally evaporated layers is determined by the user; when the thickness monitor shows the desired thickness, the evaporation is stopped. The thickness is often lower than 500 nm due to long deposition times, these thicknesses produce layers with low conductivity. Figure 3.16 shows values of sheet resistance obtained were in the order of  $1 \Omega/\square$ , whereas sheet resistances down to  $10 \text{ m}\Omega/\square$  were obtained for screen printing. The percentage error for the sheet resistance of each paper sample is similar due to the large area ( $25 \times 25 \text{ mm}$ ) over which the four point probe measurements are taken, meaning discontinuities are averaged out. These results are seen to be very repeatable. The use of a shadow mask ensures repeatability in feature sizes, and even when the dimensions produced are not as desired, they are highly repeatable.



**Figure 3.16:** Plot of sheet resistance of thermally evaporated layers on various papers listed in order of surface roughness. 180 Gloss has a roughness (Ra) of 0.098 nm and cleanroom paper has a roughness (Ra) of 3.67 nm. Rougher papers were found to have higher sheet resistance values due to the thin layers deposited.

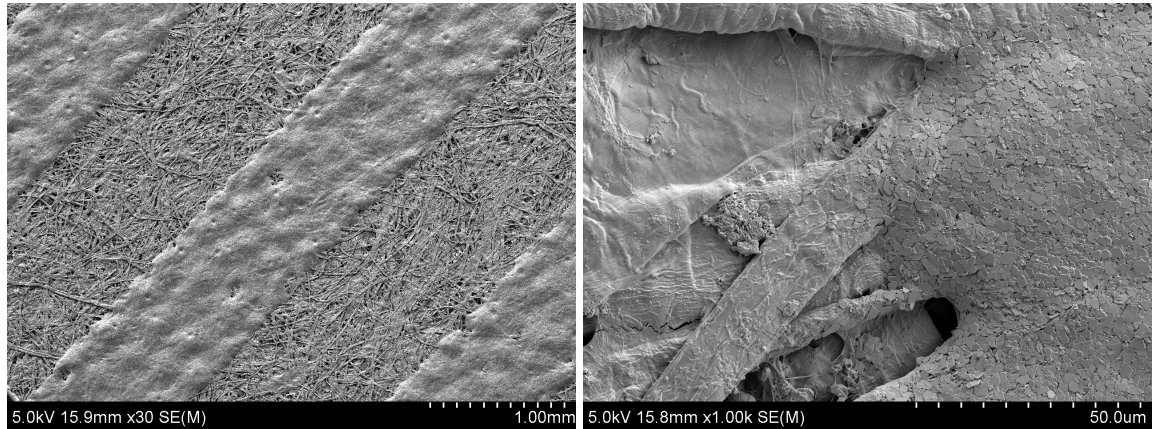
Thermal evaporation is a straightforward process as the user is only required to load samples, observe evaporation and then remove samples. It is not a messy process, although it does require long waiting times for the vacuum level to be reached. It is compatible with all papers except Parax paper, which was found not to be able to withstand the heat of the process and so curled and wilted during evaporation.

### 3.4.2 Screen Printing

Screen printing is a very quick method for depositing large areas of thick patterned material. For this work, a simple start-up kit was purchased from Novacentrix, which, compared to thermal evaporation, was inexpensive. Several inks are compatible with screen printing, including conductive, dielectric and semi-conductive inks. This work uses Metalon HPS-021LV silver nano-flake ink [10]. Silver is the most common conductive material used in screen printing [11–19], but others are also available including copper oxide, nickel and carbon [20].

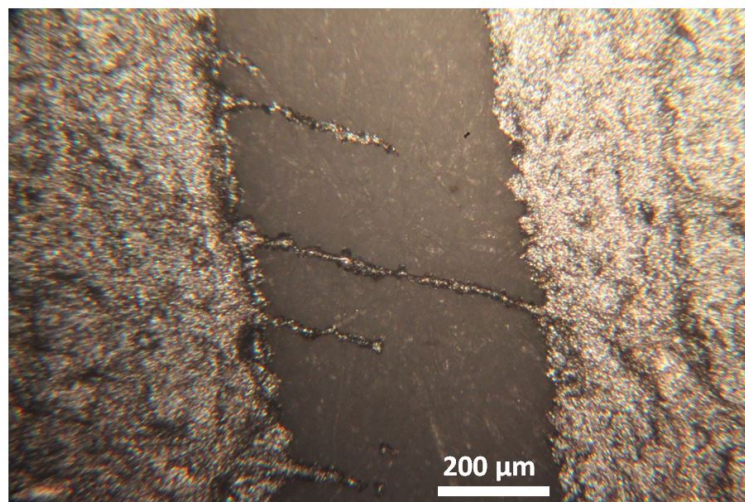
Screens are used to pattern the deposited conductive layer and were made in house, as detailed in Chapter 2, with the minimum feature size being limited by the quality of the screen. Stainless steel screens can produce minimum feature sizes down to approximately 200 μm, whereas the polyester screens used in this work were limited to 500 μm. Scanning electron microscope images of screen-

printed lines 1 mm wide can be seen in Figure 3.17. These are printed on matt paper and so the roughness of the paper leads to a non-uniform layer of ink. However, due to the thickness of the ink (between 10 and 23  $\mu\text{m}$ , determined using a Dektak profilometer), the non-uniformity does not affect the sheet resistance of the printed layers. Although the layer shows some non-uniformity, there is a clear distinction between the ink and the paper at the edge of the printed area.



**Figure 3.17:** SEM image of screen-printed 1 mm lines using silver ink on 199 gsm matt paper.

It was found that gaps between features smaller than 500  $\mu\text{m}$  suffered from thin short circuits, illustrated in Figure 3.18. This was found to be the main concern during screen printing and was due to the poor tension across the mesh of the screens made in house. During printing, the screen should ‘snap off’ the substrate as it is being printed, and the only contact between the screen and substrate should be at the point of contact of the squeegee. When the tension is poor, the screen does not ‘snap off’ and so after printing the screen must be peeled off the substrate and small amounts of ink are flicked off, producing the shorts. This can be overcome by using a screen with higher tension across the mesh.



**Figure 3.18:** Image illustrating shorting between two screen-printed lines due to insufficient tension in the mesh.

### 3.4.3 Sheet Resistance

It is important to know the sheet resistance which can be achieved for metallic layers deposited by thermal evaporation and screen printing on each paper when producing devices. Sheet resistance measurements were taken for  $20 \times 20$  mm squares of 110 nm thick aluminium deposited by thermal evaporation and  $30 \times 30$  mm squares of screen-printed Metalon HPS-LV silver nano-flake ink. The values were obtained using a four point probe set up. As it is a time-consuming process to deposit the metal with thermal evaporation, not all samples were tested; however at least one sample of each type of paper has been tested.

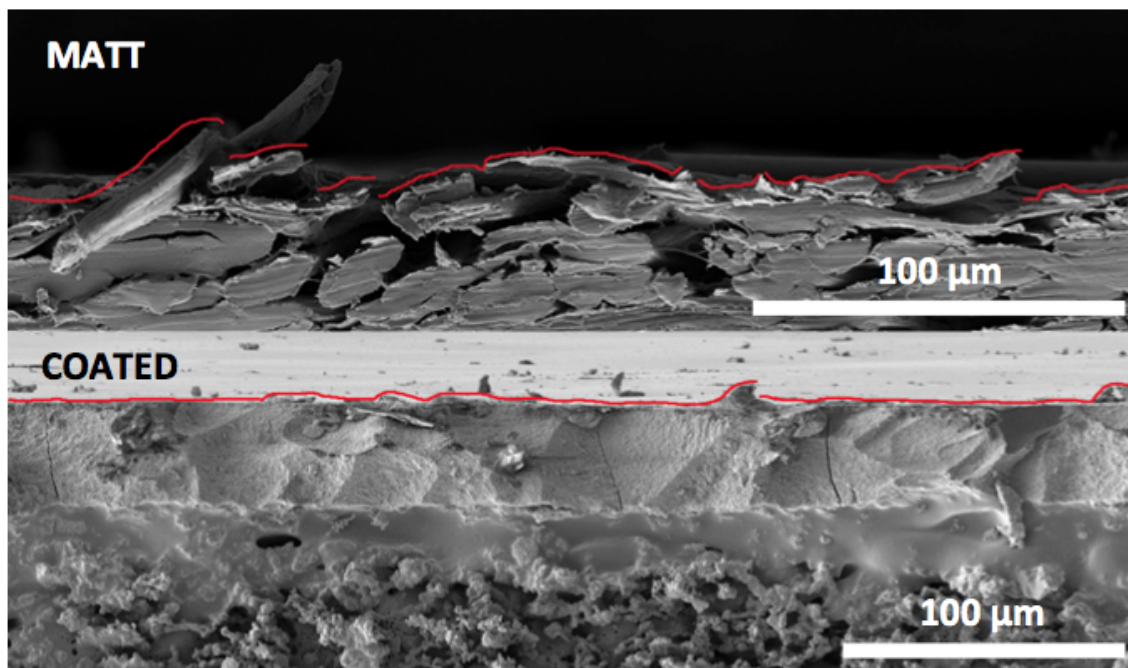
Values for sheet resistance of a selection of papers are presented in Table 3.4. As some papers were found not to withstand high temperatures, and the screen-printed samples were sintered at  $120^\circ\text{C}$  for 30 min, they were found not to produce conductive tracks. The values presented here and in Table 3.6 marked with a ‘\*’ are those measured without sintering, for example Parax papers.

**Table 3.4:** Comparison of sheet resistance values obtained for thermally evaporated and screen-printed layers on various papers.

Paper	Sheet Resistance ( $\Omega/\square$ )	
	Thermal Evaporation	Screen Printing
Gloss/Gloss Photo	0.47	0.018
Epson Photo	0.50	0.11
Baking	0.5	0.013
Cleanroom	1.23	0.012
Neenah	3.96	0.015
Parax	4.92	0.93*

#### Layers Deposited by Thermal Evaporation

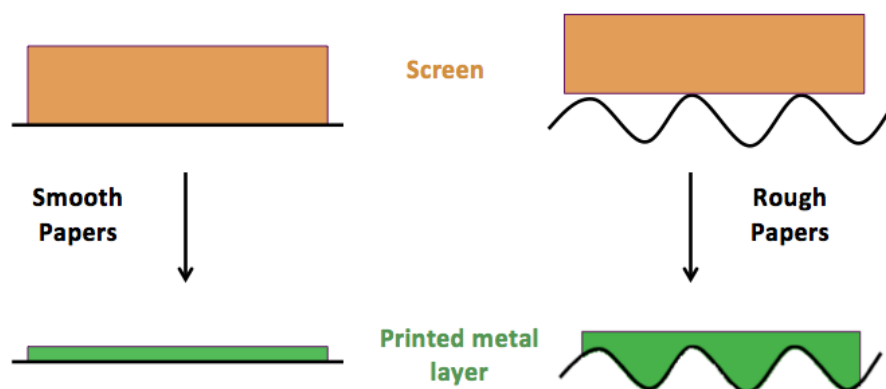
Thermally evaporated layers of metal deposited on matt papers were found to have a higher sheet resistance than those deposited on coated papers. This can be explained by looking at the surface topography of the paper. Thermally evaporated layers result in a conformal coating of the metal. For papers which are not coated, the layer of deposited metal follows the profile of the paper and results in a longer path length compared to those papers which are coated and have a smoother surface. This is illustrated in Figure 3.19, to the right of the image, the red line is clearly broken, which will lead to areas of no connection, also increasing the resistance.



**Figure 3.19:** Adapted SEM images illustrating the difference in theoretical metal layers (shown in red) deposited on matt (top) and coated papers (bottom).

### Layers Deposited by Screen Printing

Conversely to the thermally evaporated layers, the screen-printed layers will be much thicker (10-20  $\mu\text{m}$  where evaporated layers are 50-100 nm). Therefore, rather than having metal layers as shown in Figure 3.19, the metal layers will fill in all the voids in the matt papers between the fibres and be thicker. As the screen is placed on top of the paper and the metal ink is applied to the same thickness as the mesh, the coated papers will have an actual metal thickness the same as the thickness of the mesh, whereas the matt papers will have a metal layer of this thickness plus anything which is below the highest points on the paper surface where the screen will rest, meaning a thicker layer of ink. This theory is illustrated in Figure 3.20. Thicker layers of ink produced on matt papers will therefore have a lower sheet resistance than thinner ones printed on coated papers.



**Figure 3.20:** Illustration to show the difference between screen-printed layers on smooth and rough papers.

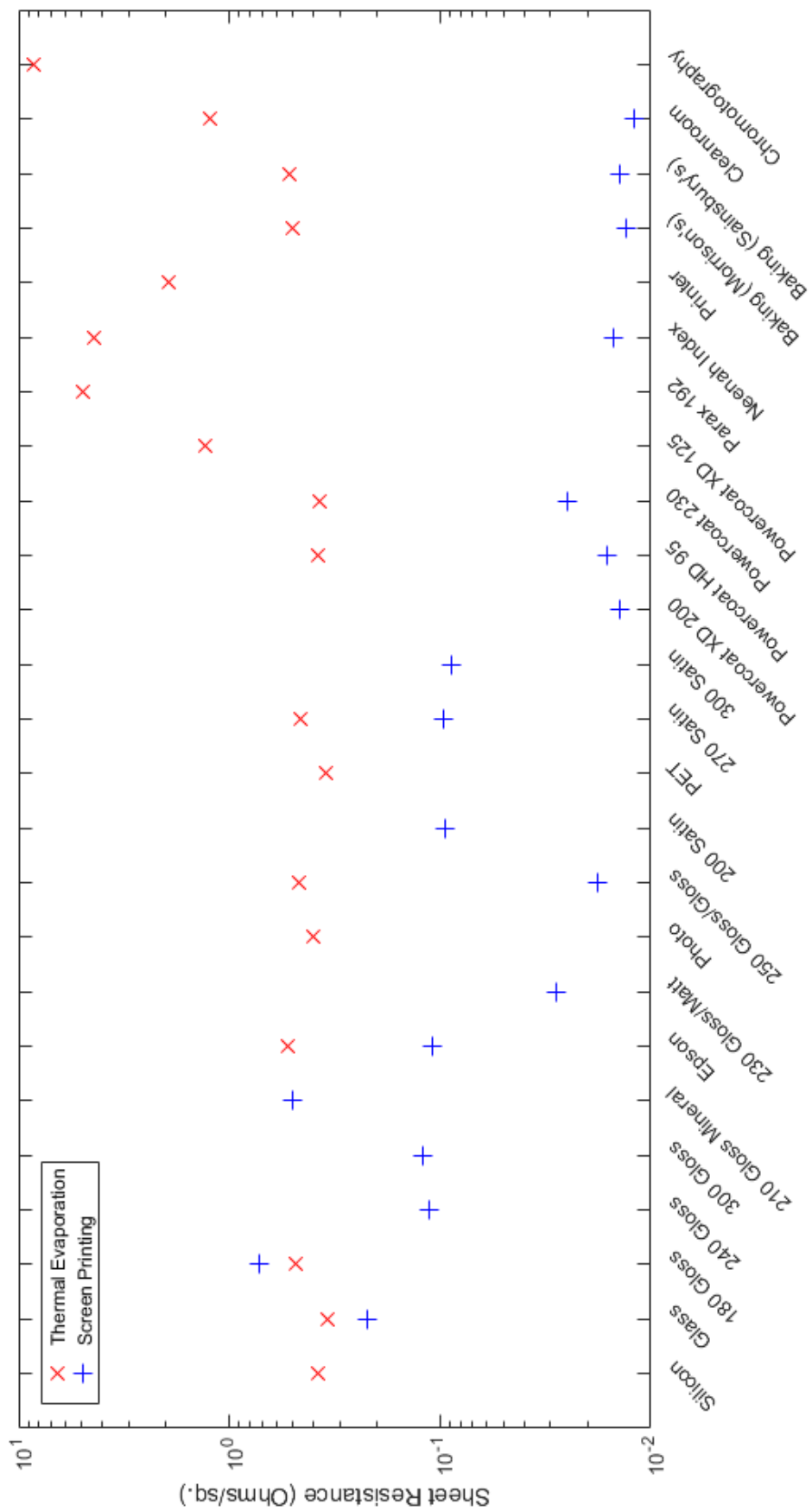


### 3.4.4 Surface Roughness and Sheet Resistance

From the investigations into surface roughness and sheet resistance, it was noted that there could be some trend between the two properties. Figure 3.21 shows a graph of various papers and the sheet resistance for both thermally evaporated and screen-printed layers. The papers are in order of surface roughness with 180 Gloss being the smoothest paper (with a surface roughness of  $0.098\ \mu\text{m}$ ) and chromatography paper being the roughest (with a surface roughness of  $6.15\ \mu\text{m}$ ). Glass, silicon and PET have been added as a comparison with established substrates and are discussed in more detail later in this chapter. Figure 3.21 shows clear opposing trends in sheet resistance compared to surface roughness for thermally evaporated and screen-printed conductive layers, as explained by Figures 3.19 and 3.20. Single, average, values have been plotted as varying numbers of samples were taken for each paper. Some papers were investigated in further detail and others were found to be unsuitable at an early stage. For example chromatography paper was found to be a poor choice in terms of its adhesion and surface roughness and so only one sample was tested, whereas Epson photo paper provided promising results and low resistivity for thermally evaporated samples, and so several samples were tested.

When paper is used as the substrate for electronic components, the surface topography must be considered as it has been shown here to have a large effect on the sheet resistance of deposited layers. The morphology of the paper must be carefully considered for a chosen deposition method, for thermal evaporation, a smoother paper results in lower sheet resistance whereas with screen printing, a rougher paper results in lower sheet resistance.

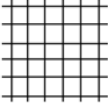
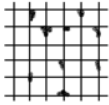
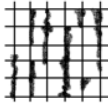
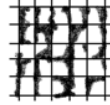
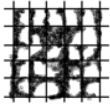
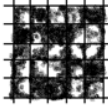




**Figure 3.21:** Sheet resistance for thermally evaporated and screen-printed metal layers on various paper samples. The substrates are listed in order of surface roughness with silicon being the smoothest (with a surface roughness of 0.016 μm) and chromatography paper being the roughest (with a surface roughness of 6.15 μm).

### 3.4.5 Adhesion

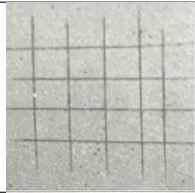
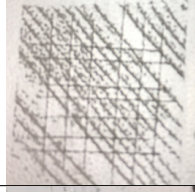
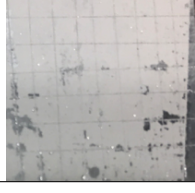
Adhesion between a conductive layer and the paper is another important factor to be considered; if the conductive layer does not adhere to the surface then devices cannot be successfully produced. The value for adhesion given in this work was based on the ISO Standard 2409:2013 Cross cut test [21]. A small area (1.5 cm square) of the deposited metal was scored using a scalpel in the pattern shown in Figure 3.22. Scotch A81925R3 Magic Tape was then placed on the area and peeled off. The number (between 0 and 5) given for adhesion was then determined by the amount of metal removed. As can be seen in Figure 3.22, '0' indicates that none of the metal has been removed from the substrate whereas '5' indicates more than 65% of the metal has been removed by the Tape. 'Split' was noted for samples when some of the paper itself was also removed by the Scotch Tape.

Appearance of Cross-cut Area						
Percentage of Metal Removed	0%	<5%	<15%	<35%	<65%	>65%
Classification	0	1	2	3	4	5

**Figure 3.22:** Illustration of ISO Standard for adhesion testing. Classification is taken to be 0 for no metal removed and 5 for more than 65% of the metal removed. The white regions are the deposited metal layer and the black regions are the paper substrate where the metal has been removed.

As it is a time-consuming process to deposit the metal with thermal evaporation, not all samples were tested; however at least one sample of each type of paper has been tested. Some examples are shown in Table 3.5. The adhesion of screen-printed layers on Epson photo paper was rated at 0 as no metal was removed, whereas the adhesion of screen-printed layers on Parax stone paper was rated at 4 as approximately half of the metal layer was removed, and the adhesion of thermally evaporated layers on Powercoat HD papers were rated at 5 as almost all of the metal was removed.

**Table 3.5:** Examples of adhesion testing, including the ISO standard rating and images of the samples after testing.

<b>Sample</b>	<b>Image</b>	<b>ISO Rating</b>
Screen-printed layer on Epson		0
Screen-printed layer on Parax		4
Thermally evaporated layer on Powercoat HD 95		5

### 3.5 Decision Matrices for Paper and Fabrication Method

Table 3.6 and Table 3.7 are presented below and contain all the experimental results for each paper and fabrication method respectively.

**Table 3.6:** Key papers and their relative properties.

Paper	Surface Roughness ( $\mu\text{m}$ )	Cost per A4 Sheet (£)	Weight per A4 Sheet (g)	Thickness (mm)	Resistance per square ( $\Omega/\text{sq}$ )		Adhesion		Heat Treatment ( $^{\circ}\text{C}$ )	Waterproof	Flexibility
					Thermal Evaporation	Screen Print	Thermal Evaporation	Screen Print			
Printer Office Depot 5226498	3.08	0.005	5.0	0.08	1.81		0	0	200+	Poor	Good
Cleanroom Berkshire B85.A4.BL.250/10	3.67	0.04	5.4	0.04	1.23	0.012	0	0	200	Average	Good
Chromatography Whatman 1	6.15	0.22	5.28	0.15	8.46		Split		200	Poor	Average
Neenah 40411	2.74	0.06	11.8	0.24	3.96	0.015	0	0	180	Poor	Good
Glossy Photo Epson S041140	0.25	0.35	15.8	0.24	0.50	0.106	0	0	175	Average	Poor
120 Matt Felix Schoeller J82270	2.59	0.14	7.3	0.12		*		2	185	Poor	Excellent
230 Matt Felix Schoeller J93270	2.61	0.36	14.4	0.22		*	Split	1	200	Poor	Good
180 Gloss Felix Schoeller J37110	0.098	0.32	12.6	0.17	0.48	0.716	0	0	185	Average	Poor
240 Gloss Felix Schoeller H62110	0.10	0.46	15.2	0.20		0.113	Split	0	165	Average	Poor
300 Gloss Felix Schoeller H72110	0.12	0.56	18.8	0.27		0.12	Split	0	165	Average	Poor
200 Satin Felix Schoeller H64219	0.75	0.37	12.5	0.17		0.094		0	175	Average	Average
270 Satin Felix Schoeller J71210	0.88	0.50	17.1	0.23	0.46	0.97	0	0	185	Average	Poor
300 Satin Felix Schoeller J72710	1.08	0.56	19.3	0.27		0.088		0	185	Average	Poor

170 Matt/Matt Felix Schoeller J87274	2.38	0.4	7.6	0.14	NC	*	5	2	185	Poor	Excellent
230 Gloss/Matt Ink2Paper	0.27	0.42	14.4	0.26		0.028		0	200	Poor	Poor
250 Gloss/Gloss Felix Schoeller J87274	0.69	0.61	16.8	0.23	0.47	0.018	0	0	175	Average	Poor
210 Matt mineral Ink2Paper	4.07	0.075	14.8	0.19		*	5	0	120	Average	Excellent
210 Satin mineral Ink2Paper	1.08	0.094	14.6	0.18		*	0	0	100	Average	Poor
210 Gloss mineral Ink2Paper	0.21	0.11	21.1	0.21		0.502*	5	2	150	Average	Poor
Parax 168 gsm	1.41	0.074	10.1	0.13		*	2		100	Excellent	Excellent
Parax 192 gsm	1.68	0.082	12.1	0.14	4.92	0.93*		4	100	Excellent	Excellent
Parax 216 gsm	1.58		13.5	0.14		0.85*	2	4	100	Excellent	Excellent
Powercoat 230	1.39	0.31-0.41	13.4	0.21	0.37	0.025	5	0	200+	Good	Poor
Powercoat HD 95	1.34	0.31-0.41	6.0	0.08	0.38	0.016	5	0	200+	Good	Good
Powercoat XD 200	1.33	0.10-0.21	12.5	0.18		0.014		1	200+	Poor	Average
Powercoat XD 125	1.47	0.10-0.21	8.0	0.11	1.31	0.015	0	1	200+	Poor	Average
Baking Sainsbury's	3.65	0.037	2.8	0.02	0.52	0.014	0	5	200+	Good	Excellent
Baking Tesco's	3.54(Matt) 3.03(Gloss)	0.025	2.4	0.04			5	2	200+	Poor	Excellent
Baking Morrison's	3.56	0.025	2.6	0.03	0.5	0.013	0	5	200+	Good	Excellent
Cigarette Rizla Green	3.35	0.13	1.1	0.02			Ripped		200+	Very poor	Excellent

**Table 3.7:** Fabrication methods and their relative properties as determined in this work.

<b>Property</b>	<b>Thermal Evaporation</b>	<b>Screen Printing</b>
<b>Available Materials</b>	Low melting point metals	Silver
<b>Process Repeatability</b>	Very Good	Average
<b>Minimum Feature Size</b>	200 $\mu\text{m}$	500 $\mu\text{m}$
<b>Paper Compatibility</b>	All but Parax	All but baking paper
<b>Thickness Range of Deposited Layer</b>	Up to 500 nm	1 - 100 $\mu\text{m}$
<b>Ease of use</b>	Straightforward, long waiting times	Straightforward, messy

### 3.5.1 Determining an Optimum Paper and Fabrication Method

The optimum paper and fabrication method for paper-based electronic devices must be determined in parallel. Results have been presented here which show that matt papers are more suited to screen printing whereas gloss papers are more suited to thermal evaporation.

As can be seen from Table 3.6 and the results presented here, papers vary greatly in terms of their properties. Despite this, it can be seen that the same ‘types’ of paper have similar characteristics. For example, all matt papers are cheap, rough and flexible whereas gloss coated papers are expensive, smooth and water resistant. When deciding on an optimum substrate for a particular application, a type of paper is likely to be chosen and then a specific brand and paper decided on after.

Although thermal evaporation was found to be more repeatable than screen printing and relatively straightforward, it was not considered optimal for this work due to the thickness of conductive layers attainable and the following lower conductivity of devices and difference in results when using different papers. In addition to this, the area over which conductive materials can be deposited is far smaller than screen printing. In industry, this area can be increased, but in this work the patterning area for thermal evaporation was approximately 20% of that of screen printing.

Screen printing has been shown to be compatible with nearly all papers used in this work. It is a very easy process, it produces layers with sheet resistances less than  $20 \text{ m}\Omega/\square$  and can produce feature sizes down to 500  $\mu\text{m}$ . It was decided that for this work, screen printing was the optimal fabrication method. It has been shown there were issues with shorting between smaller feature sizes but it was determined that this could be overcome by optimisation of the process.

Screen printing has been shown to produce metallic layers of lower sheet resistance when used with rougher papers. For this reason, it was decided a matt paper should be used. Some matt papers were not compatible with the screen-printing process, due to chemical interactions with the ink. Neenah

paper was provided with the screen-printing kit used in this work and it produced ideal prints, and so it was decided that this would be the substrate used for this work. As many matt papers have very similar characteristics, several papers may be suitable for one application and there may not be only one optimum solution.

### **3.6 Comparison of Paper with Established Substrate Materials**

Table 3.8 compares a selection of different types of paper with silicon, glass and polyethylene terephthalate (PET) which are established substrates and materials in current electronics fabrication.

A silicon wafer with an oxide layer was used to prevent conduction through the silicon.

**Table 3.8:** Comparison of paper samples with silicon, glass and PET

Substrate	Surface Roughness ( $\mu\text{m}$ )	Cost per A4 Sheet (£)	Weight per A4 Sheet (g)	Thickness (mm)	Resistance per square ( $\Omega/\text{sq.}$ )	Adhesion	Heat Treatment ( $^{\circ}\text{C}$ )	Waterproof	Flexibility
Printer Paper	3.08	0.005	5.0	0.008	5.5	0	200	Poor	Good
Photo Paper (Epson)	0.25	0.35	15.8	0.24	0.50	0	175	Average	Poor
270 Satin Paper	0.88	0.50	17.1	0.23	0.46	0	185	Average	Poor
250 Gloss/Gloss Paper	0.69	0.61	16.8	0.23	0.47	0	175	Average	Poor
Baking Paper (Morrison's)	3.56	0.025	2.6	0.03	0.5	0	200+	Good	Excellent
Parax Paper 192 gsm	1.68	0.082	12.1	0.14	4.92	2	100	Excellent	Excellent
Silicon Oxide Wafer	0.016	317	45.2	0.35	0.37	2	200+	Excellent	Very Poor
Glass Microscope Slide	0.019	155	176.76	1.13	0.33	3	200+	Excellent	Very Poor
PET	0.5	10.7	4.19	0.06	0.35	2	190	Excellent	Excellent



It can be seen from Table 3.8 that the established substrates have a much higher cost than paper. This is due to the raw materials and also the manufacturing process being much more complex and expensive. They also have much lower surface roughness values than all other papers. This leads to the thought that when a metal is thermally evaporated onto them, the metal layer will have a much lower resistance. This is not the case, as the resistance of the metal layers measured is lower but still of the same order of magnitude as those on paper. This is likely due to the cleanliness of the substrates. It can be seen in Table 3.8 that the surface roughness of PET is comparable with that of glossy papers; however, when prepared for standard fabrication, this roughness value would be much lower. During testing, all substrates were handled in the same way, they were not cleaned or treated in any way before metal deposition and no extreme care was taken when handling the samples. With paper, this has been shown to make little difference, but with silicon, glass and PET, the lack of preparation has resulted in a higher resistance than the values which can be obtained with cleaning. This also leads to an issue with the adhesion; when silicon, glass and PET are cleaned and treated before deposition, the adhesion would rate a 0 on the ISO standard scale, however, when they are 'dirty' the metal does not have good adhesion with the substrate and is rated 2 or 3.

These results highlight another advantage paper has over current substrates for electronics. Paper does not need to be cleaned or treated in some way before fabrication, like silicon, glass or PET do. In reality, silicon, glass and PET can give much lower resistance than can be obtained using paper, and so paper is a suitable substrate to be used alongside silicon where its properties are more suited for the application and not as a replacement for silicon or glass.

### **3.7 Conclusion**

The term paper is a diverse term: this chapter has shown how paper may refer to fundamentally different substrates, which may not even include cellulose. Matt papers, consisting of cellulose fibres and calcium carbonate, were compared to gloss papers, which are essentially matt paper coated with polymers, and speciality papers.

Thermal evaporation and screen printing have both been shown to produce conductive films on papers. However, screen printing combined with matt paper resulted in thicker films with higher conductivity, and were thus the preferred option for the devices presented in the next chapters.

One of the key results reported in this chapter is the compilation of two decision matrices to aid the selection of paper and conductive film deposition, targeted to a specific application. Other

combinations (instead of matt paper and screen printing) may be more suitable for developing devices and circuits which have different requirements: for example, being waterproof or providing an extremely smooth substrate.

It was also found that the adhesion of metal films on matt paper is aided by the natural paper porosity, resulting in a substrate which is easier to handle than silicon or plastics. As small particles do not affect the adhesion, as they are trapped in the paper voids, the overall deposition process can take place outside a cleanroom. If commercially scaled, the relaxed requirements on a tight environment control result in considerable cost savings.

## References

- [1] M. A. Hubbe, "Acidic and alkaline sizings for printing, writing, and drawing papers," *The Book & Paper Group annual*, vol. 23, p. 139, 2004.
- [2] R. L. Hills, *Papermaking in Britain, 1488-1988: A short history*. Athlone Press, 2015.
- [3] Mondi, "Nautilus Super White (PCF) Technical Datasheet," 2016.
- [4] Berkshire, "BCR Cleanroom Bond Technical Datasheet," 2016.
- [5] Neenah Paper Inc, "Exact Papers Safety Data Sheet," 2014.
- [6] Arjowiggins, "Powercoat hd Technical Datasheet," 2011.
- [7] <http://www.paraxpaper.co.uk/>. Accessed: 2015-07-02.
- [8] <http://www.terraskin.com/>. Accessed: 2015-07-02.
- [9] Y. X. Zhou, A. T. Johnson, J. Hone, and W. F. Smith, "Simple fabrication of molecular circuits by shadow mask evaporation," *Nano Letters*, vol. 3, no. 10, p. 1371, 2003.
- [10] Novacentrix, "Materials safety datasheet for metalon hps-021lv silver nano-flake ink," 2013.
- [11] Z. Cui, C. Zhou, Z. Chen, C. Ma, J. Zhao, and W. Su, *Printed electronics: Materials, technologies and applications*. John Wiley & Sons, 2016.
- [12] A. E. Ostfeld, I. Deckman, A. M. Gaikwad, C. M. Lochner, and A. C. Arias, "Screen printed passive components for flexible power electronics," *Scientific Reports*, vol. 5, p. 15959, 2015.
- [13] R. Faddoul, N. Reverdy-Bruas, and A. Blayo, "Formulation and screen printing of water based conductive flake silver pastes onto green ceramic tapes for electronic applications," *Materials Science and Engineering B: Solid-State Materials for Advanced Technology*, vol. 177, no. 13, 2012.
- [14] K. K. Adhikari, Y. Jung, H. Park, G. Cho, and N. Y. Kim, "Silver-nanoparticle-based screen-printing and film characterization of a disposable, dual-band, bandstop filter on a flexible polyethylene terephthalate substrate," *Journal of Nanomaterials*, 2015.
- [15] D. Y. Shin, Y. Lee, and C. H. Kim, "Performance characterization of screen printed radio frequency identification antennas with silver nanopaste," *Thin Solid Films*, vol. 517, no. 21, 2009.
- [16] J. W. Kim and S. B. Jung, "Electrical characterization of screen-printed conductive circuit with silver nanopaste," *Japanese Journal of Applied Physics*, vol. 48, no. 6, 2009.
- [17] M. Mraović, T. Muck, M. Pivar, J. Trontelj, and A. Pleteršek, "Humidity sensors printed on recycled paper and cardboard," *Sensors (Basel, Switzerland)*, vol. 14, no. 8, p. 13628, 2014.
- [18] O. J. Arenas, E. L. D. L. Jarrige, and F. Boone, "Creating screen-printed passive components for microwave applications," *Microelectronics International*, vol. 27, no. 2, p. 84, 2010.
- [19] A. Eshkeiti, A. S. G. Reddy, S. Emamian, B. B. Narakathu, M. Joyce, M. Joyce, P. D. Fleming, B. J. Bazuin, and M. Z. Atashbar, "Screen printing of multilayered hybrid printed circuit boards on different substrates," *IEEE Transactions on Components, Packaging and Manufacturing Technology*, vol. 5, no. 3, p. 415, 2015.
- [20] F. Khan and V. Solanki, "Paper moisture sensor based on microwave resonator," *National Conference on Knowledge, Innovation in Technology and Engineering*, p. 321, April 2015.
- [21] "ISO 2409:2013. Cross cut test," 2013.

## Chapter 4

# Screen Printing Optimisation

### 4.1 Introduction

From the decision matrices compiled in the previous chapter, it was determined that the best paper was Nengah 199 gsm matt combined with the screen-printing process. The work presented in this chapter addresses the optimisation of the screen-printing process to achieve small features and high reproducibility.

The effects of the actual screen mesh density, thread size and mesh tension were investigated in detail. Furthermore, the choice of squeegee profile, pressure, angle, pass speed and number of passes, was shown to affect the quality of the print out. It was also found that curing the ink film improved its sheet resistance. Constraints regarding the maximum temperature that paper could be exposed to were determined and correlated to the ink properties.

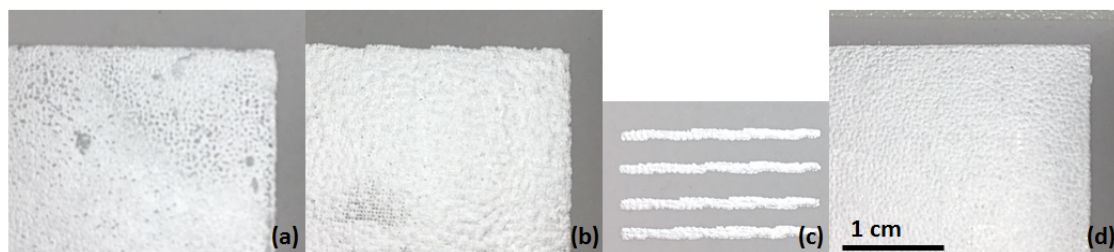
The work presented was carried out on a manually operated screen-printing system. Nevertheless, the process is scalable, and commercial, automated, roll-to-roll systems exist. The manual system is however sufficient to identify the optimal printing parameters, and the developed process can be easily scaled-up to larger systems.

As a demonstrator for assessing the performance of the developed process, passive electrical components, such as capacitors and inductors, were printed. The performance of the inductors was directly comparable with state-of-the-art inductors screen printed on PET.

## 4.2 The Screen

The minimum achievable feature size and the quality of the screen were found to be the main drawbacks of screen printing in the preliminary investigation. The minimum feature size can be decreased by improving the quality of the screen and by using a finer mesh. Initially, screens were produced by stretching 90T mesh over a photo frame by hand and fastening with drawing pins. This method produced screens which did not have uniform tension across the mesh and the frames warped over time, meaning continuous contact with the substrate was not possible.

To improve the quality of the screen, wooden frames were constructed at a local framing shop (Season's Gallery, Durham) and the mesh was attached there with uniform tension. The initial screen exhibited a  $3\text{ cm} \pm 0.5\text{ cm}$  deflection when a 3 kg weight was added in the centre, while the new screen, created by the framing shop only exhibited a  $0.5\text{ cm} \pm 0.1\text{ cm}$  deflection when the same weight was added. This new screen did not warp with time and print quality was greatly improved. As the new screen had sufficient, uniform tension, 'snap off' occurred and so shorting between the tracks was no longer an issue. For tracks with a  $500\text{ }\mu\text{m}$  gap between them, the yield of successful printing with no shorts for the old screen was 40% and for the new screen 90%. The improved quality of printing is shown in Figure 4.1.

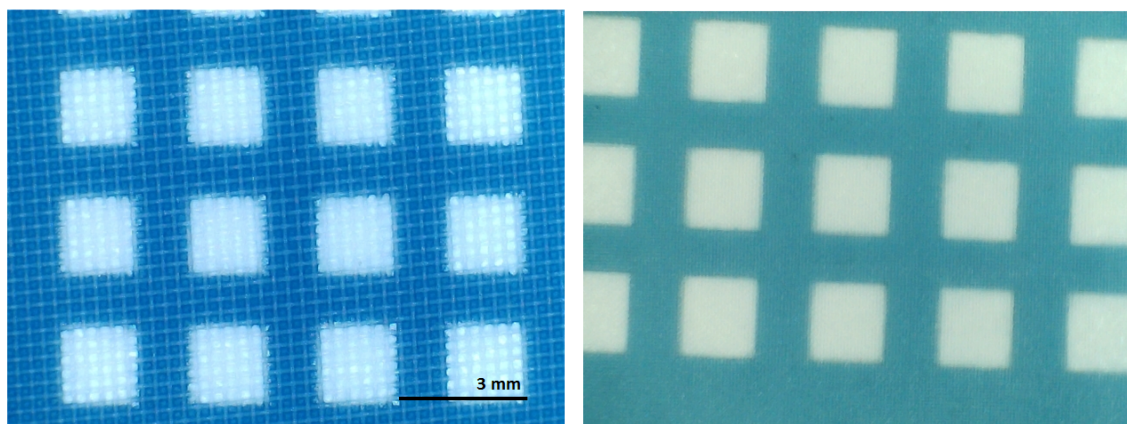


**Figure 4.1:** Images illustrating the difference in print quality when using different screens. (a) Preliminary printing with a 90T mesh screen made in-house, (b) and (c) printing with a 32T mesh screen made by a framing shop, d) printing with an 90T mesh screen made by a framing shop and after optimisation. All images are the same scale.

The mesh count of the screen is another important factor to consider: the lower the mesh count, the poorer the quality of the print as also shown in Figure 4.1. 32T, 55T, 90T and 120T mesh counts were considered in this investigation and their relevant properties are listed in Table 4.1. A 32T mesh count yielded a much thicker printed layer and the larger mesh opening meant smaller feature sizes were not possible. For a screen with a 32T mesh count, the screen was much rougher to the touch and the threads themselves were visible. A comparison of 32T and 120T mesh count screens, patterned with simple squares, is shown in Figure 4.2. The screen with 32T mesh has larger threads which are visible in this image, leading to a more pixelated pattern and poorer detail than the 120T mesh.

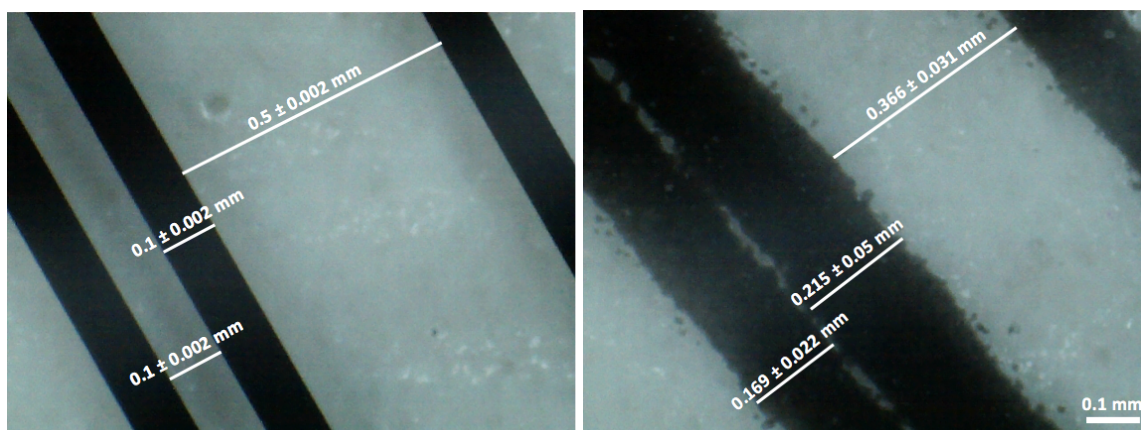
**Table 4.1:** Details on mesh properties of polyester meshes with different thread counts.

Mesh Count	Thread Diameter ( $\mu\text{m}$ )	Mesh Opening ( $\mu\text{m}$ )	Open Surface (%)	Weight ( $\text{g}/\text{m}^2$ )
32T	100	200	44.5	90
55T	63	115	41.75	65
90T	48	63	32.5	50
120T	33	51	36.75	35



**Figure 4.2:** Comparison of a screen with 32T mesh (left) and a screen with a 120T mesh (right), highlighting the larger, more visible threads in the 32T mesh and the poorer definition in features.

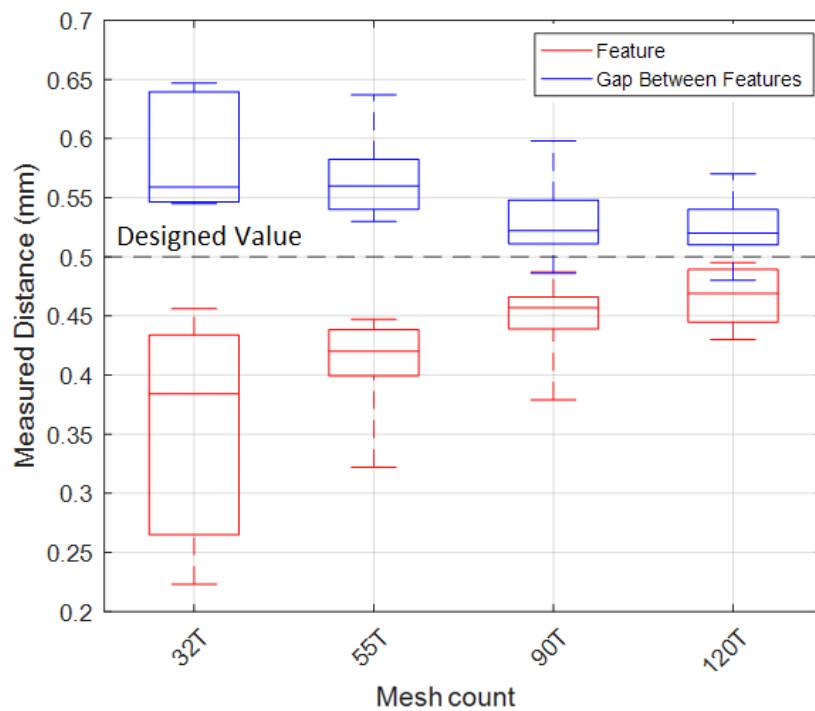
The patterning method of the screens is detailed in Chapter 2; the screens were coated in photo-emulsion and then a patterned acetate was used to harden certain areas and create the final patterned screen. Two methods of producing acetate were considered here, one was created in house using a standard printer and one was created commercially, by Microlithographic service limited (Essex, UK). The acetate produced by Microlithographic service limited had much more defined features which were measured to be at the designed dimensions, whereas the one created in house had features which could be out by over 100%; examples of both acetates are shown in Figure 4.3. These dimensions are measured using a usb camera, a known microscope scale and ImageJ software.



**Figure 4.3:** Comparison of feature sizes of acetate masks produced commercially (left) and in house (right), highlighting the poorer quality for those produced in house.

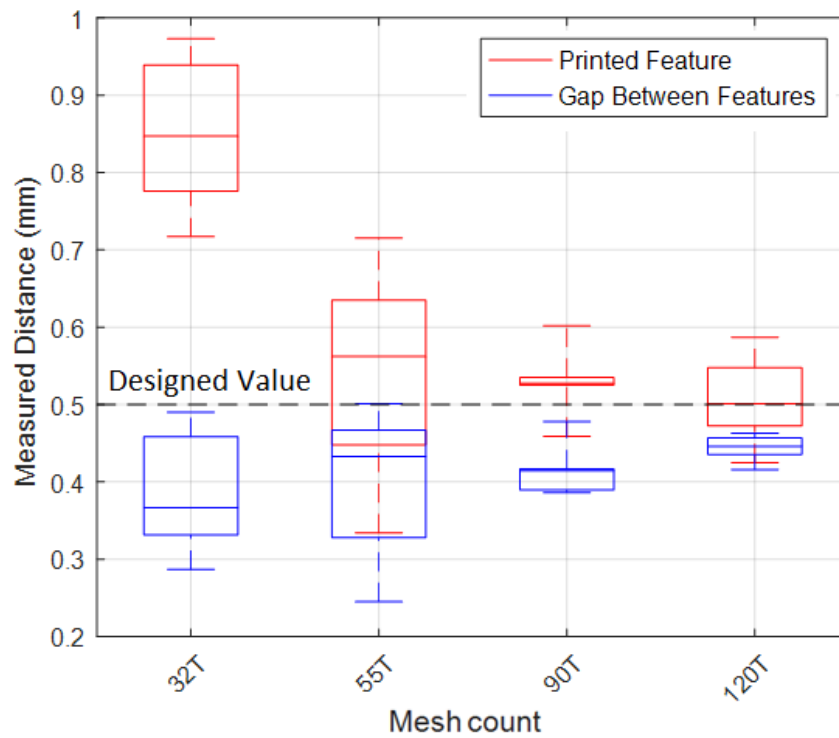
Both acetates were used to create screens, the error for the commercially made mask was 20% better than the one made in house. As the acetate produced by Microlithographic service limited cost nearly £100, it was decided that the in-house masks would be used and were improved upon by using a better-quality printer, reducing the error by half.

The feature sizes and gaps between feature sizes on the screen itself were measured for all four mesh counts and are displayed in Figure 4.4 (the designed values are 0.5mm for both). It can be seen that as the mesh count was increased, the measured values became closer to the designed values and exhibited fewer errors. As detailed earlier, the higher the mesh count, the smaller the opening between threads and so the more accurate the smaller features were.



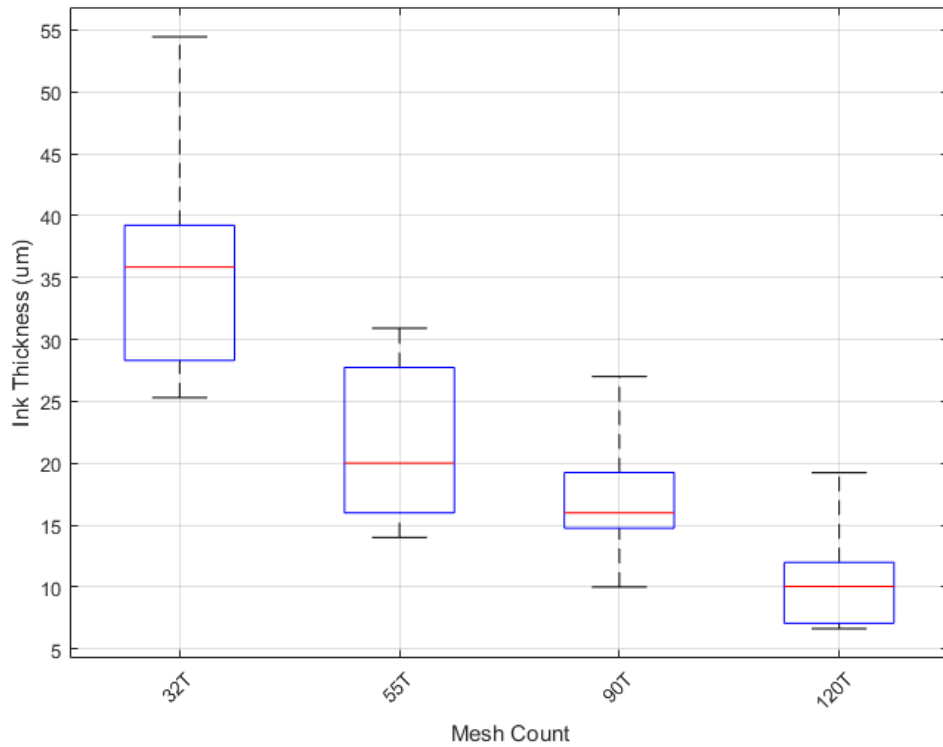
**Figure 4.4:** Comparison of feature sizes and gaps between features on the screen for various mesh thread counts. The whiskers of the box plots show the maximum and minimum values measured.

Similarly, the feature sizes and gaps between features were measured for printed tracks, again with both dimensions intended to be 0.5 mm with results shown in Figure 4.5. For these results, the results of the screen itself must be considered. As the lower mesh counts had poorer results, it was assumed that this variation would then carry through to the prints. This was shown to be the case but it was also seen that as the mesh count decreased, the printed results were more spread out than the screen itself. When using a lower mesh count, more ink can be held within the screen as it is much thicker. This leads to a higher volume of ink being transferred to the substrate which will spread and create larger resulting dimensions.

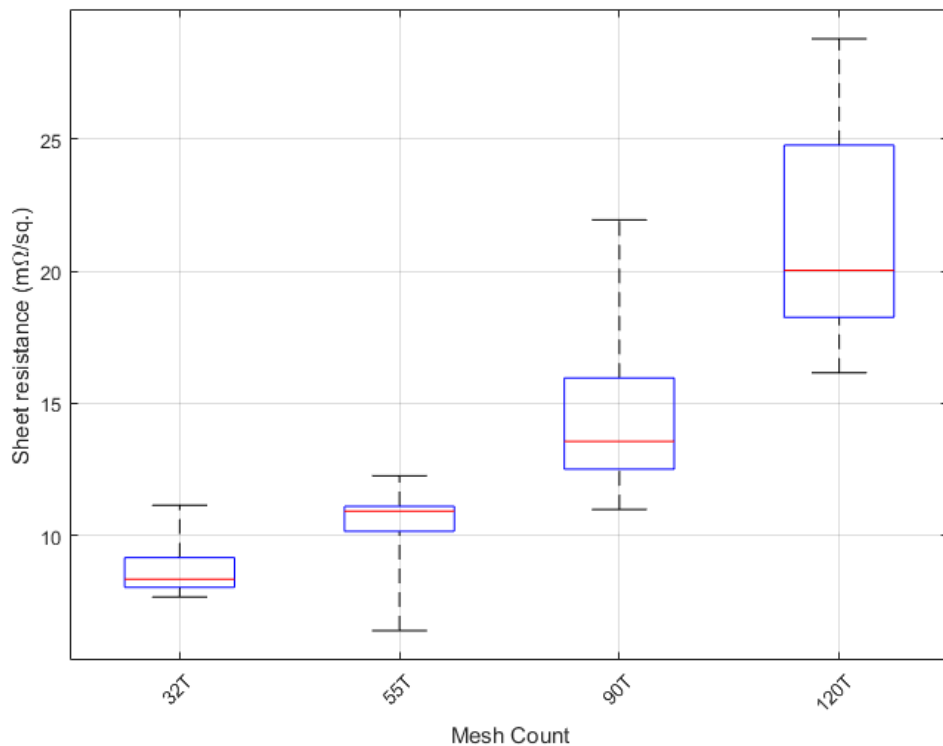


**Figure 4.5:** Comparison of feature sizes and gaps between features for printed structures printed using meshes with various thread counts. The whiskers of the box plots show the maximum and minimum values.

As the volume of ink increases with decreasing mesh count, it was expected that the thickness of the prints would increase and the sheet resistance would decrease. Both of these theories were confirmed by Figures 4.6 and 4.7 which show thickness measurements taken using a Dektak profilometer and sheet resistance measurements taken using a four point probe setup. In addition to showing the increasing ink thickness with decreasing mesh count, it was shown that the variation in thickness was much larger at lower mesh counts. This was likely due to the larger volume of ink leading to weeping and movement of the ink and so less uniform layers. The variation with sheet resistance was increased with increasing mesh count; this was likely due to the decrease in thickness and so any discontinuities along the substrate surface were more dominant.



**Figure 4.6:** Comparison of thicknesses of printed structures using meshes with various thread counts. Measurements were taken using a Dektak profilometer. The whiskers of the box plots show the maximum and minimum values.



**Figure 4.7:** Comparison of sheet resistance values for squares printed using meshes with various thread counts. The whiskers of the box plots show the maximum and minimum values.

Increasing the mesh count of the screen increases the sheet resistance but also decreases the attainable feature sizes and the error associated with them. The ink thickness is also reduced and



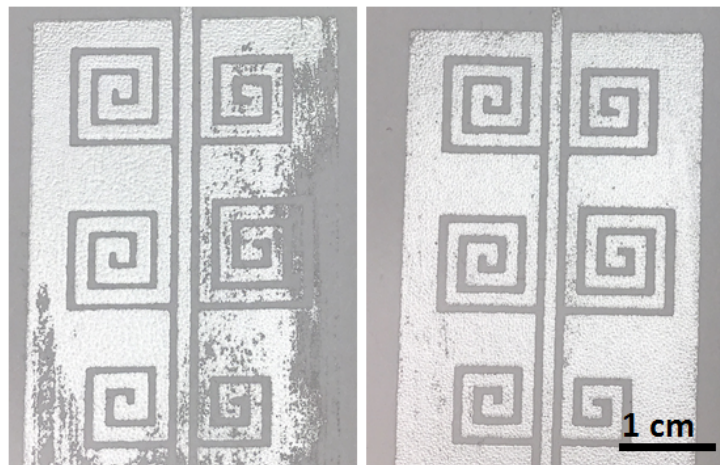
so minimises the volume of ink used. The sheet resistance can be considered acceptable for all mesh counts used, but lower values are more highly desired. The optimal mesh count was determined to be 90T to optimise both sheet resistance and feature size/definition. Results detailed below are for 90T mesh counts using screens produced at the framing shop.

### 4.3 The Printing Process

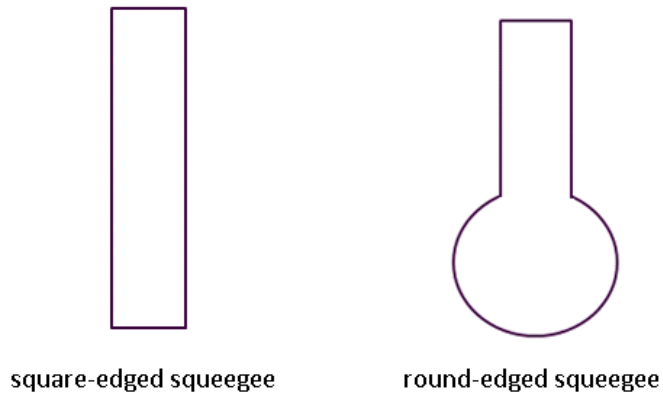
During screen printing, the squeegee is the component that forces the ink through the screen and onto the substrate. There are several factors which affect the quality of the resulting print, including squeegee pressure, angle, speed and the type/material of squeegee used. The type of squeegee used in this work was a 60 durometer square-edged squeegee, which was provided by the supplier of the initial screen-printing kit.

#### Type of Squeegee

A round-edged squeegee was trialed in addition to the square-edged squeegee and found to produce sub-optimal results as shown in Figure 4.8. Square-edged is the most common squeegee profile and is used for cylinder and manual systems. Round-edged is normally limited to the textile industry and applications which require deposition of much thicker layers. The side profiles for both a square-edged and round-edged squeegee can be seen in Figure 4.9.



**Figure 4.8:** Comparison of printed features using a round-edged squeegee (left) and a square-edged squeegee (right).

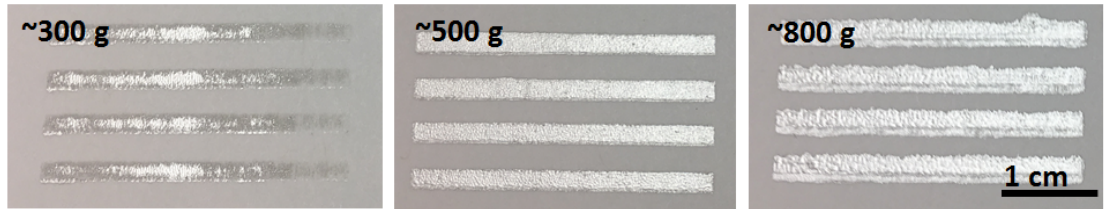


**Figure 4.9:** Illustration of the side profile of a square-edged squeegee (left) and a round-edged squeegee (right).

As evident in the image of the resulting prints, the square-edged squeegee transferred a complete, uniform layer of ink to the substrate and the printed features were well-defined. This is considered an acceptable result and an example of what was sought after in this investigation. The print on the left, produced by the round-edge squeegee, was not a complete uniform layer and the right-hand side features were not well defined. The difference in the two prints was due to the contact shape of the squeegee and the screen. With a square-edged squeegee, the contact area had a defined edge which had a large amount of traction on the screen. This was not the case with the round-edged squeegee as it had a curved contact shape which meant it was more likely to slide along the screen. This tendency to slide provided less control over the print and resulted in areas of ink not being pushed through to the substrate.

### **Pressure on the Squeegee**

When little pressure was applied to the squeegee, the vertical distance between the substrate and the screen was not overcome and so less ink reached the substrate. Increasing the pressure applied to the squeegee increased the amount of ink received by the substrate. However, large pressures could lead to slipping of the screen/substrate and less control over the print. This can be seen in Figure 4.10 where an applied mass of middling magnitude produced the more defined and uniform print. The mass was measured rather than the pressure as the contact area between the squeegee and the screen was difficult to measure as it deformed during printing and was not constant.



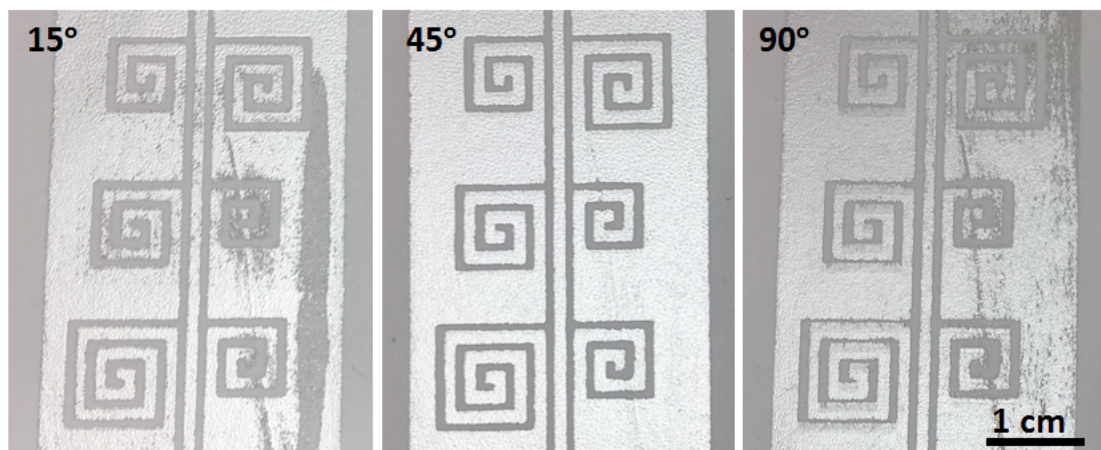
**Figure 4.10:** Comparison of printed features using different forces applied to the squeegee. Equivalent mass values are shown for each print.

To achieve these results, an existing setup was reconfigured to measure the equivalent mass acting on the squeegee. This setup was created to measure several changes in resistance at the same time. An analogue to digital converter with multiple inputs was used to measure the change in voltage of several Wheatstone bridge formations with one common reference. The voltages were read by an Arduino Mega and processed in Matlab. For this work, the Wheatstone bridge formations were each connected to a force sensitive circular sensor with 0.5” diameter.

The setup was calibrated using a balance. The sensors were each adhered to the balance and the voltage was recorded for several different applied masses. The sensors were then taped to the table under the substrate and the voltage values measured during printing allowed the equivalent mass to be determined.

### Squeegee Angle

The angle of the squeegee and the force applied to the squeegee are related. As the force was increased, the angle between the squeegee and the substrate decreased, however the angle could be independently investigated by keeping the force constant, equivalent to applying approximately 500 g. Similarly to the force, the optimum angle was somewhere between the extremes (0 and 90°) with resulting prints shown in Figure 4.11.

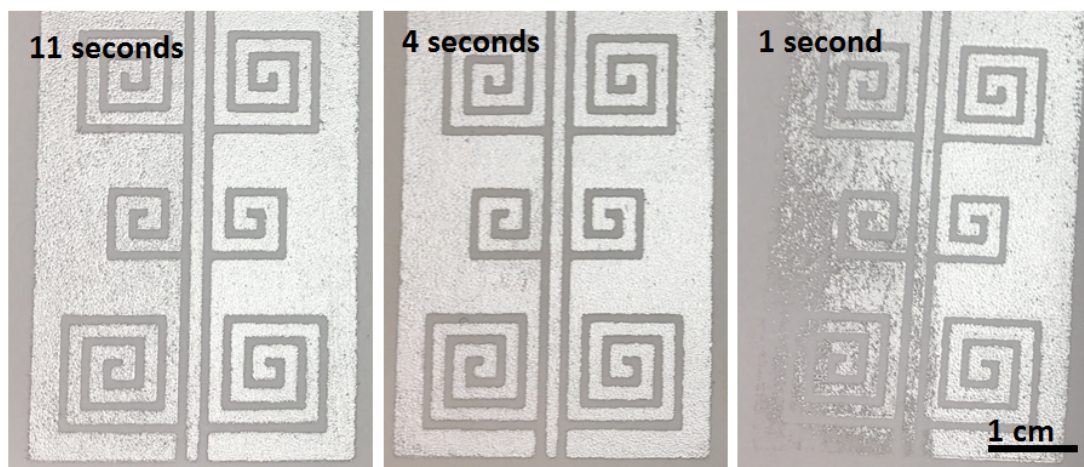


**Figure 4.11:** Comparison of printed features using different squeegee angles while printing.

When the angle was at the extremes, the user had little control over the print and so a non-uniform layer was produced. When printing with an angle of  $15^\circ$ , it was more difficult to apply the required force to the squeegee and it resulted in the majority of the force being applied to the centre and unbalanced pressure along the squeegee. The print produced with an angle of  $90^\circ$  showed slipping where the user had lost control and the screen had slipped along the substrate, decreasing the gaps between features.

### Speed of Printing

The faster the squeegee was pulled over the screen, the poorer the quality of the print, as shown in Figure 4.12. As with the other printing parameters, this was due to the control of the user. When printing very quickly, the user had less control and so the print was no longer uniform and features were lost due to non-uniform pressure along the squeegee. However, above four seconds for one print was determined to be redundant as a uniform layer with well defined features could be printed over four seconds; further time decreases efficiency with no added benefits.



**Figure 4.12:** Comparison of printed features when printing took place over different speeds.

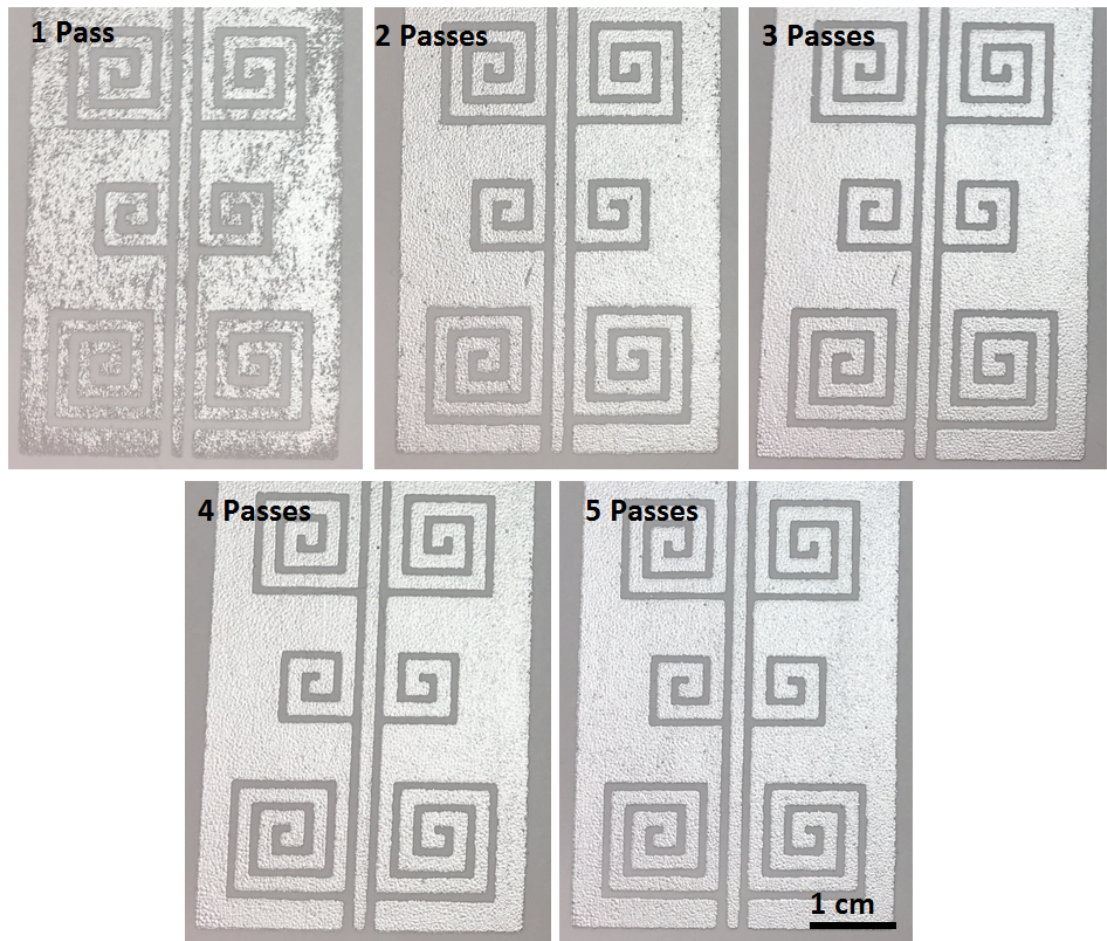
The length of the print was 25 cm and so speeds of 2.3 cm/s, 6.3 cm/s and 1 cm/s were achieved.

### Number of Passes with the Squeegee

More than one pass during printing was required to produce an optimal print; above this, results are acceptable as shown in Figure 4.13. The number of passes quantified how many times the squeegee was pulled over the screen to produce a print. With the first print, although the screen was always flooded, the ink could adhere to the screen itself and so not all of the ink was transferred to the substrate. For multiple passes, there was already a layer of ink which had adhered to the screen and



so a larger percentage of the ink deposited on the screen was transferred to the paper and a thicker, more uniform layer was produced. Similarly to the speed of printing, the optimum number of prints was minimised to improve efficiency.



**Figure 4.13:** Comparison of printed features when different number of passes with the squeegee has taken place.

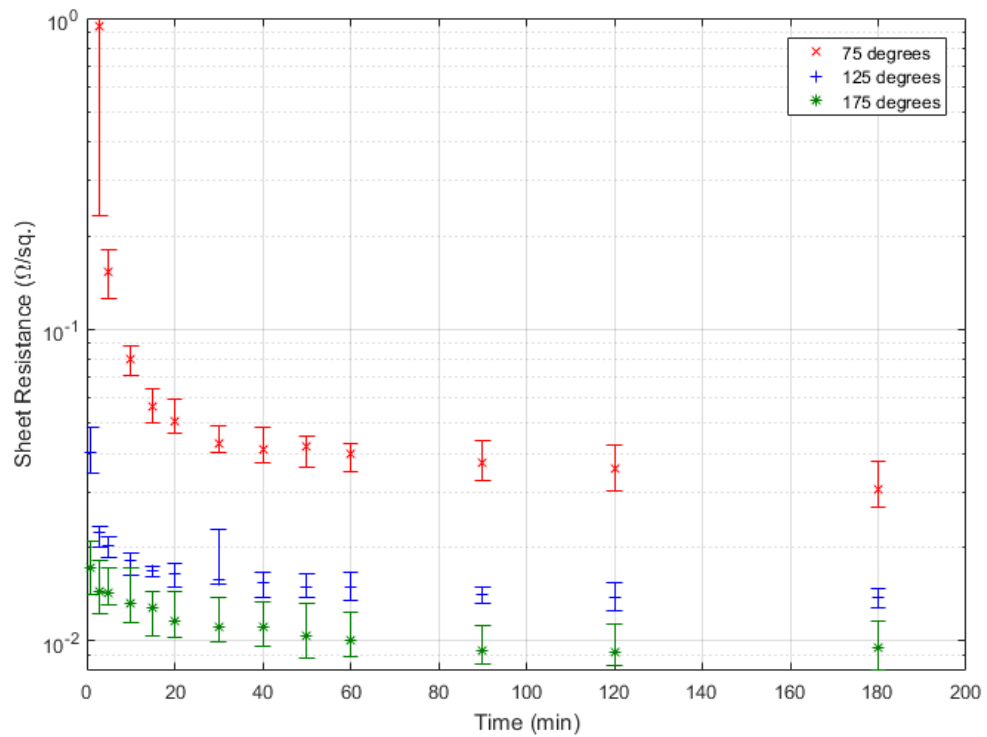
Many of the factors considered for the printing process were user controlled and so it is important that users follow the prescribed, well-defined process detailed in this work. This process can then be used to scale up screen printing for an automated system.

#### 4.4 Curing of the Ink

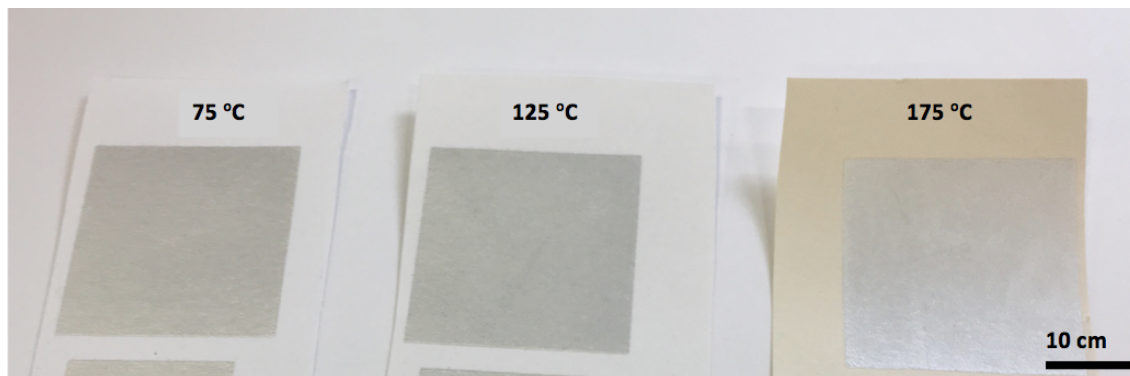
There are three types of silver ink commonly used for printed electronics: silver nanoparticle, silver nanowire and silver flake. Silver nanoparticles are between 1 - 100 nm in size for all dimensions, silver nanowires are around 10 nm in width and 10  $\mu\text{m}$  in length and silver flakes are single micrometers in size. Silver nanoparticle inks produce thinner layers via processes like inkjet printing which can often be more desirable and is not achievable with flake inks. Silver nanowire inks can be made to be transparent and can also be desirable for some applications [1]. However, in this work, the thickness

and transparency of the ink is not important for the application. In addition to this, silver flake ink has higher conductivity and lower cost, which is advantageous for the components in this work, with a view to them being low cost, disposable, with a high performance.

To increase the conductivity of the ink, prints must be cured. For this work, prints were cured in a Medline OV-11 oven at 75, 125 and 175 °C with sheet resistance measurements taken periodically as shown in Figure 4.14. It was found that samples cured at higher temperatures resulted in lower sheet resistance and the sheet resistance decreased with time before stabilising after 30 minutes. However, the difference in sheet resistance for samples cured at 125 °C and at 175 °C was not great enough to outweigh the physical change in samples shown in Figure 4.15. At higher temperatures, the paper curled and yellowed but this effect was minimal/acceptable for samples cured at 125 °C but was too extreme at 175 °C.

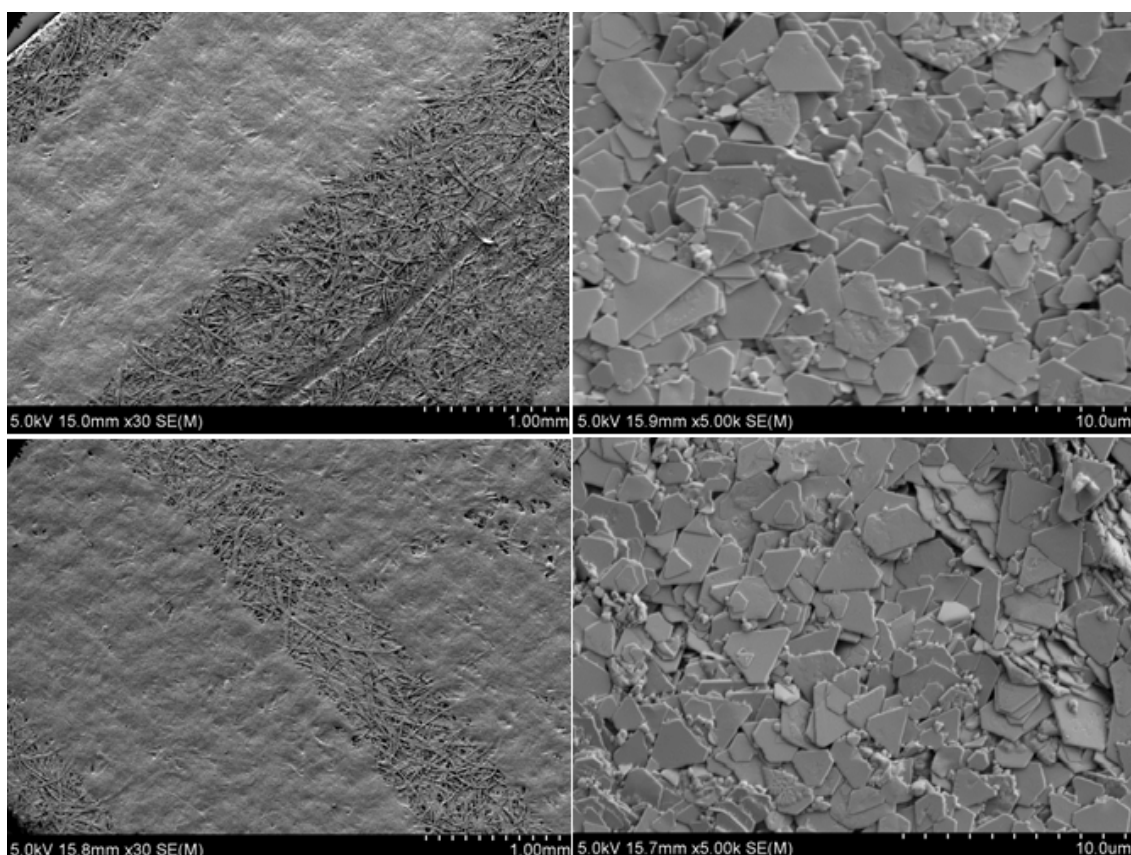


**Figure 4.14:** Sheet resistance values of printed squares over time with different curing temperatures.



**Figure 4.15:** Image of samples after being cured at 75, 125 and 175 °C for 30 minutes.

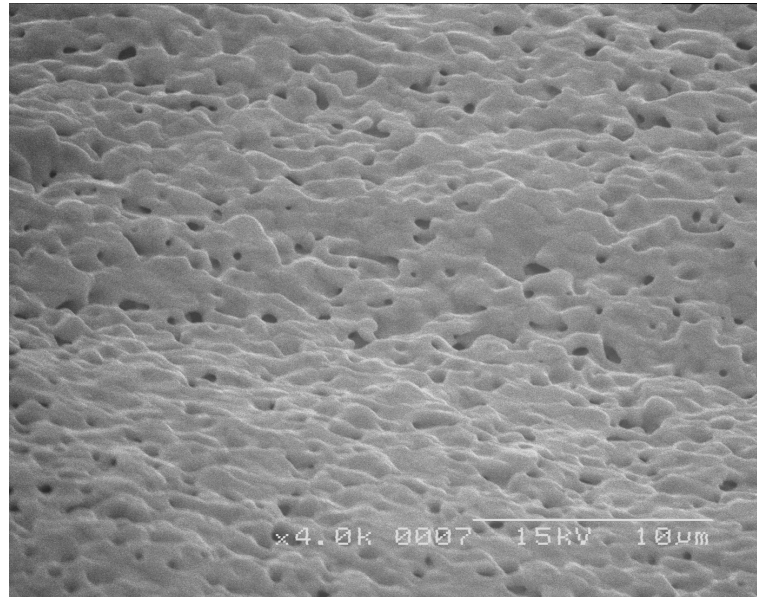
No physical changes were seen within the ink after curing. Scattering electron microscopy images of the ink structure before curing and after three hours of curing at 120 °C are shown in Figure 4.16 and it can be seen that there was no change in the structure of the silver flakes. At temperatures below 250 °C, the silver particles within inks are not able to melt however more binder within the ink is removed with increasing temperature [2]. Although this is not visible on the SEM images, the decrease in sheet resistance can be seen in Figure 4.14.



**Figure 4.16:** SEM images of screen-printed samples prior to curing (top) and samples which have been cured for three hours at 125 °C (bottom).

Increasing the curing temperature to above 250 °C caused the flakes to coalesce and the resistivity to be reduced even further. Even though this is much lower than the melting temperature of bulk silver, this is possible due to the high surface area to volume ratio of the silver flakes. The silver atoms

on the surface of the flakes have fewer interatomic bonds and so much less energy is required to break these bonds than those of a silver atom in the centre of the flake which has many more bonds. Due to the high temperatures required for the flakes to coalesce, this was not possible when using paper substrates, however a sample was printed on glass and cured at 500 °C for 30 minutes. The resulting structure of the ink is shown in Figure 4.17.

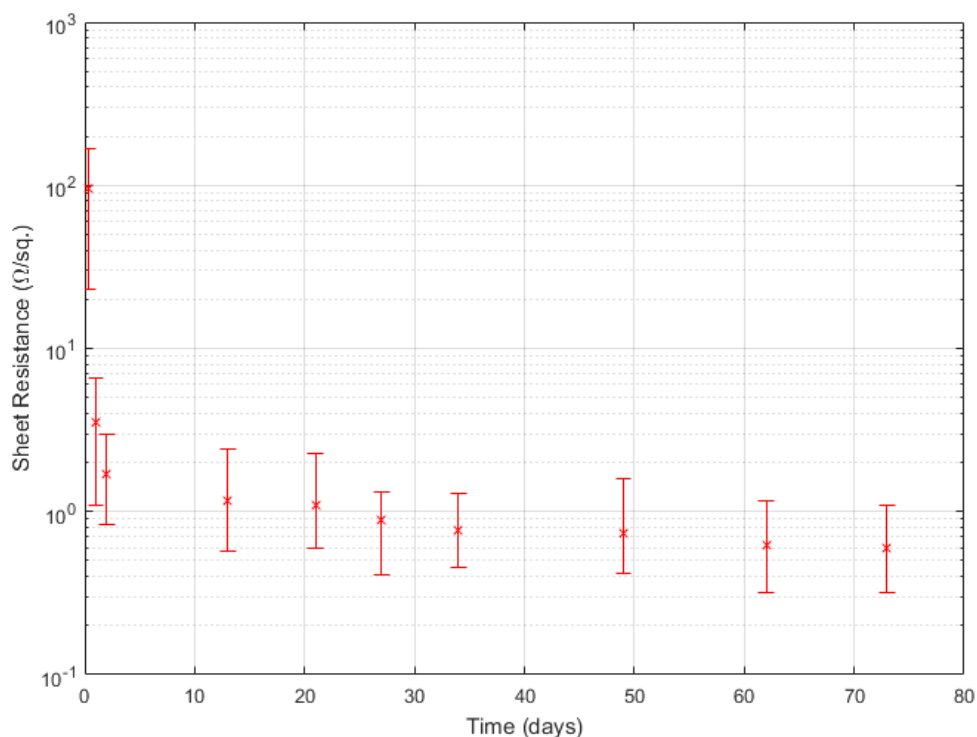


**Figure 4.17:** Curing of screen-printed silver ink on glass, cured at 500 °C for 30 minutes.

Following this investigation, it was decided that curing samples for 30 minutes at 125 °C would be optimal to avoid any changes within the substrate, while simultaneously providing high reductions in sheet resistance. All screen-printed samples and devices throughout this work have therefore been cured in this way. The sheet resistance obtained for this curing was less than 15 m $\Omega$ /□ for 80% of samples and under 20 m $\Omega$ /□ for 100% of samples.

Samples left at room temperature to dry for 70 days achieved a minimum sheet resistance of 0.3  $\Omega$ /□ as shown in Figure 4.18. These samples were found to be mostly insulating until at least eight hours after being printed. This confirmed the need for curing of the samples to ensure acceptable values of sheet resistance and fast production of working devices.

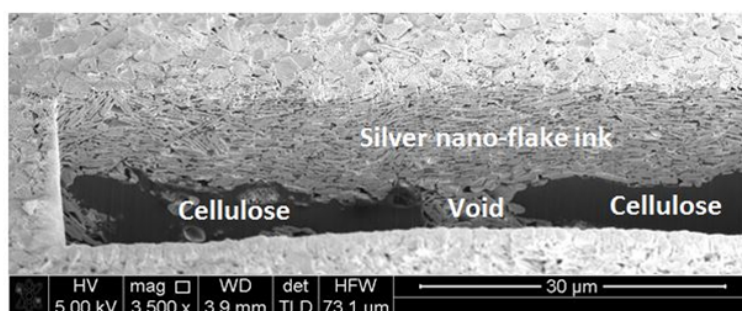




**Figure 4.18:** Sheet resistance values of screen-printed samples which have been air dried for over 70 days at room temperature.

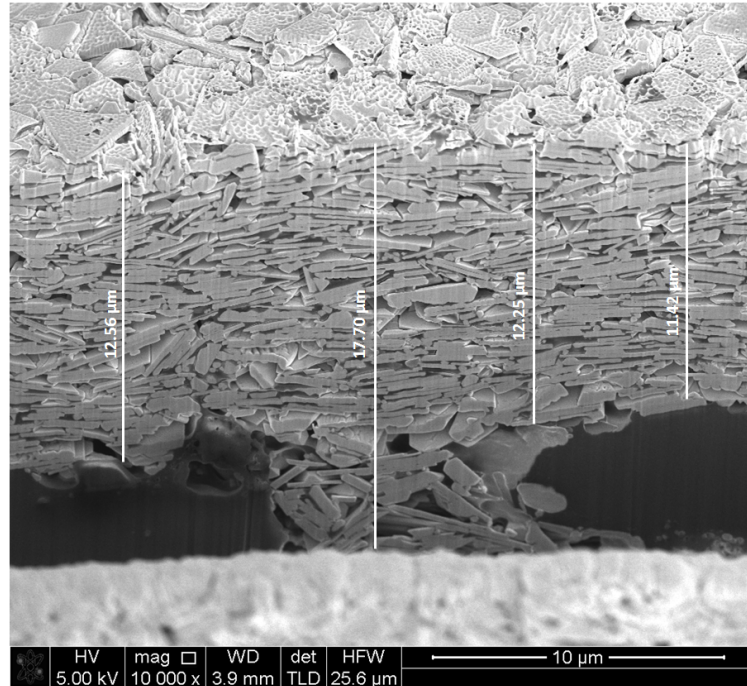
## 4.5 Ink/Paper Interface

To investigate the interface of the ink and paper, focused ion beam milling was used to mill a trough in samples, and images were taken of the cross-section. An example of these images is shown in Figure 4.19. The paper substrate consisted of cellulose fibres, starches and calcium carbonate, whereas the ink was made up of silver flakes. Although the fibres in the paper were several mm long and approximately 200  $\mu\text{m}$  wide, and the silver flakes were less than 5  $\mu\text{m}$  in lateral size, it was found that the ink flakes formed a layer on top of the surface of the cellulose fibre matrix and did not penetrate into deeper layers, giving rise to a well-defined interface, except for voids larger than 10  $\mu\text{m}$  in the cellulose fibre matrix, which were filled with the flakes. This was likely due to the high viscosity of the ink and resulting surface tension not allowing the flakes to penetrate deeper into the cellulose matrix.

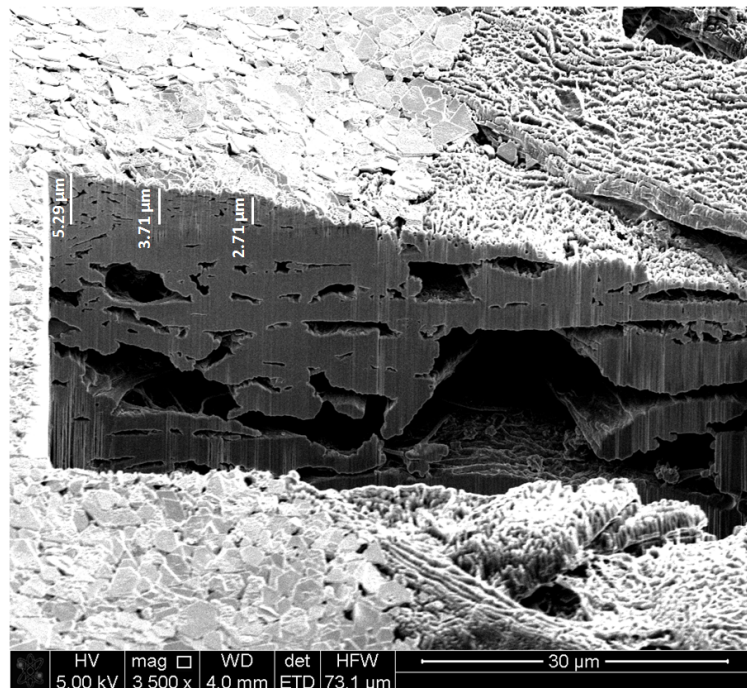


**Figure 4.19:** SEM image of a focused ion-beam milled section of screen-printed silver ink on paper.

These voids led to a variation in ink thickness across the print, as shown in Figure 4.20; in this small section the ink thickness varied from 11  $\mu\text{m}$  to over 17  $\mu\text{m}$  in the void. This reinforced the theory that rougher papers have thicker layers of ink in some areas, which leads to higher conductivity as detailed in Chapter 3. There was a clear incline at the edges of the printed track as shown in Figure 4.21, where the thickness of the ink decreased from 5.5  $\mu\text{m}$  to 0. This was due to the spreading of the ink as the screen was removed while printing.



**Figure 4.20:** SEM image of a focused ion-beam milled section of screen-printed silver ink on paper with thickness values added.



**Figure 4.21:** SEM image of a focused ion-beam milled section of the edge of screen-printed silver ink on paper with thickness values added.

## 4.6 Screen-printed Passive Components

To demonstrate the quality of the screen-printing method that has been optimised here, passive components were fabricated and compared to state-of-the-art passive components screen printed by other groups. Measurements of capacitance and inductance were taken using a HP 4192A low frequency impedance analyser between 100 Hz and 10 MHz. All components here were screen printed using Metalon HPS-021LV silver nano-flake ink on 199 gsm Neenah paper.

### 4.6.1 Resistors

Due to the high conductivity of the silver nano-flake ink it would not be suitable for producing resistors, however rectangles were printed and treated as proof-of-concept resistors. Rectangles of varying length were printed to compare measured resistance to calculations using  $R = \rho_s L/W$  where  $L$  is the length of the resistor,  $W$  is the width and  $\rho_s$  is the sheet resistance, taken to be  $20 \text{ m}\Omega/\square$ . For rectangles  $1 \text{ mm} \times 20 \text{ mm}$ , the resistance was measured to be  $0.5 \Omega$  (expected to be  $0.4 \Omega$  from calculations). All of the samples were found to be within 30% of the calculated value of resistance and any discrepancies could be explained by the differences in actual dimensions printed and variations in thickness, changing the sheet resistance.

Other inks are available which have lower conductivities and would be more suited to produce resistors. Table 4.2 shows required dimensions for example silver, nickel and carbon resistors assuming a thickness of  $15 \mu\text{m}$ . This table highlights the need for materials with lower conductivity to produce resistors.

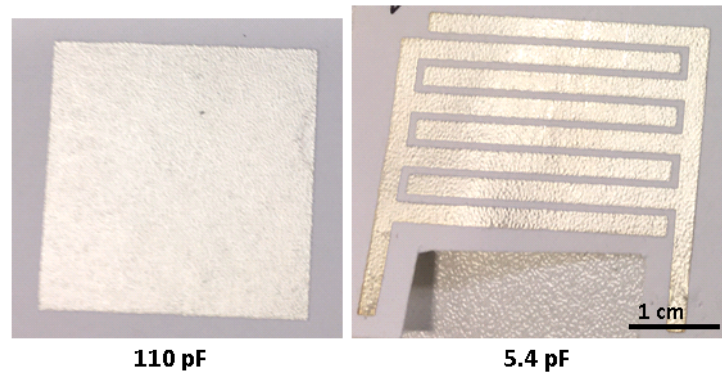
**Table 4.2:** Example dimensions for screen-printed resistors using differing metal inks.

Resistor Dimensions	Silver Ink	Nickel Ink	Carbon Ink
	Resistance (Ohms)	Resistance (Ohms)	Resistance (Ohms)
$5 \mu\text{m} \times 100 \mu\text{m}$	0.4	200	20k
$5 \mu\text{m} \times 1 \text{ mm}$	4	2k	200k
$5 \mu\text{m} \times 10 \text{ mm}$	40	20k	2M
$5 \mu\text{m} \times 1 \text{ m}$	4k	2M	200M

### 4.6.2 Capacitors

Parallel plate and interdigitated capacitors have been considered in this work and examples are shown in Figure 4.22. The values shown are the measured capacitance for geometries covering a similar area. The work here concentrated on parallel plate capacitors, as interdigitated structures were

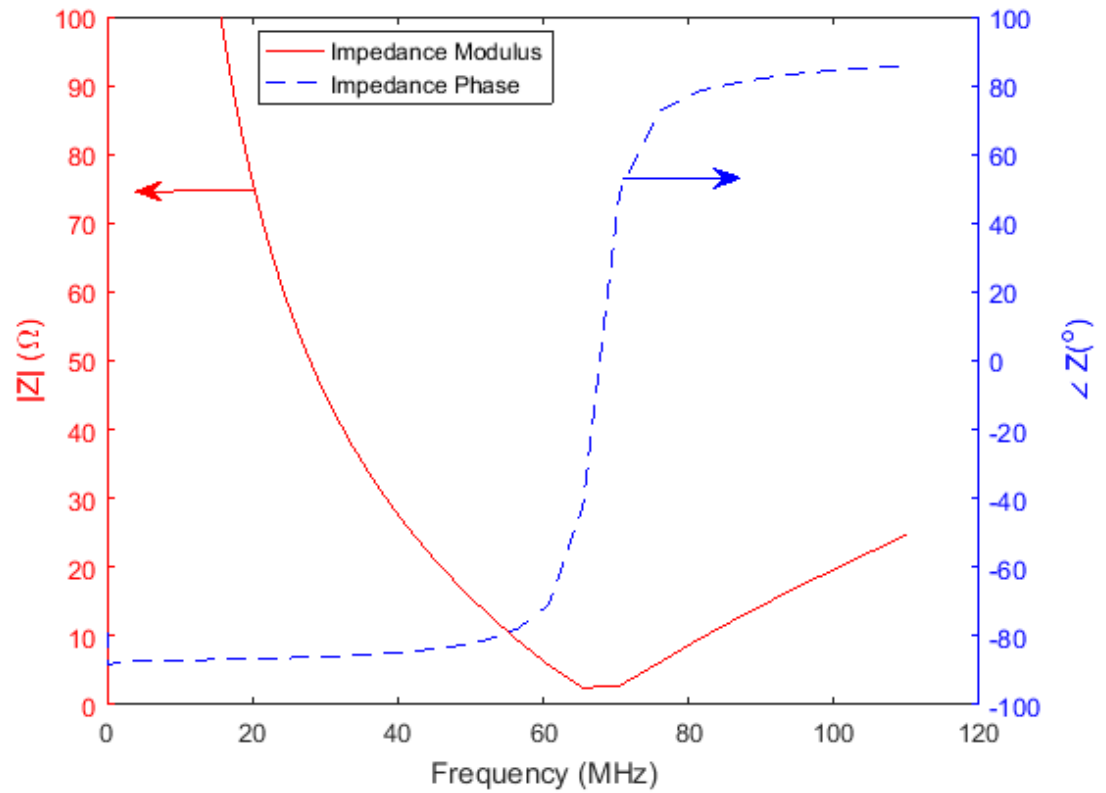
considered later for their use as touch pads (Chapter 5). Although interdigitated structures have a lower capacitance, they were found to be more touch sensitive.



**Figure 4.22:** Examples of screen-printed parallel plate (left) and interdigitated capacitors (right) with their respective capacitance values.

To produce parallel plate capacitors, squares of 20, 30 and 40 mm were printed on both sides of a selection of papers. The capacitance of these components was measured and compared to the equation  $C = \epsilon_o \epsilon_r A/d$ , where  $A$  is the area of the printed squares,  $d$  is the thickness of the paper,  $\epsilon_o$  is the relative permittivity of free space and  $\epsilon_r$  is the permittivity of the paper. As the capacitance is measured here and the thickness of the paper was previously measured to be  $235 \pm 8 \mu\text{m}$  by a micrometer, the permittivity of the paper can be calculated. Capacitance values in the pF range have been achieved. For a  $30 \times 30$  mm square, the measured capacitance was  $110 \text{ pF} \pm 10 \text{ pF}$  from 400 Hz to 20 MHz, above which the inductive nature of the device dominated, shown in Figure 4.23. Several repeats of the different sizes were printed and found to have very good repeatability; 100% of samples resulted in a value for  $\epsilon_r$  within 5% of 3.25. This is a realistic value for paper, which is often found to have a permittivity of between 2 and 6 [3–5]. The permittivity of the paper was a key factor in later work presented in Chapter 6.

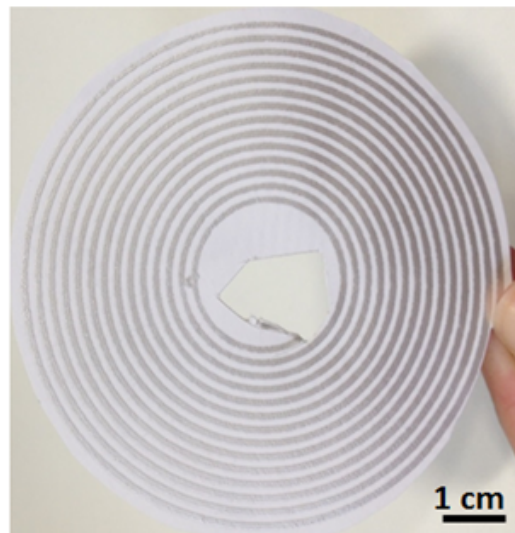
The impedance of the capacitors was measured using the impedance analyser with typical results shown in Figure 4.23. It can be seen that there is a resonating structure; below 66 MHz, the device behaves like a capacitor and, above 71 MHz, the device behaves like an inductor. This is explained by the fact that this structure is not purely capacitive, the parallel plates are capacitive but the leads are inductive, creating a series LC (inductor capacitor) circuit.



**Figure 4.23:** Capacitance and phase against frequency for the parallel plate capacitor shown in Figure 4.22.

### 4.6.3 Inductors

Circular spiral inductors were printed on paper to maximise the inductance and minimise the resistance, and an example is shown in Figure 4.24. Track spacing was set at 1 mm, track widths of 1 mm and 2 mm were considered and the inner diameter of the spirals was 20 mm. The maximum number of turns was 15 and, due to the nature of paper, coils could be cut easily to reduce the number of turns.



**Figure 4.24:** Example of a screen-printed inductor with 1 mm track width and spacing, an outer diameter of 76 mm and 14 turns.

The inductance of the spirals was calculated using Equation (4.1), taken from [6], where  $n$  is the number of turns,  $c_{1-4}$  are pre-determined coefficients 1, 2.46, 0 and 0.2 respectively,  $d_{avg}$  is the average of the inner and outer diameters of the spiral and  $\rho$  is the fill factor, calculated by  $\rho = (d_{out} - d_{in}) / (d_{out} + d_{in})$ .

$$L = \frac{\mu_0 n^2 d_{avg} c_1}{2} \left[ \ln \left( \frac{c_2}{\rho} \right) + c_3 \rho + c_4 \rho^2 \right] \quad (4.1)$$

In order to maximise inductance, the number of turns and the outer diameter of the spirals should be maximised. The resistance should be minimised by maximising the track width and keeping dimensions within the constraints of the application. Results from some of the trialled geometries are shown in Table 4.3, comparing theoretical calculations to measured values. It can be seen that although the measured resistance values are higher than those calculated, the inductance is comparable.

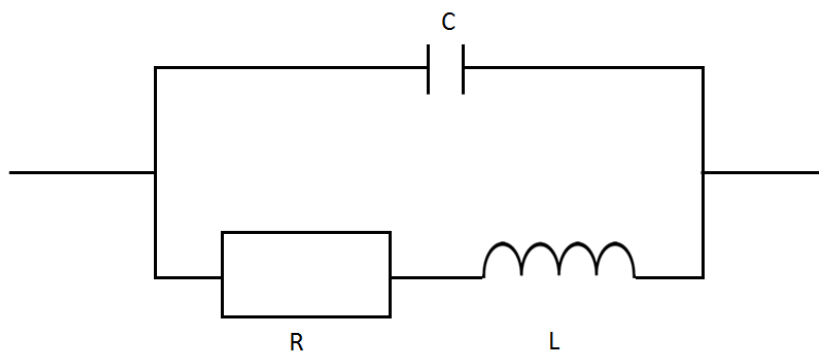
**Table 4.3:** Screen-printed inductors, comparing measured values of inductance and resistance with theoretical calculations.

Number of turns	Track width (mm)	Track spacing (mm)	Outer Diameter (mm)	Calculated Inductance ( $\mu\text{H}$ )	Measured Inductance ( $\mu\text{H}$ )	Calculated Resistance ( $\Omega$ )	Measured Resistance ( $\Omega$ )
14	1	1	76	8.91	8.37	40.46	54.0
11	2	1	98	5.85	5.90	17.28	28.6
9	2	1	74	3.64	3.50	12.44	34.3

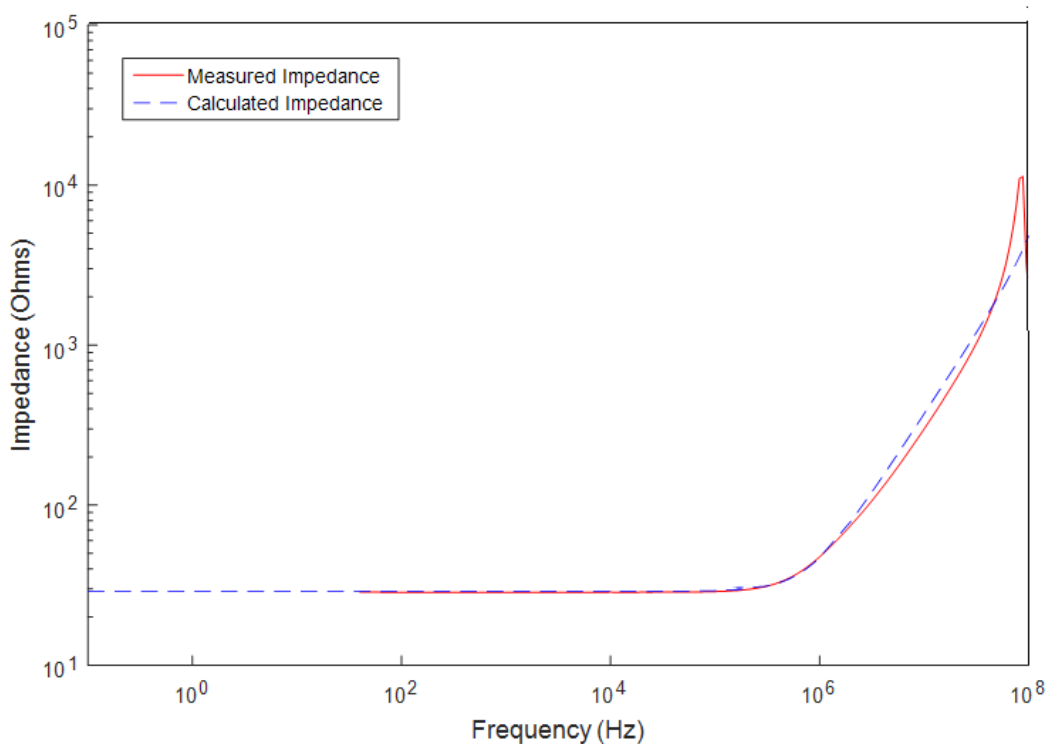
These devices are comparable to work by Ostfeld et al who have produced screen-printed passive components on polyethylene terephthalate (PET) for flexible power electronics [7]. Their findings are for spirals with a similar number of turns but with a line width and spacing of 500  $\mu\text{m}$ , resulting in a smaller outer diameter. Inductances of approximately 5  $\mu\text{H}$  were achieved, which are comparable with the results in this work, presented in Table 4.3. Ostfeld et al have achieved a sheet resistance of 4  $\text{m}\Omega/\square$ . However, this required six coats of ink, leading to a slower process and issues with alignment.

The a.c. characteristics of the inductors should be considered to determine operating frequency of the devices. An example spiral with 2 mm track width, 1 mm spacing and 11 turns was considered here. The inductance was stable at a value of  $5 \pm 1 \mu\text{H}$  between 10 kHz and 50 MHz and so could be used for such MHz devices as those by Ostfeld et al.citeOstfeld2015. The inductor could be approximated using the simple model in Figure 4.25 where the resistance represents the series resistance of the tracks and the capacitance represents the capacitance between the tracks. The impedance and phase could be calculated from combining the impedances of the resistance  $R$ , the capacitance  $(-1/i\omega C)$  and the inductance  $(i\omega L)$ . The values for resistance and inductance were measured and calculated and are

listed in Table 4.3 and the value of capacitance could then be chosen to minimise the error between the theoretical and measured data. Other models and various values for R, L and C were trialled however this method produced the best fit for the measured data. The values  $28.6\ \Omega$  and  $5.9\ \mu\text{H}$  for the resistance and inductance were taken from the middle row of Table 4.3. The value of  $0.1\ \text{nF}$  for the capacitance was chosen as it provided the best fit with the data, as shown in Figure 4.26.



**Figure 4.25:** Model of paper-based spiral inductors for a.c. analysis.



**Figure 4.26:** Typical plot of impedance with frequency for inductors on paper, comparing theory with measurements.

## 4.7 Conclusion

This chapter has presented work on the optimisation of the in-house screen printing process. This has included investigating the properties of the screen itself, the printing procedure and the curing temperature and time. To illustrate the capabilities of the improved printing process, passive



components were then screen printed onto Neenah paper.

From the optimisation process, it was determined that the screen must be manufactured to have uniform tension and so screens were created at a local photo-framing company. There is a trade off, when choosing the screen mesh, between ink thickness (and resulting conductivity) and the feature size which can be obtained, in this work a 90T mesh has been used. When printed, the feature size is approximately 0.1 mm larger than the designed value but a minimum feature size of 500  $\mu\text{m}$  was still repeatedly achievable.

Through the optimisation of the ink curing, it was found that the optimum temperature was 125 °C. Above this, the paper yellowed and curled and, below this, suboptimal sheet resistance values were achieved. Coalescing of the ink does not occur on paper as temperatures over 250 °C are required.

Passive components were printed using the optimised process and it was determined that the silver ink is not suitable to create resistors but carbon and nickel inks are more suited. Both parallel plate capacitors and interdigitated capacitors were produced and the use of these as touch pads is investigated in the next chapter. Spiral inductors were produced which are comparable with state-of-the-art work by other groups who have screen printed spiral inductors on plastic.

## References

- [1] S. Nanowire, L. Hu, H. S. Kim, J.-y. Lee, P. Peumans, and Y. Cui, "Scalable Coating and Properties of transparent Ag nanowire," *ACS nano*, vol. 4, no. 5, pp. 2955–2963, 2010.
- [2] D. A. Roberson, R. B. Wicker, L. E. Murr, K. Church, and E. MacDonald, "Microstructural and process characterization of conductive traces printed from Ag particulate inks," *Materials*, vol. 4, no. 6, pp. 963–979, 2011.
- [3] C. Beisteiner and B. G. Zagar, "Dielectric permittivity measurement of paper substrates using commercial inkjet printers," *30th Euroensors Conference*, 2016.
- [4] L. Yang, A. Rida, R. Vyas, and M. M. Tentzeris, "RFID tag and RF structures on a paper substrate using inkjet-printing technology," *IEEE Transactions on Microwave Theory and Techniques*, vol. 55, no. 12, p. 2894, 2007.
- [5] G. Shaker, S. Safavi-Naeini, N. Sangary, and M. M. Tentzeris, "Inkjet printing of ultrawideband (UWB) antennas on paper-based substrates," *IEEE Antennas and Wireless Propagation Letters*, vol. 10, p. 111, 2011.
- [6] S. S. Mohan, M. D. M. Hershenson, S. P. Boyd, and T. H. Lee, "Simple accurate expressions for planar spiral inductances," *IEEE Journal of Solid-State Circuits*, vol. 34, no. 10, p. 1419, 1999.
- [7] A. E. Ostfeld, I. Deckman, A. M. Gaikwad, C. M. Lochner, and A. C. Arias, "Screen printed passive components for flexible power electronics," *Scientific Reports*, vol. 5, p. 15959, 2015.



## Chapter 5

# Fabrication and Characterisation of Interdigitated Touch Sensors

### 5.1 Introduction

Electronic systems often include sensors or devices with a number of inputs and outputs. A common example is the touch pad. Touch sensors on paper could potentially be integrated with disposable sensors to create completely disposable devices. These offer the promise of a low-cost, recyclable or disposable solution for everyday applications. It is possible that such applications could include simple fast-food menus, accessible packaging, interactive posters, and medical devices. Such devices have the potential to revolutionise cost-effective interactive packaged items as well as helping to meet carbon footprint requirements for waste.

This chapter presents work on screen-printed interdigitated capacitance devices and their use as touch sensors. A proof-of-concept touch detector based on paper sensors and an embedded system (an Arduino microcontroller) is presented. Numerical simulations (using COMSOL) were carried out to support the experimental results.

Changes in the device geometry are correlated to changes in the device operation and performance. Work was undertaken to study how different users may interact with the touch pads, and how this has an effect on the overall operation of the device. Finally the environmental effects, such as humidity, on the touch pad performance were considered.

Various examples of paper-based and flexible electronic devices were detailed in Chapter 1. Many of these device applications require a user interface. Therefore, a large amount of research is ongoing

into various touch pads on flexible substrates for integration into flexible and disposable sensors. Current, commercial touch screens, for example those on smart phones, can be a complex structure of several layers of different materials, which can be expensive and require a complex fabrication process, and therefore flexible touch pads on cheaper substrates are desirable. An example of work where touch pads have been developed as part of a system has been presented by Kanaparthi et al. who produced touch, temperature, pH and humidity sensors on paper [1]. In addition to being flexible and foldable, touch sensors on paper are also cuttable, meaning that a variety of designs can be achieved with multiple touch points and a central control node [2].

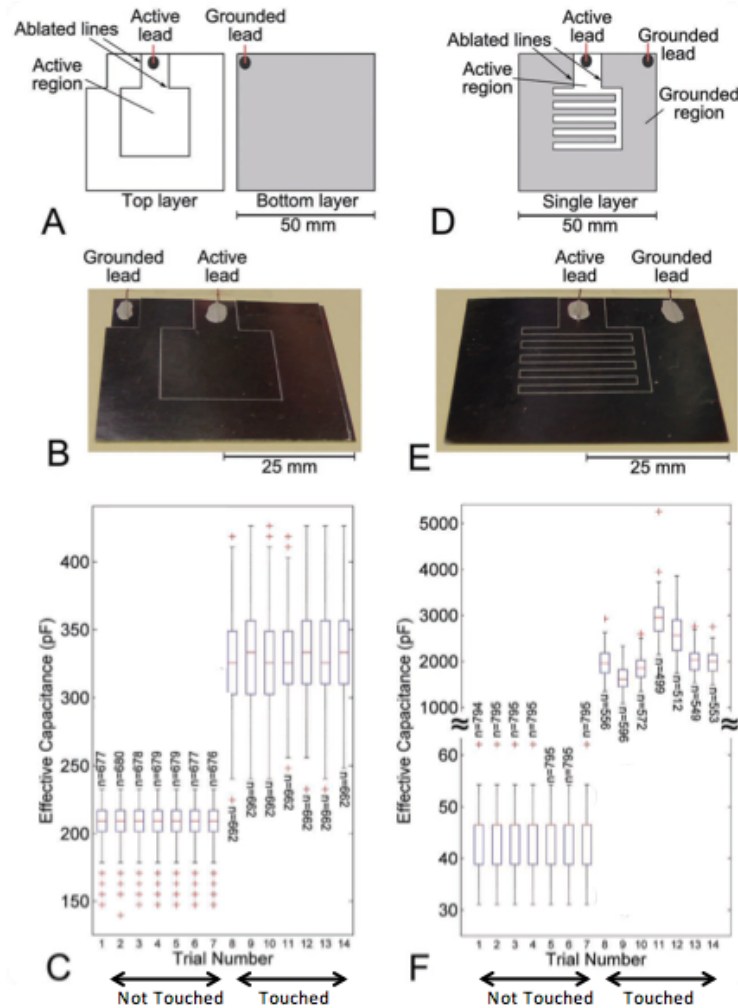
Flexible touch pads can be used for anti-tamper devices on packages [3, 4], keyboards [5–7] and interactive pop-up books for children [8, 9]. Gestural input surfaces have been designed which can be mounted on the fingertip or nail and use capacitive sensing to act as touch pads [10, 11]. Table-top games can be improved with capacitive coupling between the user’s chair and their touch, the location of the touch of each use can be determined by location-dependent electric fields [12]. Savage et al. have created prototypes of interactive objects, one of which is a ‘papercraft pinball machine’ which highlights the foldability of paper and integration of touch pads to a larger system [13].

As flexible touch pads are a high area of interest, a large amount of research is ongoing into the theory and operation of touch sensors. Holz et al. look at the theory behind capacitive touch screens and how the user acquires their target and the errors this leads to [14]. Several groups have used computer modelling to determine the effect of the device with touch. However, the finger is often modelled as a single material [15–17].

Resistive [18], inductive [19], pressure sensitive [6, 20, 21], piezoelectric [22–26], piezoelectret [27, 28] and pyroelectric [29] touch sensors have all been investigated and groups have also produced devices which can be used on a person; for example, nail or finger pads which can be mounted on parts of the hand and react to gestures [10, 11]. For the majority of these designs, paper or plastic is the chosen substrate for the device to provide flexibility and is not the active component within the device. For the piezoelectric touch sensors, materials such as zinc oxide nanowires are used [22]. Silver nanowires are often used for their flexibility and compatibility with printing methods to create touch pads on flexible substrates [24, 30].

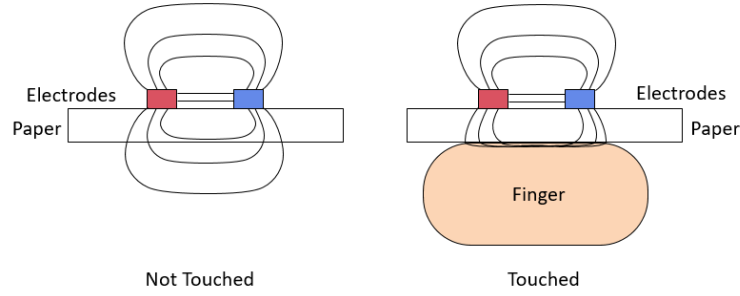
More commonly, capacitive designs are used as touch pads with parallel plate or interdigitated structures. Parallel plate structures can use paper as the dielectric, or some other material such as graphene oxide [31]. Manabe et al. used several capacitive sensors in series which require only two contact points with the measurement system [32]. Mazzeo et al. [4] have produced paper-based

capacitive touch pads from metallised paper and determined that an interdigitated structure produces a larger change in capacitance than a parallel plate structure of a similar size. The two structures are shown in Figure 5.1 along with the values of capacitance for both the structures when they are touched and not touched.



**Figure 5.1:** Capacitance buttons fabricated on metallised paper, highlighting the greater increase in capacitance when using an interdigitated structure. Adapted from [4].

Both structures are produced by laser ablation of the metallised paper. The parallel plate design (Figure 5.1 A - C) uses two sheets of the metallised paper and so has two planes, the interdigitated design (Figure 5.1 D - F) is only in one plane and has two sets of electrodes which are separated by laser ablated lines. The parallel plate design is governed by the equation  $C = \epsilon_o \epsilon_r A/d$  and so the change in capacitance with touch is due to the change in  $d$ , the thickness of the paper dielectric which is minimal. The interdigitated structure is dominated by the electric field as shown in Figure 5.2.



**Figure 5.2:** The electric field patterns for both the un-touched and touched states of the interdigitated touch pad design.

It should be noted that this figure is not to scale and the thickness of the electrodes is less than one tenth of the thickness of the paper. This means that the horizontal component of the electric field between the electrodes is insignificant in comparison to the three dimensional electric field within the paper and the air. When the sensor is touched, the electric field will be constrained within the finger rather than the paper due to its significantly higher permittivity (approximately 550 compared to 3). As the parallel component of the electric field ( $E$ ) and the normal component of the electric displacement ( $D$ ) are conserved at the boundary between the finger and the paper and  $D = \epsilon_0 \epsilon_r E$ , the field will be very close to the surface of the finger and not easily visible within the finger. This change in gradient at the boundary has been reduced in Figure 5.2 for illustrative purposes however in the later simulations, the field cannot be seen within the finger on this scale as it is very close to the surface of the finger. This results in a large change in capacitance (at least an order of magnitude) which is larger than that of the parallel plate design. For this reason, the majority of flexible touch pads have an interdigitated electrode structure [1, 24, 33–38].

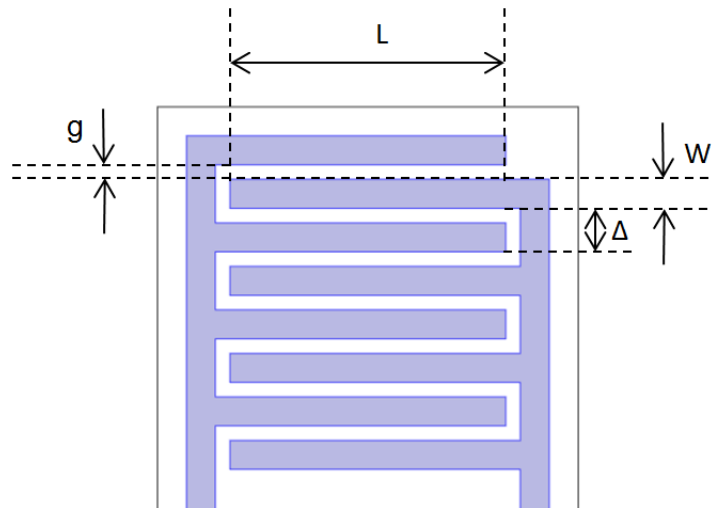
Li et al. fabricated interdigitated capacitive touch pads by direct write of silver ink through a syringe pump [24]. The electrode finger width and the gap between electrode fingers were 0.5 mm and the electrode finger length was varied between 4 and 16 mm. Devices with 2 - 10 electrode fingers were considered. The resulting capacitance of the device varied between 1 and 5 pF when untouched and between 5 and 35 pF when touched. The rise time of the devices was measured and converted to a capacitance value using an Arduino. Four touch pads were connected to LEDs as proof of concept and the bending radius altered with no change in response.

Kanaparthi et al. fabricated touch pads by direct write of 5B pencils on filter paper [38]. The electrode finger width and the gap between electrodes was 0.6 mm and the finger length was varied between 5 and 15 mm. Devices with 4 - 20 electrode fingers were considered. The resulting capacitance of the device varied between 1 and 3.5 pF when untouched and between 5 and 23 pF when touched. The devices were measured using the same technique as Li et al. with an Arduino.

Yun et al. fabricated touch pads using home inkjet printing onto photo paper [34]. The electrode finger width and the gap between electrodes were 1 mm and 0.5 mm respectively, and the finger length was varied between 5 and 15 mm. Devices with 12 electrode fingers were considered. The resulting capacitance of the device varied between 228 and 236 pF when untouched and between 340 and 564 pF when touched. The devices were measured using the same technique as Li et al. with an Arduino. The larger capacitance for the work by Yun et al. in comparison with others is caused by the use of a large ground plane rather than ground electrodes. This is the same design as used by Mazzeo et al. in [4] shown in Figure 5.1.

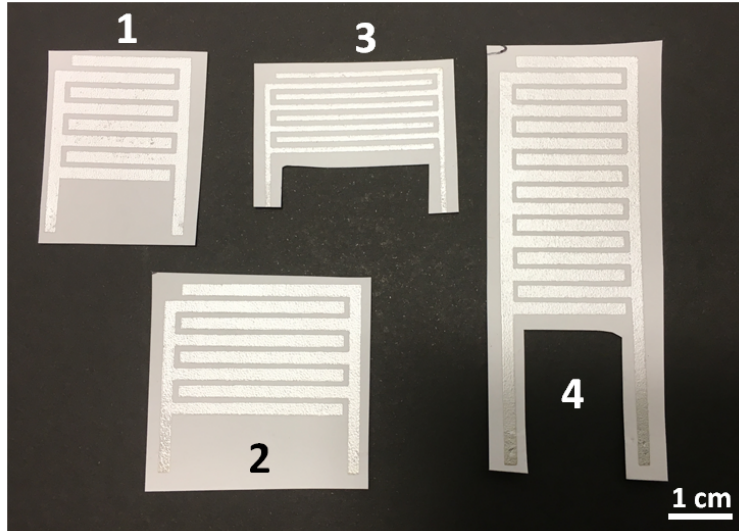
## 5.2 Interdigitated Capacitive Sensor Geometries

This work considered four different designs of interdigitated electrodes in order to look at the effect of changing different parameters on the capacitance of the sensor. An example interdigitated design is shown in Figure 5.3 which labels the electrode finger length,  $L$ , the electrode finger width,  $W$ , the gap between the electrode fingers,  $g$ , and the combination of the electrode finger width and the gap,  $\Delta$ .



**Figure 5.3:** Illustration of an interdigitated capacitive sensor with key dimensions added.

The four designs are shown in Figure 5.4 and details of their relative dimensions are listed in Table 5.1.



**Figure 5.4:** Four designs of interdigitated capacitive touch pads considered in this work.

**Table 5.1:** Dimensions of interdigitated touch sensor designs.

Sensor Design	Number of Fingers	Finger Width (W, mm)	Gap (g, mm)	Finger Length (L, mm)	Yield (%)
1	8	2	1	20	95
2	8	2	1	30	90
3	8	1	1	30	60
4	16	2	1	20	90

Design 2 looked at the effect of increasing the electrode finger length L, which would increase the capacitance of the device due to the higher surface area between the two sets of electrode fingers. Design 3 looked at the effect of increasing the electrode finger length but also decreasing the electrode finger width. When compared to Design 1, Design 3 should have had higher capacitance as the change in electrode finger length was much greater than the change in width. However, compared to Design 2, Design 3 should have had a lower capacitance as the electrode finger width was smaller, but the length was the same. Design 3 should also have a lower yield than the other designs due to the smaller feature sizes. Design 4 looked at the effect of increasing the number of electrode fingers in the device, which should have increased the capacitance compared to Design 1 and so should have had the largest capacitance of all the four designs.

In Chapter 4, the deviation in feature size of the screen-printing method was considered. The feature size and gap between features, when both designed to be 0.5 mm, were between 0.46 - 0.60 mm and 0.38 - 0.48 mm respectively. For this reason, the capacitive devices were designed so that the minimum feature size was 1 mm. For all designs, the gap between electrodes was designed to be 1 mm to achieve maximum capacitance but remain within the fabrication parameters.

Designs with features larger than those designed here would not be considered suitable as touch pads. Design 1 was considered the most suitable for use as a touch device based on its dimensions. This was approximately a square with 2 cm long sides and was the smallest of the touch devices designed. The size of an adult finger is not larger than this and so this design can maximise device density. For this reason, this device was used as the example data throughout this work. It is understood that using a higher quality fabrication method could result in features which could mean the same capacitance was achieved within a smaller area. However, this work showed a proof-of-concept which could then be improved using a higher quality process at a later stage.

## 5.3 Theoretical Analysis of the Interdigitated Sensors

### 5.3.1 Analytical Expression for the Sensor Capacitance

A simple analytical expression was used to determine the sensor capacitance prior to design and to ensure the values were in a measurable range. The change in capacitance between designs must also be measurable. Several equations have been proposed to determine the capacitance of interdigitated electrodes [24, 36, 38–41]. This work uses Equation (5.1), taken from [41], as this considers all dimensions which have been varied between the designs. The calculated values using Equation (5.1) for Designs 1, 2, 3 and 4 were 1.73, 2.74, 2.16 and 3.46 pF respectively. These calculated values of capacitance showed the same trend which was hypothesised above when considering the differences in parameters between the designs.

$$\frac{NC_1L}{2} \quad \text{where} \quad C_1 = 2(1 + \epsilon_r)(6.5s^2 + 1.08s + 2.37) \quad (5.1)$$

where  $C$  is the capacitance,  $\epsilon_r$  is the relative permittivity of the substrate,  $N$  is the number of electrode pairs,  $C_1$  is a variable used to simplify the calculation of  $C$ ,  $L$  is the length of the electrode fingers and  $s$  is the ratio  $W/\Delta$ .  $W$  is the electrode finger width and  $\Delta$  is equal to the electrode finger width and the gap between electrode fingers. All dimensions are labelled on Figure 5.3.

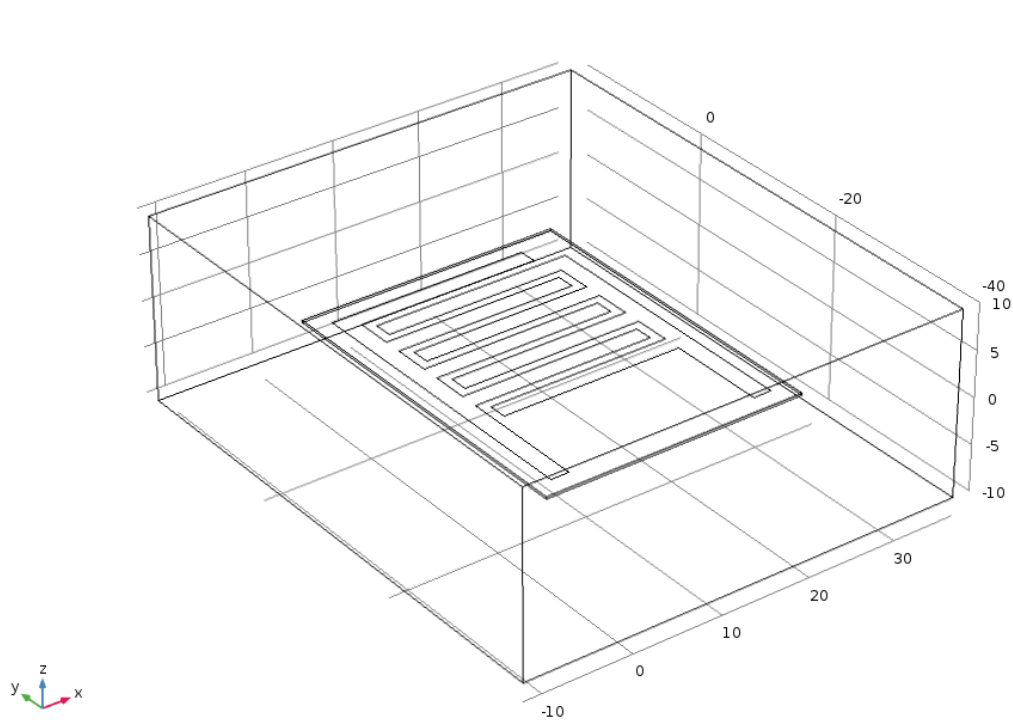
These values were all within the pF range and so are measurable using devices such as impedance analysers, vector network analysers and LCR meters. The change in capacitance between the designs was also greater than 0.4 pF for all and so, should also have been within a measurable range.

### 5.3.2 COMSOL Modelling of the Sensors

As Equation (5.1) only provides a single value for the capacitance of the sensors, COMSOL modelling was used to include the material properties of the sensor and determine more information about the sensor operation. Using COMSOL modelling, the electric field patterns of the sensor could be simulated. The addition of a human finger to the model was also possible with COMSOL and was able to provide a great deal of information about the sensor when used as a touch pad.

#### Modelling of the Sensor

An example of sensor design 1, modelled in COMSOL, is shown in Figure 5.5 and details of the parameters of the model are listed in Table 5.2. The paper thickness was measured using a micrometer and the electrode finger parameters were taken from Table 5.1. The metal properties were determined in Chapter 4 for the screen-printing method. The permittivity was taken to be 3.25 as calculated from measurements using parallel plate capacitors in Chapter 4.



**Figure 5.5:** Example of Design 1 touch sensor created in COMSOL. All units are in mm.

The paper was modelled as a block of size 29 x 38 x 0.235 mm, which covered the whole touch pad. An air block with dimensions 49 x 58 x 30 mm was used to simulate the touch pad being surrounded by air.

The values of capacitance for Designs 1, 2, 3, and 4 were determined to be 2.81, 4.00, 3.42 and 5.75 pF respectively using the COMSOL model. Design 4 had double the number of electrode fingers

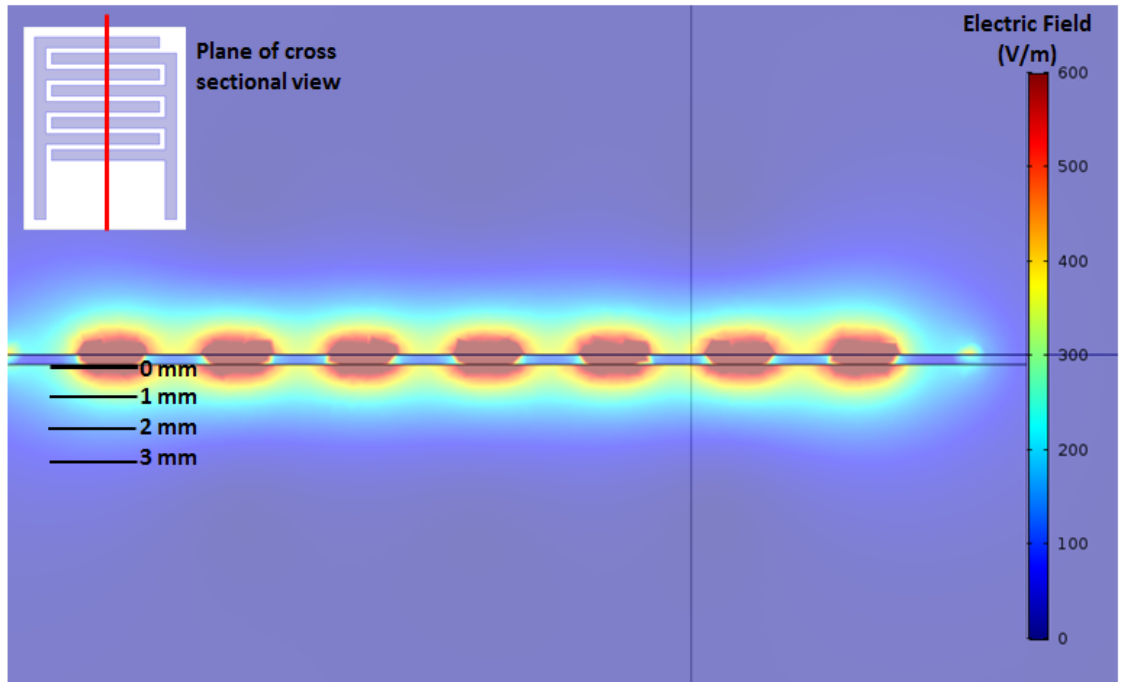


**Table 5.2:** Parameters and dimensions used in the COMSOL modelling of the touch sensors.

Parameter	Value
Paper Thickness	235 $\mu\text{m}$
Paper Permittivity	3.25
Electrode Finger Width	20 mm
Electrode Finger Height	2 mm
Gap Between Electrode Fingers	1 mm
Number of Electrode Finger Pairs	4
Metal Thickness	16 $\mu\text{m}$
Metal Conductivity	$4.17 \times 10^6 \text{ S/m}$

than Design 1 and subsequently had double the capacitance, as would be expected. Design 2 had electrode fingers which were 50% longer than Design 1, the increase in capacitance (42%) was in keeping with this. Design 3 had an electrode finger width 50% less than Design 2, which resulted in a 17% decrease in capacitance. These values were in agreement with the values calculated by Equation (5.1) and showed the same trend with increasing capacitance moving from Designs 1, 3, 2 and then 4. The difference in values of capacitance between Equation (5.1) and the COMSOL modelling was likely due to the modelling accounting for material properties and providing a more accurate value.

The electric field was confined within the paper and then decayed in the air, as shown in Figure 5.6. This was a cross section of the device in the plane shown in the insert of the Figure. The paper had a higher dielectric constant than air and so the change between high and low field regions of electric field were much more defined as it was harder for the electric field to penetrate these regions. There was no visible change in the field strength on this scale at distances more than 3 mm away from the paper, which showed that a finger placed further than 3 mm from the sensor was unlikely to have an effect on the electric field.



**Figure 5.6:** Cross-sectional view to show the electric field for sensor design 1 as modelled by COMSOL when one set of electrodes are set to 1V and the other to 0V. The electrodes are situated on top of the paper substrate.

### Modelling of the Finger in Contact with the Sensor

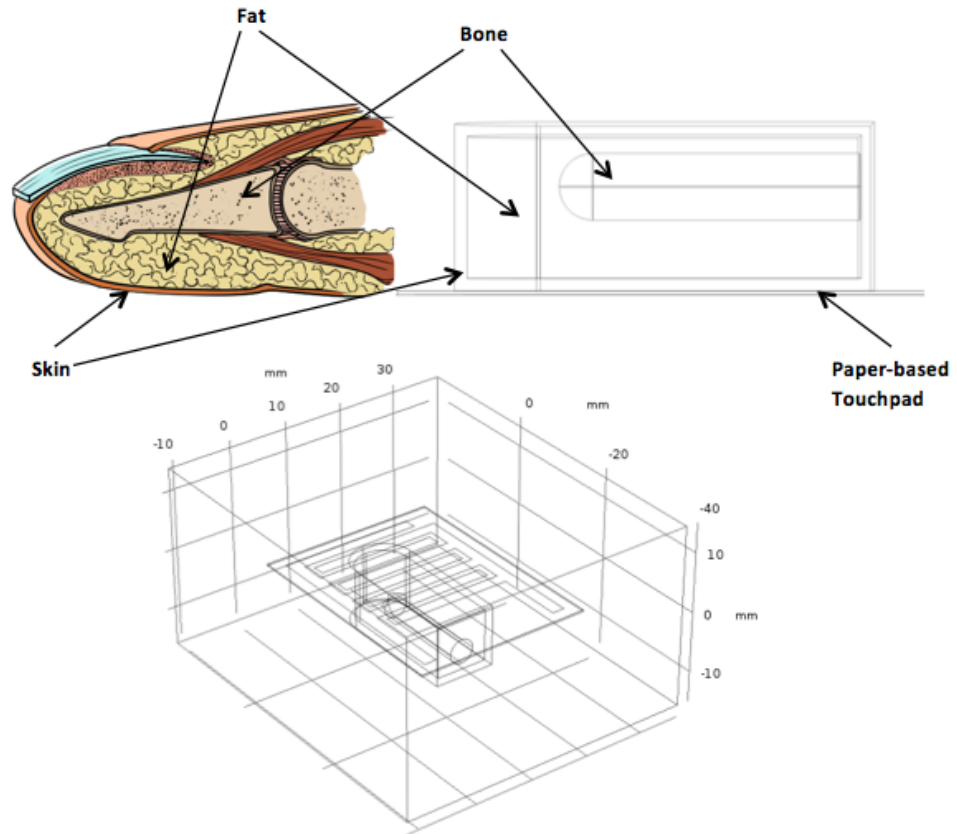
When considering the interdigitated electrodes for use as a touch sensor, the individuality of different users and their relative touch must be included. People use touch devices in several ways, with different fingers and different positions of their finger relative to the touch pad. Initially, the angle between the finger and the sensor was considered and other differences included later in the chapter when measurements of the sensors have been taken. A finger perpendicular to the touch pad, a finger at  $45^\circ$  to the touch pad and a finger parallel to the touch pad were modelled in COMSOL and are illustrated in Table 5.3.

**Table 5.3:** Comparison of the original three finger models trialled in COMSOL. In reality, touch pads are touched on the back, the front is shown here for clarity.

Description	Photo	Illustration	Contact Area Shape
Finger perpendicular to device			
Finger at $45^\circ$ to device			
Finger parallel to device			

Modelling the finger perpendicular to the touch pad was proved not to be realistic as the finger nail often caused the finger to be forced at an angle to the sensor. Modelling the finger at  $45^\circ$  to the touch pad was more realistic of the way in which people would use a touch device. However, the model became complex at the point where the finger contacted the pad. The model was made using a cylinder and a sphere connected. At the point of contact with the pad, the sphere had to be sliced in order to allow a contact region which produced a non-uniform skin thickness. As the COMSOL model was used later in this chapter to simulate altering the contact area between the finger and the touch pad, the model at  $45^\circ$  to the touch pad was unsuitable as the area could not be easily altered and led to further complexity. Although modelling the finger parallel to the touch pad was not how touch devices are commonly used, it was how the touch pad was measured in this work; the user placed their finger parallel with the touch pad to ensure stability and repeatability of the measurements.

The final model is shown in Figure 5.7. The model was made up of three layers; skin, fat and bone and was compared to an anatomical model of the finger. In reality, the finger was found to be much more complex than the model shown here, but a large portion of the interior structure of the finger tip is made up of fat [42]. However, this model was found to be sufficient in modelling the relative change in capacitance with touch. The finger in the model is in contact with the unprinted side of the touch pad rather than the printed side, which was to prevent conduction between the metal electrodes.



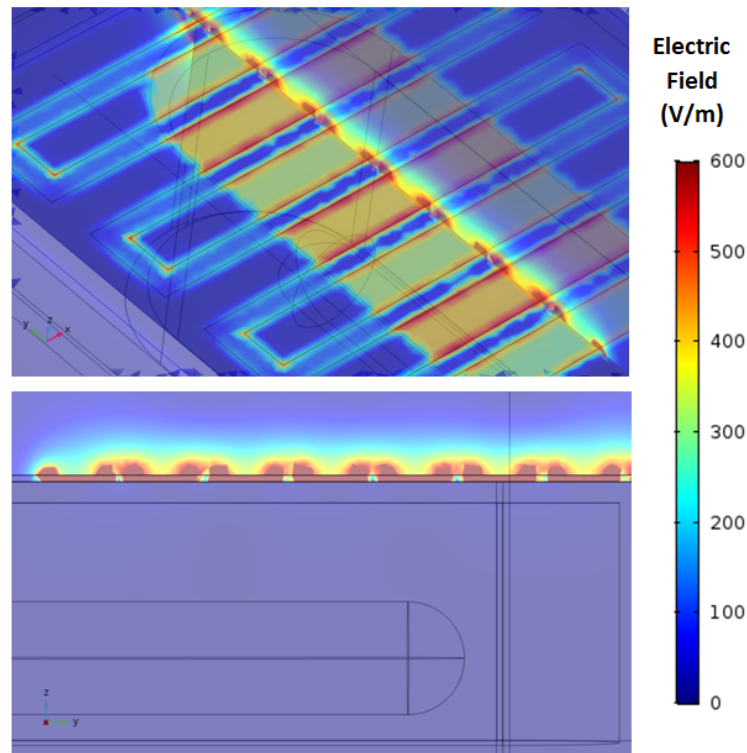
**Figure 5.7:** Anatomical and COMSOL model of the human finger with skin, fat and bone labelled. The anatomical drawing has been adapted from [43].

When a finger was placed parallel to the touch pad, this was the simplest shape which best represented the contact area. The finger was taken to be 1 cm wide and 2 cm long as these were the measured dimensions of the contact area of the user's finger. An average adult human index finger is 16-20 mm long (from the tip to the first knuckle) [44]. However, the contact area with a touch pad is smaller than this due to the curvature of the finger. In this work, the curvature of the finger has been ignored for the simplicity of the model.

The distance between the 'tip' of the finger and the spherical end of the bone was determined to be approximately 3.8 mm according to Buryanov et al. who took an average of measurements from the x-rays of 66 adult hands [45]. The position of the bone in the z-axis (the distance from the plane of the paper) was set to 3.5 mm from the top of the fat and 0.5 mm from the bottom of the fat. This was an educated guess based on findings from Buryanov et al. [45]. The thickness of the skin was taken to be 0.75 mm, as it is known to vary between 0.05 mm for eyelids and 1.5 mm for the soles of feet [46].

The permittivity values for the skin, fat and bone were taken from the work by Gabriel et al. [47] which was re-constructed using Matlab code. Values of permittivity taken at 3.4 MHz were used in this work as this is the frequency at which the measurement system operates. The permittivity value

of skin was taken to be 540, which is the value for dry skin; however the value could be varied between this and the value for wet skin (860). For the sake of this model, the epidermis and the dermis were considered as one uniform skin layer. The relative permittivity value for bone was taken to be 106, which is the value for cortical bone. Although a finger contains cancellous bone as well (permittivity equal to 110), the majority is cortical and the permittivity values are so similar, therefore 106 was used. The value of permittivity used for the fat layer was 21.3, which is that of subcutaneous fat as would be found in the finger. All other material properties for the finger were provided by the COMSOL material library for skin, fat and bone.

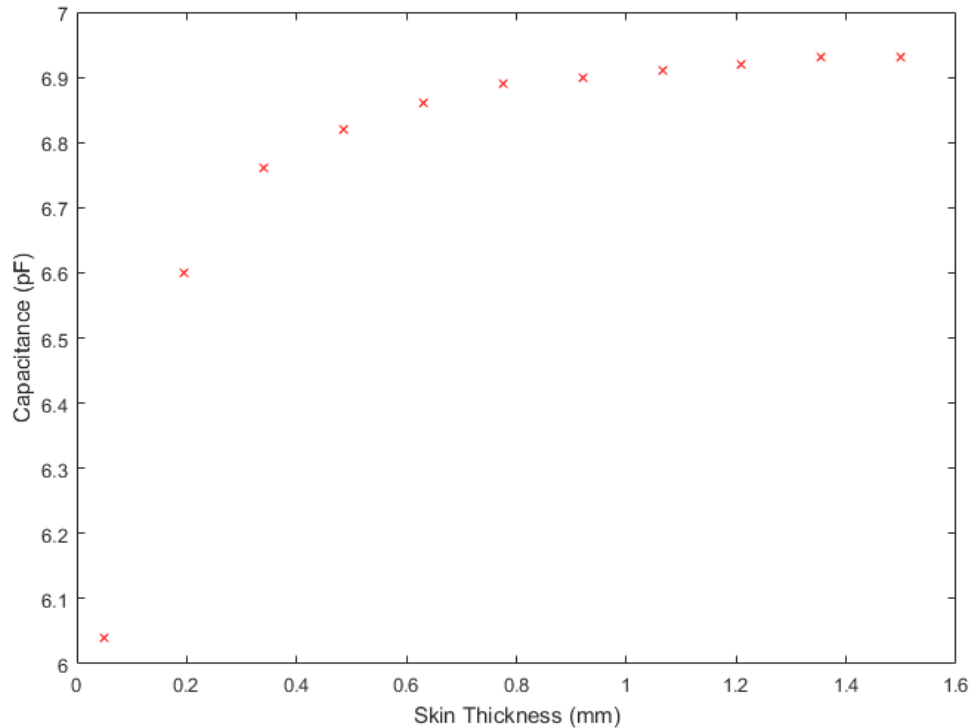


**Figure 5.8:** Example of the electric field for Design 1 touch sensor in contact with the finger as calculated by COMSOL.

The electric field was seen to alter dramatically when the finger was added to the model, as in Figure 5.8. The electric field was restricted to the paper owing to the high dielectric constant of the skin in comparison to both paper and air. To compensate for this, the regions of high electric field were much larger within the paper. As detailed previously, the finger was modelled as a rectangle and a circle which were combined and extruded. This led to a ‘flat’ finger and is obvious in Figure 5.8 where the curve of the finger is taken into account on the sides but not on the bottom of the finger. The high permittivity of the skin meant that there was no change due to changes of the fat or bone. The capacitance value when the touch sensor was touched with this finger model was 6.88 pF according to the COMSOL modelling.

The effect of skin thickness on the capacitance was investigated to ensure the thickness value used

was suitable. Increasing the thickness was shown to increase the capacitance of the device up to a point and then the capacitance value saturates, with results shown in Figure 5.9. As there was less than 2% increase in capacitance when the skin thickness was increased above 0.6 mm, the chosen value should not have had an effect on the capacitance. The thickness of the skin was not likely to be lower than 0.6 mm on fingers due to their robust and well-used nature.



**Figure 5.9:** Change in capacitance as the thickness of the skin layer is varied between 0.05 and 1.5 mm in the COMSOL model.

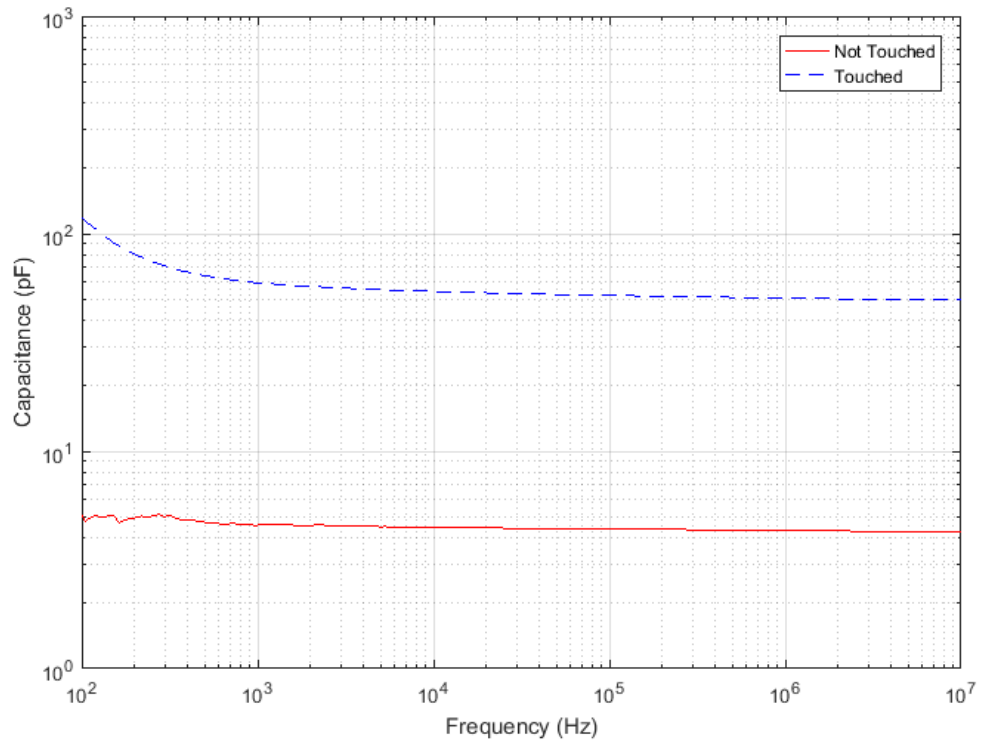
Altering the dimensions of the fat or bone layers was shown to have no effect on the capacitance. As the permittivity of the skin was so high and the electric field did not penetrate into the fat or bone layers, altering the fat or bone should have had no effect on the capacitance. Moving the bone in the z-axis within the fat layer showed no change in capacitance, the value was found to remain at 6.89 pF.

The conductivity of the skin, fat and bone did not need to be considered in this model as the user touched the back side of the touch pad with no direct contact to the metal.

## 5.4 Impedance Measurement of the Interdigitated Sensors

As in Chapter 4, a Hewlett-Packard 4192A Low Frequency Impedance Analyser (Hewlett-Packard, California, US) was used to measure the impedance, phase and capacitance of the interdigitated structures in the range 40 - 100 MHz. A 16047E adapter was used so that devices could easily be connected to the system. The analyser was calibrated, including the adapter, using open, short and

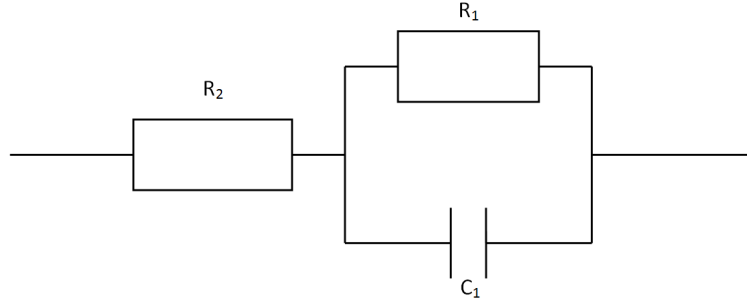
load standards. An example of the capacitance data measured using the impedance analyser is shown in Figure 5.10; this is for a Design 1 sensor.



**Figure 5.10:** Capacitance data taken from an impedance analyser for a Design 1 touch sensor in the touched and untouched states.

It can be seen that there was an increase in capacitance when the device was touched, and it also showed that the response was stable between 10 kHz and 10 MHz. The increase in capacitance when the sensor was touched was from approximately 3.2 pF to 50 pF at 3.4 MHz. This was much higher than the change in the COMSOL modelling and was likely due to the proximity of the finger to the adapter and the resulting effect on capacitance. The change in capacitance with frequency when the sensor was touched was likely due to the frequency dependence of the permittivity of the finger.

An equivalent model for the touch devices was determined and was constructed from a capacitor and resistor in parallel which are both in series with a resistor, as illustrated in Figure 5.11.  $R_1$  represents the resistance of the substrate (in this case, paper),  $R_2$  represents the resistance of one set of electrode fingers and  $C$  represents the capacitance between the two sets of electrode fingers.



**Figure 5.11:** A schematic of the equivalent model for the touch sensors used in this work. The ends of the circuit are equivalent to the ‘legs’ on the sensors.

The impedance and phase could be determined by calculating the total impedance considering  $Z_R = R$  and  $Z_C = -1/i\omega C$ . The total impedance due to the resistance,  $R_1$ , and the capacitance,  $C$ , was equal to:

$$\frac{1}{Z_1} = \frac{1}{Z_{R_1}} + \frac{1}{Z_C} = \frac{Z_C + Z_{R_1}}{Z_C Z_{R_1}} = \frac{1 - i\omega C R_1}{R_1} \quad (5.2)$$

and so

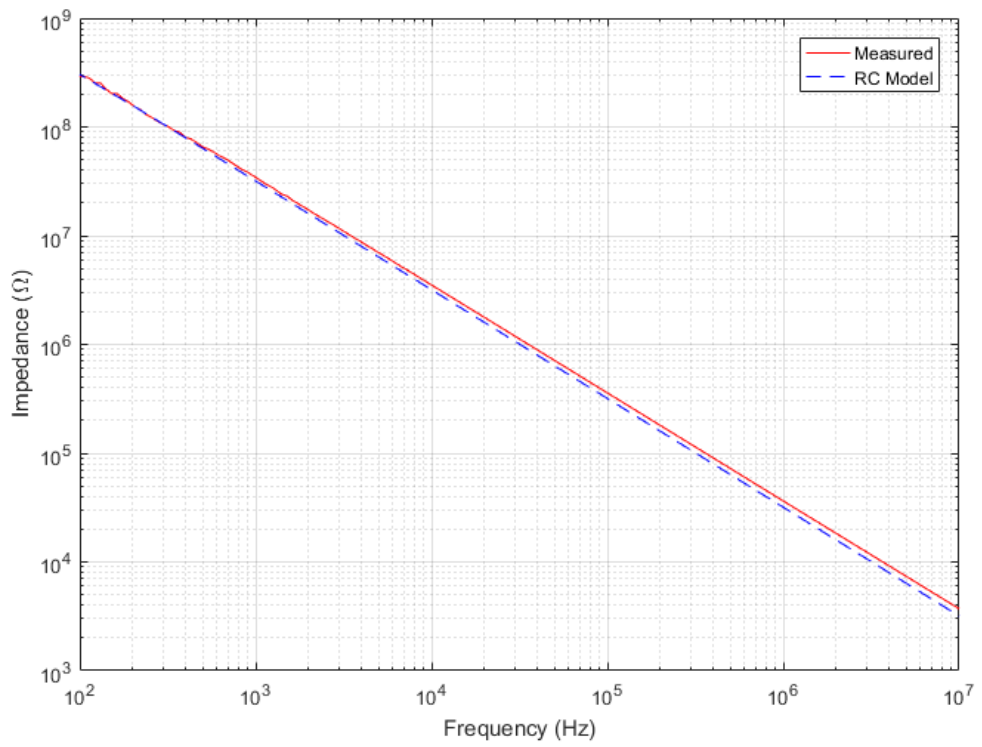
$$Z_1 = \frac{R_1}{1 + (\omega C R_1)^2} + \frac{i\omega C R_1^2}{1 + (\omega C R_1)^2} \quad (5.3)$$

where  $Z_1$  was the combined impedance of  $R_1$  and  $C$ ,  $Z_{R_1}$  was the impedance of  $R_1$ ,  $Z_C$  was the impedance of  $C$  and  $\omega$  was the frequency. When  $R_2$  was also included, the real and imaginary parts of the impedance,  $Z_{real}$  and  $Z_{imag}$  were:

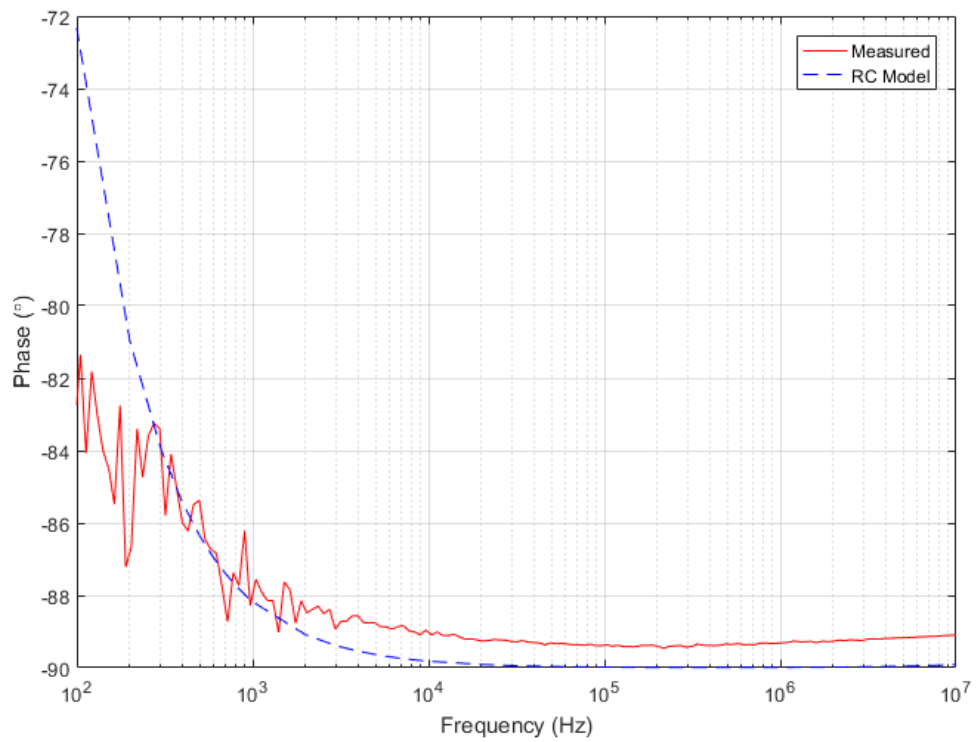
$$Z_{real} = R_2 + \frac{R_1}{1 + (\omega C R_1)^2}, \quad Z_{imag} = \frac{i\omega C R_1^2}{1 + (\omega C R_1)^2} \quad (5.4)$$

This total impedance and the corresponding phase was plotted with the measured data in Figures 5.12 and 5.13 respectively. To fit the model data to the measured values, the capacitance was 5 pF, and  $R_1$  and  $R_2$  were 1 G $\Omega$  and 5  $\Omega$  respectively.





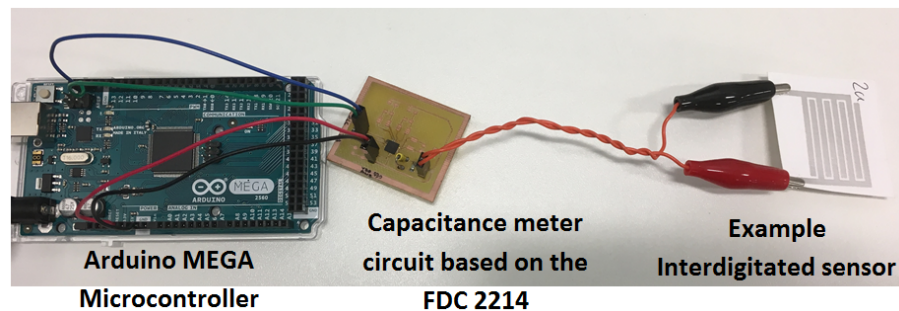
**Figure 5.12:** Comparison of impedance data taken from the impedance analyser and RC modelling technique.



**Figure 5.13:** Comparison of the corresponding phase data taken from the impedance analyser and RC modelling technique.

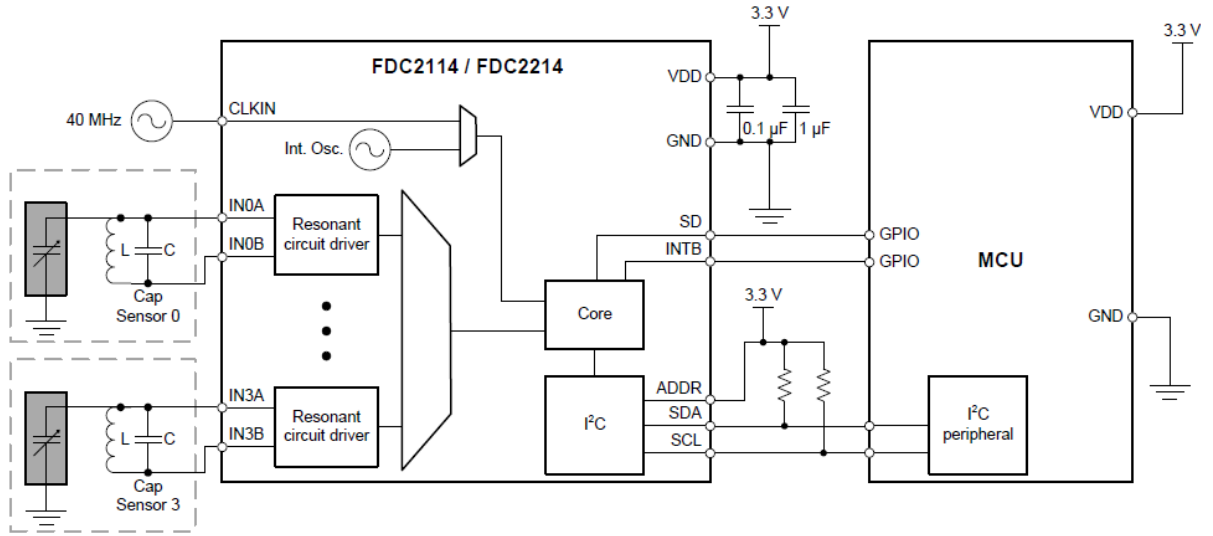
## 5.5 Measurement of the Sensors using an Embedded System

Although the impedance analyser provides information on the capacitance and impedance with frequency, it is not portable and so may not be suitable for many applications. In the majority of touch sensor applications, only a ‘touched’ or ‘not touched’ response is required rather than information on the impedance and phase of the sensor. For this reason, a system was designed and built to measure the capacitance of the touch pads using a Texas Instruments FDC 2214 chip (Texas Instruments, Texas, US), an Arduino MEGA Microcontroller and Matlab to interface with the measurement system and extract capacitance values. An image of the system can be seen in Figure 5.14.



**Figure 5.14:** The custom-built measurement system for the touch sensors consisting of an Arduino MEGA, a PCB with FDC 2214 chip and RLC components and an example of a Design 2 interdigitated sensor.

The FDC 2214 chip is a multichannel capacitance-to-digital converter for implementing capacitive sensing solutions, and a schematic taken from the data sheet is shown in Figure 5.15 [48]. A change in the LC tank, shown in Figure 5.15 where  $L$  is an inductance and  $C$  is a capacitance, could be observed by a change in the resonant frequency which was then extracted as a digital value proportional to the frequency. The digital value was read out through an Arduino using an  $I^2C$  peripheral. The value of  $L$  and  $C$  for the LC tanks were known and, by comparing the measured resonant frequency with the known resonant frequency, the capacitance of the capacitive device in the shaded box could be determined by the equation  $f_r = 1/\sqrt{LC}$ . To achieve a resonant frequency of 3.4 MHz, which was within the operating frequency of the chip, an inductance of 22  $\mu\text{H}$  and a capacitance of 100 pF were chosen for  $L$  and  $C$  respectively. The FDC 2214 chip was chosen as it is capable of having connections to four touch pads and so, in an application, four touch sensors could be used at the same time.



**Figure 5.15:** Schematic of the PCB and Arduino system, taken from [48].

It was understood that any changes in  $L$  and  $C$  within the LC tank would result in large changes in frequency and, because of this, the tolerances of both the fixed inductor and capacitor were of importance. In this case, the tolerance of the inductor and the capacitor were  $\pm 10\%$  and  $\pm 5\%$  respectively. Any following variations in measurements would affect the absolute values for capacitance read by the Arduino. In this investigation the concern was the relative change in capacitance with touch which would not be affected by the variations and tolerances of the components.

The oscillator-based measurement system is highly stable and drift free. A sample was left for 15 minutes and the capacitance varied in the range  $4.93 \pm 0.04$  pF. Several standard capacitors were measured using the system and the capacitance values were all within the tolerances of the components.

The oscillator-based measurement system, as well as measuring the state of the sensor (touched or not touched), is also accurate in measuring the capacitance of the sensors. Table 5.4 compares the capacitance values determined by Equation (5.1), COMSOL modelling, the impedance analyser and the oscillator-based system. The value of capacitance quoted here for the impedance analyser is the capacitance measured at 3.4 MHz to be directly comparable to the value measured using the oscillator-based system. It can be seen that the oscillator-based system was directly comparable with the other methods and showed the same trend in capacitance with changing design.

The large variation in capacitance values with the impedance analyser was due to measurement difficulties rather than the touch pad fabrication method. There was limited availability of connection modules for the impedance analyser, resulting in movement of the sample when touched. This could have been avoided with an alternative connection module but would incur added costs which were not

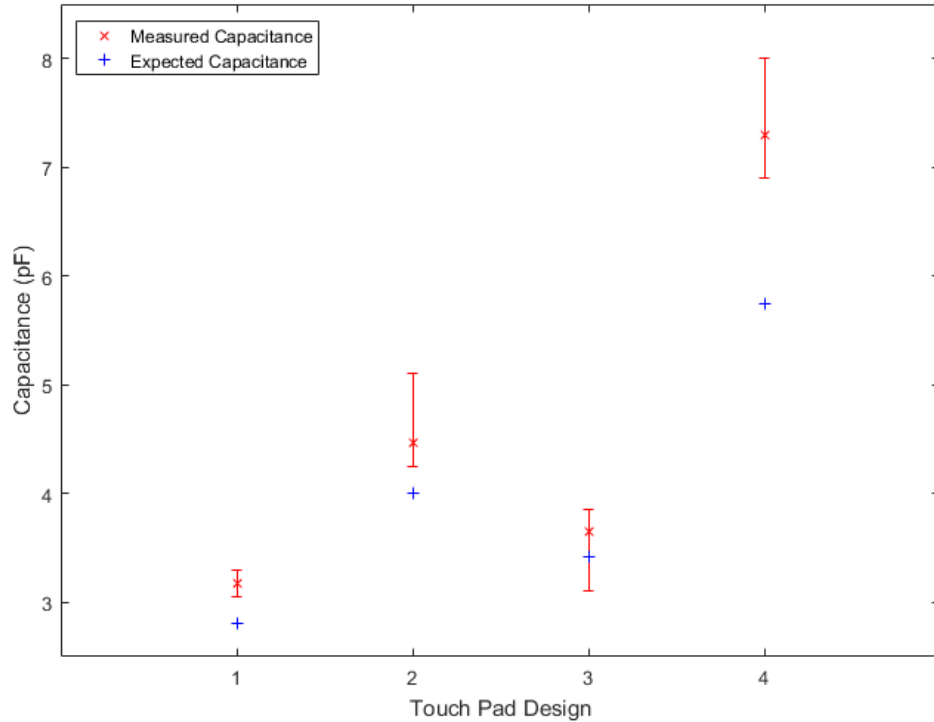
available for this work. The oscillator-based measurement system was shown to give results that were comparable to the impedance analyser, with less variation due to its configuration for measurements. Therefore there was confidence that the data from this was of a sufficient accuracy to continue future measurements using that system alone.

**Table 5.4:** Comparison of capacitance values for the touch pad designs calculated by Equation (5.1), COMSOL modelling, measured by the impedance analyser and the oscillator-based system.

Sensor Design	Capacitance (pF)			
	COMSOL	Equation (5.1)	Impedance Analyser	Oscillator-based System
1	2.81	1.73	2 - 8	3.1 - 3.3
2	4.00	2.74	4.5 - 15	4.2 - 5.1
3	3.42	2.16	3.8 - 12	3.1 - 3.9
4	5.75	3.46	2 - 9	6.8 - 8.0

### 5.5.1 Repeatability of the Fabrication Method

In Chapter 4, the deviation in feature size and thickness of the screen-printing method was considered. It was shown that the ink thickness for this method varied between 14 - 31  $\mu\text{m}$ . The feature size and gap between features, when both designed to be 0.5 mm, were between 0.46 - 0.60 mm and 0.38 - 0.48 mm respectively. These changes in dimensions due to the fabrication method could lead to over a 25% change in dimensions and therefore capacitance. Capacitance values for 20 samples of each of the four designs were found to be within  $\pm 15\%$  of the average value, as shown in Figure 5.16, which was within the variation of the fabrication method.



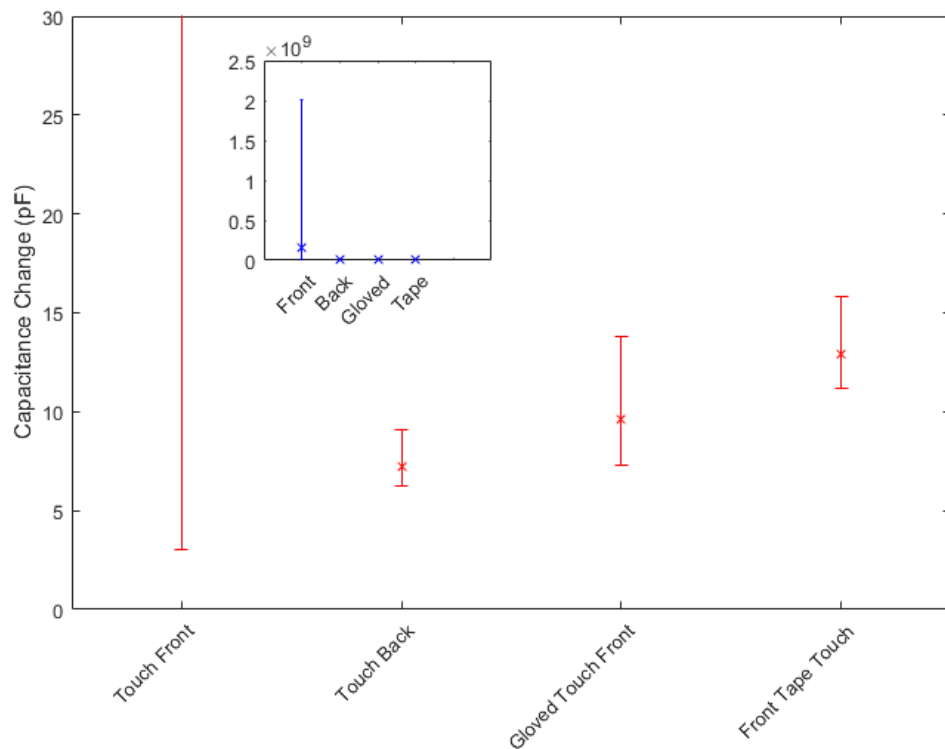
**Figure 5.16:** Repeatability of the fabrication method for the interdigitated touch pads.

Design 1 was shown to be more repeatable than the other designs and the variation was no more than  $\pm 4\%$  of the average value. This was due to the larger electrode finger width and shorter electrode finger length of this design. These factors meant there was less area for the print to contain defects, but the features were large enough to be distinct from each other and not merge together. Defects could have included shorting between the electrode pairs, thinner (or no) ink being deposited or weeping of the ink during printing which would have led to larger electrodes and a smaller gap. Due to the lower variation in fabrication and the lower area, Design 1 was used for the example results throughout this chapter unless stated otherwise.

### 5.5.2 Comparing Touch of the Printed and Non-printed Sides of the Sensor

As the printed side of the capacitive device was not coated, unlike the designs from other groups, the change in capacitance when this side was touched was highly variable in comparison to touching the non-printed side. In this work, the ‘front’ side refers to the printed side and the ‘back’ side refers to the non-printed side. Touching the front of the capacitive device could cause shorting between the two sets of electrode fingers, especially if the finger was warm and moist. Although the COMSOL model did not include the conductive nature of the finger, in reality the finger was slightly conductive ( $< 20 \mu\text{S}$ ) [49]. When the finger was moist due to sweat or water, this conductivity increased.

Touching the back of the device, wearing gloves while touching the front of the device or touching the front when it had been covered with tape (or some other dielectric material) was shown to have smaller variation when compared to touching the uncoated front of the device. Example results for touching the device under each of these conditions are shown in Figure 5.17. To show the data clearly, the scale of the y-axis was chosen so that it did not include the full data range of the capacitance when the front of the touch pad was touched. This data actually ranged from 3 pF to 2 nF as can be seen in the figure inset.

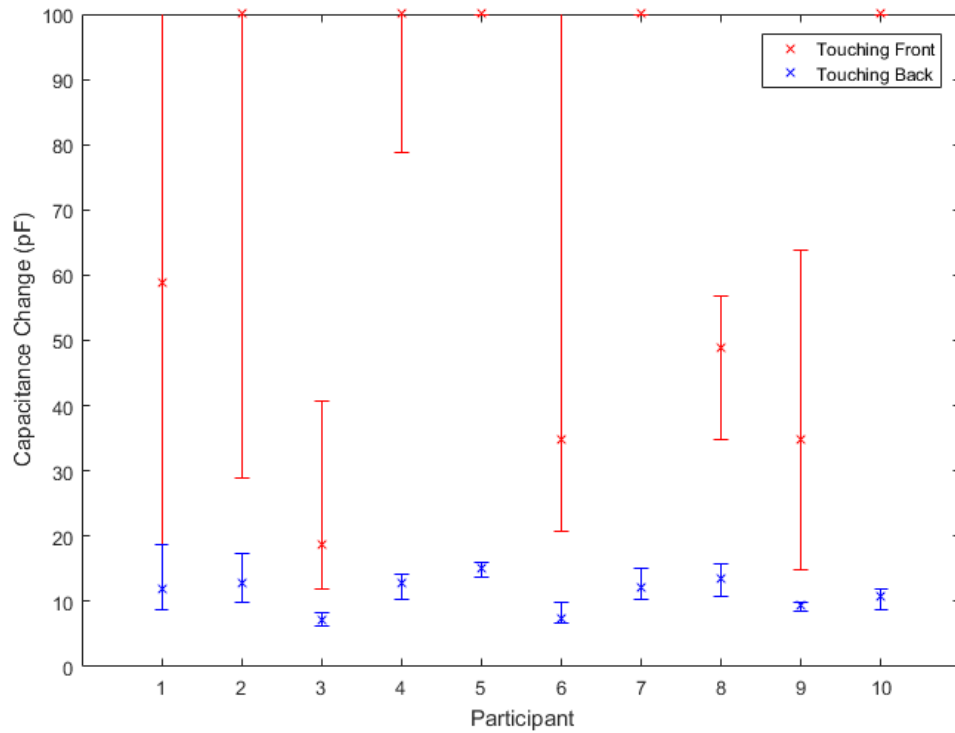


**Figure 5.17:** Comparison of capacitance values for touching the touch pad in different ways. Touching the front, touching the back, touching the front of the touch pad with gloves on and touching the front when it had been covered in a layer of tape.

Adding tape to the printed side of the sensor or wearing gloves prevented connection between the two pairs of electrodes which could happen when the printed side was contacted with bare skin. However, as the sensor could simply be turned over, the addition of gloves or tape would increase the cost of the device. Touching the back side of the sensor also allowed the addition of an application-based design on the non-printed side of the sensor. For example the keys on a keyboard could be drawn on the non-printed side to indicate the touch sensitive areas to the user.

As touch sensors are used by a highly diverse audience, further measurements were taken with different users touching an example device, results are shown in Figure 5.18. The users included a variety of sexes, nationalities and body types in order to accommodate the possible diversity of users. When touching the front of the sensors, the capacitance varied between pF and  $\mu$ F between different

users. This was due to the change in conductivity of the users' fingers, some were warmer and more moist than others. The variability in capacitance values for different users touching the back of the device was due to the difference in force and contact area among users. Even with this variation, the results for touching the back of the touch sensor were within a more reasonable range. These results emphasised the difference in repeatability when touching the front and back of the device. Any results presented below for touched devices are for those touched on the back of the device.

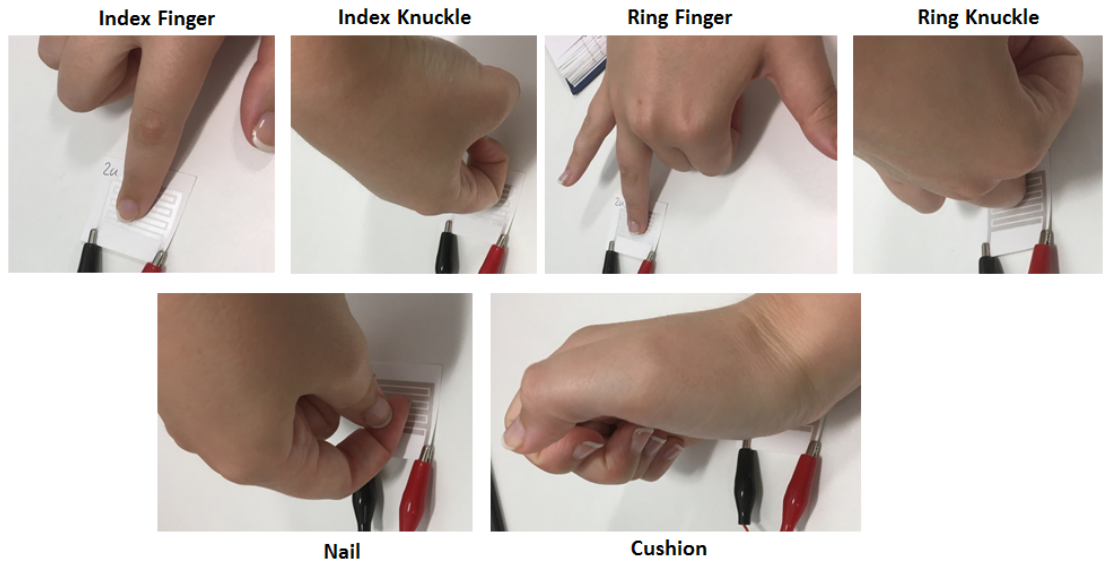


**Figure 5.18:** Example data for various users touching the front and back of a touch pad.

### 5.5.3 Comparing Touch of the Sensor Using Different Parts of the Hand

In addition to comparing a variety of users, it was important to consider the part of the body used to touch the touch pad. Although many users use their index finger to touch a sensor, some may use other fingers or parts of their hand. Some applications or situations may mean that the index finger is not available and maybe the knuckle or another finger is used. As detailed when developing the COMSOL model, a simple model of the finger can be made up of three layers: skin, fat and bone which all have varying mechanical and electrical properties. In reality, the finger is far more complicated than this and is made up of many more layers and materials, and different parts of the hand are also made of different materials with different structures. To illustrate using different parts of the hand to contact the sensor, the index finger and knuckle, the ring finger and knuckle, the nail and the cushion were considered and are shown in Figure 5.19. It is shown that the front of the touch pad is touched

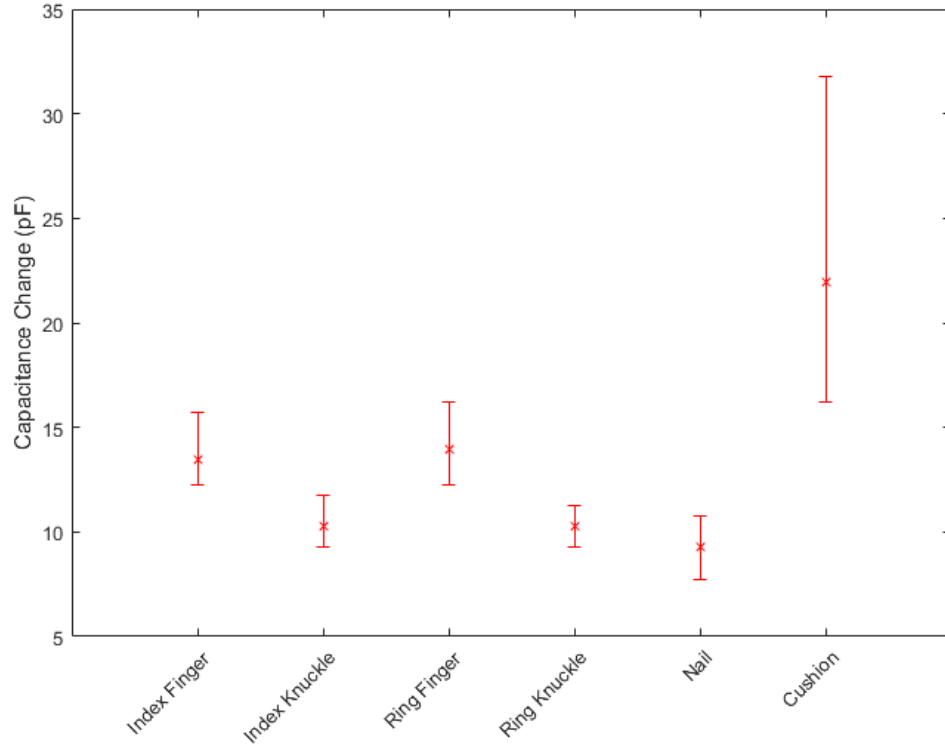
for better illustration although measurements were taken on the back of the touch sensor.



**Figure 5.19:** Various parts of the hand used to compare the difference in capacitance when each part is used to touch the sensors. In reality, the sensor was touched on the back, however the front has been shown for clarity.

Using any section of the finger was found to produce more repeatable results than using the ‘cushion’ part of the hand, with results shown in Figure 5.20. In a real situation, it is unlikely that the cushion part of the hand would be used but it is important to consider many possibilities and find a working range based on this. These results showed that the touch sensor was operational for all parts of the hand tested. The larger variation in capacitance change when using the cushion part of the hand was due to the variable area and force which would be used, this was much easier to control when using the fingers or knuckles.





**Figure 5.20:** Measured capacitance values when different parts of the hand are used to touch the touch pad.

#### 5.5.4 Untouched and Touched Capacitance of the Sensors

The capacitance value was found to more than double for each design when touched. Capacitance values for each design in their untouched and touched states are listed in Table 5.5. Designs 2 and 4 are seen to have a much higher change in capacitance with touch, which was due to their larger area. A larger area will lead to a larger contact area between the touch pad and the finger and so the effective permittivity will increase, increasing the capacitance. This should be taken into account when designing a touch pad.

**Table 5.5:** Capacitance values for the various designs in touched and untouched states measured using the custom set-up. All values represent the maximum and minimum data.

Sensor Design	No Touch (pF)	Touch (pF)	Capacitance Change (pF)
1	$3.2 \pm 0.12$	$7.7 \pm 1.4$	$4.5 \pm 1.5$
2	$4.7 \pm 0.4$	$14.4 \pm 2$	$10.0 \pm 2$
3	$3.5 \pm 0.4$	$10.0 \pm 1$	$6.4 \pm 1.5$
4	$7.3 \pm 0.8$	$17.0 \pm 1$	$9.7 \pm 4$

The dimensions of the electrode fingers were comparable with those detailed in the literature, all of which resulted in capacitances in the low pF range. The change in capacitance was 30 pF for Li et al. [24], 20 pF for Kanaparthi et al. [38] and 100 pF for Yun et al. [34] when the touch devices were touched. The change in capacitance for the sensors here was lower than work by Yun although

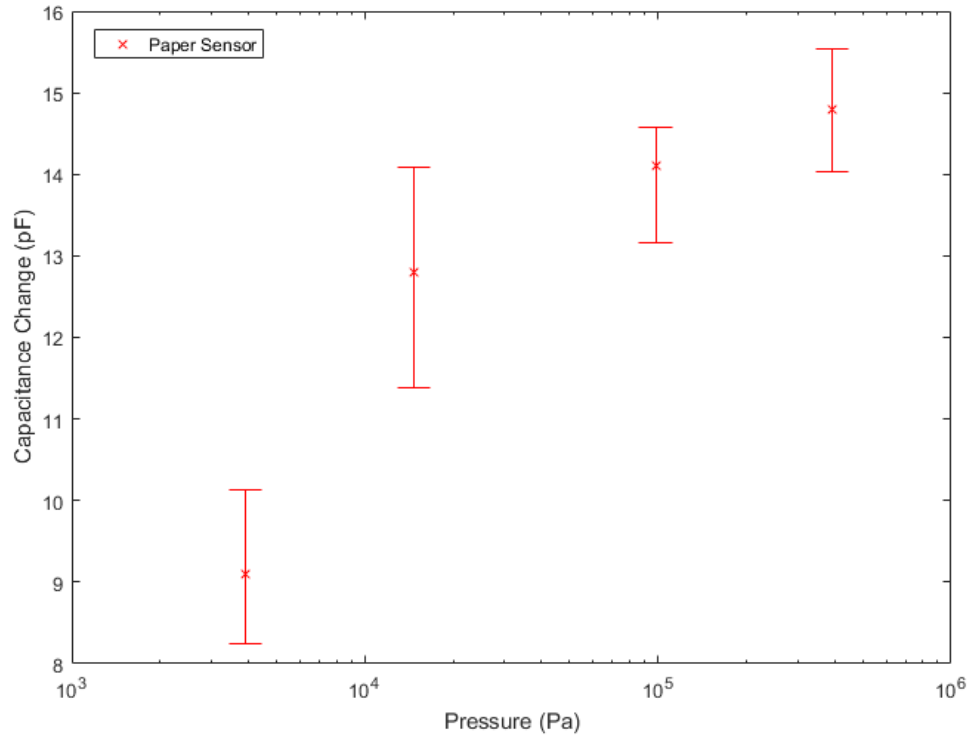
in keeping with work by Li and Kanarparthi. This comparison is shown in Table 5.6.

**Table 5.6:** Comparison of capacitance values for untouched and touched sensors for work by different groups.

Group	Dimensions	Fabrication Method	Untouched Capacitance (pF)	Touched Capacitance (pF)
Li et al. [24]	W and g = 0.5 mm L varied 4 - 16 mm N = 2 - 10	Direct write syringe pump	1 - 5	5 - 35
Kanarparthi et al. [38]	W and g = 0.6 mm L varied 5 - 15 mm N = 4 - 20	Direct write 5B pencil	1 - 3.5	5 - 23
Yun et al. [34]	W = 1 mm g = 0.5 mm L varied 5 - 15 mm N = 12	Inkjet printing	228 - 236	340 - 564
This Work	W = 1 - 2 mm g = 1 mm L varied 20 - 30 mm N = 8 - 16	Screen print	3 - 8	6.5 - 18

### 5.5.5 Varying the Touching Pressure

Increasing the force applied to the sensor was shown to increase the resulting capacitance. A touch pad was secured to a digital balance and the mass measured was converted into a force. From the equation  $P = F/A$ , where P is the touching pressure, F is the force and A is the contact area between the finger and the touch pads. The pressure was calculated and has been used to present the results in Figure 5.21. The area was taken to be  $2\text{ cm}^2$  and was measured based on the contact area of the user for this experiment. The user touched the touch pad, ensuring the same mass was registered on the scale, 20 times at each level.

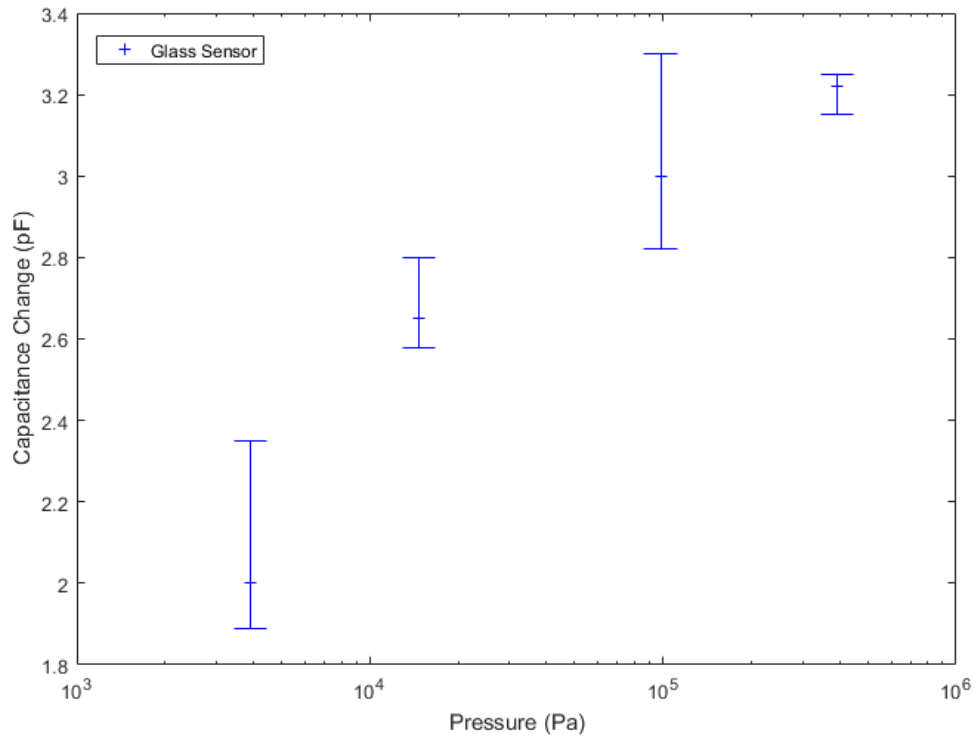


**Figure 5.21:** Measured capacitance values when different forces were applied to a touch pad with a paper substrate.

It is thought that increasing the force was not directly causing the change in capacitance but that it was due to the resulting decrease in the air gap between the device and the finger. The finger was modelled in COMSOL as a flat surface in direct contact with the device, however this is not the case in reality since, as the finger is both curved and ridged, the contact area and air gap between the device and the skin will vary based on the force applied by the user. When a force is applied resulting in a pressure of  $1 \times 10^4$  Pa, the finger will deform and the contact area between the device and the finger will increase. The air between the fingerprint ridges will be decreased and so both the area decreases and the effective permittivity increases, increasing the capacitance dramatically. When a larger force is applied, resulting in a pressure of  $1 \times 10^5$  Pa and then  $15 \times 10^5$  Pa, the amount of deformation possible will reduce and so less air is removed and the contact area tends towards a maximum value. This explains why increasing the force increases the capacitance by large amounts to begin with and then by less as more force is applied.

To ensure that the change in capacitance was not related to the compression of the substrate, an identical touch pad was printed on a 1 mm thick glass substrate and tested in the same way as the paper-based device. The results shown in Figure 5.22 for the glass substrate show the same trend as those for the paper substrate. Therefore, the change in capacitance was not due to compression of the substrate. The lower change in capacitance in comparison to the paper substrate was due to the

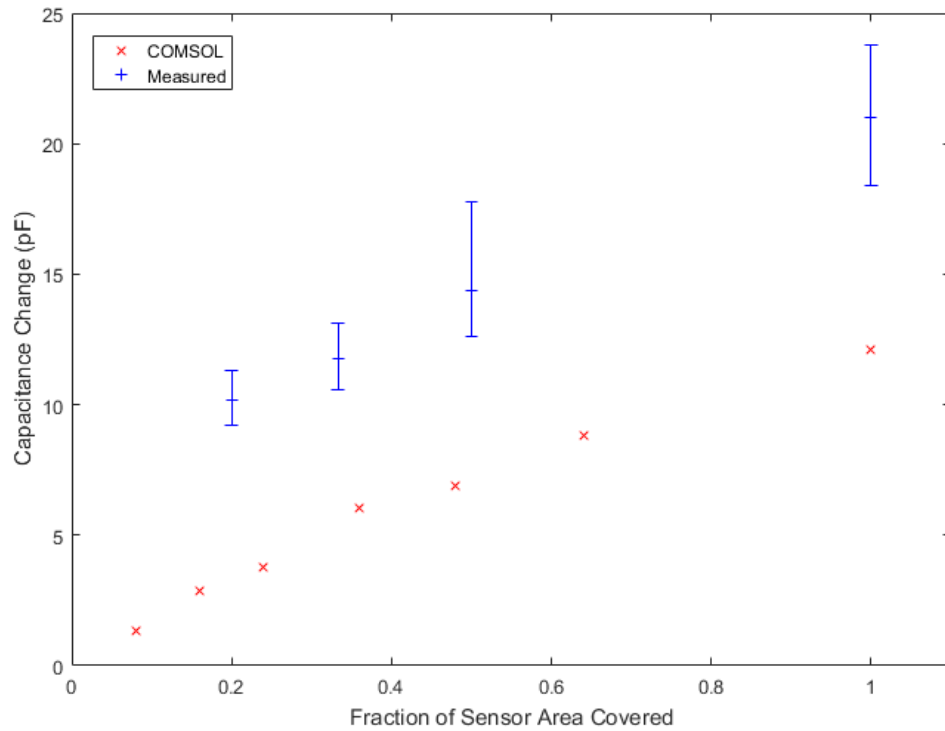
thickness of the glass being four times that of the paper and so there was less interaction with the electric field.



**Figure 5.22:** Measured capacitance values when different forces were applied to a touch pad with a glass substrate.

### 5.5.6 Varying the Contact Area Between the Finger and Sensor

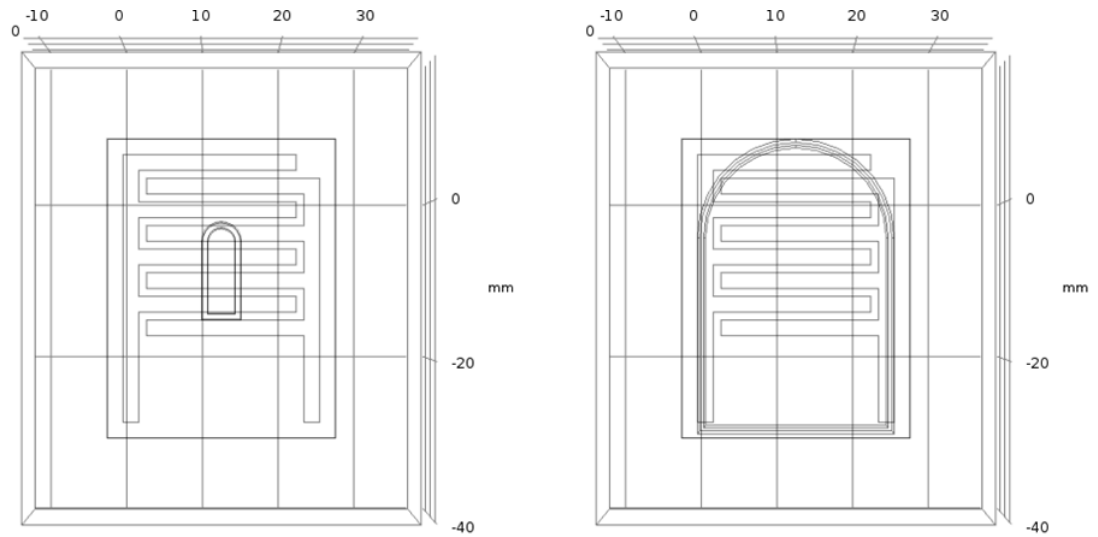
Users of any touch sensor have varying finger sizes, even one user has different sized fingers which can be used to contact the sensor. Increasing the contact area between the capacitive device and the finger was shown to increase the capacitance both in the measurement and COMSOL modelling, as shown in Figure 5.23. Both results were for when the finger was in contact with the back of the touch pad.



**Figure 5.23:** Comparison of measured and simulated capacitance values when the contact area between the finger and touch pad was varied.

In measurements, the contact area was changed by placing the finger so it covered  $1/5$ ,  $1/3$  and  $1/2$  of the device. To achieve an area of 1, two fingers were used close together to cover all of the pad. At each point, the measurements were taken 10 times. Due to the subjective nature of ensuring a certain fraction of the device was covered, the variation in the measurements was high, approximately  $\pm 20\%$ . Although the variation was high, there was a clear trend between contact area and capacitance. When the finger covered a larger area of the touch pad, the effective permittivity increased for that area, leading to an increase in capacitance.

The finger model used in the COMSOL model was varied between the sizes shown in Figure 5.24. Again, as the area was increased, the effective permittivity was increased and so the capacitance was increased. The COMSOL model parameter sweep was independent of any other factors and only the area was varied in this case. The area and capacitance did not vary completely linearly as expected for the COMSOL results. This was due to the shape of the finger and an area equal to 1 including the connection ‘legs’. As the finger is increased, a portion of the finger may not be in proximity to the electrodes but instead, is in proximity to the space between the legs, leading to a lower capacitance than if it was covering electrodes.

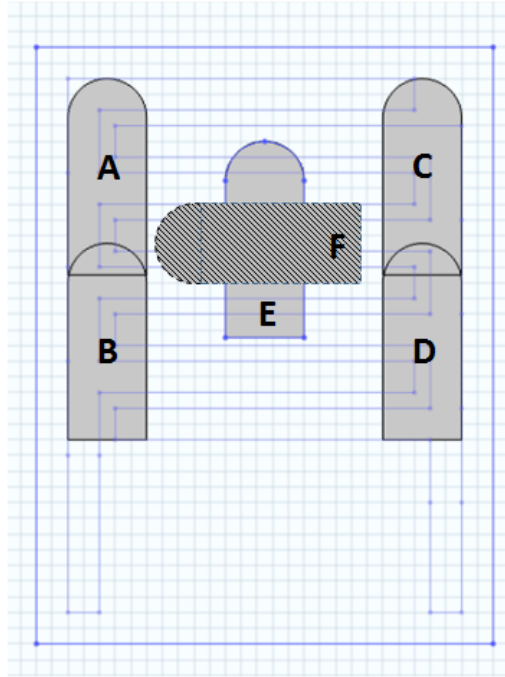


**Figure 5.24:** Illustration of the smallest and largest contact area between the finger and touch pad when using the COMSOL modelling.

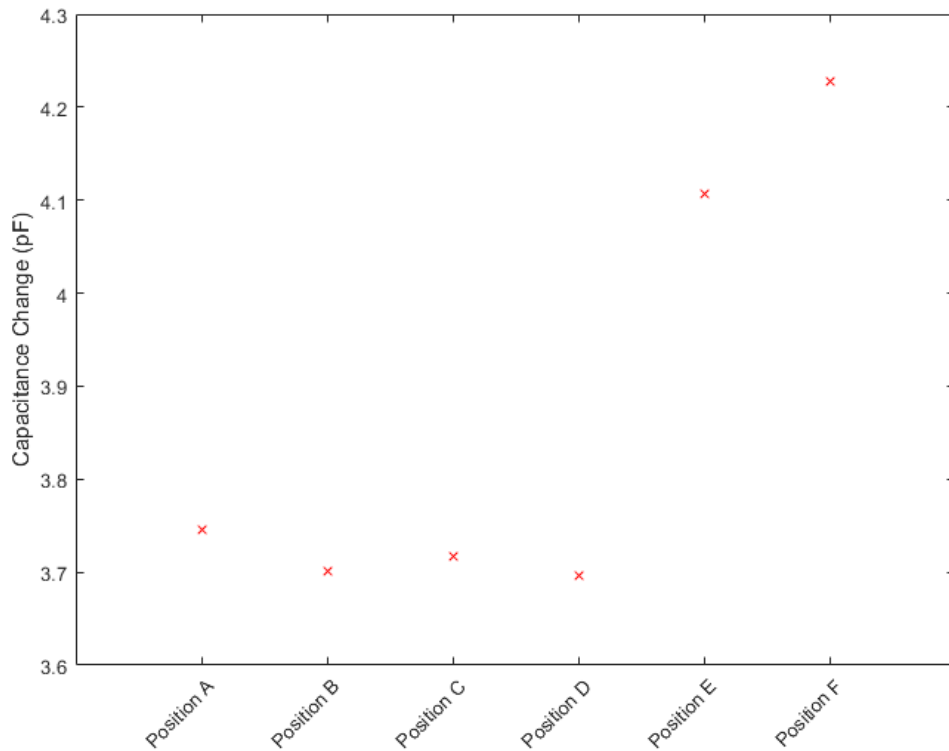
Both the COMSOL modelling and measurements indicated that there was a linear trend between contact area and capacitance, and so the resulting capacitance based on an area could be calculated. The gradient for the COMSOL modelling was  $14.75 \text{ pF/m}^2$  and the gradient for the measured values was  $11.71 \text{ pF/m}^2$ . These values were within the variation of the measured values and in good agreement with each other. The difference in intercept of the graph was due to the use of modelled touch pads and printed touch pads. The printed touch pads had different dimensions to the model due to the 25% variation in printed features determined in Chapter 4. The added complexity of an actual finger compared to the model would also have affected the results.

### 5.5.7 Varying the Position of the Finger on the Sensor

The change in position of the finger around the outside of the device was shown to have no effect on capacitance but using the middle of the touch pad was shown to increase the capacitance. These results are shown in Figure 5.26, the positions A to F are labelled in Figure 5.25. The dimensions of the finger model used in this section were reduced in order to have distinct positions of the finger with minimal overlap. In this investigation, the finger was 0.5 cm wide and 1 cm long.



**Figure 5.25:** Illustration of the various positions of the finger in the COMSOL model to determine any change in capacitance with position.



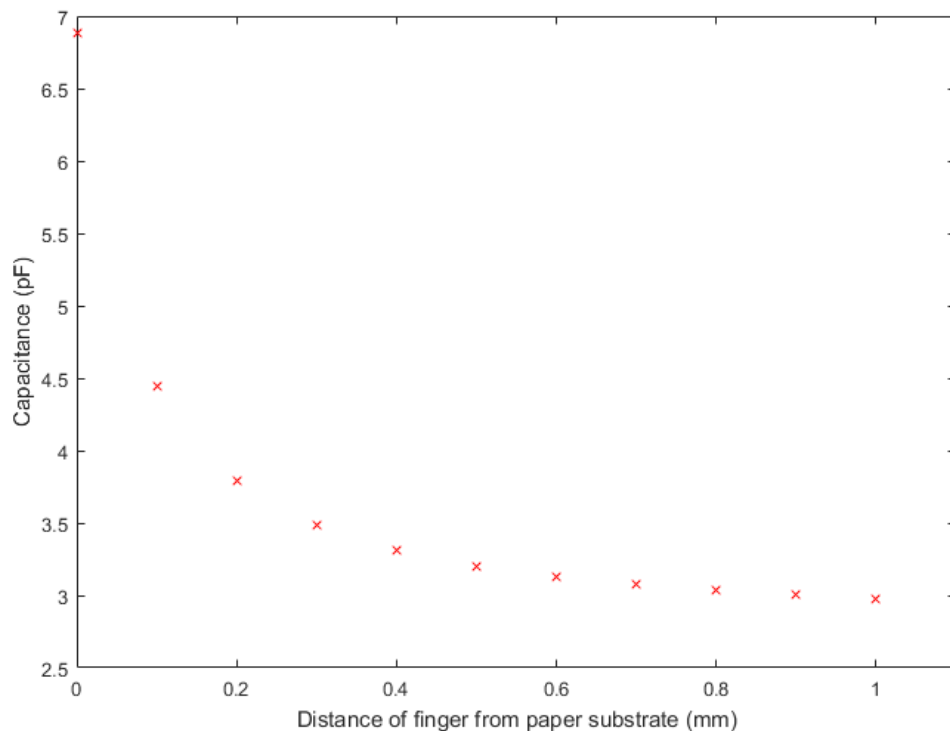
**Figure 5.26:** Simulated capacitance values for a finger touching the touch pad in different positions.

When the finger was placed in the centre of the device, there was more interaction between the finger and the electric field than when it was along the edge of the device. Measurements taken using the same principle of moving the finger showed large variation, which was likely due to changes in contact area and pressure and so results have not been presented here.

### 5.5.8 Varying the Proximity of the Finger to the Sensor

Figure 5.6 showed that the electric field exists out of the paper substrate, meaning that the touch sensor should be proximity sensitive as well as force and area sensitive. Using the custom set up, the wires were found to be proximity sensitive and so it was not possible to take measurements regarding the proximity sensitivity of the touch sensors. When the touch pad was face up or face down or not connected at all, the largest change in capacitance due to proximity of the hand with the wires was 2 pF. The change in capacitance of the device when touched ‘lightly’ on the back was 9 pF, therefore, the change in capacitance from touch was not simply proximity to the wires.

COMSOL modelling has been used to determine the effect of proximity on the capacitance of the touch sensors. The finger was moved so that the distance between it and the device was increased up to 1 mm, with results shown in Figure 5.27. The capacitance dropped dramatically from 6.9 pF to 2.9 pF within this distance. This was in agreement with the figures showing the electric field as the electric field strength was non-linear with distance from the paper.



**Figure 5.27:** Simulated capacitance values when the proximity of the finger and the touch pad was varied between 0 and 1 mm.

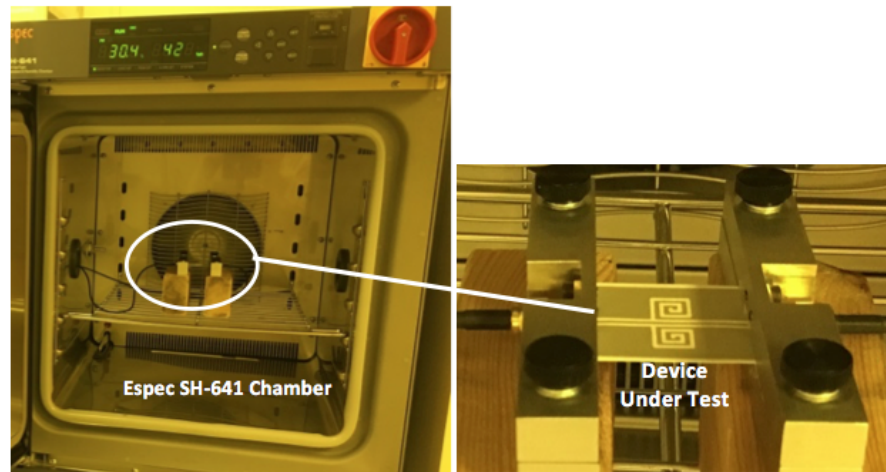
## 5.6 Effect of Humidity on the Sensors

The effect of humidity on paper substrates is widely known and a great concern in the printing industry and has been discussed in detail previously (Chapter 1). As the design of the capacitive

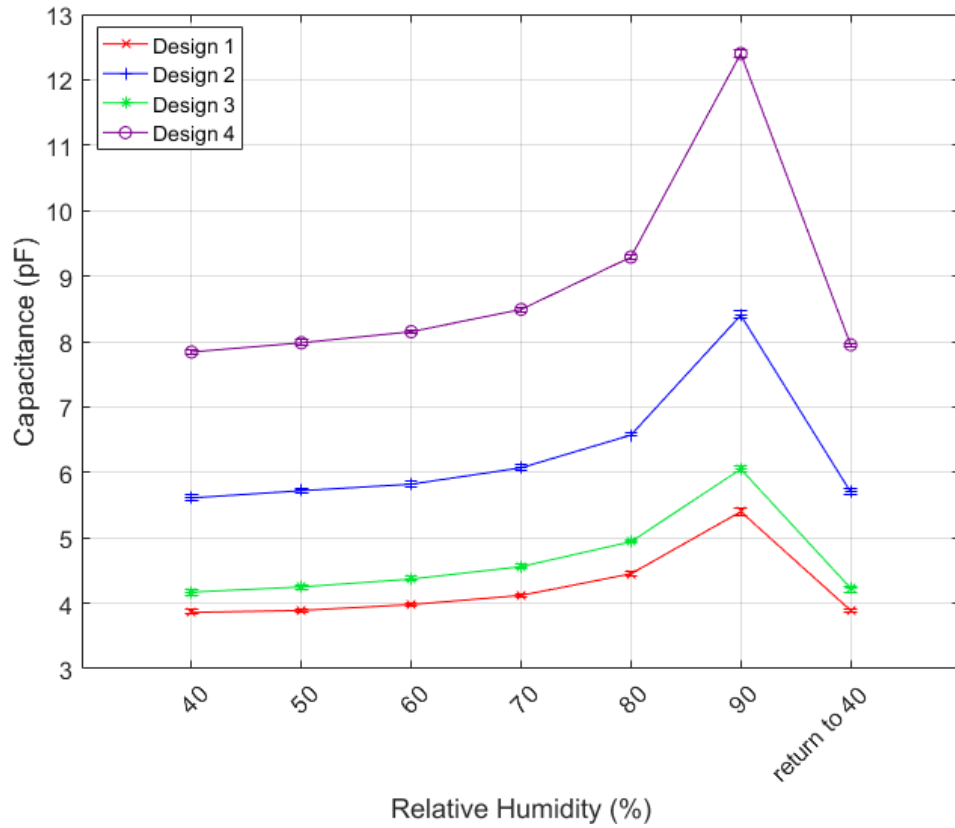


sensors has now been established and the change in capacitance with different users considered, the effect of humidity on the sensors was also investigated to determine possible environments where they might no longer operate as touch sensors.

The effect of relative humidity on the response of the touchpads was determined by recording the variation of capacitance in an Espec SH-641 bench-top type temperature and humidity chamber, where the relative humidity was systematically varied between 40% and 90% in 10% steps. The set up is shown in Figure 5.28 and the results are shown in Figure 5.29. Throughout this work, the temperature was constant, at 30 °C.



**Figure 5.28:** Set-up for humidity measurements showing an example device under test. An environmental chamber and the custom measurement system were used to vary the relative humidity and simultaneously measure the capacitance of the touch pads.



**Figure 5.29:** Measured capacitance values for the four touch sensor designs when the relative humidity is varied from 40 to 90% and returned again to 40%.

Due to the hygroscopic nature of paper, the substrate for the touch sensors will absorb water as the humidity is increased. Therefore, the permittivity of the substrate will increase as the permittivity of water is greater than that of paper (approximately 80 compared to 3.25 for paper). As the permittivity of the substrate increases, the capacitance will increase proportionally. Based on this, it can be seen that the amount of water absorbed by the substrate increases at a higher rate with humidity. The increase in water content and the resulting change in permittivity is explained in detail in Chapter 6.

The increasing change in capacitance between designs was due to the change in substrate area. The paper substrate was cut around the sensor leaving a 1 mm gap between the edge of the printed area and the edge of the paper. The areas of each of the sensors used in this investigation were 858, 958, 796 and 1096 mm<sup>2</sup> for Designs 1, 2, 3 and 4 respectively. The area of sensor designs 2 and 4 were higher than that of 1 and 3 and so the change in capacitance was greater as more water could be absorbed.

The change in capacitance was less than 1 pF for all four designs when the humidity was varied between 40 and 70%. When the humidity was increased above this, the capacitance increased greatly with maximum change being 1.5, 1.9, 2.8 and 4.5 pF for Designs 1, 3, 2 and 4 respectively. The maximum change for each design with humidity was lower than the average change when touched,

shown in Table 5.5. However, in any environment in which the relative humidity will rise above 70%, this change in capacitance should be taken into account.

## 5.7 Conclusion

The results in this chapter have shown that it is possible to fabricate reliable touch pads on paper for use in systems which require a touch interface. This is a significant requirement for the development of a final device which includes an interactive element and has the potential to be integrated with the sensing elements detailed in Chapter 7.

Interdigitated capacitive structures have been screen printed for use as touch sensors with successful results showing a measurable increase in capacitance when touched. The measured results achieved have been supported by COMSOL modelling and are comparable with the performance of interdigitated touch pads by other groups, which have often been produced with more costly fabrication techniques.

The sensors were found to be compatible with a large range of users who have different body types and they produced a distinct, measurable change in capacitance when touched. Increasing both the force of touch and the contact area between the finger and touch pad was found to increase the change in capacitance when touched owing to the increase in relative permittivity. The touch pads were also found to be proximity sensitive, however only in regions close to the touch pad.

As paper is hygroscopic, the effect of humidity on the interdigitated sensors was considered. All of the designs were humidity sensitive, with approximately a 50% increase in capacitance from 40 to 90% relative humidity. It was found that the larger area touch pads had a larger change in capacitance with humidity due to the larger water intake and therefore the larger change in relative permittivity of the substrate. This increase in capacitance is lower than the change when the device was touched, but should still be taken into consideration when used in applications.

## References

- [1] S. Kanaparthi and S. Badhulika, "Solvent-free fabrication of paper based all-carbon disposable multifunctional sensors and passive electronic circuits," *Royal Society of Chemistry Advances*, vol. 6, no. 98, p. 95574, 2016.
- [2] S. Olberding, N.-W. Gong, J. Tiab, J. A. Paradiso, and J. Steimle, "A cuttable multi-touch sensor," *Proceedings of the 26th Annual ACM Symposium on User Interface Software and Technology*, p. 245, 2013.
- [3] H. E. Nilsson, T. Unander, J. Siden, H. Andersson, A. Manuilskiy, M. Hummelgard, and M. Gulliksson, "System integration of electronic functions in smart packaging applications," *IEEE Transactions on Components, Packaging and Manufacturing Technology*, vol. 2, no. 10, p. 1723, 2012.
- [4] A. D. Mazzeo, W. B. Kalb, L. Chan, M. G. Killian, J. F. Bloch, B. A. Mazzeo, and G. M. Whitesides, "Paper-based, capacitive touch pads," *Advanced Materials*, vol. 24, no. 21, p. 2850, 2012.
- [5] B. K. Mishra, B. S. Choudhary, and T. Bakshi, "Touch based digital ordering system on Android using GSM and Bluetooth for restaurants," *12th IEEE International Conference on Electronics, Energy, Environment, Communication, Computer, Control*, 2016.

- [6] K. Lee, J. Lee, G. Kim, Y. Kim, S. Kang, S. Cho, S. G. Kim, J. K. Kim, W. Lee, D. E. Kim, S. Kang, D. E. Kim, T. Lee, and W. Shim, "Rough-surface-enabled capacitive pressure sensors with 3D touch capability," *Small*, vol. 13, no. 43, p. 38, 2017.
- [7] A. McPherson, "TouchKeys: Capacitive multi-touch sensing on a physical keyboard," *Proceedings of the International Conference on New Interfaces for Musical Expression*, 2012.
- [8] J. Qi and L. Buechley, "Electronic Popables: Exploring paper-based computing through an interactive pop-up book," *International Conference on Tangible, Embedded and Embodied Interaction*, p. 121, 2010.
- [9] J. Wang, X. Zhang, X. Huang, S. Wang, Q. Qian, W. Du, and Y. Wang, "Forced assembly of water-dispersible carbon nanotubes trapped in paper for cheap gas sensors," *Small*, vol. 9, no. 22, p. 3759, 2013.
- [10] H.-L. Cindy, A. Dementyev, J. A. Paradiso, H.-L. C. Kao, A. Dementyev, J. A. Paradiso, and C. Schmandt, "NailO: Fingernails as an input surface," *Proceedings of the Annual ACM Conference on Human Factors in Computing Systems*, 2015.
- [11] L. Chan, R.-H. Liang, M.-C. Tsai, K.-Y. Cheng, C.-H. Su, M. Y. Chen, W.-H. Cheng, and B.-Y. Chen, "FingerPad: Private and subtle interaction using fingertips," *Proceedings of the 26th Annual ACM Symposium on User Interface Software and Technology*, p. 255, 2013.
- [12] P. Dietz and D. Leigh, "DiamondTouch: A multi-user touch technology," *Proceedings of the Annual ACM Symposium on User Interface Software and Technology*, p. 219, 2001.
- [13] V. Savage, X. Zhang, and B. Hartmann, "Midas: Fabricating custom capacitive touch sensors to prototype interactive objects," *Proceedings of the 25th Annual ACM Symposium on User Interface Software and Technology*, p. 579, 2012.
- [14] C. Holz and P. Baudisch, "Understanding touch," *Proceedings of the Annual ACM Conference on Human Factors in Computing Systems*, p. 2501, 2011.
- [15] C. K. Devi and M. N. Sundaram, "Design and simulation of MEMs based sensor for artificial hand," *Proceedings of the 2013 COMSOL Conference in Bangalore*, 2013.
- [16] A. Talarico, M. Malvezzi, and D. Prattichizzo, "Modelling the human touch: A FEM model of the human hand fingertips for haptic application," *Proceedings of the 2014 COMSOL Conference in Cambridge*, 2014.
- [17] S. Choi, S. Eom, M. M. Tentzeris, and S. Lim, "Inkjet-printed electromagnet-based touchpad using spiral resonators," *Journal of Microelectromechanical Systems*, vol. 25, no. 5, p. 947, 2016.
- [18] M. Bhattacharjee and D. Bandyopadhyay, "Simple and economic paper based graphitic touch-pad for multipurpose applications," *The Electrochemical Society: InMeeting Abstracts*, no. 14, p. 892, 2016.
- [19] A. Rahbar, M. Rahbar, and B. L. Gray, "Flexible touchpads based on inductive sensors using embedded conductive composite polymer," *Nanosensors, Biosensors, and Info-tech Sensors and Systems*, vol. 9060, 2014.
- [20] R. K. Kramer, C. Majidi, and R. J. Wood, "Wearable tactile keypad with stretchable artificial skin," *Proceedings - IEEE International Conference on Robotics and Automation*, p. 1103, 2011.
- [21] X. Zou, T. Liang, N. Lopez, M. Ahmed, A. Ajayan, and A. Mazzeo, "Arrayed force sensors made of paper, elastomer, and hydrogel particles," *Micromachines*, vol. 8, no. 12, p. 356, 2017.
- [22] Y.-H. Wang, X. Li, C. Zhao, and X. Liu, "A paper-based piezoelectric touch pad integrating zinc oxide nanowires," *IEEE International Conference on Micro Electro Mechanical Systems*, p. 781, 2014.
- [23] S. Emamian, B. B. Narakathu, A. A. Chlaihawi, and M. Z. Atashbar, "Fabrication and characterization of piezoelectric paper based device for touch and force sensing applications," *Proceedings of the 30th anniversary Eurosensors Conference, Budapest, Hungary*, vol. 168, p. 688, 2016.
- [24] R. Li, A. Hu, T. Zhang, and K. D. Oakes, "Direct Writing on Paper of Foldable Capacitive Touch Pads with Silver Nanowire Inks," *ACS Applied Materials and Interfaces*, vol. 6, p. 21721, 2014.
- [25] B. S. F. Martinot, F. Giraud, P. Plénacoste, K. Talbi, N. Tiercelin, C. Chaillou, and P. Pernod, "Touch analysis and tactile device design: An overview of 'STIMTAC' project," *Proceedings of Virtual Concept, Biarritz, France*, 2005.
- [26] S. Emamian, B. B. Narakathu, A. A. Chlaihawi, B. J. Bazuin, and M. Z. Atashbar, "Screen printing of flexible piezoelectric based device on polyethylene terephthalate (PET) and paper for touch and force sensing applications," *Sensors and Actuators, A: Physical*, vol. 263, p. 639, 2017.
- [27] Q. Zhong, J. Zhong, X. Cheng, X. Yao, B. Wang, W. Li, N. Wu, K. Liu, B. Hu, and J. Zhou, "Paper-based active tactile sensor array," *Advanced Materials*, vol. 27, no. 44, p. 7130, 2015.
- [28] G. Buchberger, R. Schwödiauer, and S. Bauer, "Flexible large area ferroelectret sensors for location sensitive touchpads," *Applied Physics Letters*, vol. 92, no. 12, 2008.
- [29] C. Rendl, P. Greindl, and M. Haller, "PyzoFlex: printed piezoelectric pressure sensing foil," *Proceedings of the Annual ACM Symposium on User Interface Software and Technology*, p. 509, 2012.
- [30] Z. Cui, F. R. Poblete, G. Cheng, S. Yao, X. Jiang, and Y. Zhu, "Design and operation of silver nanowire based flexible and stretchable touch sensors," *Journal of Materials Research*, vol. 30, no. 1, p. 79, 2014.
- [31] H. Tian, Y. Yang, D. Xie, T.-L. Ren, Y. Shu, C.-J. Zhou, H. Sun, X. Liu, and C.-H. Zhang, "A novel flexible capacitive touch pad based on graphene oxide film," *Nanoscale*, vol. 5, p. 890, 2013.

- [32] H. Manabe and W. Yamada, "A capacitive touch sensing technique with series-connected sensing electrodes," *Proceedings of the Annual ACM Symposium on User Interface Software and Technology*, 2017.
- [33] J. Kim, J. H. Jong, and W. S. Kim, "Repeatedly bendable paper touch pad via direct stamping of silver nanoink with pressure-induced low-temperature annealing," *IEEE Transactions on Nanotechnology*, vol. 12, no. 6, p. 1139, 2013.
- [34] T. Yun, S. Member, S. Eom, and S. Lim, "Paper-based capacitive touchpad using home inkjet printer," *Journal of Display Technology*, vol. 12, no. 11, p. 1411, 2016.
- [35] M. T. Rahman, A. Rahimi, S. Gupta, and R. Panat, "Microscale additive manufacturing and modelling of interdigitated capacitive touch sensors," *Sensors and Actuators, A: Physical*, vol. 248, p. 94, 2016.
- [36] A. V. Mamishev, "Interdigital Sensors and Transducers," *Proceedings of the IEEE*, vol. 92, no. 5, p. 808, 2004.
- [37] D. L. Ma, Y. Ma, Z. W. Chen, and A. M. Hu, "A silk fabric derived carbon fibre net for transparent capacitive touch pads and all-solid supercapacitors," *Journal of Material Chemistry A*, p. 20608, 2017.
- [38] S. Kanaparthi and S. Badhulika, "Low cost, flexible and biodegradable touch sensor fabricated by solvent-free processing of graphite on cellulose paper," *Sensors and Actuators B: Chemical*, vol. 242, p. 857, 2016.
- [39] J. M. Nassar, M. D. Cordero, A. T. Kutbee, M. A. Karimi, G. A. T. Sevilla, A. M. Hussain, A. Shamim, and M. M. Hussain, "Paper skin multisensory platform for simultaneous environmental monitoring," *Advanced Materials Technologies*, 2016.
- [40] C. L. Dai, "A capacitive humidity sensor integrated with micro heater and ring oscillator circuit fabricated by CMOS-MEMS technique," *Sensors and Actuators, B: Chemical*, vol. 122, no. 2, p. 375, 2007.
- [41] N. Kidner, Z. Homrighaus, T. Mason, and E. Garboczi, "Modeling interdigital electrode structures for the dielectric characterization of electroceramic thin films," *Thin Solid Films*, vol. 496, no. 2, p. 539, 2006.
- [42] I. G. Petrou, E.-E. Betsi, P. Schertenleib, and A. Gray, "Lipofilling: A promising tool for digital pulp reconstruction," *European Journal of Plastic Surgery*, vol. 40, no. 6, p. 587, 2017.
- [43] F. W. Memon, "Results of vertical figure-of-eight tension band suture for finger nail disruptions with fractures of distal phalanx," vol. 46, p. 346, 2012.
- [44] K. Dandekar, B. I. Raju, and M. A. Srinivasan, "3-D finite-element models of human and monkey fingertips to investigate the mechanics of tactile sense," *Journal of Biomechanical Engineering*, vol. 125, no. 5, p. 682, 2003.
- [45] A. Buryanov and V. Kotiuk, "Proportions of hand segments," *International Journal of Morphology*, vol. 28, no. 3, p. 755, 2010.
- [46] <https://emedicine.medscape.com/article/1294744-overview>. Accessed: 2017-10-05.
- [47] C. Gabriel, R. W. Lau, and C. Gabriel, "The dielectric properties of biological tissues: III. Parametric models for the dielectric spectrum of tissues," *Physics in Medicine & Biology*, vol. 41, p. 2271, 1996.
- [48] T. Instruments, "FDC2214 Capacitance-to-Digital Converter Technical Datasheet," 2015.
- [49] R. Gomez and S. McLaren, "The effects of reward and punishment on response disinhibition, moods, heart rate and skin conductance level during instrumental learning," *Personality and Individual Differences*, vol. 23, no. 2, p. 305, 1997.

## Chapter 6

# Paper-based Microwave Transmission Lines

### 6.1 Introduction

The work in this chapter aims at designing and characterising microwave transmission lines, screen printed on Neenah paper, in the frequency range 300 kHz–3 GHz. Transmission lines are the building blocks for many microwave circuits and can be used to determine the working range of parameters, such as characteristic impedance and propagation velocity, and any losses that may arise from the ink and paper combination. Coplanar waveguides (CPW) have been chosen as they are printed only on one side, so simplifying the printing process. The chapter first details the theory on transmission lines, discussed in detail in [1], which closely follows Heaviside’s approach [2]. The effect of humidity was also considered as the hygroscopic nature of paper will affect the operation of CPWs at different humidity levels.

As detailed in Chapter 1, when discussing paper-based devices, radio frequency identification (RFID) tags and antennas are common high frequency devices to be created on paper. These devices often operate around the MHz frequency range to be used with WiFi or bluetooth components. Devices operating at microwave frequencies are required to be smaller and so paper is often unsuitable owing to the less accurate and larger feature sizes. However, there is a great deal of literature on the topic of microwave devices if paper is disregarded [1, 3–9]. Paper-based microwave devices result in a thinner substrate which has lower permittivity when compared to traditional microwave components. This leads to a higher propagation velocity but also a higher characteristic impedance as shown in the

results for this chapter. Paper is also hygroscopic so in environments with varying humidity, the permittivity of the substrate will vary between 3.25 and 80, the effects of this are highlighted within this chapter.

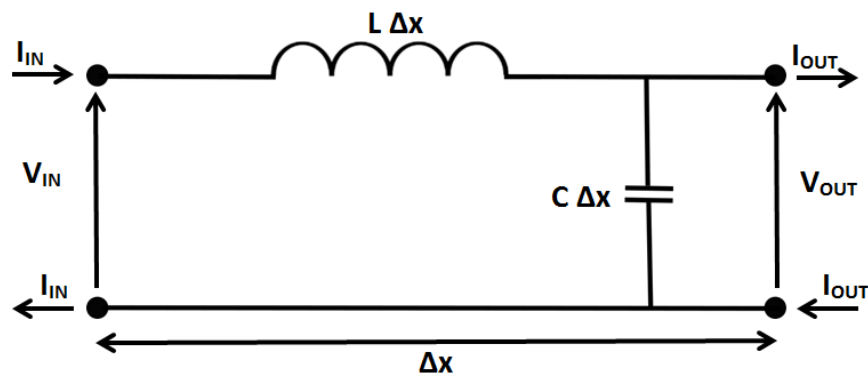
Printed resonators can be used to measure the permittivity of paper and plastic substrates [10, 11]. Sahu et al. take this a step further by determining both the dielectric properties of flexible substrates and the conductive properties of the deposited metal [12].

Coplanar waveguides are an example of microwave devices, made up of two ground planes and a signal track in between with a gap either side [13]. They have an advantage over other structures like microstrips as everything can be fully printed on one side of the substrate. Examples of touch pads using coplanar waveguides on paper are presented in [14–17]. A serpentine transmission line covers a large area and a touch event causes a change in the local impedance of the waveguide, generating a reflection of the signal towards the input.

## 6.2 Transmission Line Theory

### 6.2.1 Lossless Transmission Line

An ideal transmission line provides a link between two points where the voltage and current changes are transmitted instantly with no losses. In most of the literature an ideal transmission line is considered as two linear, lossless and infinitely long conducting wires running parallel to each other. The simple model used for an ideal transmission line with no losses is shown in Figure 6.1, where the line has been split into several sections  $\Delta x$  long, each with a corresponding series inductance, due to the wire, and a parallel capacitance, due to the coupling between the two wires.



**Figure 6.1:** Simple model for an ideal transmission line. Two parallel, lossless wires of infinite length were split into sections made up of series inductance  $L$  and parallel capacitance  $C$  per unit length.

At low frequencies, it is possible to ignore this inductance and capacitance. However, at microwave

frequencies, these values must be taken into account. The voltage across the inductor and the current through the capacitor can be determined by Equations (6.1) and (6.2) respectively.

$$V_L = L\Delta x \frac{\partial I(x, t)}{\partial t} = V(x, t) - V(x + \Delta x, t) \quad (6.1)$$

$$\begin{aligned} I_C &= C\Delta x \frac{\partial V(x + \Delta x, t)}{\partial t} \simeq C\Delta x \frac{\partial}{\partial t} \left[ V(x, t) + \frac{\partial V(x, t)}{\partial x} \Delta x \right] \\ &= C\Delta x \frac{\partial V(x, t)}{\partial t} + C \frac{\partial}{\partial t} \left[ \frac{\partial V(x, t)}{\partial x} \right] \Delta x^2 \\ &\simeq C\Delta x \frac{\partial V(x, t)}{\partial t} = I(x, t) - I(x + \Delta x, t) \end{aligned} \quad (6.2)$$

where  $V$  and  $I$  are the amplitudes of the voltage and current waves propagating along the line respectively,  $L$  and  $C$  are the series inductance and parallel capacitance of the transmission line per unit length respectively,  $x$  is the length of the transmission line and  $t$  is time. Dividing Equations (6.1) and (6.2) by  $\Delta x$  and taking the limit  $\Delta x \rightarrow 0$  results in the Telegrapher's equations, which were developed by Oliver Heaviside in the 19<sup>th</sup> century [2]:

$$L \frac{\partial I}{\partial t} = - \frac{\partial V}{\partial x} \quad (6.3)$$

$$C \frac{\partial V}{\partial t} = - \frac{\partial I}{\partial x} \quad (6.4)$$

Taking the derivative of Equation (6.3) with respect to  $x$  and the derivative of Equation (6.4) with respect to  $t$ , we obtain the wave equation:

$$\frac{\partial^2 V}{\partial t^2} = \frac{1}{LC} \frac{\partial^2 V}{\partial x^2} \quad (6.5)$$

Applying the reverse procedure to Equations (6.3) and (6.4), we obtain:

$$\frac{\partial^2 I}{\partial t^2} = \frac{1}{LC} \frac{\partial^2 I}{\partial x^2} \quad (6.6)$$

The propagation velocity ( $v$ ) of the voltage and current waves is given by:

$$v = \frac{1}{\sqrt{LC}} \quad (6.7)$$



## 6.2.2 Characteristic Impedance

To determine the characteristic impedance of a transmission line, an infinite lossless transmission line was considered. The Telegrapher's equations state that to support an oscillating voltage, an oscillating current is required. Assuming there is a constant relationship between the two sinusoidal signals propagating in the forward direction:  $V_+(\omega) = Z_0(\omega)I_+(\omega)$  where  $Z_0$  is the characteristic impedance,  $V_+$  and  $I_+$  are the amplitudes of the voltage and current signals propagating in the forward direction and  $V = V_+e^{-i\beta x}e^{i\omega t}$  and  $I = I_+e^{-i\beta x}e^{i\omega t}$ , the second Telegrapher's equation (Equation (6.4)) can be written as:

$$i\omega CV_+e^{-i\beta x}e^{i\omega t} = i\beta I_+e^{-i\beta x}e^{i\omega t} \quad (6.8)$$

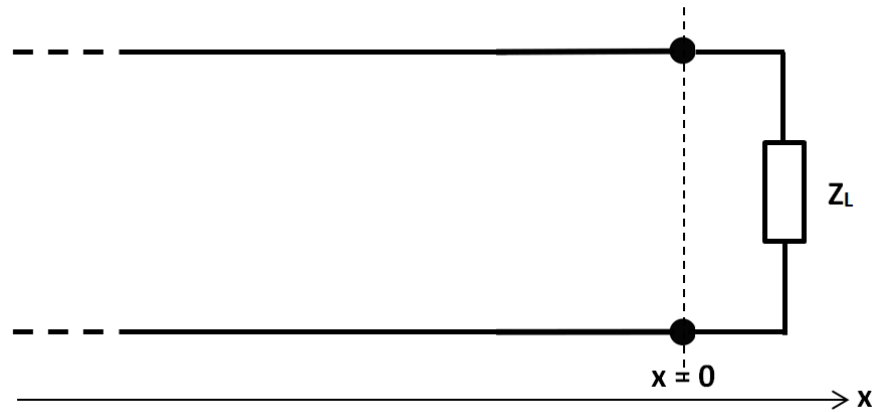
where  $\beta$  is the phase constant of the signals. Simplifying, using Equation (6.7) and  $\beta = \omega/v$ , Equation (6.8) can be re-written as:

$$V_+ = \sqrt{\frac{L}{C}}I_+ \quad (6.9)$$

Therefore, the characteristic impedance is equal to:

$$Z_0 = \sqrt{\frac{L}{C}} \quad (6.10)$$

When a transmission line is terminated with a complex load impedance,  $Z_L$  as shown in Figure 6.2, part of the voltage and current signals is reflected and part is dissipated by the load.



**Figure 6.2:** Simple model for an ideal transmission line terminated with a load impedance  $Z_L$

The overall voltage and current is the sum of the forward and reflected waves. At the point of the load impedance, when  $x = 0$ , the ratio between the voltage and current is set by the load impedance:

$$\frac{V(0, t)}{I(0, t)} = \frac{V_+ + V_-}{V_+ - V_-} Z_0 = Z_L \quad (6.11)$$

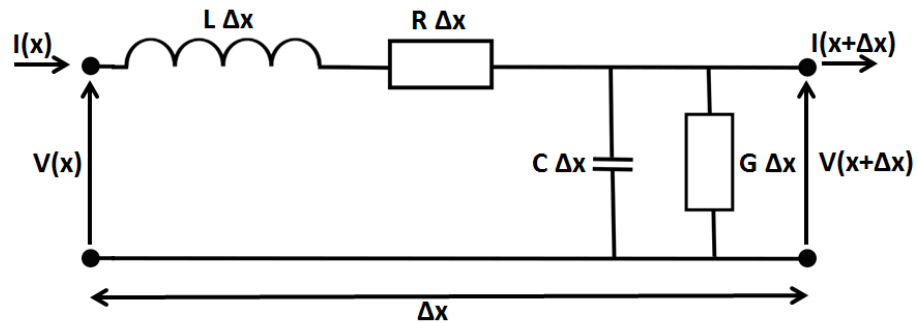
where  $V_-$  is the amplitude of the reflected voltage signal. This leads to a relationship between the forward and reflected voltage amplitudes  $V_+$  and  $V_-$ :

$$V_- = \frac{Z_L - Z_0}{Z_L + Z_0} V_+ = \Gamma V_+ \quad (6.12)$$

where  $\Gamma$  is the reflection coefficient. When  $Z_L$  is equal to a short circuit, the reflection coefficient is equal to -1. When  $Z_L$  is equal to an open circuit, the reflection coefficient is equal to 1 and total reflection occurs. When  $Z_L$  is equal to  $Z_0$ , the transmission line is said to be terminated on a matched load and the reflection coefficient is equal to 0. In the final case, there is the same response as if it were an infinitely long transmission line.

### 6.2.3 Transmission Lines with Losses

Real transmission lines have power losses which must be accounted for, typically due to the finite resistance of the tracks and the substrate. These power losses can be accounted for by the series resistance of the tracks,  $R$ , and the shunt conductance of the dielectric substrate,  $G$ , resulting in the model shown in Figure 6.3.



**Figure 6.3:** Simple model for a real transmission line. Two parallel wires of infinite length are split into sections made up of series inductance  $L$ , resistance  $R$ , parallel capacitance  $C$  and conductance  $G$  per unit length.

If we limit this to the signal propagating in the forward direction (i.e.  $V = V_+ e^{-i\beta x} e^{i\omega t}$ , as we are considering the impedance). Equations (6.3) and (6.4) then become:

$$\gamma V_+ = Z(\omega) I_+ \quad (6.13)$$

$$\gamma I_+ = Y(\omega) V_+ \quad (6.14)$$

where, in a lossy line,  $Z(\omega)$  is the series impedance per unit length and is equal to  $(i\omega L + R)$ ,  $Y(\omega)$  is the shunt admittance per unit length and equal to  $(i\omega C + G)$  and  $\gamma$  is the propagation constant and

is equal to  $\gamma = \alpha + i\beta$ . In addition to the phase constant  $\beta$  (as in the lossless transmission line), there is now also the attenuation constant,  $\alpha$ , which results in a wave that decays exponentially along the direction of propagation.

Multiplying Equations (6.13) and (6.14) together, the propagation constant is then equal to  $\gamma = \sqrt{Z(\omega)Y(\omega)}$  and the characteristic impedance equal to  $Z_0 = \sqrt{Z(\omega)/Y(\omega)}$ . By substituting the series impedance and shunt admittance in terms of  $R, G, L$  and  $C$ , the propagation constant can be represented by:

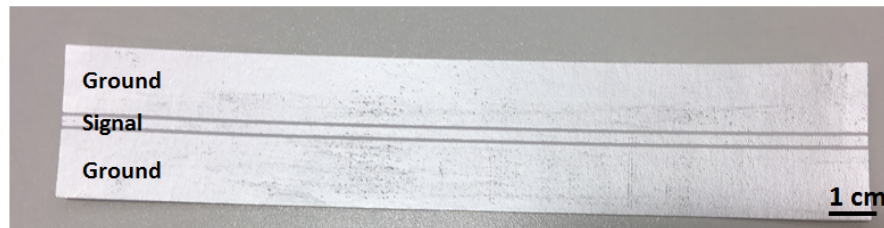
$$\begin{aligned}\gamma &= \sqrt{(i\omega L + R)(i\omega C + G)} \\ &= i\omega\sqrt{LC}\sqrt{1 - i\left(\frac{R}{\omega L} + \frac{G}{\omega C}\right) - \frac{RG}{\omega^2 LC}}\end{aligned}\quad (6.15)$$

In the limit of low losses ( $R \ll \omega L$  and  $G \ll \omega C$ ), the propagation constant can be approximated by:

$$\gamma \simeq i\omega\sqrt{LC} + \frac{1}{2}\left(R\sqrt{\frac{C}{L}} + G\sqrt{\frac{L}{C}}\right)\quad (6.16)$$

### 6.3 Transmission Line Parameter Extraction from Measured Scattering Parameters

An example of a screen-printed transmission line on matt paper is shown in Figure 6.4 (for information on the fabrication method, see Chapter 4). Metalon HPS-021LV silver-flake ink was used in this case as it has a high conductivity which minimises losses and optimises transmission. Scattering parameters (s-parameters) were measured using a HP 8753C Vector Network Analyser (VNA).



**Figure 6.4:** Example transmission line geometry using the coplanar waveguide structure which includes a signal track and two ground planes all printed on one side of a paper substrate. This example is 17 cm long with 2 mm and 15 mm signal and ground track widths respectively.

The s-parameters can be calculated from the transmitted and reflected signals at ports 1 and 2 as shown in Figure 6.5 and Equation (6.17). Further detail on the operation of the VNA and signals a and b was presented previously in Chapter 2.

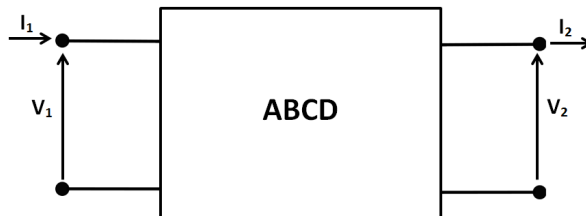


**Figure 6.5:** Illustration for transmitted and reflected signals for a two port microwave device, used to calculate the scattering parameters. This should be considered in conjunction with Equation (6.17).

$$\begin{bmatrix} b_1 \\ b_2 \end{bmatrix} = \begin{bmatrix} s_{11} & s_{12} \\ s_{21} & s_{22} \end{bmatrix} \begin{bmatrix} a_1 \\ a_2 \end{bmatrix} \quad (6.17)$$

where  $s_{11}$  and  $s_{22}$  are the ratios of reflected signal to the incident signal at port 1 and port 2 respectively,  $s_{12}$  is the ratio of the transmitted signal received at port 1 to the incident signal from port 2 and  $s_{21}$  is the ratio of the transmitted signal received at port 2 to the incident signal from port 1 [6].

The same network can also be defined or represented using the ABCD matrix, often known as the transmission matrix. The ABCD matrix is well suited to cascading two-port networks and has been used in this work for the conversion between s-parameters and the line parameters  $\alpha$ ,  $v$  and  $Z$ . The ABCD matrix can be defined by considering the input/output voltages and currents, as shown in Figure 6.6 and Equation (6.18) [5].



**Figure 6.6:** Illustration for the transmission (ABCD) matrix in terms of port 1 and 2 voltages and currents. This should be considered in conjunction with Equation (6.17).

$$\begin{bmatrix} V_1 \\ I_1 \end{bmatrix} = \begin{bmatrix} A & B \\ C & D \end{bmatrix} \begin{bmatrix} V_2 \\ I_2 \end{bmatrix} \quad (6.18)$$

The model for a transmission line with losses, described previously by Figure 6.3, using the series resistance, inductance and shunt capacitance, and conductance per unit length is a simple model of the lossy transmission line and in reality was not well suited to the transmission lines investigated here, so the line parameters were considered. The conversion from the s-parameters to the propagation velocity ( $v$ ), the losses ( $\alpha$ ) and the characteristic impedance ( $Z$ ) was not trivial. However, the reverse was much more straightforward.

The ABCD matrix for a transmission line can be determined from:

$$(ABCD) = \begin{bmatrix} \cos(g) & iZ_L \sin(g) \\ iZ_L^{-1} \sin(g) & \cos(g) \end{bmatrix} \quad (6.19)$$

where  $g = -i\gamma_L l = \beta l - i\alpha l$  and  $l$  is the physical length of the line [18]. The ABCD matrix can then be converted to the s-parameters using the conversion in [19].

In order to determine the line parameters, an initial guess of  $\alpha$ ,  $v$  and  $Z$  was determined, which was then converted to the ABCD matrix and the s-parameters. These calculated s-parameters were then compared to the measured ones. This process was repeated to minimise the error and determine line parameters to fit the data.

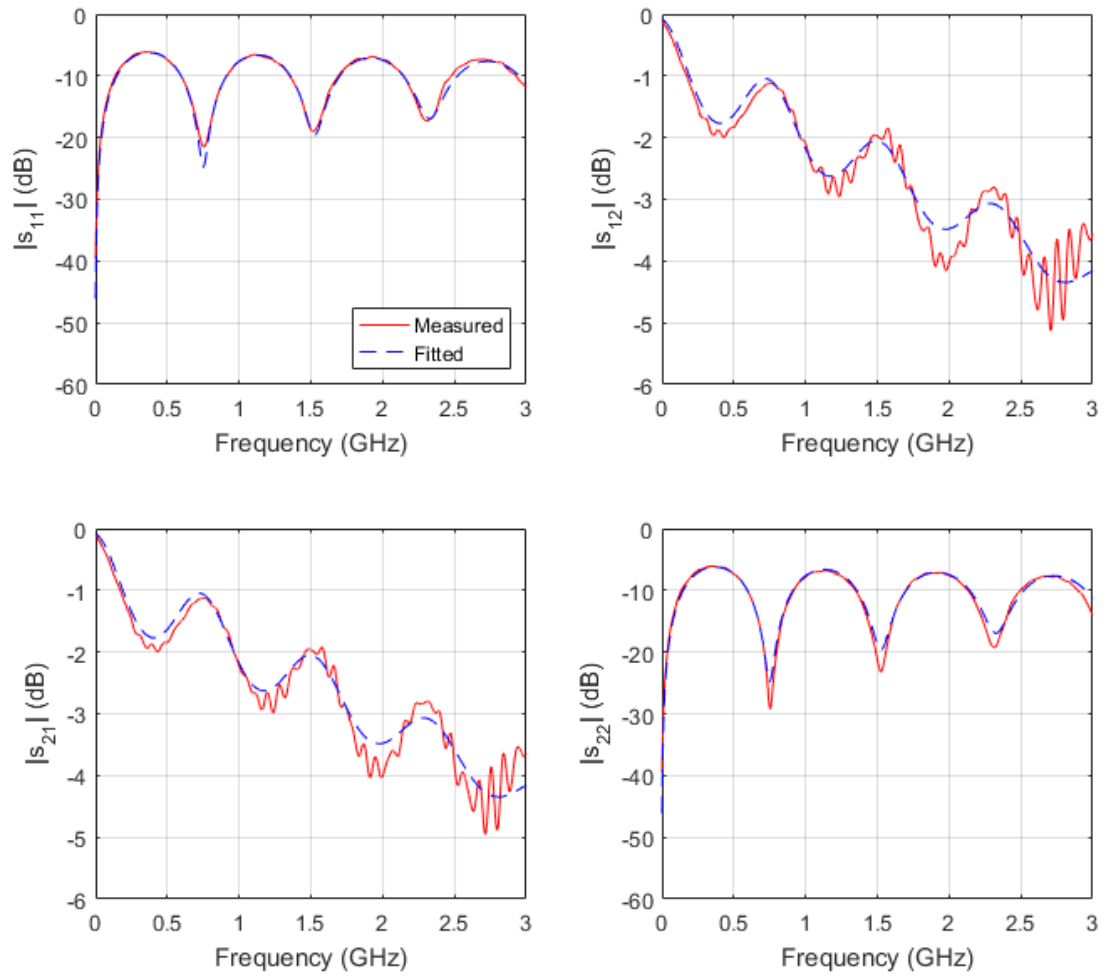
The Taylor's expansion of  $\alpha$ ,  $v$  and the magnitude and phase of  $Z$  with frequency using three coefficients were used as the initial guess for the calculated s-parameters:

$$\begin{aligned} \alpha &= \alpha_0 + \alpha_1 f + \alpha_2 f^2 \\ \beta &= \beta_0 + \beta_1 f + \beta_2 f^2 \\ Zr &= Zr_0 + Zr_1 f + Zr_2 f^2 \\ Zi &= Zi_0 + Zi_1 f + Zi_2 f^2 \end{aligned} \quad (6.20)$$

where  $f$  is the frequency and  $\alpha_{0-2}$ ,  $\beta_{0-2}$ ,  $Zr_{0-2}$  and  $Zi_{0-2}$  are the coefficients for the expansion of  $\alpha$ ,  $\beta$ , the real and imaginary parts of the characteristic impedance respectively.

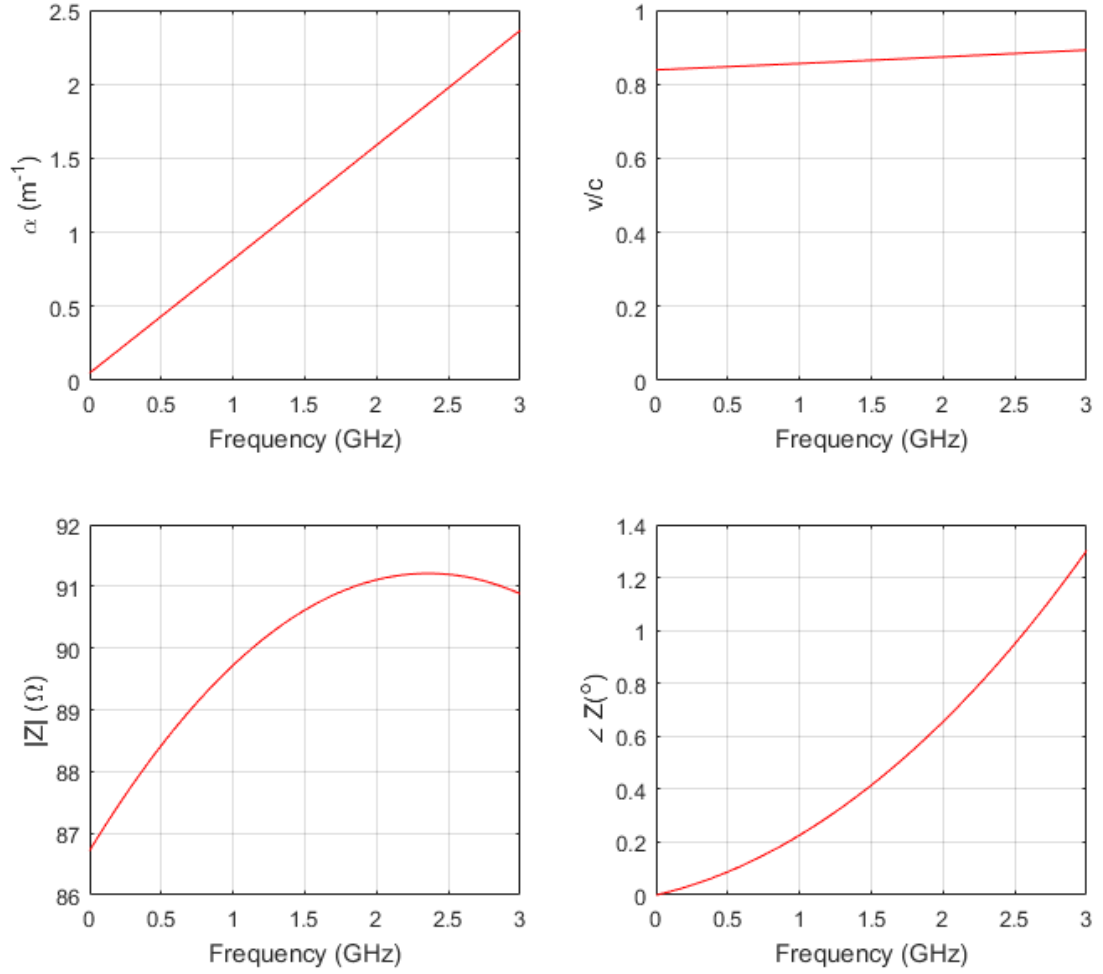
Using more than three coefficients was found to have negligible increase in the accuracy of the scattering parameter fit but resulted in an increase in computation time. The 'fminsearch' function in Matlab was utilised to minimise the error between the calculated and measured s-parameters to find the combination of  $\alpha$ ,  $\beta$ ,  $Zr$  and  $Zi$ , i.e. the function  $\|\mathbf{s}_c(f) - \mathbf{s}_e(f)\|$  is minimised, where  $\mathbf{s}_c(f)$  are the calculated s-parameters from the Taylor's expansion and  $\mathbf{s}_e(f)$  are the measured s-parameters. When the error is small, the values of the input parameters can be ascribed to those of the 'fitted' parameters.

Example measured and fitted s-parameter data are shown in Figure 6.7 for the geometry in Figure 6.4. It can be seen that the fitted data represent the measured data well and remove the calibration artefacts, smoothing the data.



**Figure 6.7:** Comparison of measured and fitted scattering parameters for a 17 cm long transmission line with a 2 mm wide signal track. The fitted scattering parameters have been constructed by taking an initial guess of the line parameters and calculating the ABCD matrix. From this, the s-parameters could be extracted and the error between these and the measured values limited.

The losses, propagation velocity and magnitude/phase of the characteristic impedance produced from the scattering parameters in Figure 6.7 can be seen in Figure 6.8.



**Figure 6.8:** Corresponding losses, propagation velocity and magnitude/phase of the characteristic impedance for the same transmission line as the results shown in Figure 6.7. These line parameters were constructed by the fitting algorithm detailed in the text.

The values for  $v$  and  $Z$  can easily be verified graphically. When the length of the transmission line is equal to  $n\lambda/2$ , transmission is at a maximum ( $|s_{11}|$  is a minimum and  $|s_{12}|$  is a maximum). The propagation velocity at this point was calculated to be  $0.85c$  at the first minimum of  $|s_{11}|$  (at  $0.75$  GHz) from  $\lambda = v/f = 2\pi/k$ . This is in agreement with Figure 6.8 where  $v = 0.86c$  at this point.

When the length of the transmission line is equal to  $\lambda/4$ ,  $Z_{eq} = Z_x^2/Z_0$ , where  $Z_{eq}$  is the equivalent characteristic impedance and  $Z_x$  is the characteristic impedance. The  $\lambda/4$  transformer equation:

$$s_{11} = \frac{Z_{eq} - Z_0}{Z_{eq} + Z_0} \quad (6.21)$$

can be rearranged to:

$$Z_x = Z_0 \sqrt{\frac{1 + s_{11}}{1 - s_{11}}} \quad (6.22)$$

Taking the first maximum of  $|s_{11}| = 6.1$  dB, where  $l = \lambda/4$ ,  $Z_x$  can be calculated to be  $86 \Omega$  which is

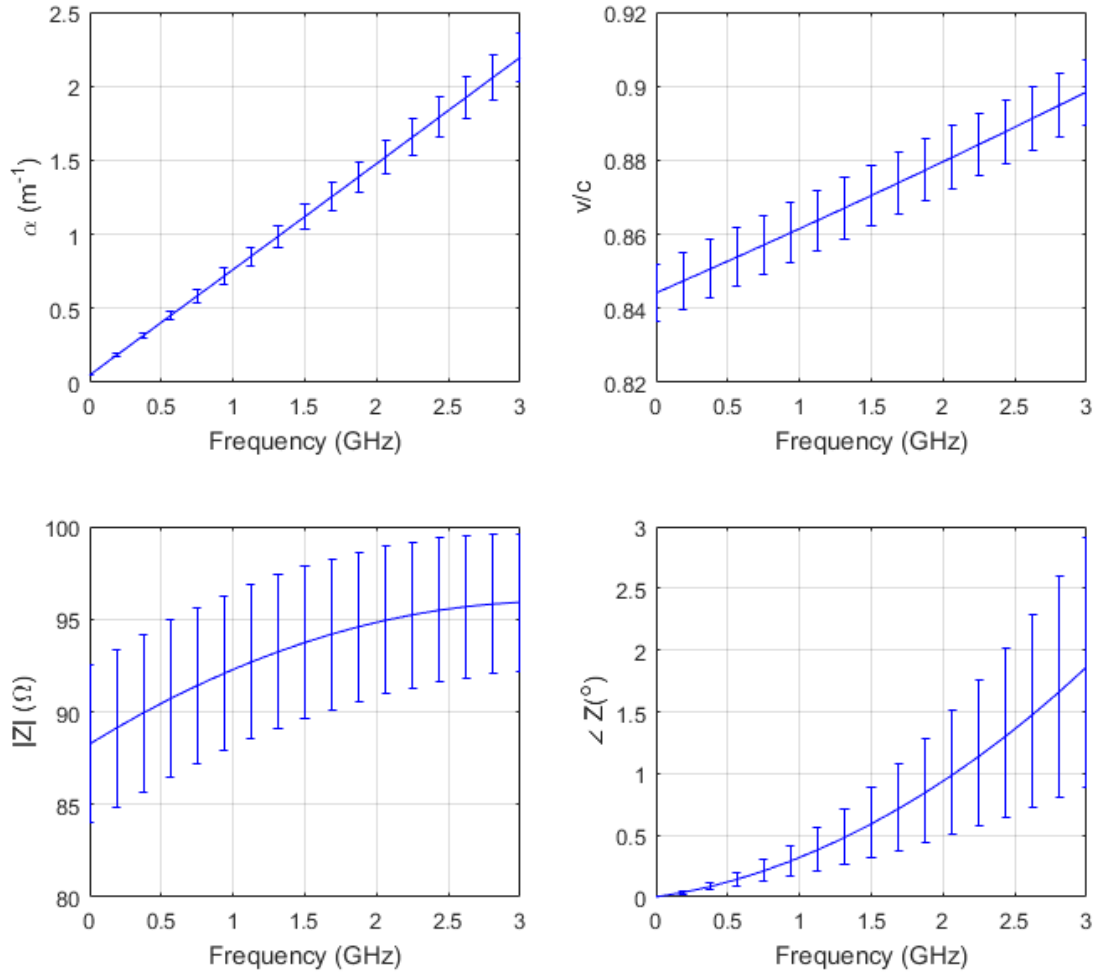
also in agreement with Figure 6.8. Although this is only true for real impedances, it can be used as a good estimate to verify the values obtained for the characteristic impedance.

Although many microwave components require a characteristic impedance of  $50\Omega$ , this is a somewhat arbitrary traditional value taken as a compromise for coaxial cables. In fact the value of characteristic impedance required will vary depending on the circuit requirements. The value for the characteristic impedance achieved for this work is the most convenient value within the limitations of the fabrication method. The ability to alter this characteristic impedance is of high importance when designing devices with multiple components.

## 6.4 Effect of Changing Transmission Line Parameters on the Transmission Line Response

The s-parameters and line parameters ( $\alpha$ ,  $v$  and  $Z$ ) for transmission lines with differing properties and geometries have been considered here to determine a working parameter range and the effect of varying parameters on transmission line response. The repeatability of the fabrication process is of key importance in device design. Ten identical transmission lines, 17 cm long with 2 mm and 15 mm signal and ground track widths respectively, as in (Figure 6.4), were measured and the extracted line parameters are shown in Figure 6.9.

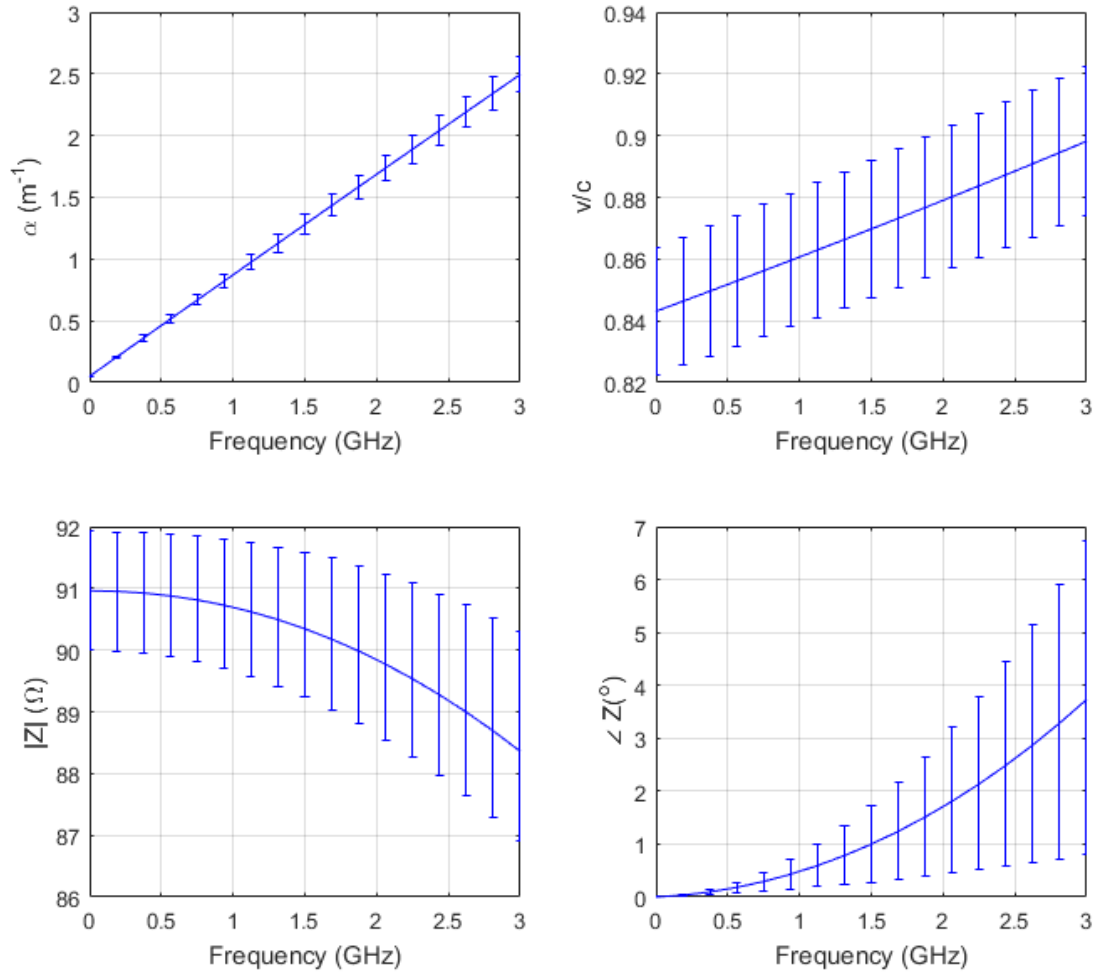




**Figure 6.9:** Line parameters of ten transmission lines with identical geometry to show repeatability of the devices. The maximum deviation is  $3\sigma$  from the magnitude of the characteristic impedance.

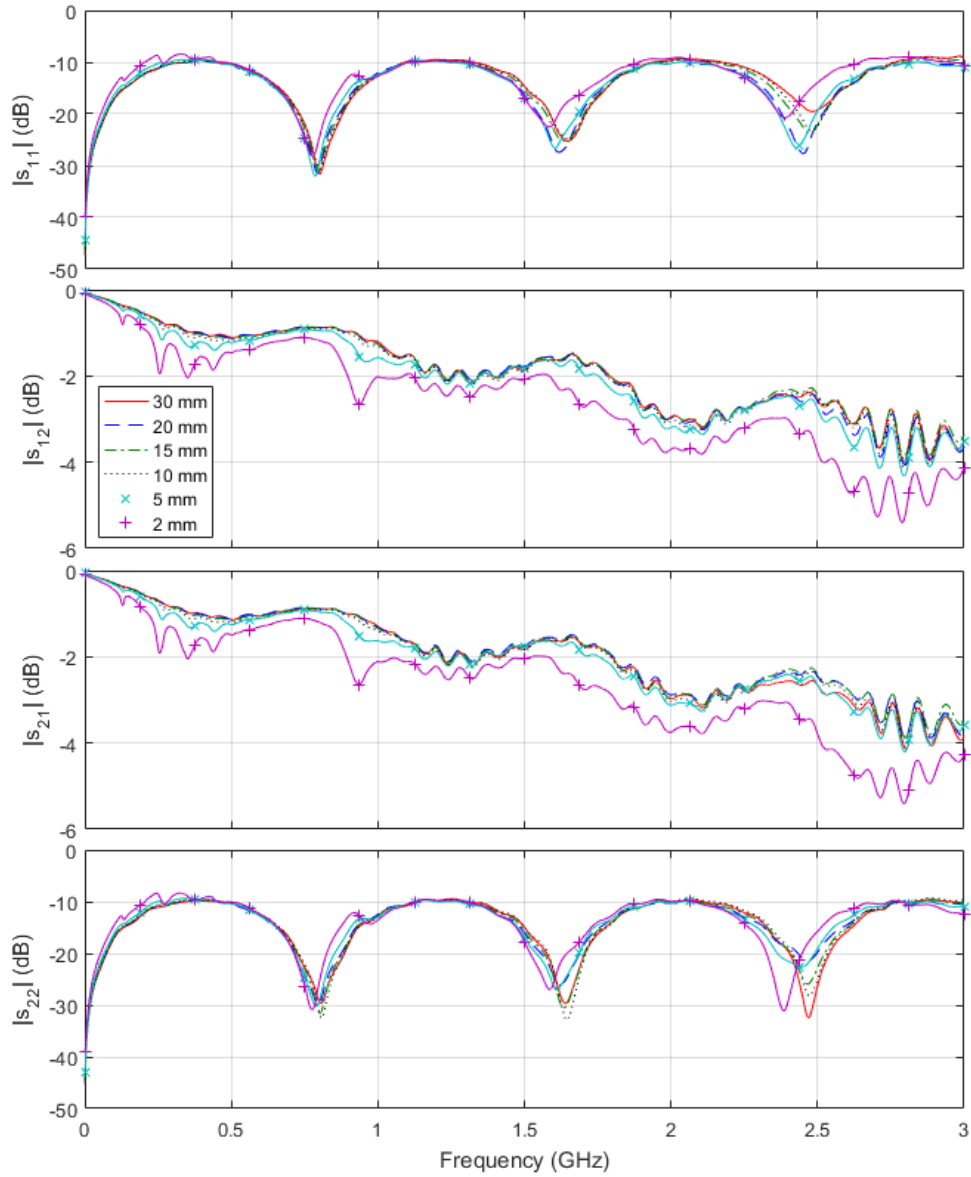
The scattering parameters when the same transmission line was measured ten times were identical and so the changes seen in Figure 6.9 were not due to fluctuations in the measurements. The error bars show the maximum and minimum values at each frequency for all of the data taken from the ten different transmission lines. Although the variations look large, for transmission lines on paper fabricated by screen printing, these were good results as they could be fully explained by the fabrication method. As detailed in Chapter 4, the variation for the fabrication method was 25%. The increase in variation with frequency was due to the larger change which could be more easily measured; the percentage change was the same.

The length had no effect on the line parameters, as shown in Figure 6.10 where an example transmission line was reduced in length from 17 to 5 cm in 2 cm steps. Again, any discrepancies were likely due to the fabrication method. If sections of the transmission line where the ink is much thinner are removed, then the response will differ accordingly. Lengths below 5 cm provided an unphysical response owing to the proximity of the connectors to each other.



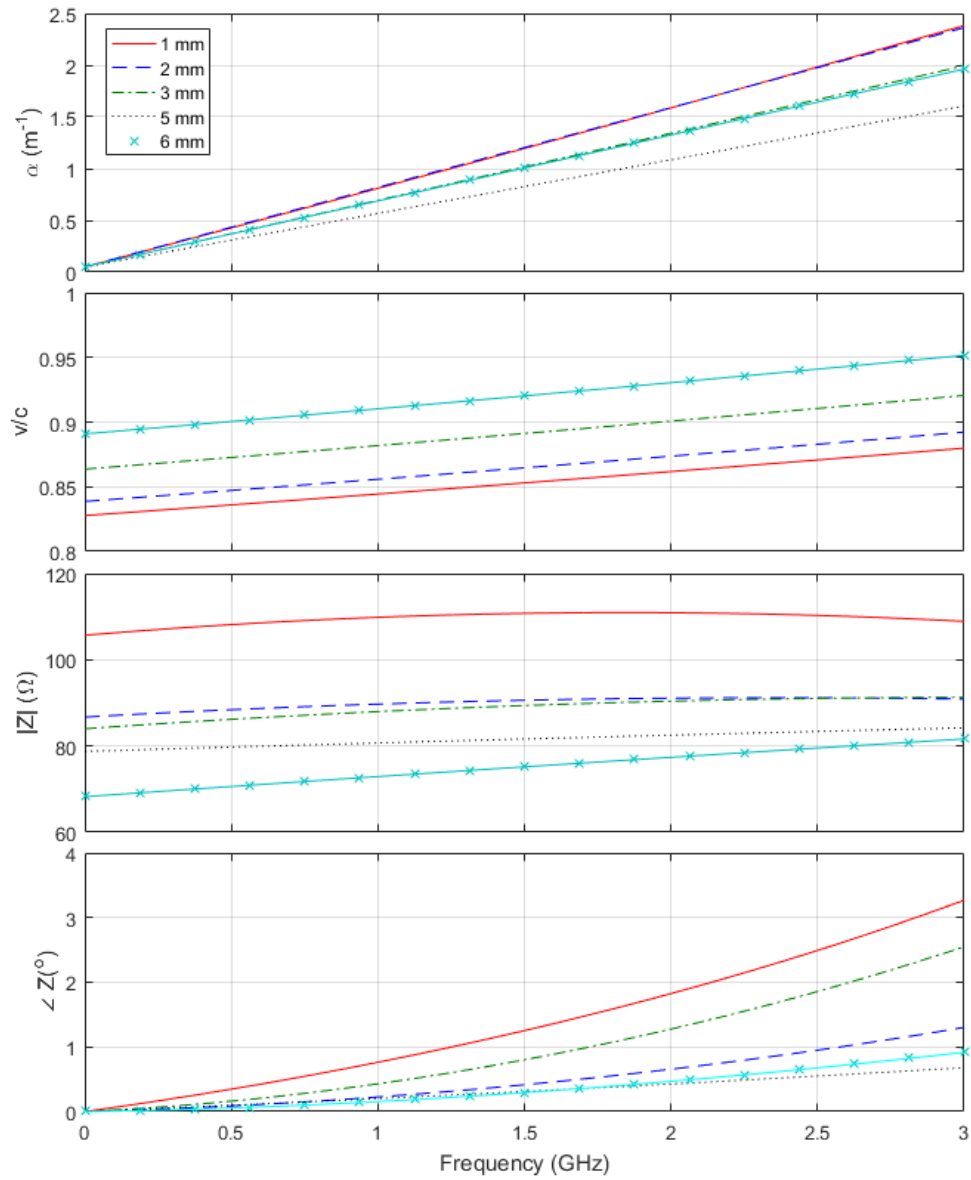
**Figure 6.10:** Line parameters of a transmission line with length varied between 17 and 5 cm in 2 cm steps. Results show a maximum deviation of  $2\sigma$  from the magnitude of the characteristic impedance.

The width of the ground plane also had negligible effect on the s-parameters or line parameters until sizes comparable with the gap between the signal and ground tracks, as seen in Figure 6.11. The s-parameters are presented rather than the line parameters, to highlight the noise added to the response as the ground width approaches that of the gap (1 mm). In theory, it is assumed that the ground plane is infinite and so is often designed to be as large as the device will allow; however, this increases costs and so is normally limited. It is shown here that ground planes above 10 mm, for a gap of 1 mm between the signal and ground track, are sufficient.



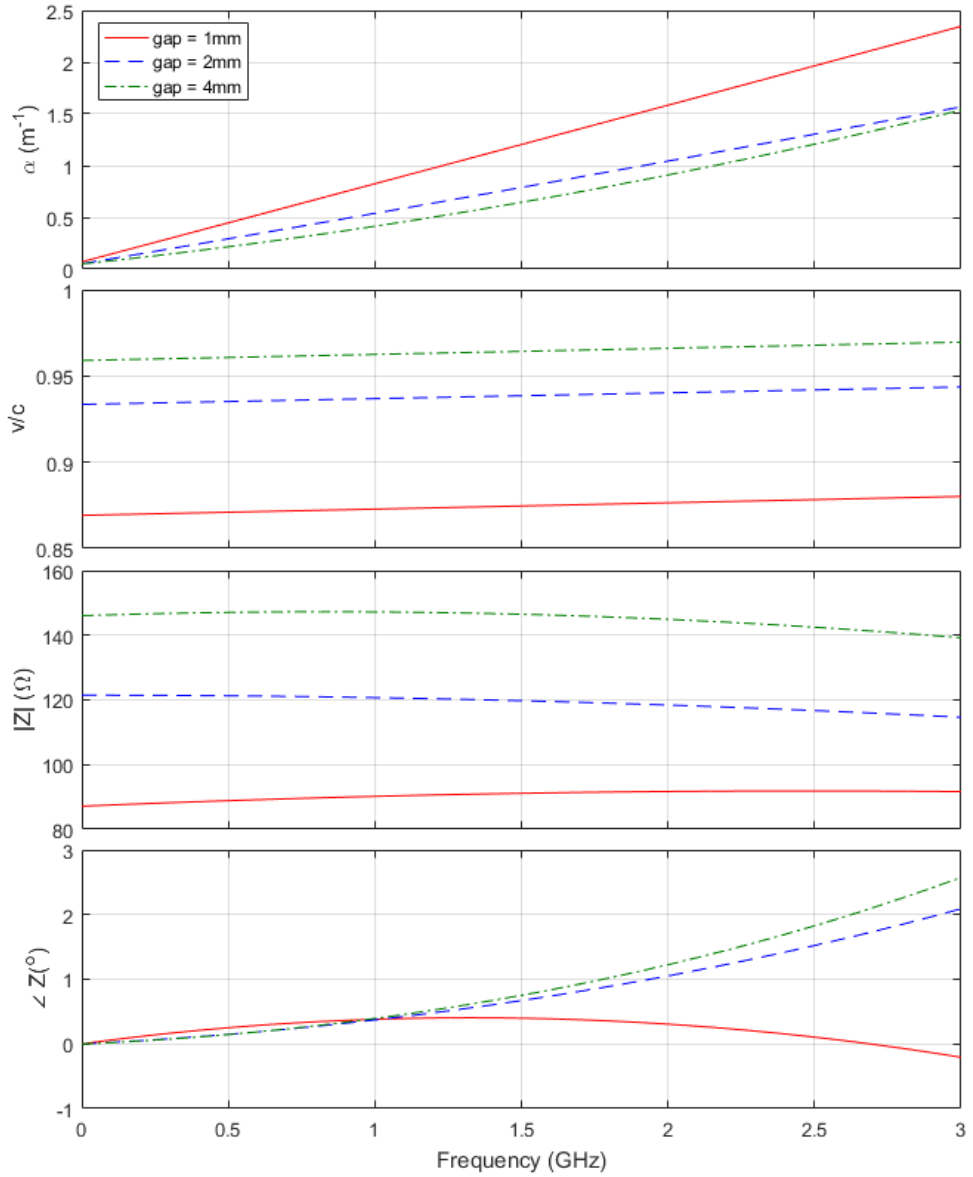
**Figure 6.11:** Scattering parameters of transmission line with ground plane width varied between 30 and 2 mm.

Unlike the ground plane, the signal track width was found, as expected, to alter the line parameters, with results shown in Figure 6.12. Increasing the signal track width increases the capacitance as there is a larger area for the electric field to interact between the signal and ground tracks. Increasing the signal track width causes the inductance to decrease because, as the track is increased, the magnetic field strength will decrease. The inductance decreases and the capacitance increases so, from Equation (6.10), the characteristic impedance will decrease. As can be seen from Figure 6.12, the propagation velocity increases with signal track width and so the decrease in inductance must dominate over the increase in capacitance, if Equation (6.7) is considered.



**Figure 6.12:** Line parameters of transmission lines with signal track widths of 1, 2, 3, 5 and 6 mm.

Varying the gap between the signal and ground tracks changes the capacitance per unit length of the transmission line; increasing the gap lowers the capacitance. From Equations (6.7) and (6.10), lowering the capacitance increases the characteristic impedance and the propagation velocity. This trend is seen in Figure 6.13. As the characteristic impedance is increased, the ratio between the voltage and current will increase and so the current will decrease. As the ohmic losses are directly linked to the current, the ohmic losses will decrease, as evident in Figure 6.13.

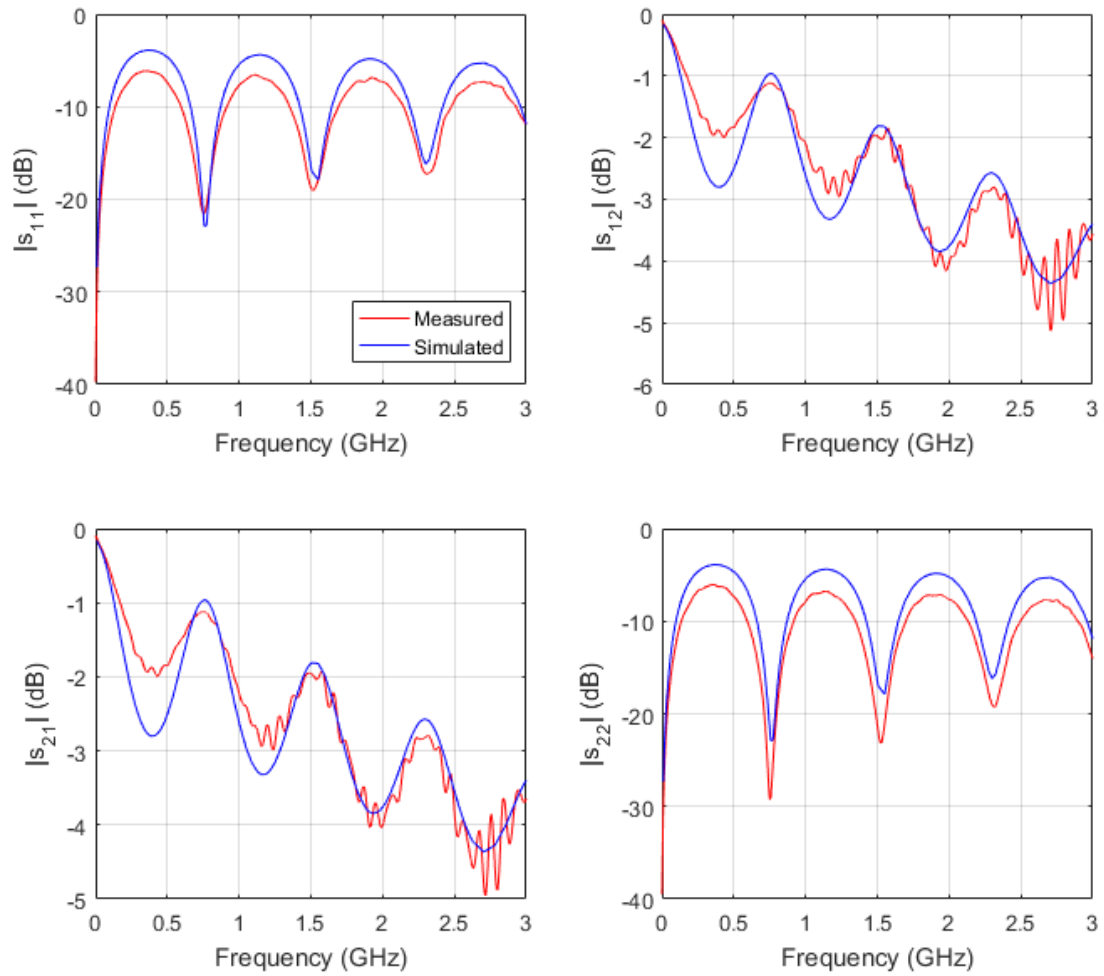


**Figure 6.13:** Line parameters of transmission lines with a gap between signal and ground of 1, 2 and 4 mm.

Agilent Advanced Design System (ADS) was used to simulate the effect of varying the substrate thickness and permittivity, as well as the metal thickness and conductivity, as these cannot be easily modified with fabricated samples. In all cases, the permittivity of the substrate was 3.25, the loss tangent was equal to 0.14, the thickness of the substrate was 235  $\mu\text{m}$ , the conductivity of the metal was  $4 \times 10^6$  S/m and the thickness of the metal was 16  $\mu\text{m}$ , unless stated otherwise. The length of the transmission line was 17 cm and the signal track width and ground plane were 2 and 15 mm respectively. The value of permittivity was decided based on measurements detailed earlier in Chapter 4.

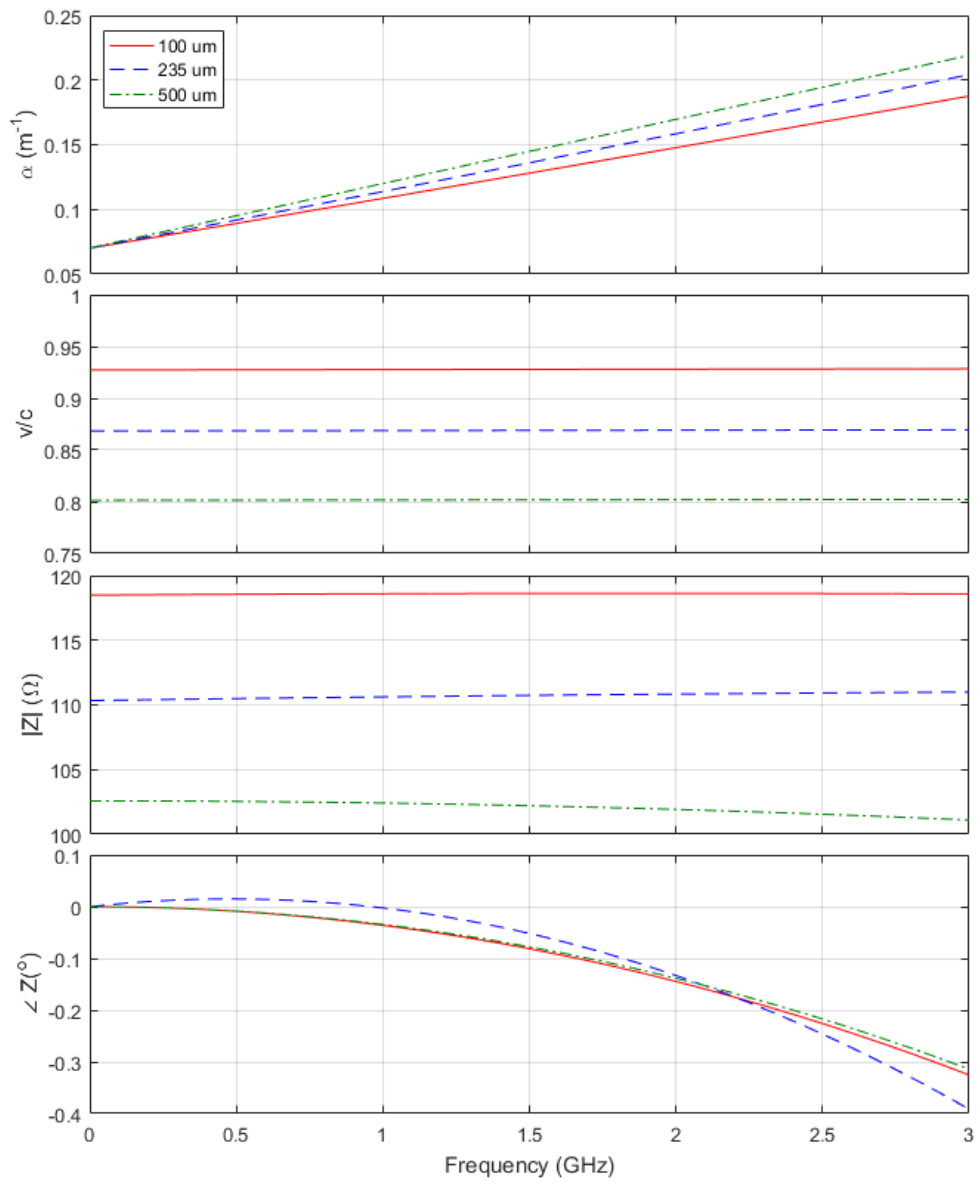
An example comparison of measured and simulated s-parameters is shown in Figure 6.14 using the parameters mentioned. It can be seen that the simulated data shows higher response in  $|s_{11}|$  and  $|s_{22}|$  when compared to the measured, meaning lower losses, which is expected from a simulated

transmission line. In the simulation software, all layers are assumed to be uniform, without defects and do not take into account the real-life complex geometries.

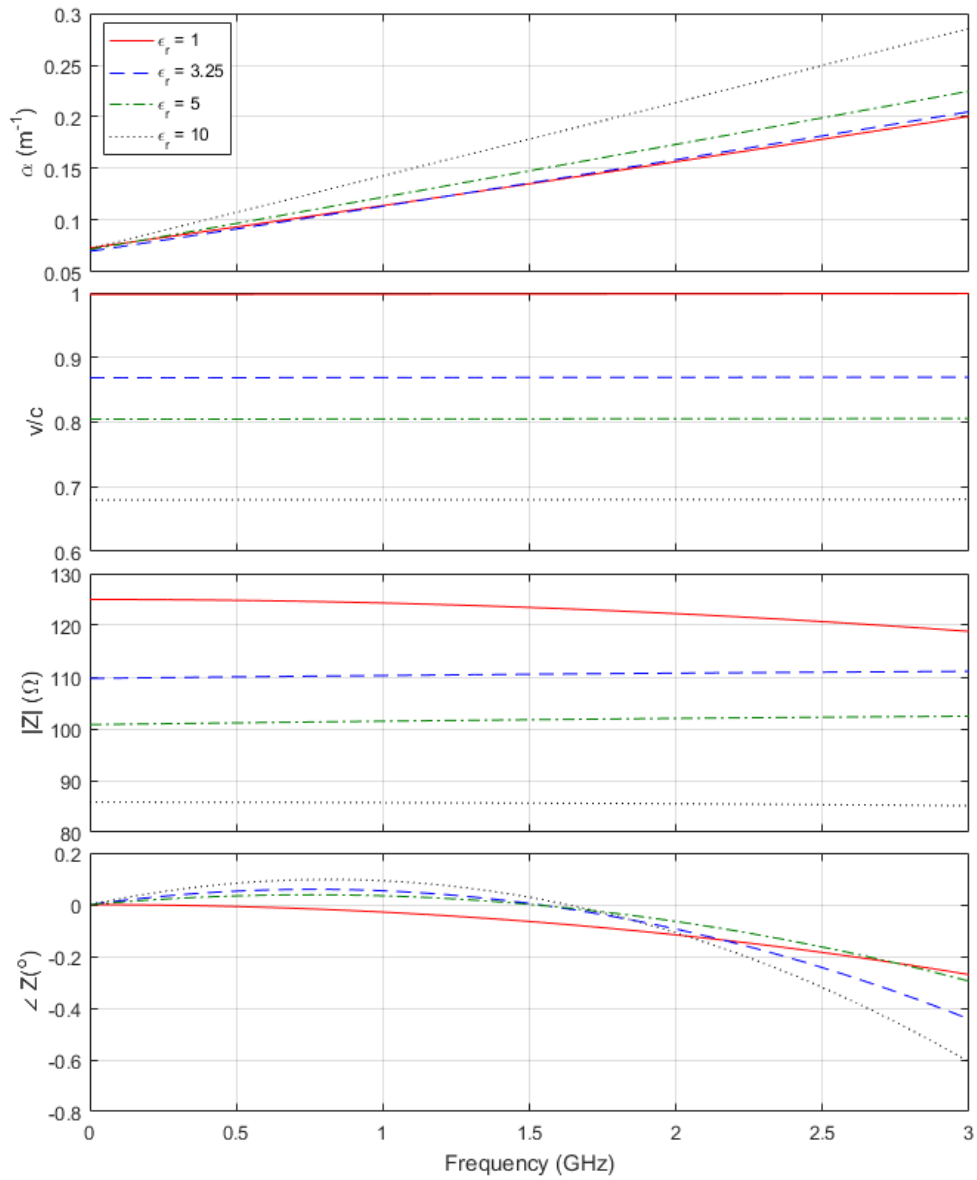


**Figure 6.14:** Comparison of measured and simulated scattering parameters for a transmission line that is 17 cm long with 2 mm signal track width and 15 mm ground track width.

Increasing the thickness of the substrate increases its effective permittivity and so these properties should be considered together. The increase in substrate permittivity with thickness is caused because a larger part of the electric field is contained in the substrate and not in air. This increase in effective permittivity will increase the capacitance and so, from Equations (6.7) and (6.10), the characteristic impedance and propagation velocity will decrease, as shown in both Figures 6.15 and 6.16 where the substrate thickness and permittivity have been varied independently. The propagation speed of the signal is higher in air compared to the paper substrate and so if more of the signal is confined to the paper, the propagation speed will decrease. In addition to this, as more of the field is in the substrate, the substrate losses will increase and so  $\alpha$  increases.



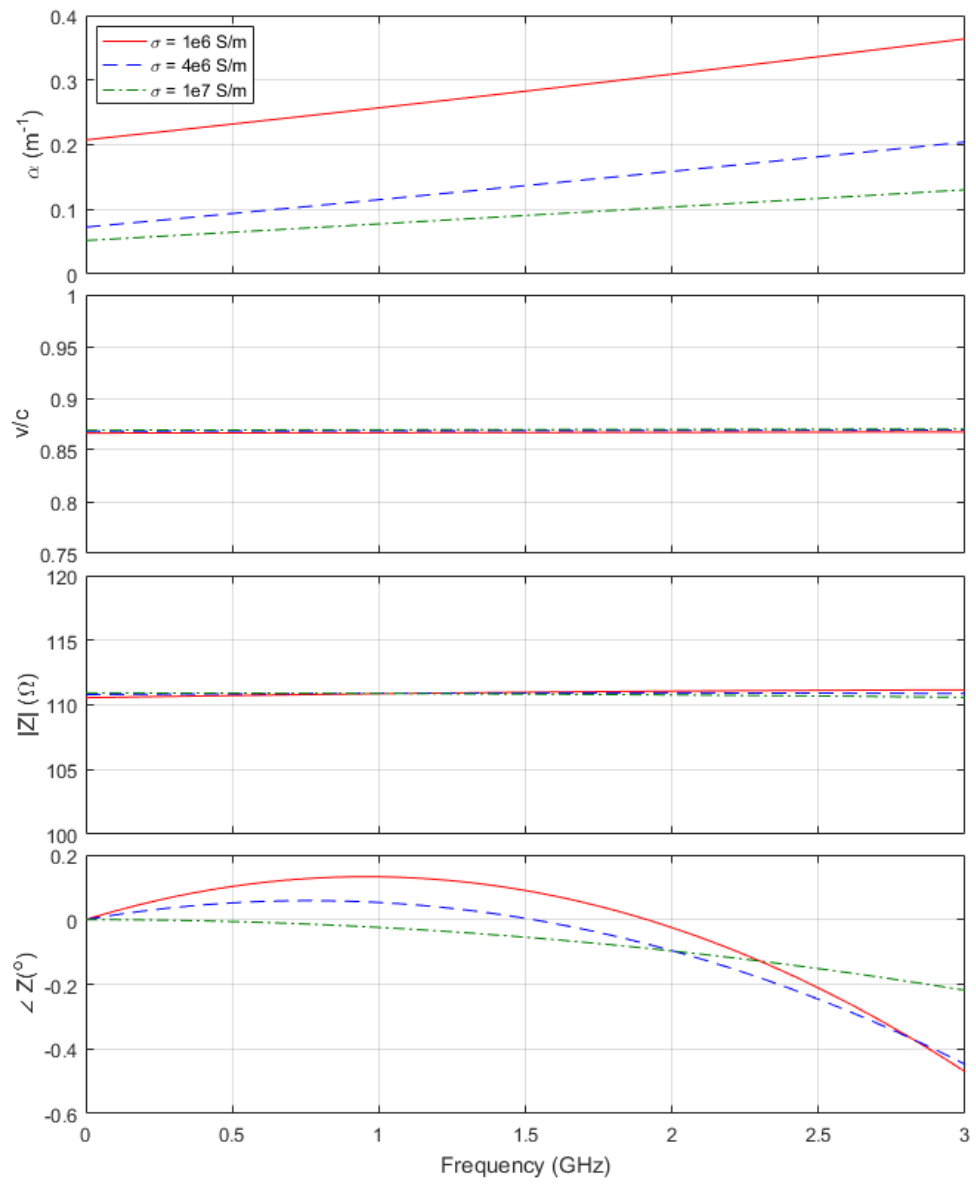
**Figure 6.15:** Simulated line parameters of transmission lines of substrate thickness varying between 100 and 500  $\mu\text{m}$ . Scattering parameters were simulated using ADS software and line parameters extracted.



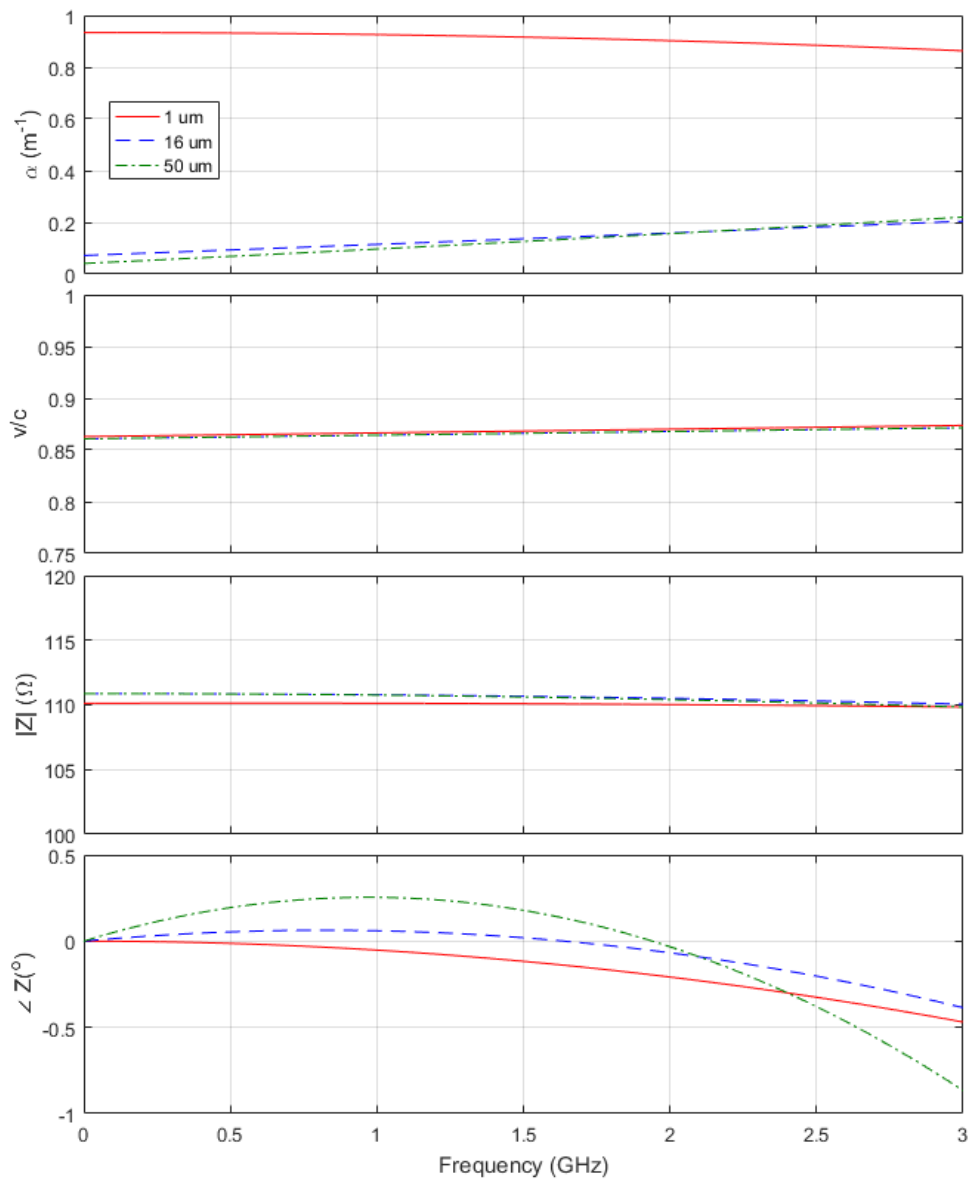
**Figure 6.16:** Simulated line parameters of transmission lines varying the substrate permittivity between 1 and 10. Scattering parameters were simulated using ADS software and line parameters extracted.

Increasing the metal thickness changes both the geometry and the conductivity of the ink and so these properties should be considered together. Increasing the conductivity of the metal results in fewer metallic losses and so  $\alpha$  decreases, as shown in both Figures 6.17 and 6.18. The propagation velocity and characteristic remain the same since the inductance is unaffected by altering the metal layer properties within this range. Considering the geometric changes when increasing the substrate thickness, the inductance will only be affected when the aspect ratio is drastically altered by an increase in thickness, which was not the case in this instance as it was only changed between 1 and 50  $\mu m$ . Increasing the thickness will also impact on the effect of skin depth. As the thickness is always large in comparison to the skin depth, this will not have an effect in this work.





**Figure 6.17:** Simulated line parameters of transmission lines varying the metal conductivity between  $1 \times 10^6$  and  $1 \times 10^7$  S/m. Scattering parameters were simulated using ADS software and line parameters extracted.



**Figure 6.18:** Simulated line parameters of transmission lines varying the metal thickness between 1 and 50  $\mu\text{m}$ . Scattering parameters were simulated using ADS software and line parameters extracted.

The effect of changing each parameter is summarised in Table 6.1. The relationship with  $\alpha$ ,  $v$  and  $Z$  has been considered for varying each parameter. The terms ‘moderate’ and ‘considerable’ have been used to show the relative effect of changing parameters, the absolute values can be found in the results presented earlier in this chapter.

**Table 6.1:** The effect of changing various transmission line parameters on  $\alpha$ ,  $v$  and  $Z$ .

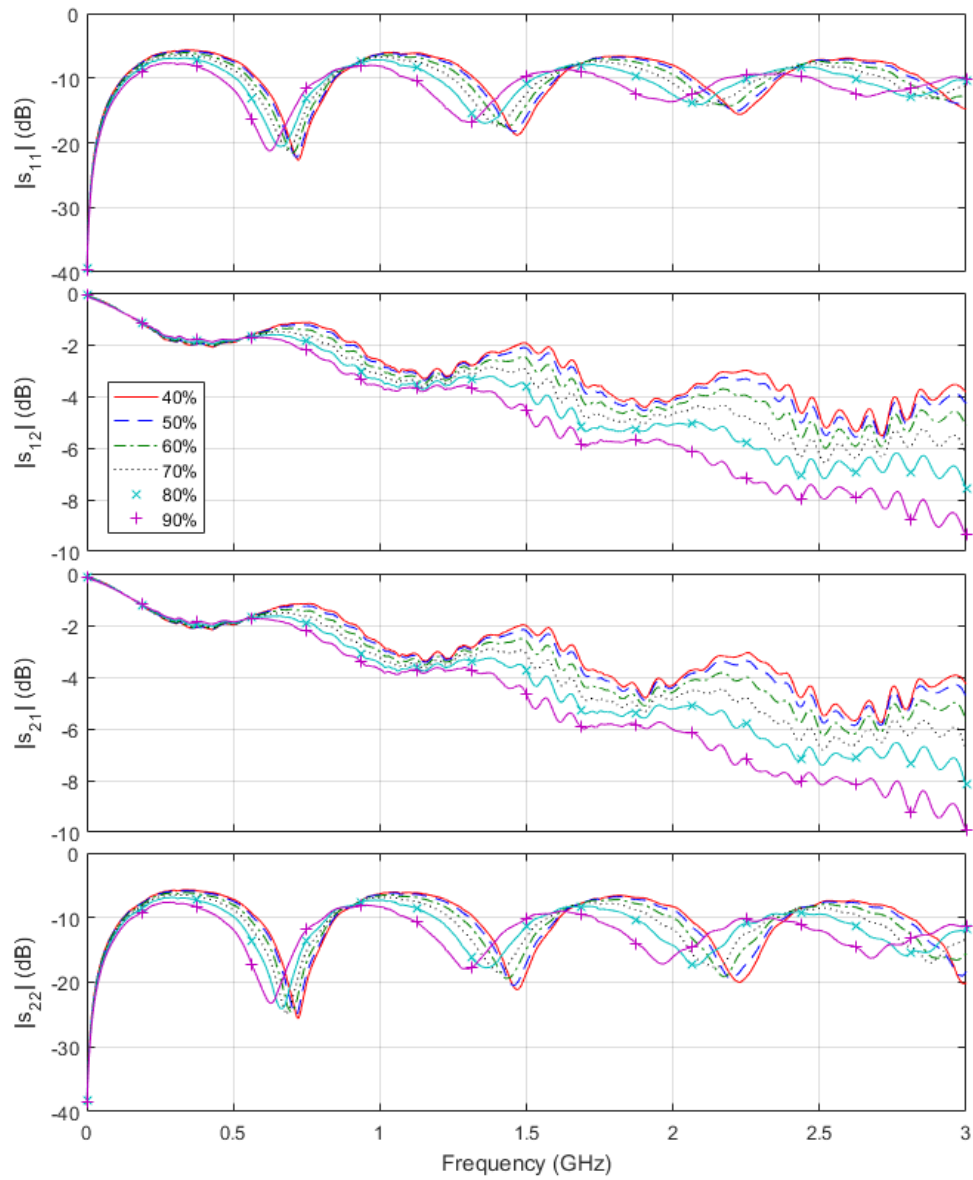
Parameter	Effect on transmission line response	Relationship with $\alpha$ , $v$ and $Z$
Length	None	No change to $\alpha$ , $v$ and $Z$
Ground Plane Width	None (as long as larger than gap)	No change to $\alpha$ , $v$ and $Z$
Signal Track Width	Considerable	Increasing width: increases $v$ decreases $\alpha$ and $Z$
Gap between signal and ground tracks	Considerable	Increasing gap: increases $v$ and $Z$ decreases $\alpha$
Substrate Thickness	Moderate	Increasing thickness: increases $\alpha$ decreases $v$ and $Z$
Substrate Permittivity	Moderate	Increasing permittivity: increases $\alpha$ decreases $v$ and $Z$
Metal Conductivity	Moderate	Increasing conductivity: decreases $\alpha$ No change to $v$ and $Z$
Metal Thickness	Moderate	Increasing thickness: decreases $\alpha$ No change to $v$ and $Z$

## 6.5 Effect of Humidity at Microwave Frequencies

### 6.5.1 Scattering Parameters and Line Parameters

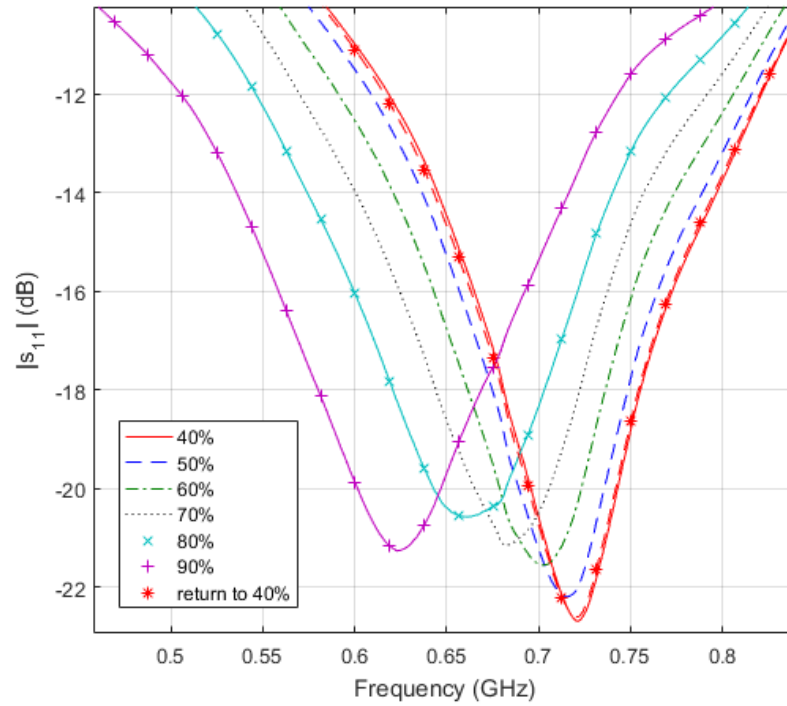
The effect of relative humidity on the response of the transmission lines was determined by recording the variation of s-parameters in an Espec SH-641 bench-top type temperature and humidity chamber, where the relative humidity was systematically varied between 40% and 90% in 10% steps. The set up is shown in Figure 5.28 in Chapter 5. Throughout this work, the temperature was constant, at 30 °C.

Readings were taken periodically at 1-minute intervals for the first 15 minutes, then 10-minute intervals for two hours. The humidity was shown to vary the s-parameters with higher changes occurring at higher humidities, as seen in Figure 6.19. Unless stated otherwise, the results shown here are for a transmission line which was 17 cm long with 2 and 15 mm signal and ground track width respectively. There are no error bars on Figures 6.19 and 6.20 so as not to overpopulate the plots, at each humidity the measurements were within 2% of the value shown.



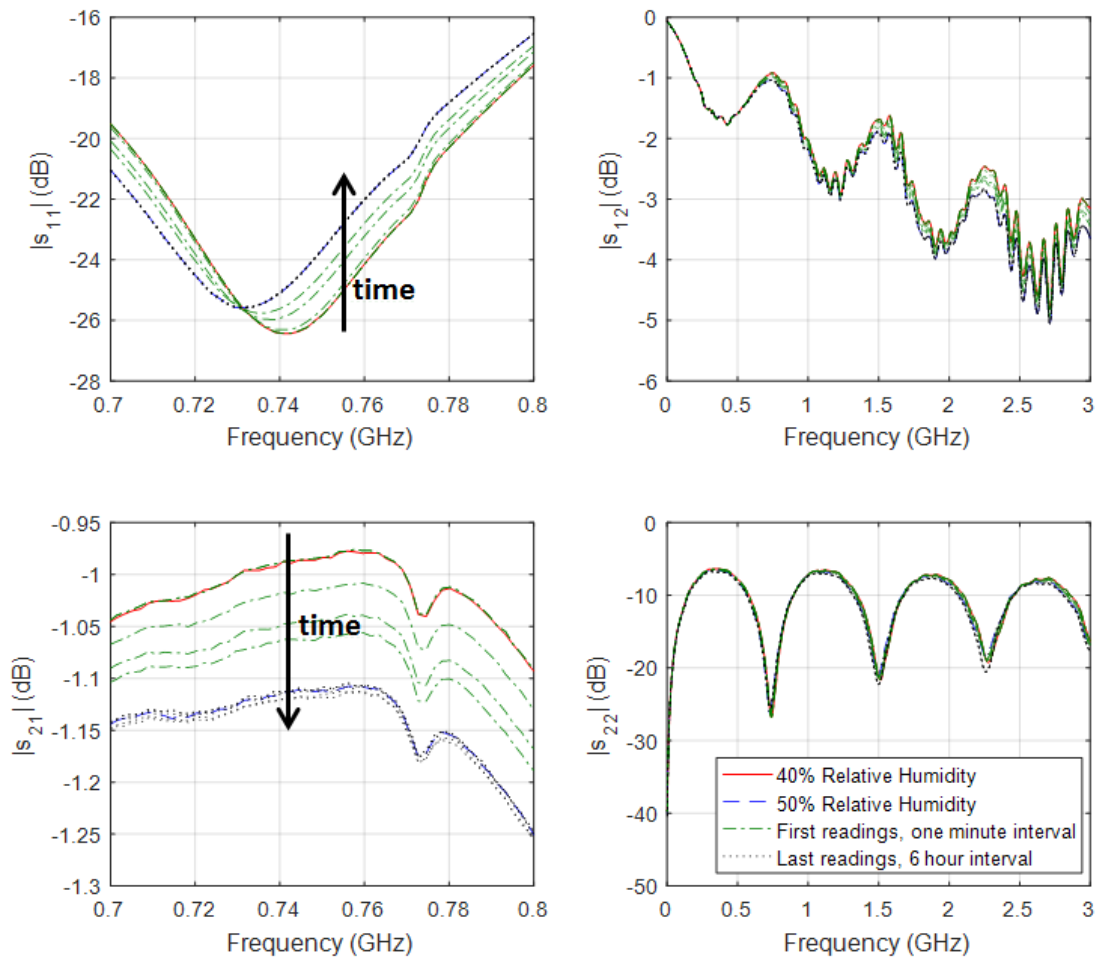
**Figure 6.19:** Measured scattering parameters for a transmission line 17 cm long with 2 and 15 mm signal and ground track width respectively as the relative humidity was varied between 40 - 90% in 10% steps.

This change in response with relative humidity is not permanent but rather reversible, such that when the relative humidity was reduced back to 40%, the s-parameters returned to the initial values measured at 40%, results to confirm this are shown in Figure 6.20.



**Figure 6.20:** Measured scattering parameter  $s_{11}$  for a transmission line 17 cm long with 2 and 15 mm signal and ground track width respectively as the relative humidity was varied between 40 - 90% in 10% steps and then returned to 40%.

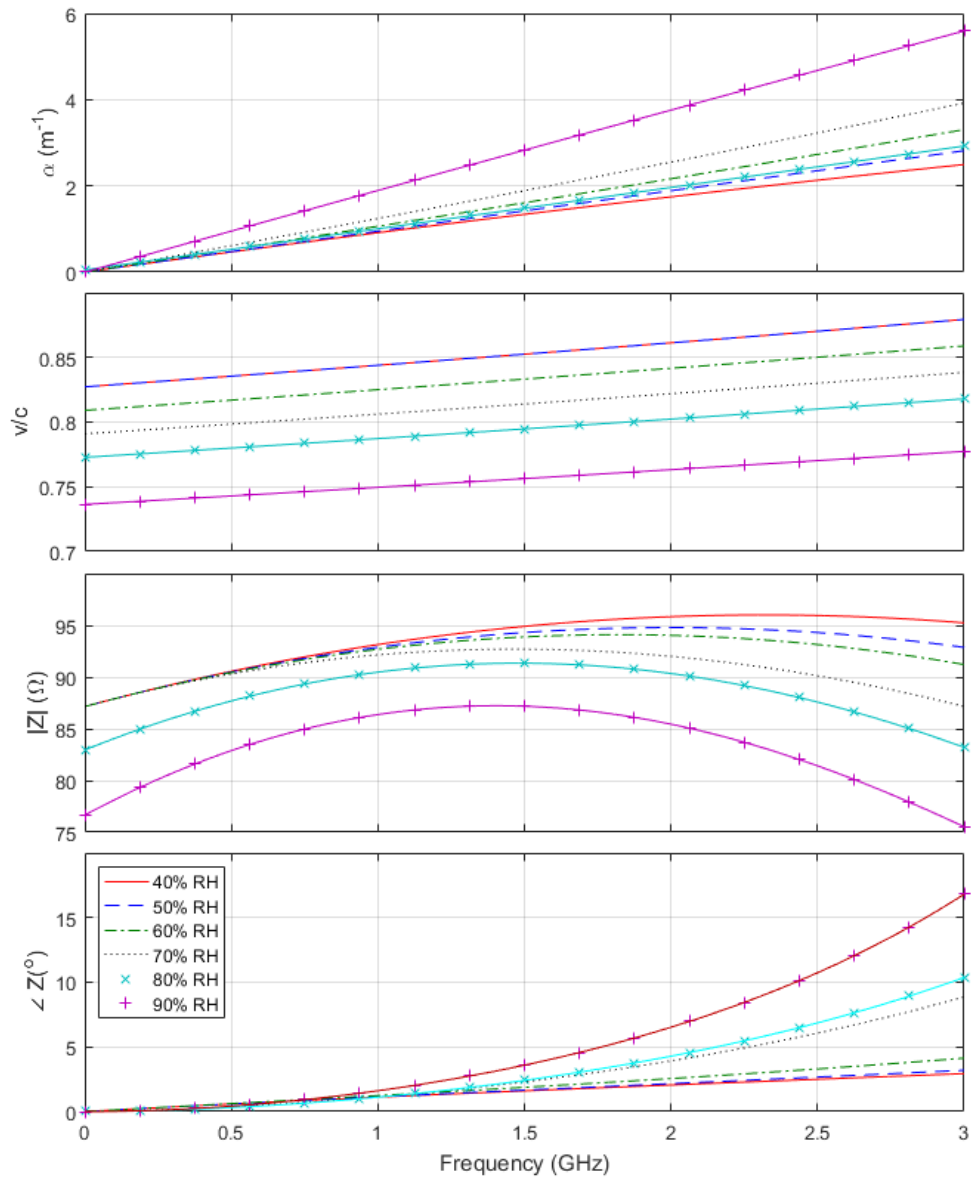
It was also found that there was a faster rate of change in response when the humidity was first changed, which then slowed down. This is expected as paper acclimatises quickly to its environment [20]. Within 15 minutes, 95% of the total change had occurred and, after this time, the response was determined to be stable. This supports the idea that water is absorbed into the paper within two minutes but takes longer to be desorbed. Little change in response was found for a transmission line where the humidity was increased from 40 to 50% and left for a week, as shown in Figure 6.21.



**Figure 6.21:** Measured scattering parameters for a transmission line 17 cm long with 2 and 15 mm signal and ground track width respectively as the relative humidity was varied between 40 - 50% and left for one week.

After the first five minutes of measurements, further results varied owing to slight variations in humidity rather than a further change in the transmission line response due to humidity. The chamber is a dynamic system and so the humidity may vary slightly with time. The scattering parameters did not change after the relative humidity was left to settle for 30 minutes. Holding the sample at 50% relative humidity for a long period showed that the response due to lower humidities was not just slower compared with those at higher humidities.

Using the fitting algorithm detailed previously in this chapter, the losses, propagation velocity and characteristic impedance were extracted at each relative humidity; these are presented in Figure 6.22. As expected, these show the same changes as with the s-parameters where the change in response between 40 and 50% relative humidity was much lower than between 80 and 90%. The change in propagation velocity is not visible between 40 and 50%, whereas it decreased by 0.05 between 80 and 90%.



**Figure 6.22:** Measured line parameters for a transmission line 17 cm long with 2 and 15 mm signal and ground track width respectively as the relative humidity was varied between 40 - 90% in 10% steps.

The losses ( $\alpha$ ) can be seen to increase with humidity in Figure 6.22; this could be due to metallic losses, dielectric losses or a combination of both. The metallic losses could be as a result of the paper absorbing water and swelling, stretching the ink and changing its conductive properties. The dielectric losses could be as a result of the effective permittivity of the paper increasing as the water content increased.

The propagation velocity was seen to decrease with humidity. When using the simple model for a transmission line consisting of resistance and inductance of the metal tracks and the capacitance and conductance of the substrate, as in Figure 6.3, the propagation velocity is inversely proportional to the square root of the inductance-capacitance product ( $v = 1/\sqrt{LC}$ ). If the dielectric constant of paper increases with added water, the capacitance per unit length will increase, and so the propagation

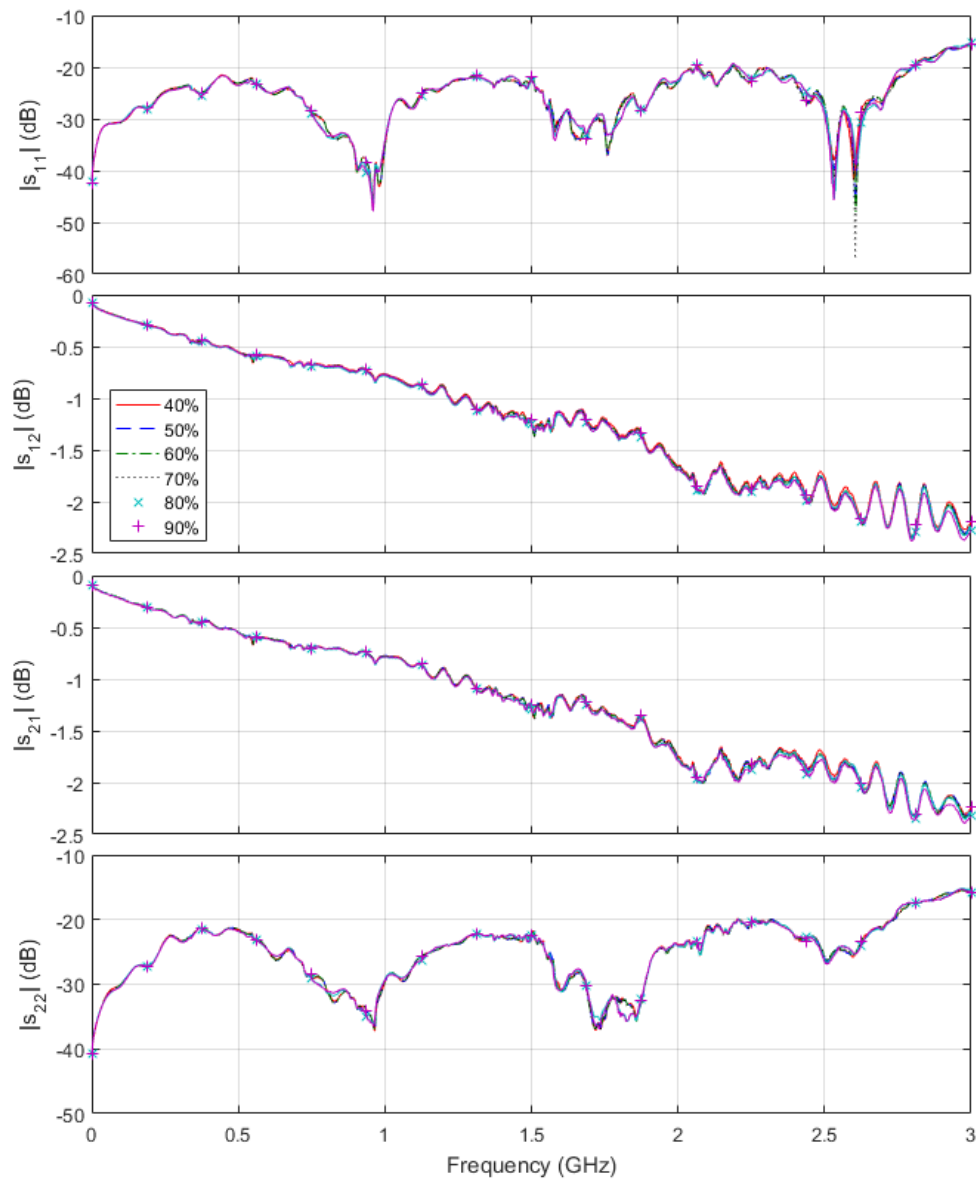
velocity will decrease. Similarly, if the geometry of the transmission line changes such that the length increases and the gap decreases, the propagation velocity would decrease.

The characteristic impedance decreases with relative humidity and this can be explained with the same theory as that used for the changes in propagation velocity. These possible changes for  $\alpha$ ,  $v$  and  $Z$  are likely caused by changes in the effective permittivity of the substrate or changes in the geometry from swelling of the cellulose fibres, which could also lead to differences in the conductivity of the ink.

### **6.5.2 Effect of Humidity on the Ink**

As seen with simulations in Figure 6.17, altering the conductivity of the ink does not cause changes to the characteristic impedance and the propagation velocity. Further investigation took place to confirm that the changes in line parameters were not due to structural changes within the ink. In order to prevent water absorption into the substrate, an identical transmission line was printed on glass and measured in the same way as the paper-based sample, with results shown in Figure 6.23.

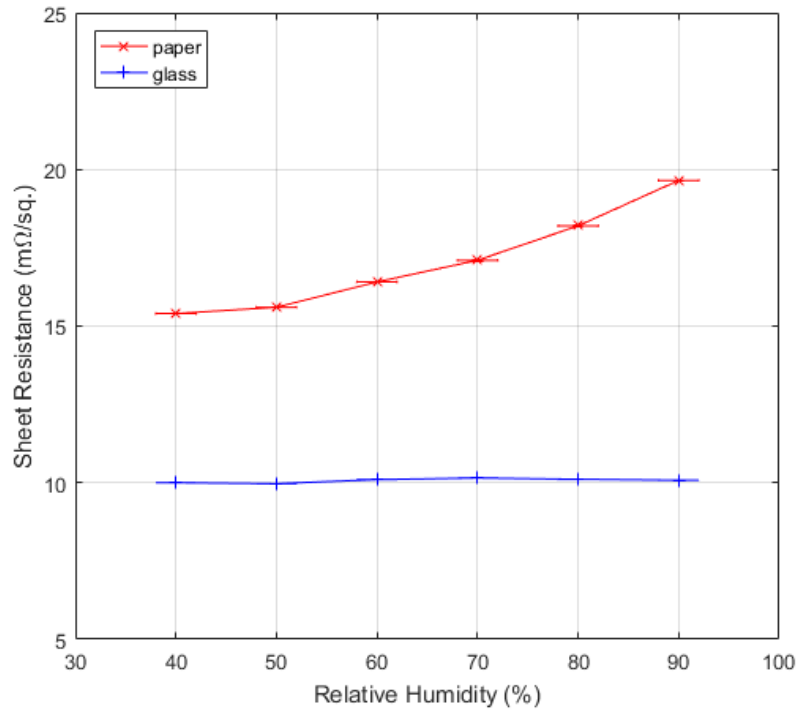




**Figure 6.23:** Measured scattering parameters for a transmission line printed on glass as the relative humidity was varied between 40 - 90% in 10% steps. The transmission line was 17 cm long with 2 and 15 mm signal and ground track width respectively.

The s-parameters presented in Figure 6.23 for the transmission line printed on glass were found not to change with humidity, leading to the conclusion that there is no change in the ink itself with changing humidity. The scattering parameters differed from those obtained when using paper as a substrate, as the characteristic impedance of the glass sample tends towards  $50 \Omega$ , and so the reflection ( $s_{11}, s_{22}$ ) is minimal. There are calibration non-idealities as the calibration does not account for the connectors; these are more dominant in the glass sample as the reflection is lower. The interaction of the glass and the ink in comparison to the interaction of the paper and the ink will differ hugely. The ink will adhere less to the glass than the paper, as shown in Chapter 3 with adhesion testing, and so these material issues must also be considered when comparing Figure 6.19 with Figure 6.23.

The d.c. sheet resistance values of the ink on both glass and paper were measured at relative humidities between 40 and 90% using a four point probe method, with results shown in Figure 6.24.



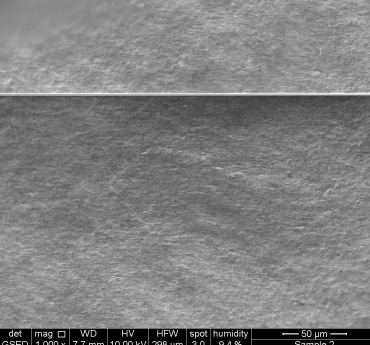
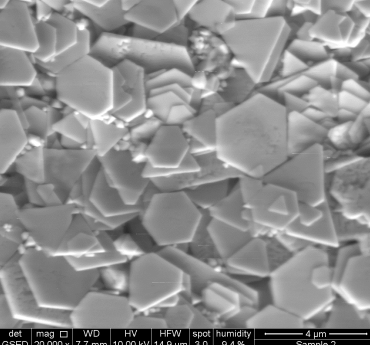
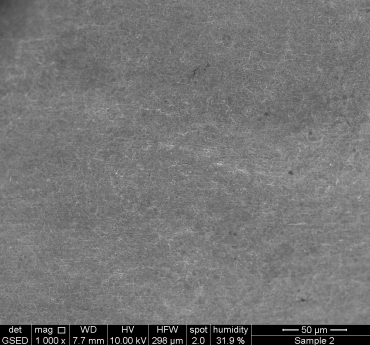
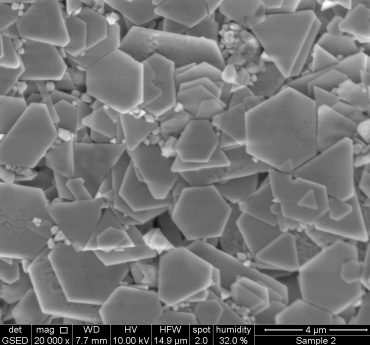
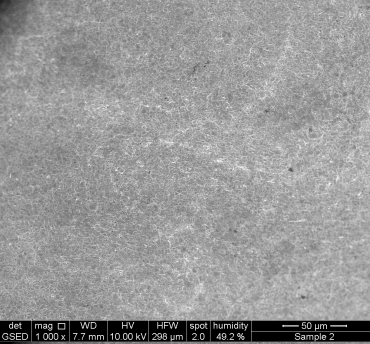
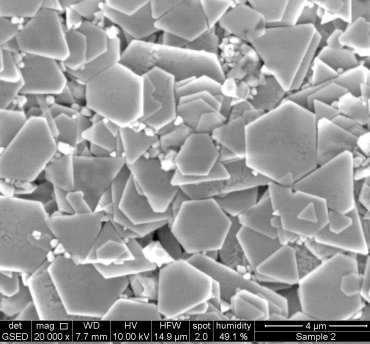
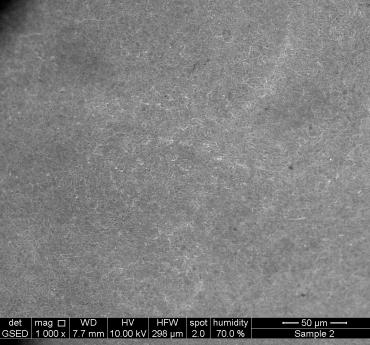
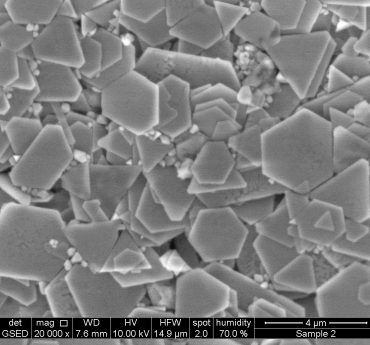
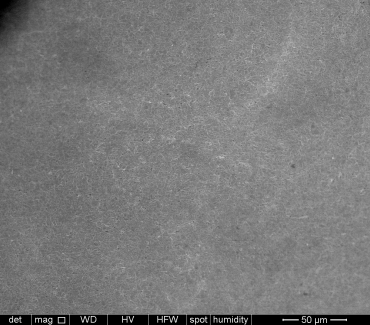
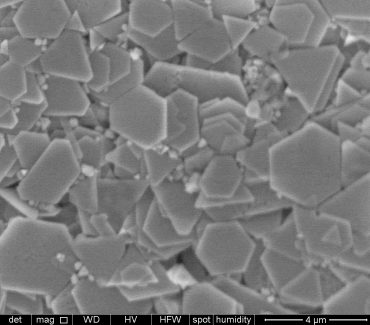
**Figure 6.24:** Variation in measured sheet resistance for screen-printed silver ink on glass and paper substrates as the relative humidity was varied. Measurements were taken using a four point probe method.

The sheet resistance of the ink on glass was shown not to vary, in keeping with s-parameter measurements taken, and which further proved that there were no changes within the ink at differing humidities. The sheet resistance of the ink on the paper sample was shown to increase with relative humidity due to the swelling of paper fibres with increased water content, leading to sagging of the sample and hence a longer path. The increase in d.c. sheet resistance was minimal, rising from 15.4 to 19.7 mΩ/□. From the ADS simulations (Figure 6.17), it can be seen that much larger changes in conductivity produce no changes in the propagation velocity and characteristic impedance, and so this cannot be the cause of the changes seen for  $v$  and  $Z$  in Figure 6.22. The change in  $\alpha$  in Figure 6.17 is not as large as that in Figure 6.22, and so the increase in conductivity of the ink may likely contribute to an increase in  $\alpha$  but cannot be the only cause. The ink is made up of silver flakes, at d.c. an increase in distance between the flakes will result in a longer path length as the flakes must be in direct contact with each other for an electrical connection. In a.c. an increase in distance between the flakes is not problematic as no direct contact is required for an electrical connection. Any capacitive effects which may occur from increasing gaps between the flakes as the path length is increased will be negligible at the frequencies measured here.

In addition to the comparison of transmission lines on paper with transmission lines on glass,

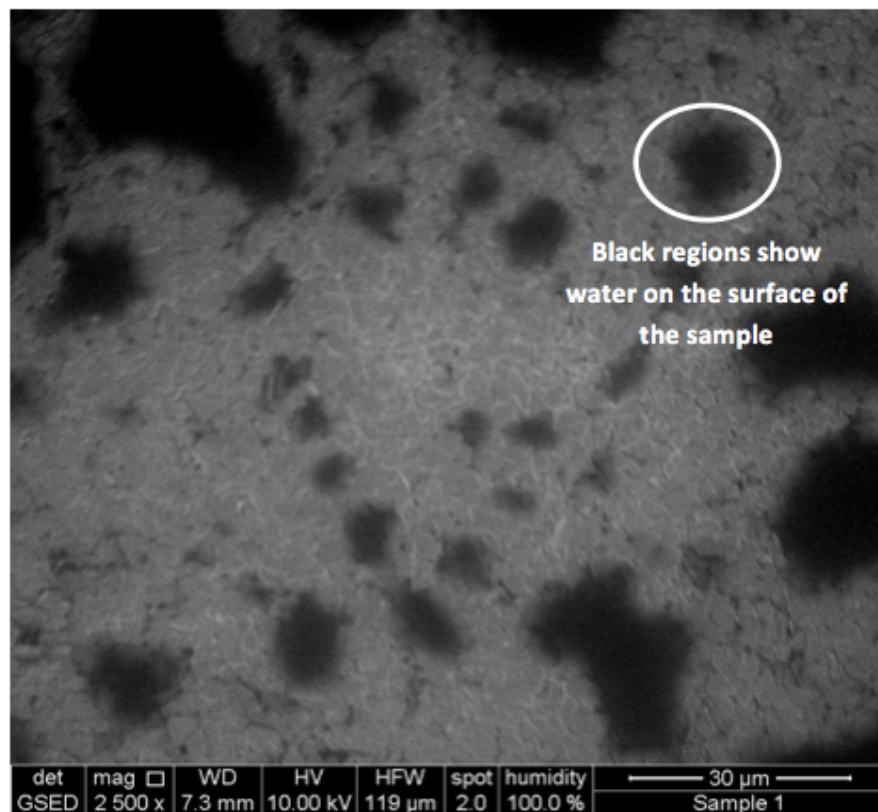
Environmental SEM (ESEM) images of the silver ink on paper were taken. No change was seen within the ink layer as shown in Table 6.2. Imaging was undertaken by Richard Walshaw at Leeds University using an FEI Quanta 650 Field Emission Gen Environmental Scanning Electron Microscope (FEGSEM). This operates in a similar way to a conventional SEM, as described in Chapter 2, and utilises the changing of water content within the air with temperature and pressure to vary the humidity within the chamber. In order to increase the relative humidity within the chamber, the temperature was maintained at 3 °C and the pressure was increased between 0.7 and 5.6 Torr. This achieved a relative humidity between 10% and 100%. These results confirmed the lack of change in morphology of the ink with increased relative humidity. The small scale of the sample (1 cm<sup>2</sup>) used in ESEM does not illustrate the sagging of the sample at high relative humidities and so any movement of flakes caused by this are not obvious here.

**Table 6.2:** Environmental Scanning Electron Microscope (ESEM) images of silver flake ink on matt paper at relative humidities between 10 and 90%.

Relative humidity	ESEM Images	
10%	 <p>det mag WD HV HFW spot humidity GSED 1 000 x 7.7 mm 10.00 kV 236 µm 3.0 9.4 %</p> <p>50 µm Sample 2</p>	 <p>det mag WD HV HFW spot humidity GSED 20 000 x 7.7 mm 10.00 kV 14.9 µm 3.0 9.4 %</p> <p>4 µm Sample 2</p>
30%	 <p>det mag WD HV HFW spot humidity GSED 1 000 x 7.7 mm 10.00 kV 236 µm 2.0 31.9 %</p> <p>50 µm Sample 2</p>	 <p>det mag WD HV HFW spot humidity GSED 20 000 x 7.7 mm 10.00 kV 14.9 µm 2.0 32.0 %</p> <p>4 µm Sample 2</p>
50%	 <p>det mag WD HV HFW spot humidity GSED 1 000 x 7.7 mm 10.00 kV 236 µm 2.0 49.2 %</p> <p>50 µm Sample 2</p>	 <p>det mag WD HV HFW spot humidity GSED 20 000 x 7.7 mm 10.00 kV 14.9 µm 2.0 49.1 %</p> <p>4 µm Sample 2</p>
70%	 <p>det mag WD HV HFW spot humidity GSED 1 000 x 7.7 mm 10.00 kV 236 µm 2.0 70.0 %</p> <p>50 µm Sample 2</p>	 <p>det mag WD HV HFW spot humidity GSED 20 000 x 7.6 mm 10.00 kV 14.9 µm 2.0 70.0 %</p> <p>4 µm Sample 2</p>
90%	 <p>det mag WD HV HFW spot humidity GSED 1 000 x 7.6 mm 10.00 kV 236 µm 2.0 88.4 %</p> <p>50 µm Sample 2</p>	 <p>det mag WD HV HFW spot humidity GSED 20 000 x 7.6 mm 10.00 kV 14.9 µm 2.0 88.4 %</p> <p>4 µm Sample 2</p>

The porosity of paper meant that the pressure must be increased above 5.6 Torr to confirm water saturation on the surface of the paper. At 100% relative humidity, the water vapour is contained

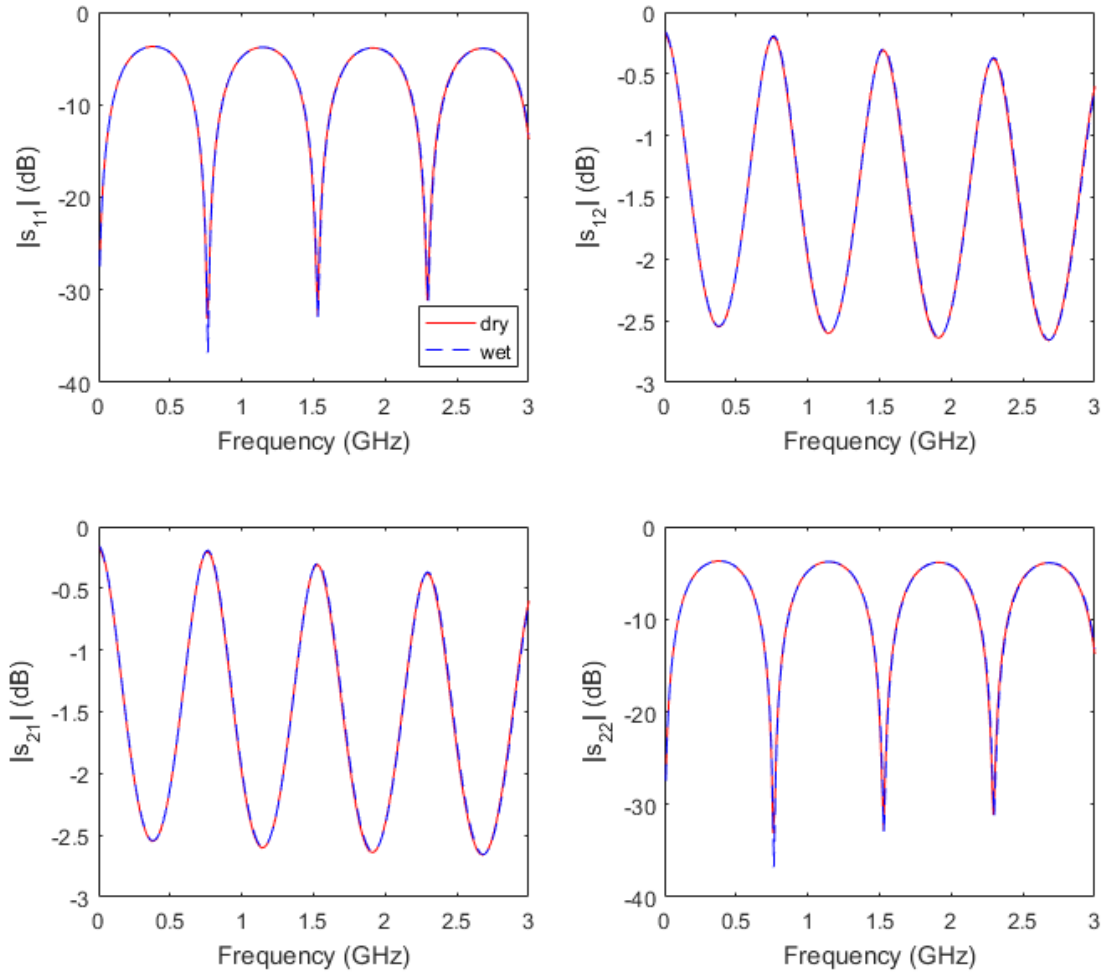
within the paper and ink structure and so water saturation cannot be verified on the image. An image of a saturated sample with evident water droplets formed on the surface is shown in Figure 6.25, where the pressure has been increased to 7.1 Torr.



**Figure 6.25:** An ESEM image of silver flake ink on paper at a temperature of 3 °C and a pressure of 7.1 Torr showing the saturation of the sample with water and evident water on the sample surface. This combination of temperature and pressure results in a relative humidity past the point of 100%. The water droplets are the darker regions on the sample surface.

### 6.5.3 Water Absorption of Paper

Dimensional changes of the paper in x and y directions (length and width), due to added water content, were found to have no effect on the response of the transmission line as determined by simulations, with results in Figure 6.26. Paper samples were completely soaked in water and a maximum of 3%  $\pm 1.5$  increase in dimensions in the x, y directions was measured by vernier callipers. Figure 6.26 shows simulation results for a 5% increase in dimensions, resulting in no change to the scattering parameters. The changes in length and width of the paper can be seen to have no effect on the response of the transmission line.

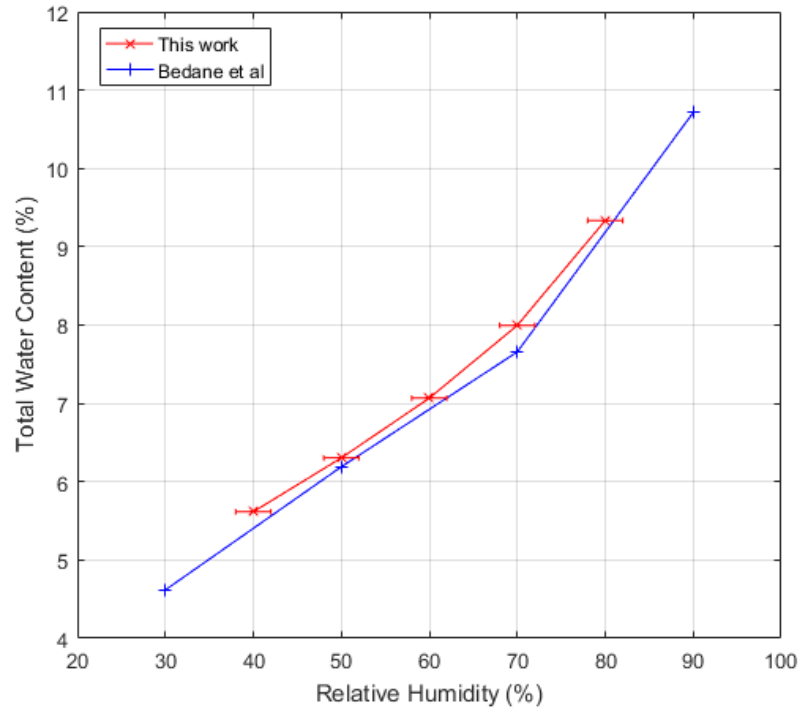


**Figure 6.26:** Simulations for a 5% increase in x and y dimensions of the transmission line due to water intake of the paper. The substrate thickness was kept constant as the effect of this has been shown previously.

It has been shown in Figures 6.15 and 6.16 that increasing the substrate thickness will produce a similar effect to increasing the effective permittivity of the substrate. It is thought that both of these are the key factors in the change of line parameters with humidity. It has been shown in Figures 6.15 and 6.16 that increasing both the substrate thickness and substrate permittivity can cause changes in the line parameters similar to those seen in Figure 6.22. Altering either the substrate thickness or permittivity will change the effective permittivity of the substrate, changing the capacitance per unit length.

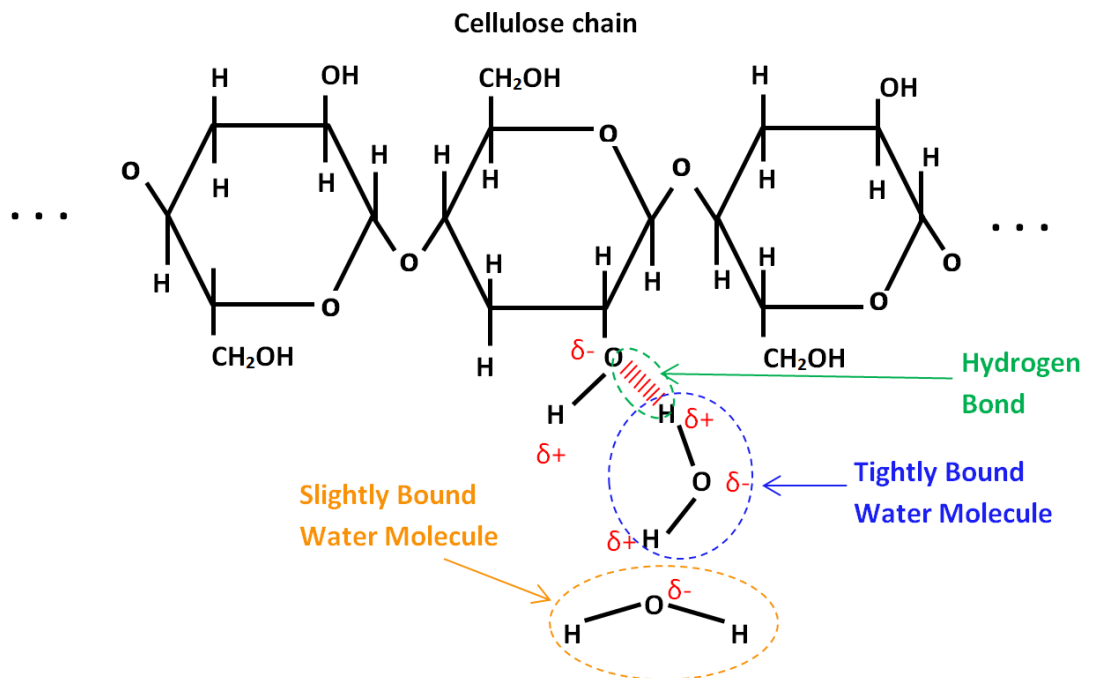
The water content of paper with relative humidity was found to follow the same trend as the s-parameters and line parameters in Figures 6.19 and 6.22. The mass of a transmission line was measured immediately after being placed on a hotplate at 125 °C for 30 minutes to determine the mass of paper with no water. It was then measured again in the environmental chamber as the relative humidity was varied from 40 to 80%. The balance was rated to 85% relative humidity and so measurements at 90% were not possible. The water content as a percentage is presented in Figure 6.27

and is seen to have a higher change between 70 and 80% than at 40 and 50% relative humidity.



**Figure 6.27:** Total water content of paper when relative humidity was varied between 30 and 90%. The blue line represents data taken from [21], the red line represents measurements from this work.

The water content in paper is made up of three types of water-paper absorption mechanisms [21–25]: non-freezing water (tightly bound water), freeze-bound water (slightly bound water) and freezing-unbound water (free water). Tightly and slightly bound water-paper absorption mechanisms are shown in Figure 6.28.



**Figure 6.28:** Illustration of tightly and loosely bound water mechanisms in water-paper mixtures.

Tightly bound water is hydrogen bonded to the polymer matrix of the cellulose fibres. Hydrogen bonding is an attraction between two polar groups; the bond between oxygen and hydrogen is polar because oxygen is more electronegative than hydrogen and so the oxygen in water is attracted to the hydrogen of the ‘OH group’ in the cellulose chain. Slightly bound water is attracted to the cellulose and the monolayer of water hydrogen bonded to the cellulose; however the molecules are not hydrogen bonded. This attraction is called a Van der Waal force and is also due to the polarity of two molecules but is much weaker than a hydrogen bond. The cellulose chains combine together into a plane, and these planes are then ‘stacked’ on top of each other. The planes are not connected by any bonding to their adjacent planes, but are held together with Van der Waal forces. The addition of water on the surface of the planes will also result in Van der Waal forces and slightly bound water. Free (freezing unbound) water is held to other water molecules by capillary forces and is not bonded in any way to the cellulose.

To determine the relative permittivity for the three types of water-paper mechanisms, the relaxation time is required, as in [26]. The relaxation time is a measure of the mobility of a material’s molecules and is equal to the time taken for dipoles to become orientated in an electric field. Molecules which are bonded to each other have little freedom to move when an electric field is applied, and so have a higher relaxation time. The frequency at which the electric field is changed must therefore be considered. If the dipoles are slow to move then they cannot keep up with a quickly alternating electric field. Above a certain frequency, both the real and imaginary parts of the dielectric constant will decrease because of this.

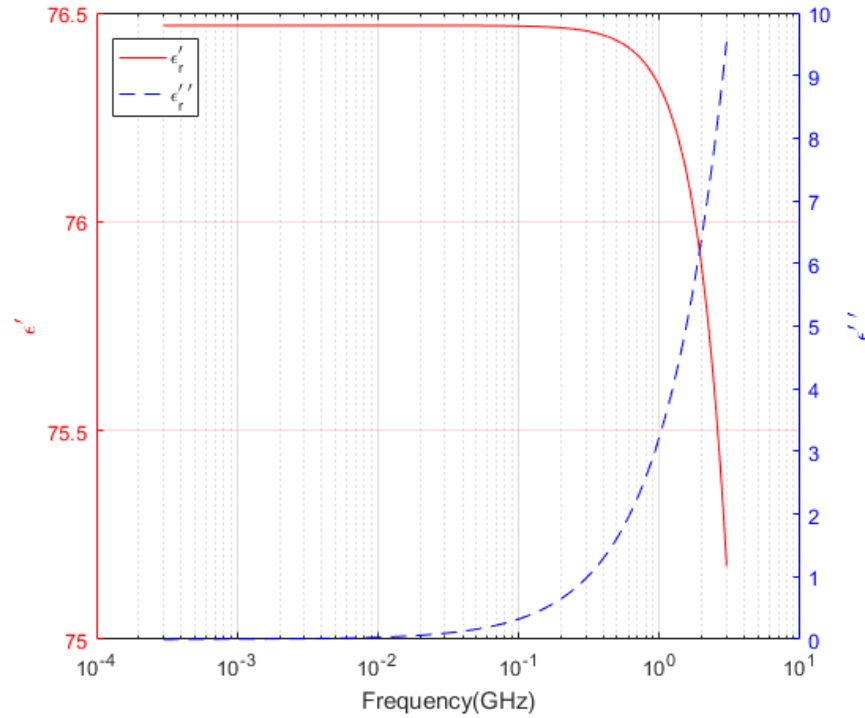
As the tightly bound water is hydrogen bonded to the cellulose, the mobility of the water molecules is greatly decreased, and so for this work the dielectric constant of the tightly bound water was considered to be equal to that of paper (3.25). The slightly bound water has reduced mobility due to the additional interactions with cellulose and the value for the dielectric constant is often approximated to 30 [27]. The relaxation time of free water is well established and the Debye relationship can be used to calculate the real and imaginary parts of the dielectric constant. The Debye equation is:

$$\epsilon(\omega) = \epsilon_{\text{inf}} + \frac{\epsilon_s - \epsilon_{\text{inf}}}{1 + i\omega\tau} \quad (6.23)$$

where  $\epsilon$  is the complex dielectric constant of the material;  $\epsilon_{\text{inf}}$  is the optical value of the dielectric constant and is equal to 4.9;  $\epsilon_s$  is the static value of the dielectric constant and is equal to 76.47; and  $\tau$  is the relaxation time and is equal to 7.2 ps. These values are all taken for water at 30 °C [26]. The



resulting plot of the complex dielectric constant against frequency is shown in Figure 6.29. The value for the dielectric constant of free water has been taken as 78 for this work [28].



**Figure 6.29:** Calculated real and imaginary parts of the relative permittivity of pure water between 300 kHz and 3 GHz using the Debye equation and values from [26].

In a similar way to Davies in [29], a simple model for the total dielectric constant of a paper-water mixture was developed based on the weighted sum of the above described different dielectric constants and is presented as Equation (6.24):

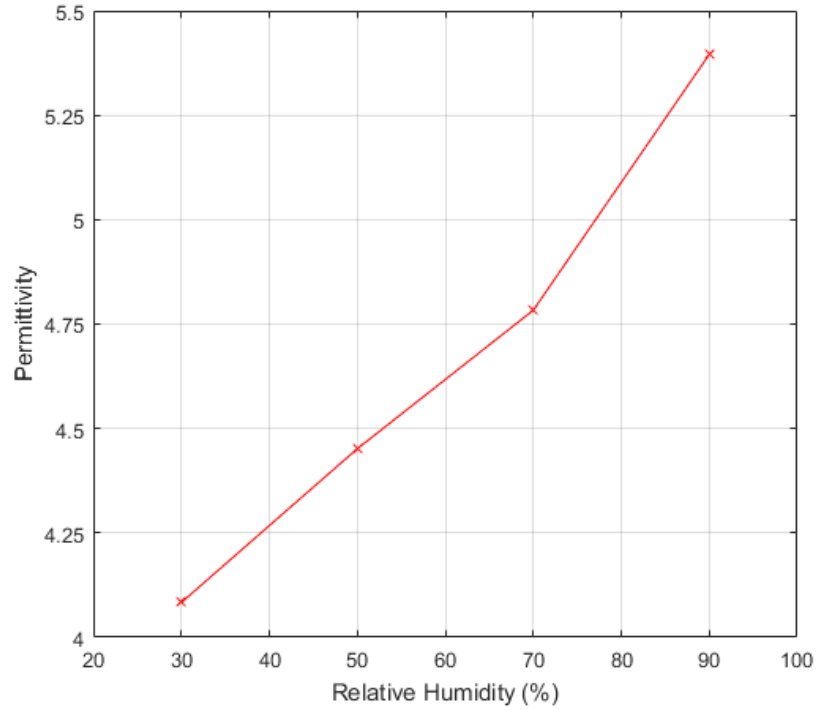
$$\epsilon_T = A\epsilon_{UBW} + B\epsilon_{FW} + C\epsilon_{NW} + D\epsilon_C \quad (6.24)$$

where  $\epsilon_T$  is the total dielectric constant of the substrate including cellulose and water;  $A, B, C$  and  $D$  are the fractions; and  $\epsilon_{UBW}$ ,  $\epsilon_{BW}$ ,  $\epsilon_{NW}$  and  $\epsilon_C$  are the dielectric constants of freezing-unbound water, freeze-bound water, non-freezing water and cellulose respectively.

The total water content values of this work and the work of Bedane et al. are shown to be in agreement in Figure 6.27, however the individual percentages for the types of water absorption could not be measured in this work. The percentages of the three forms of water at 30, 50, 70 and 90% relative humidity according to Bedane et al. for uncoated paper can be used in Equation (6.24) as  $A$ ,  $B$  and  $C$ , along with the respective values of permittivity to determine the total effective permittivity of the paper substrate with relative humidity. Values for  $A$ ,  $B$ ,  $C$  and  $D$  are shown in Table 6.3 and a plot of theoretical permittivity of the paper and water mixture with relative humidity in Figure 6.30.

**Table 6.3:** Percentages and permittivity values for non-freezing water (tightly bound water), freeze-bound water (slightly bound water), freezing-unbound water (free water) and paper at 30, 50, 70 and 90% relative humidity. Percentages have been taken from [21] for uncoated paper, permittivity of free water taken from [28] and permittivity of loosely bound water from [27].

Relative Humidity	Free		Slightly Bound		Tightly Bound		Paper	
	%	$\epsilon_r$	%	$\epsilon_r$	%	$\epsilon_r$	%	$\epsilon_r$
30 %	0.68	78	1.47	30	2.47	2.5	95.38	3.25
50 %	0.87	78	2.32	30	3.00	2.5	93.81	3.25
70 %	1.20	78	2.66	30	3.80	2.5	92.34	3.25
90 %	1.25	78	4.82	30	4.64	2.5	89.29	3.25



**Figure 6.30:** Theoretical values of the effective permittivity of a paper-based substrate with increasing relative humidity based on Equation (6.24) and values in Table 6.3.

The percentage of non-freezing water ( $C$ ) increases linearly with relative humidity; initially, water is hydrogen bonded to two anhydroglucose units of the cellulose but, as the water content is increased, these bonds break and only one anhydroglucose unit per water is hydrogen bonded. The percentage of freeze-bound water ( $B$ ) increases with relative humidity; above 70% relative humidity this increases at a higher rate due to the formation of stronger dimer/trimer assemblies of water. The percentage of freezing-unbound water ( $A$ ) increases with humidity, but at a lower rate at higher humidities due to the increase in freeze-bound water at this point.

The dramatic increase in the percentage of freeze-bound water above 70% relative humidity explains the larger change in line parameters with humidities above 70%; since the dielectric constant of the freeze-bound water is 30 whereas the dielectric constant of paper is 3.25. The change in

permittivity, as seen in Figure 6.30, between 70-90% relative humidity is double that of the change between 50-70% and 30-50%.

Neither this theory or the effect of varying substrate thickness can explain the change in line parameters with relative humidity being larger at higher frequencies. The permittivity of water is known to be highly frequency dependent and this relationship can be represented by a Debye relaxation function, as shown in Figure 6.29 [26]. In the frequency range 300 kHz to 3 GHz, the real part of the permittivity of water decreases by less than two, whereas the imaginary part increases by approximately 10, with a higher rate of change at higher frequencies. As the imaginary part of the permittivity increases with frequency, the loss tangent will therefore also increase and is the reason for the greater change in response of the transmission lines at higher frequencies.

## 6.6 Conclusion

The theory of transmission lines has been presented and used to characterise screen-printed transmission lines on matt paper. The conversion between s-parameters and line parameters  $\alpha$ ,  $v$  and  $Z$  has been presented using a Matlab code. Changing the ground plane width and length of the transmission line is found to have no effect on transmission line performance. However altering the signal width and the gap between this and the ground plane is found to affect measured parameters. Substrate and metal parameters are found to change the losses within the transmission line, and the substrate also has an effect on the propagation velocity and characteristic impedance of the line.

The hygroscopic nature of paper is found to have a large effect on the microwave characteristics of paper-based transmission lines. It has been shown that the change in microwave characteristics with relative humidity is not due to changes within the ink but to the increase in both the thickness and effective permittivity of the paper substrate caused by increased water content. There are three types of water absorption mechanisms in paper and it has been concluded that the freeze-bound (slightly bound) water is the reason for the larger change in losses at higher relative humidities. The percentage of freeze-bound water increases dramatically above 70% relative humidity and has a permittivity of 30 which is higher than that of pure cellulose. These findings must be considered in all applications using coplanar waveguides at microwave frequencies as these changes in line parameters can alter device operation significantly and have been shown to also vary with frequency.

Possible applications for screen-printed paper-based coplanar waveguides are considered in the next chapter when looking at coplanar waveguide resonators.

## References

- [1] R. Collin, *Foundations for Microwave Engineering*. McGraw-Hill, 1992.
- [2] O. Heaviside, "Electromagnetic induction and its propagation," *The Electrician*, 1885.
- [3] R. Mongia, I. Bahl, P. Bhartia, and S. Hong, *RF and Microwave Coupled-line Circuits*. Artech House, 2007.
- [4] R. N. Simons, *Coplanar Waveguide Discontinuities and Circuit Elements*, vol. 7. John Wiley and Sons, 2001.
- [5] D. Pozar, *Microwave Engineering Fourth Edition*. Wiley Global Education, 2005.
- [6] J. Choma and W. K. Chen, *Feedback Networks: Theory and Circuit Applications*. World Scientific Publishing Company, 2007.
- [7] M. Bozzi, M. M. Tentzeris, V. Lakafosis, T. Le, S. Kim, R. Vyas, A. Georgiadis, J. Cooper, B. Cook, R. Moro, A. Collado, and H. Lee, "Inkjet-printed antennas, sensors and circuits on paper substrate," *IET Microwaves, Antennas & Propagation*, vol. 7, no. 10, p. 858, 2013.
- [8] F. Alimenti, C. Mariotti, V. Palazzi, M. Virili, G. Orecchini, P. Mezzanotte, and L. Roselli, "Communication and sensing circuits on cellulose," *Journal of Low Power Electronics and Applications*, vol. 5, no. 3, p. 151, 2015.
- [9] V. Palazzi, C. Mariotti, F. Alimenti, M. Virili, G. Orecchini, P. Mezzanotte, and L. Roselli, "Demonstration of a chipless harmonic tag working as crack sensor for electronic sealing applications," *Wireless Power Transfer*, vol. 2, no. 02, p. 78, 2015.
- [10] C. Beisteiner and B. G. Zagar, "Dielectric permittivity measurement of paper substrates using commercial inkjet printers," *30th Euroensors Conference*, 2016.
- [11] M. Haghzadeh, C. Armiento, and A. Akyurtlu, "Microwave dielectric characterization of flexible plastic films using printed electronics," *87th Microwave Measurement Conference*, 2016.
- [12] A. Sahu, P. H. Aaen, A. Lewandowski, M. Shkunov, G. P. Rigas, P. T. Blanchard, T. M. Wallis, and V. Devabhaktuni, "Robust microwave characterization of inkjet printed coplanar waveguides on flexible substrates," *IEEE Transactions on Instrumentation and Measurement*, 2017.
- [13] A. Sahu, V. Devabhaktuni, A. Lewandowski, P. Barmuta, T. M. Wallis, M. Shkunov, and P. H. Aaen, "Microwave characterization of ink-jet printed CPW on PET substrates," *Proceedings from the 86th ARFTG Microwave Measurement Conference: Microwave Measurements with Applications to Bioengineering and Biomedicine*, 2016.
- [14] N. Selmene, S. Blayac, M. Muller, and G. Abib, "Compact acquisition system for a flexible large area monoport tactile surface," *21st International Conference on Microwave, Radar and Wireless Communications*, 2016.
- [15] T. Low, C. Sensitive, and P. Surfaces, "Single port, large area touch and force sensing," *IEEE Ninth International Conference of Intelligent Sensors, Sensor Networks and Information Processing, Singapore*, p. 21, April 2014.
- [16] C.-F. Huang, Y.-C. Hung, and C.-L. Liu, "Precise location of touch panel by employing the time-domain reflectometry," *SID Symposium Digest of Technical Papers*, vol. 40, no. 1, p. 1291, 2009.
- [17] R. Wimmer and P. Baudisch, "Modular and deformable touch-sensitive surfaces based on time domain reflectometry," *Proceedings of the 24th Annual ACM Symposium on User Interface Software and Technology*, no. 1, p. 517, 2011.
- [18] P. Heymann, H. Prinzier, and F. Schnieder, "De-embedding of MMIC transmission-line measurements," *IEEE Microwave Theory and Techniques Society, International Microwave Symposium Digest*, p. 1045, 1994.
- [19] D. A. Frickey, "Conversions between S, Z, Y, h, ABCD, and T parameters which are valid for complex source and load impedances," *IEEE Transactions on Microwave Theory and Techniques*, vol. 42, no. 2, p. 205, 1994.
- [20] T. Padfield, "The interaction of water vapour with paper," *Conservation Physics*, 2006.
- [21] A. H. Bedane, H. Xiao, M. Eic, and M. Farmahini-Farahani, "Structural and thermodynamic characterization of modified cellulose fiber-based materials and related interactions with water vapor," *Applied Surface Science*, vol. 351, p. 725, 2015.
- [22] S. Akinli-Kocak, "The influence of fiber swelling on paper wetting," *The University of Maine, Electronic Theses and Dissertations*, 2001.
- [23] H. Hatakeyama and T. Hatakeyama, "Interaction between water and hydrophilic polymers," *Thermochimica Acta*, vol. 308, no. 1, p. 3, 1998.
- [24] T. C. Blair, G. Buckton, A. E. Beezer, and S. F. Bloomfield, "The interaction of various types of microcrystalline cellulose and starch with water," *International Journal of Pharmaceutics*, vol. 63, no. 3, p. 251, 1990.
- [25] D. E. Kane, "The relationship between the dielectric constant and water-vapor accessibility of cellulose," *Journal of Polymer Science*, vol. 18, no. 89, p. 405, 1955.
- [26] "Agilent basics of measuring the dielectric properties of materials," *Application Note: Measurement Techniques*, p. 32, 2005.

- [27] C. Habeger and G. Baum, "The effect of sheet structure and composition on the X-band dielectric constants of water-paper mixtures," *The Institute of Paper Chemistry, Technical Paper Series*, no. 75, 1979.
- [28] U. Kaatze, "Complex permittivity of water as a function of frequency and temperature," *Journal of Chemical and Engineering Data*, vol. 34, no. 4, p. 371, 1989.
- [29] W. E. A. Davies, "The dielectric constant of fibre composites," *Journal of Physics D: Applied Physics*, vol. 7, no. 1, p. 120, 1974.

## Chapter 7

# Paper-based Microwave Resonators

### 7.1 Introduction

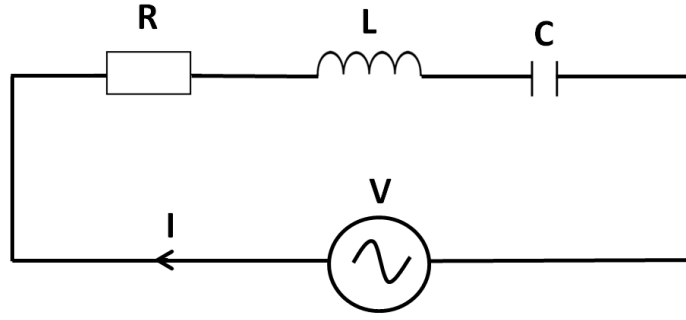
This chapter addresses the design, fabrication and measurement of screen-printed microwave resonators on Neenah paper. This follows on from the work in Chapter 6 which reported on the operation of coplanar waveguides (CPWs) and the behaviours of the ink and paper at microwave frequencies.

A device or system that has a stronger response at particular frequencies is termed a resonator and this stronger response can be exploited in many applications, for example sensors, couplers and filters. In this work, the resonant frequency was designed to be between 0.5 and 3 GHz which provides a good compromise between minimum feature size and device footprint.

First the general theory for resonators consisting of a resistor  $R$ , inductor  $L$  and capacitor  $C$ , known as RLC resonators, is detailed to introduce basic concepts. Work on transmission line stubs is then presented, followed by spiral defected ground structures. The experimental results were supported by analytical models and numerical simulations using Advanced Design Systems (ADS). Possible applications for these resonators as humidity and touch sensors are addressed at the end.

### 7.2 Theory

An RLC resonator is one of the simplest forms of electrical resonator. For this work, the series RLC resonator was considered. This can be seen in Figure 7.1.



**Figure 7.1:** Example series RLC resonator where R is the resistance, L is the inductance, C is the capacitance, V is the voltage and I is the current.

In the series RLC example, resonance occurs at the frequency where there is a periodic energy transfer between the magnetic energy of the inductor and the electrical energy of the capacitor. At this frequency, the combination of the inductance (L) and the capacitance (C) act as a short circuit and the only opposition to the current flow is from the resistance (R), which accounts for the unavoidable losses which degrade the quality of the resonator. The total impedance of the RLC circuit becomes purely real and equal to the resistance. The impedance of the circuit (Z) is:

$$Z(f) = R + Z_L(f) + Z_C(f) \quad (7.1a)$$

$$Z(f) = R + i2\pi fL + \frac{1}{i2\pi fC} \quad (7.1b)$$

$$Z(f) = R \frac{i2\pi fRC - (2\pi f)^2 LC + 1}{i2\pi fRC} \quad (7.1c)$$

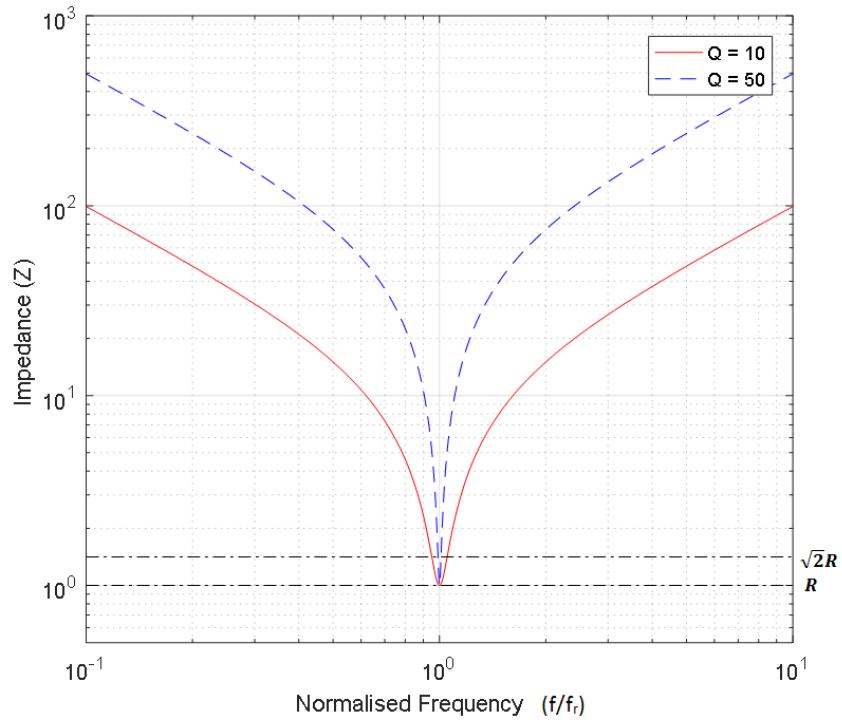
$$Z(f) = R \frac{i(1/Q)(f/f_r) - (f/f_r)^2 + 1}{i(1/Q)(f/f_r)} \quad (7.1d)$$

where  $f$  is the frequency,  $f_r$  is the resonant frequency,  $Q$  is the quality factor and:

$$f_r = \frac{1}{2\pi\sqrt{LC}} \quad \text{and} \quad Q = \frac{1}{2\pi RCf_r} \quad (7.2)$$

The quality factor describes how under-damped a resonator is. The higher the quality factor, the less damping there is. In an electrical resonator, the quality factor is equal to the ratio of the power stored in the circuit reactance and the power dissipated in the capacitor and inductor. Examples of the impedance of two series RLC circuits with differing quality factors are shown in Figure 7.2. The gradient of the plots at frequencies lower than 0.5 and above 2.5 are equal; however the circuit with the higher quality factor is seen to have a sharper minimum in impedance. A higher quality factor is often desirable in circuits and can be altered by changing the values of the resistance and the

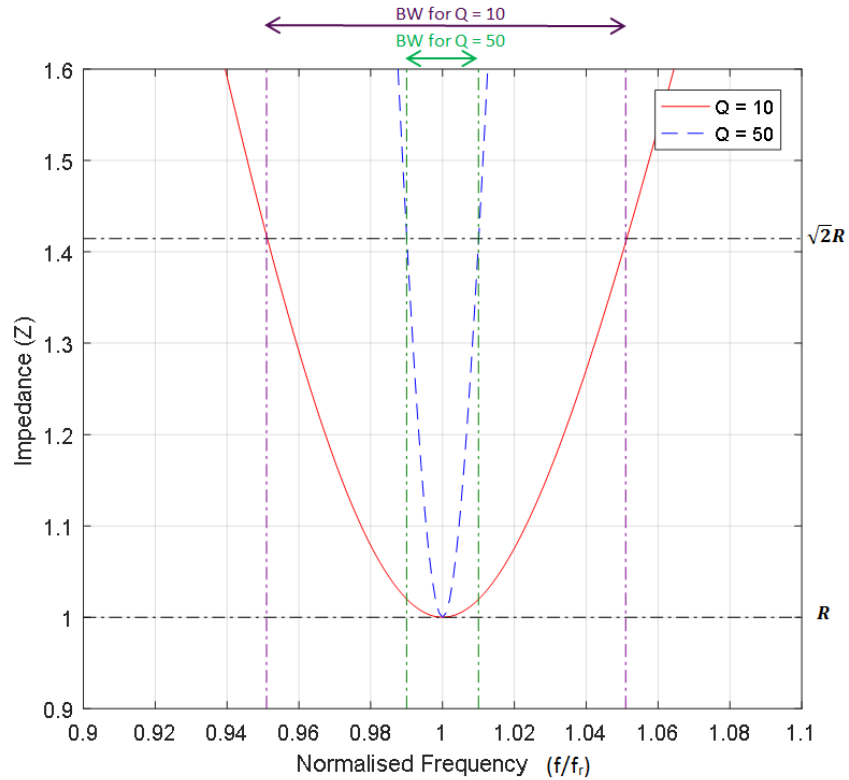
capacitance as governed by Equation (7.2).



**Figure 7.2:** Impedance plots for two example resonators with quality factors of 10 and 50.

The bandwidth of an electrical resonator is defined as the difference in frequency when the magnitude of the impedance is 3 dB (or  $\sqrt{2}$ ) above the minimum impedance (equal to  $R$ ) as shown in Figure 7.3. At resonance, the impedance is equal to the resistance and so the bandwidth can be taken as the difference between frequencies when the plot crosses the horizontal line equal to  $\sqrt{2}R$ . The bandwidth, for the two plots in Figure 7.2 are illustrated in Figure 7.3.





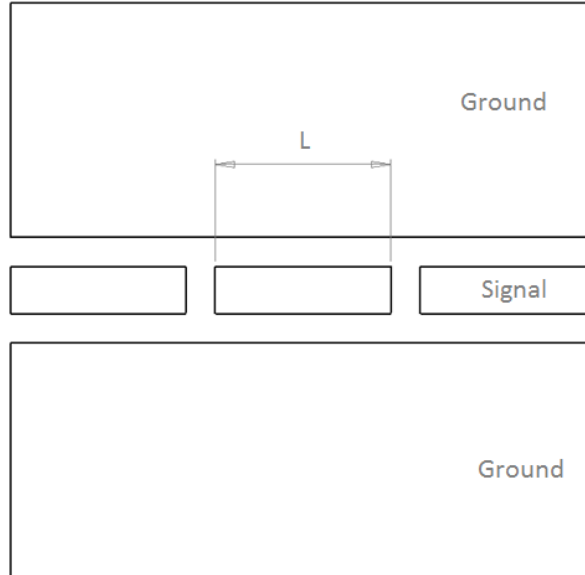
**Figure 7.3:** Impedance plots for two example resonators with different quality factors, highlighting the bandwidth for each.

The bandwidth and quality factor of an RLC resonator are related by the relationship:

$$Q = \frac{f_r}{BW} \quad (7.3)$$

where  $BW$  is the bandwidth in Hertz. A smaller bandwidth, and resulting higher quality factor, means the circuit is more selective which is often more desirable.

A resonance can be achieved at microwave frequencies by incorporating a resonator or discontinuity into transmission lines. This can be done by altering the signal line, as demonstrated in Figure 7.4, or as an addition to the transmission line. The main considerations during the design of these devices are the resonant frequency, the quality factor and the coupling. The resonant frequency is dependent on the dimensions of the resonator; in the example shown in Figure 7.4, the governing length,  $L$ , is highlighted.

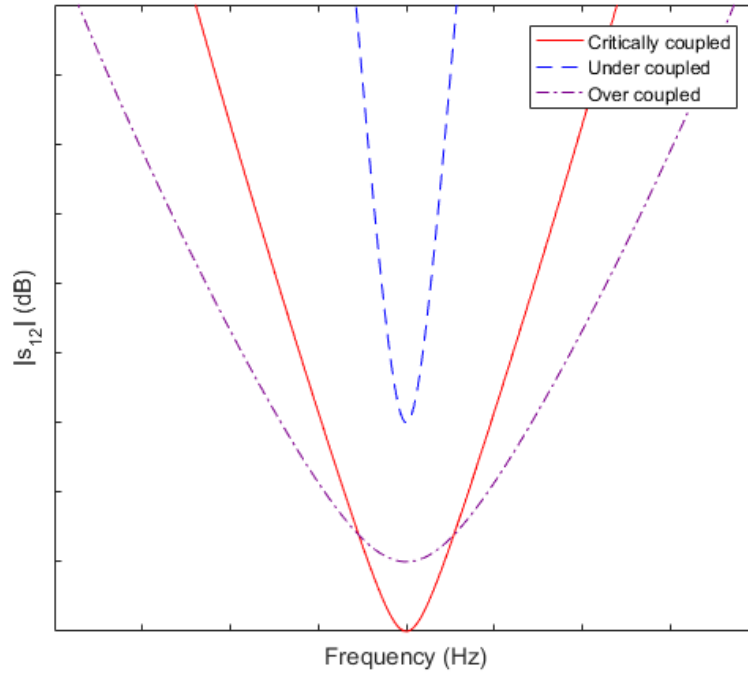


**Figure 7.4:** An example of a coplanar waveguide microwave resonator. This example is a transmission line with an altered signal track to create a resonance.

Coupling is the desirable or undesirable transfer of energy from one medium to another. This can be interference between adjacent resonators or other circuit components. Resonators need to be coupled to external circuitry, for example to the transmission lines in the example above. The level of coupling achieved varies between applications and is often determined by the proximity of the resonator and the external circuitry. A measure of the level of coupling between a resonator and a transmission line is the coupling coefficient ( $g$ ). To obtain maximum power transfer between the resonator and transmission line, they should be critically coupled. This is when the resonator is matched to the transmission line and the coupling coefficient is equal to 1. The coupling coefficient can be defined as the ratio between the unloaded quality factor of the resonator and the quality factor of the external circuit.

$$g = \frac{Q_0}{Q_e} \quad (7.4)$$

where  $Q_0$  is equal to the unloaded quality factor of the resonator and  $Q_e$  is equal to the quality factor of the external circuit. When the coupling coefficient is less than 1, the resonator is said to be under-coupled to the transmission line and when the coupling coefficient is greater than 1, the resonator is said to be over-coupled to the transmission line. When considering the fabricated resonators presented in this chapter, the coupling coefficient cannot be determined as it is not possible to calculate  $Q_0$  and  $Q_e$  independently. Examples of the scattering parameter  $s_{21}$  for a shunt resonator connected between two ports are shown in Figure 7.5 for a critically coupled, an over-coupled and an under-coupled system.

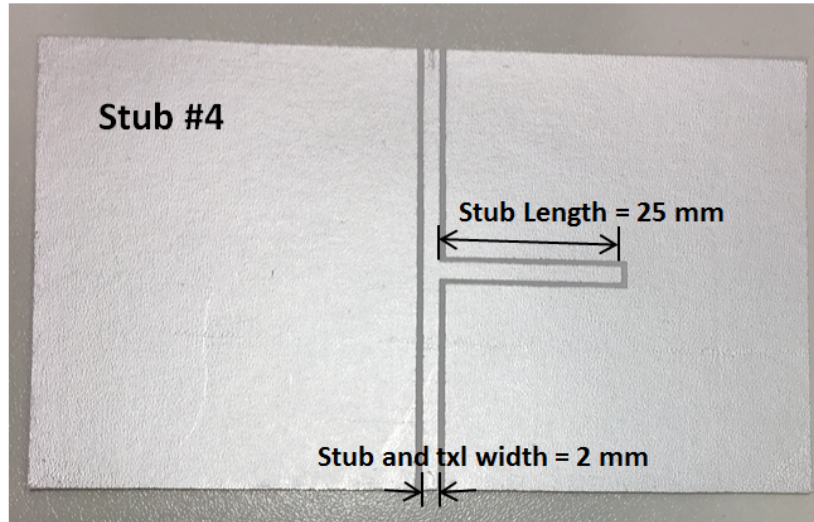


**Figure 7.5:** Examples of resonances created by systems which are critically coupled, under coupled and over coupled.

Increasing the coupling between the resonator and the transmission line increases the transmission of the system but decreases the quality factor. The over-coupled plot in Figure 7.5 shows higher peak values, however the width of the peak is broader. Decreasing the coupling between the resonator and the transmission line does the opposite of this and results in the under-coupled plot. Altering the coupling of the system has no effect on the resonant frequency but should be considered alongside the quality factor when designing and optimising resonators.

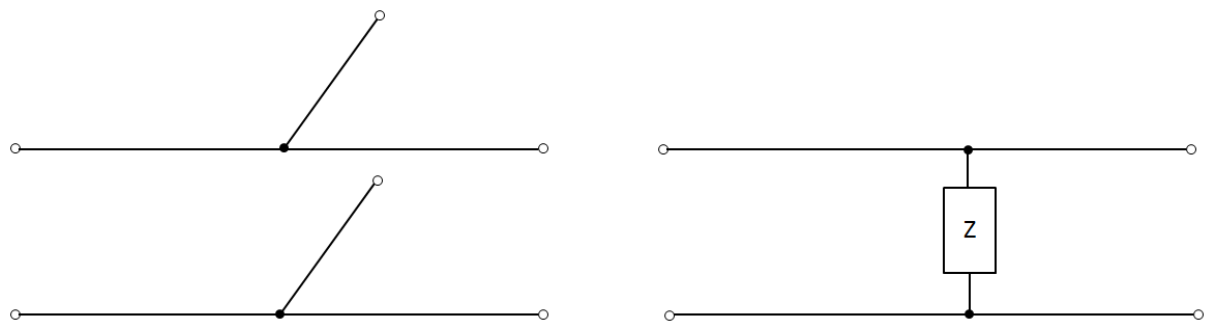
### 7.3 Transmission Line Stubs

A transmission line stub is a length of transmission line that is connected at only one end to the signal track of a transmission line. The free end of the stub is either left as an open circuit, where there is no connection to the ground plane of the transmission line, or it is connected to the ground plane, resulting in a short circuit. Multiple stubs can be used in order to create multiple resonances [1] and the length of the stub dictates the resonant frequency [2, 3]. An example of an open circuit stub fabricated in this work is shown in Figure 7.6.



**Figure 7.6:** Example of a screen-printed design 4 stub. The stub length and stub width are highlighted.

Considering a lossless transmission line, the input impedance of the stub is purely reactive, either capacitive or inductive, depending on the electrical length of the stub and whether it is a short or an open circuit. Stubs can therefore function as capacitors, inductors and resonant circuits at microwave frequencies. Transmission line stubs have been used in this work for initial characterisation of resonator circuits, as stubs have a simple design and are similar to the transmission lines characterised previously in Chapter 6.



**Figure 7.7:** Illustration of a stub in parallel with the transmission line and the equivalent circuit.

The stub is connected in parallel to the transmission line as illustrated in Figure 7.7. The maximum effect of the stub on the transmission line occurs when the impedance of the stub is equal to a short circuit (i.e.  $Z = 0$ ). This results in the scattering parameters  $s_{11}$  and  $s_{12}$  being a maximum and minimum respectively.

### 7.3.1 Analytical Modelling of Transmission Line Stubs

The test circuit for the stub can be divided into the stub itself and two adjacent transmission line sections. Each of these sections can be considered as an ABCD matrix which can then be cascaded

to provide the ABCD matrix for the whole structure. The ABCD matrix for the transmission line is that shown in Equation (7.5) as taken from [4].

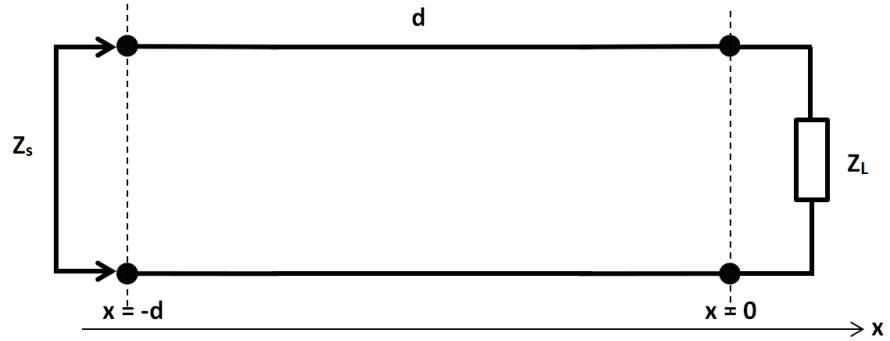
$$TXL(ABCD) = \begin{bmatrix} \cos(g) & jZ_t \sin(g) \\ jZ_t^{-1} \sin(g) & \cos(g) \end{bmatrix} \quad (7.5)$$

The ABCD matrix for the stub is that shown in Equation (7.6) as taken from [5].

$$STUB(ABCD) = \begin{bmatrix} 1 & 0 \\ \frac{1}{Z_s} & 1 \end{bmatrix} \quad (7.6)$$

where  $g = -j\gamma l = \beta l - j\alpha l$ ,  $\alpha$  is the attenuation constant,  $\beta$  is the phase constant,  $l$  is the physical length of the transmission line section,  $Z_t$  is the characteristic impedance of the transmission line and  $Z_s$  is the characteristic impedance of the stub. The resulting ABCD matrix obtained by cascading the transmission line matrix, the stub matrix and the transmission line matrix can then be converted to the s-parameters using the conversion in [6].

The characteristic impedance of the stub ( $Z_s$ ) can be determined by considering only the stub transmission line section, as illustrated in Figure 7.8, where  $Z_{eq}$  is the equivalent characteristic impedance of the stub and equal to  $Z_s$  in Equation (7.6),  $Z_L$  is the load impedance and is determined by whether an open or short circuit stub is considered.



**Figure 7.8:** Simple model for the stub where  $Z_s$  is the equivalent impedance of the stub looking from the end it is connected to the transmission line,  $Z_L$  is the load impedance determined by the end of the stub and  $d$  is the stub length.

The reflection coefficient of this transmission line section is equal to:

$$\Gamma = \frac{Z_L - Z_0}{Z_L + Z_0} \quad (7.7)$$

where  $Z_0$  is equal to the characteristic impedance ( $50 \Omega$ ). The voltage wave can be considered as:

$$V = V^+ e^{-i\beta x} e^{i\omega t} + \Gamma V^+ e^{i\beta x} e^{i\omega t} \quad (7.8)$$

where  $\omega = 2\pi f$ . Similarly, the current is:

$$I = \frac{V^+}{Z_0} e^{-i\beta x} e^{i\omega t} + \Gamma \frac{V^+}{Z_0} e^{i\beta x} e^{i\omega t} \quad (7.9)$$

Substituting Equations (7.8) and (7.9) into  $Z_s = V/I$  and setting  $x = d$ , where  $d$  is the length of the stub. The impedance of the stub ( $Z_s$ ) can be written as:

$$Z_s = Z_0 \frac{e^{-i\beta d} + \Gamma e^{-i\beta d}}{e^{-i\beta d} - \Gamma e^{-i\beta d}} Z_s = Z_0 \frac{1 + \Gamma e^{-2i\beta d}}{1 - \Gamma e^{-2i\beta d}} \quad (7.10)$$

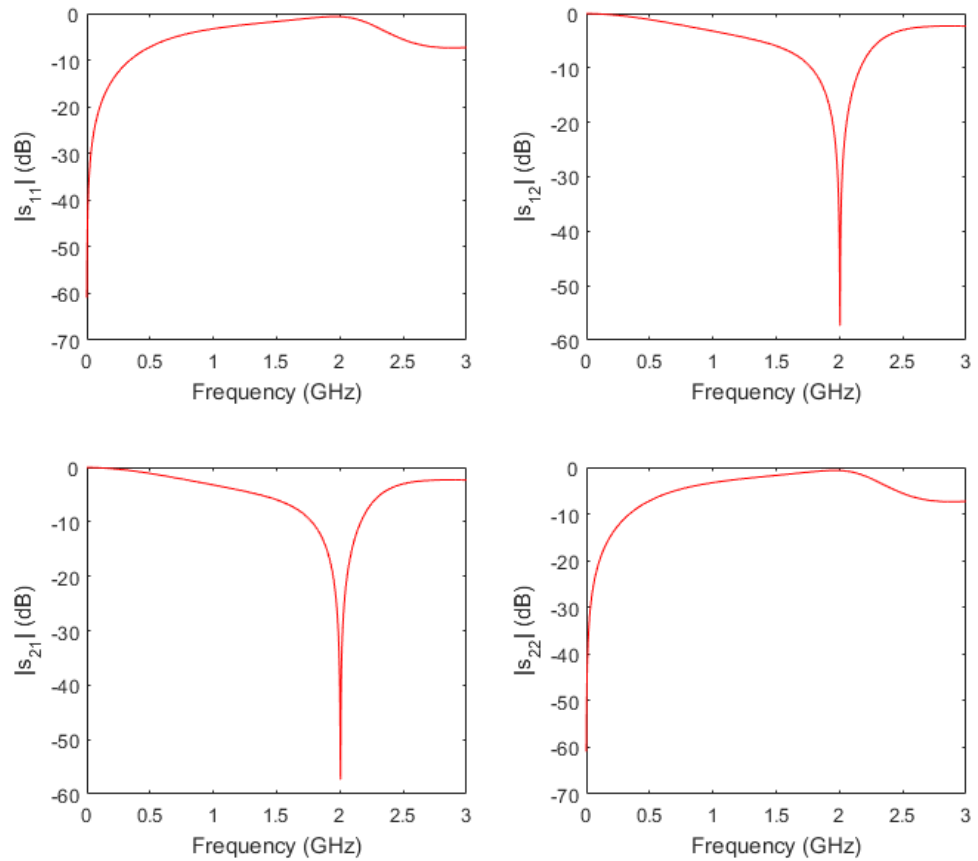
For a short circuit stub, the reflection coefficient is equal to -1 and so Equation (7.10) becomes:

$$Z_{short} = Z_0 \tan \beta d \quad (7.11)$$

For an open circuit stub, the reflection coefficient is equal to 1 and so Equation (7.10) becomes:

$$Z_{open} = -iZ_0 \cot \beta d \quad (7.12)$$

The stubs used in this work were open circuit stubs and so the point at which they acted as a short circuit and had maximum effect on the transmission line was when the length was equal to  $\lambda/4$ . The resulting impedance was equal to zero and so the stub created a resonance in the response. Example data for a design 2 stub using the analytical method is shown in Figure 7.9. Details of the dimensions for a design 2 stub are shown in the next section.



**Figure 7.9:** Scattering parameters generated by analytical modelling for a design 2 stub.

### 7.3.2 Screen-printed Transmission Line Stubs

Four stubs were designed and fabricated to determine the effect of stub length and the effect of signal track width. The aim of the designs was to achieve resonances between 1 and 3 GHz. An example of one of the stubs is shown in Figure 7.6, highlighting the stub length and signal track width. Table 7.1 lists the dimensions of the four stub designs and their resonant frequencies based on analytical calculations, simulations and measurements. All four stubs are open circuit design.

**Table 7.1:** Analytical, simulated and measured resonant frequencies for the stub designs.

Stub	Signal Width (mm)	Stub Length (mm)	Resonant Frequency (GHz)		
			Analytical	Simulated	Measured
1	6	26	2.68	2.08	$1.95 \pm 0.05$
2	6	35	1.98	1.82	$1.63 \pm 0.02$
3	2	25	2.63	2.13	$2.02 \pm 0.03$
4	2	33	1.98	1.85	$1.71 \pm 0.02$

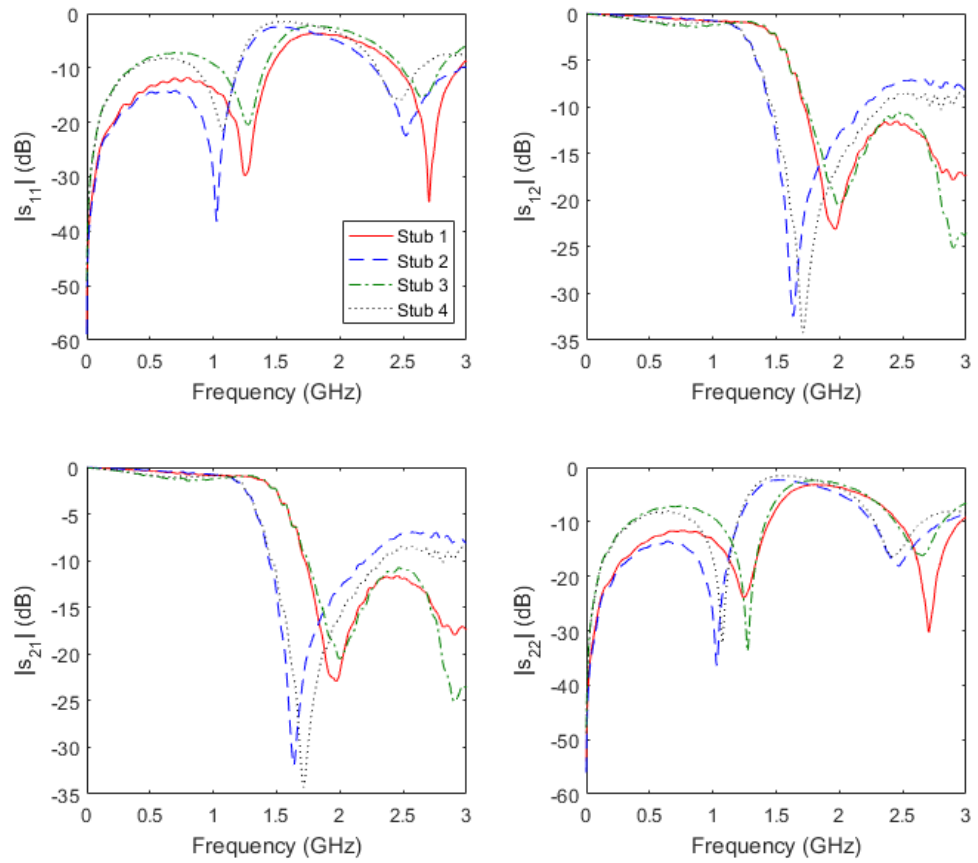
The stubs were simulated using Agilent Advanced Design Systems (ADS) software, introduced in the previous chapter, and the resulting simulated resonant frequency quoted in Table 7.1. Further

details on the simulations will be presented later in this section. The stubs were measured using a HP 8753C Vector Network Analyser (VNA) and the same connectors that were used to measure the transmission lines. The value quoted in Table 7.1 for the analytical resonant frequency is using  $f_r = v/\lambda$ , where  $v$  is equal to the propagation velocity as a fraction of the speed of light. This equation was used initially to determine the required length of the stubs for a desired resonant frequency. The stub length is equal to  $\lambda/4$  where  $\lambda$  is the wavelength in metres.

The measurement range of the VNA used is up to 3 GHz and so the designed resonant frequencies were chosen to be 2 GHz and 2.5 GHz. The propagation velocity for each stub was determined from the transmission line data taken in Chapter 6 at the frequencies chosen, for the 2 mm and 6 mm signal track width transmission lines. The values for  $v$  were  $0.9295c$ ,  $0.9227c$ ,  $0.8757c$  and  $0.8704c$  for stubs 1 - 4 respectively. As the frequency and propagation velocity were known, the wavelength and required length of the stub could be calculated.

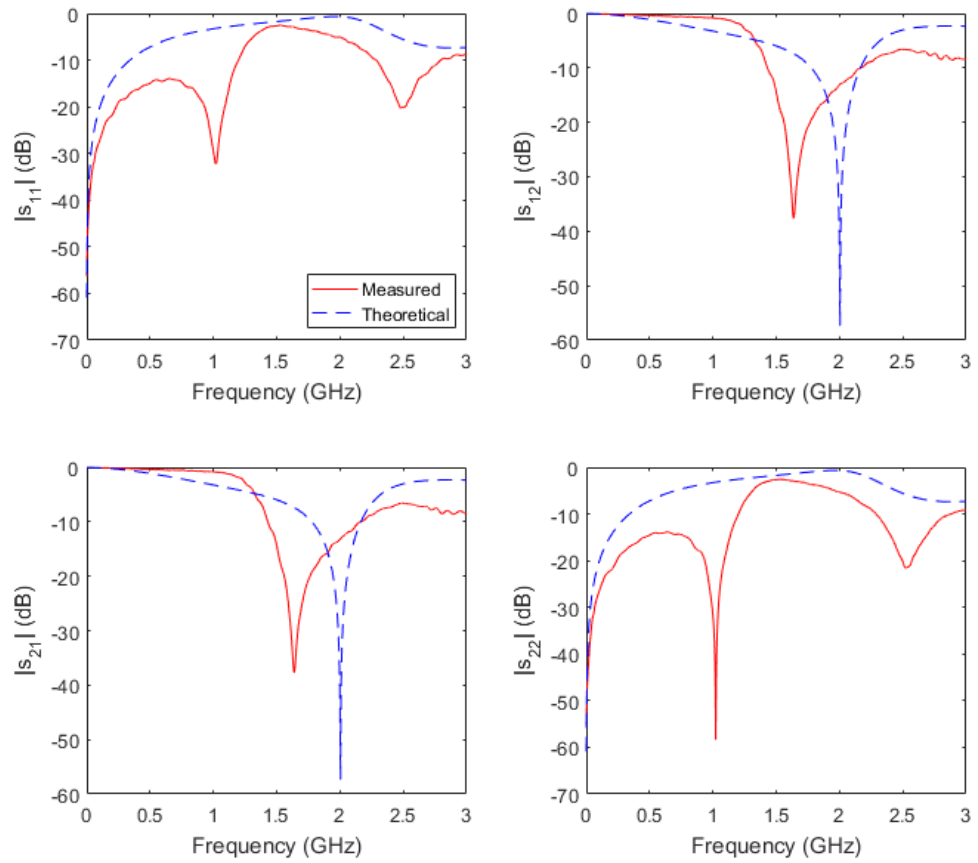
The measured scattering parameters for the four stubs are shown in Figure 7.10. The resonant frequency was the frequency at which  $s_{12}$  and  $s_{21}$  were at a minimum. The resonant frequency for the stubs with equal length were within 3% of each other. The minima in  $s_{11}$  and  $s_{22}$  were due to the transmission lines on either side of the stub; the results in Chapter 6 for the screen-printed transmission lines show the same response.





**Figure 7.10:** Measured scattering parameters for stubs with four different geometries.

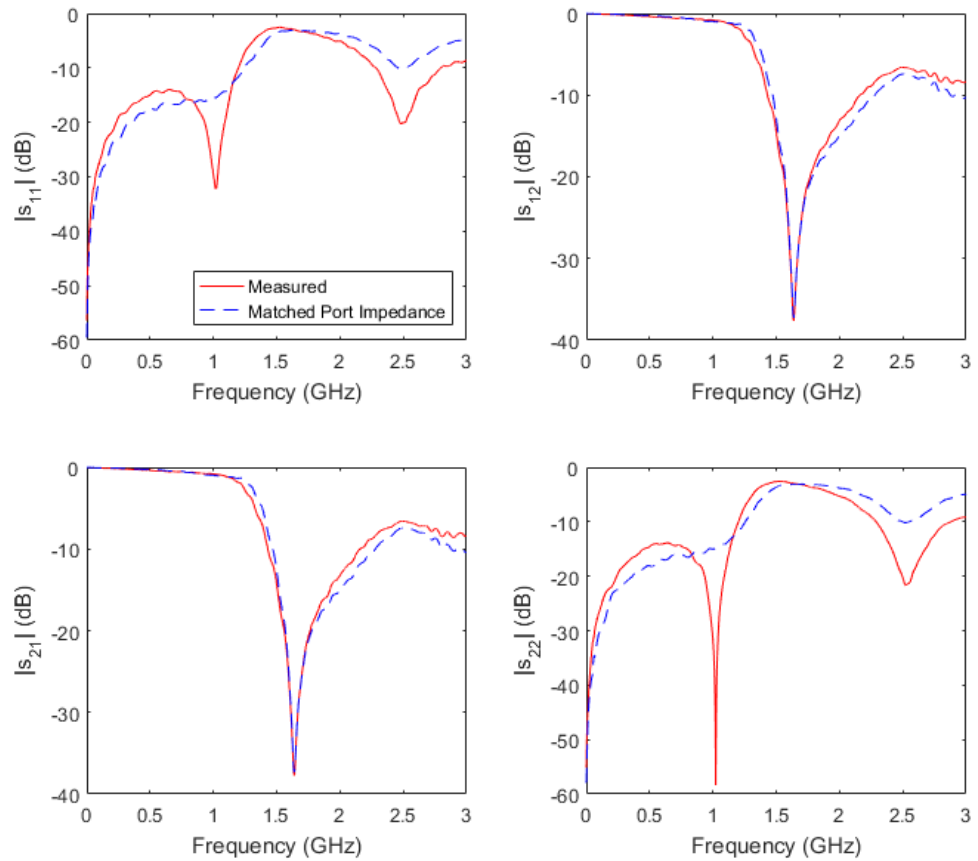
The measured and simulated resonant frequency values for each of the stubs were in agreement with each other, however the analytical values were not. Measured and analytical data for a design 2 stub are compared in Figure 7.11 and it can be seen that the resonant frequency of the measured resonator is approximately 0.4 GHz lower than the analytical one. This could be due to the impedance mismatch between the ports and the transmission line impedance; an additional effect caused by the transmission lines; fringing at the end of the stub causing a change in capacitance and a change in the electrical length of the stub; the length of the stub being measured incorrectly; or from additional modes being injected into the system. These are considered individually here with relevant theory added. Altering the shape of the device at the point where the transmission line and stub meet can minimise errors. However this was not considered here as it was beyond the scope of this project.



**Figure 7.11:** Comparison between the measured scattering parameters and those generated by analytical modelling for a design 2 stub.

### Accounting for the Mismatch Between Port and Transmission Line Impedance

The transmission lines in this work do not have a characteristic impedance equal to  $50\ \Omega$ . This led to a mismatch in impedance between the ports and the transmission line. This mismatch can result in a non-ideal response and could be a possible reason for the difference in resonant frequency of the measured and analytical values. In order to determine if this was the cause in resonant frequency shift, the measured scattering parameters were converted to the ABCD matrix using the conversion in [6] with the impedance set to  $50\ \Omega$  and then converted back to the scattering parameters using the impedance measured for a transmission line with the same signal track width. This compensated for any effects due to the mismatch of the ports. Example measured data for a design 2 stub was compared to measured data which was converted using the method above and is shown in Figure 7.12.

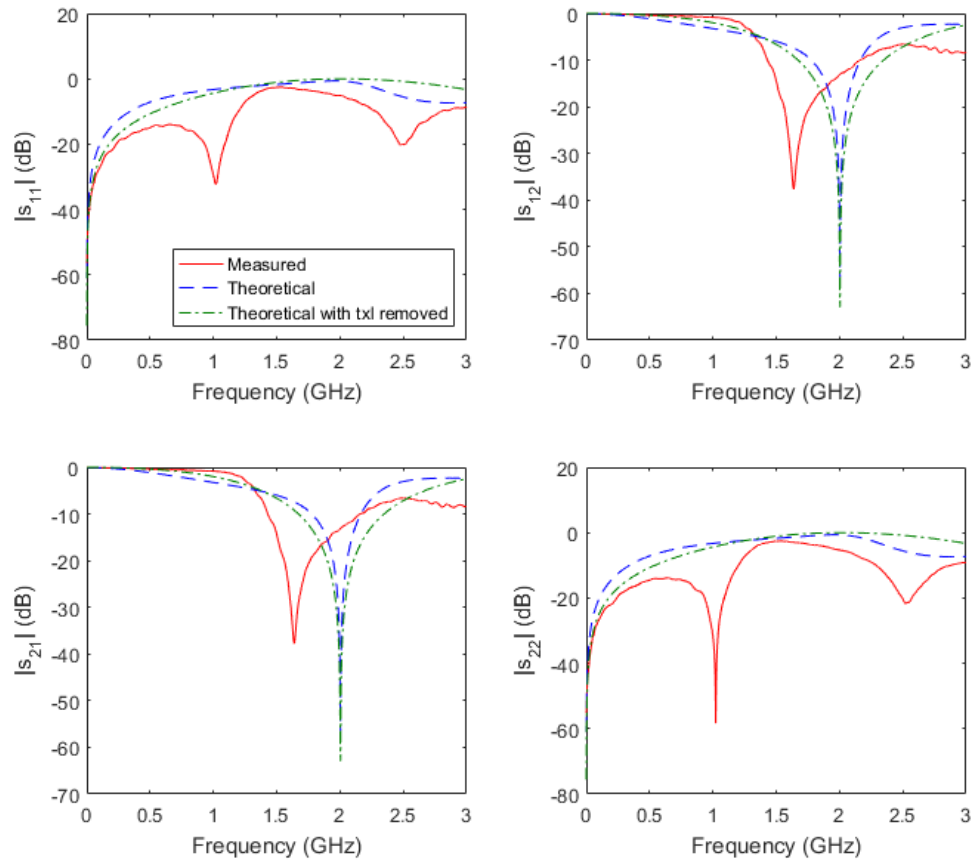


**Figure 7.12:** Measured scattering parameters for stub 2 design compared to measured scattering parameters for which the impedance mismatch of the ports and transmission lines is removed.

It can be seen that there were changes to the scattering parameters  $s_{11}$  and  $s_{22}$ , however  $s_{12}$  and  $s_{21}$  remained the same and so there was no effect on the resonant frequency. This indicated that the difference in theoretical and measured resonant frequency was not due to the mismatch in port and transmission line impedance.

### Accounting for the Effect of Transmission Lines

As the transmission lines are not lossless, they could affect the resonant frequency. In order to confirm if this was the case, the cascading method to determine the theoretical scattering parameters detailed above can be used with only the effect of the stub considered. An example of the resulting scattering parameters, which were converted from the ABCD matrix of the stub alone were compared to the measured scattering parameters and the theoretical s-parameters with the transmission lines included, shown in Figure 7.13.



**Figure 7.13:** Measured scattering parameters for stub 2 design compared to scattering parameters calculated analytically (theoretical) and scattering parameters calculated analytically with the effect of the transmission lines (txl) removed.

It can be seen that there was some change in the overall shape of all the scattering parameters when both theoretical sets of data were compared. However, there was no change in the resonant frequency and the measured resonant frequency was still approximately 0.4 GHz lower than the theoretical ones. This showed that the effect of the transmission lines was not causing the change in resonant frequency seen when comparing the theoretical and measured data.

### Accounting for the Effect of Fringing

When considering open circuit stubs, an electric field exists at the open circuit between the terminated signal track of the stub and the surrounding ground plane, giving rise to a capacitance, which is known as fringing. This capacitance is equivalent to an additional stub and so the combination of both stubs can be equated to one single, longer stub. The additional length of the stub due to fringing is denoted as  $l_{oc}$  and can be calculated from the open circuit capacitance ( $C_{oc}$ ) as in Equation (7.13). Theory and equations for considering the effect of fringing are taken from [7].

$$C_{oc} = \frac{\tan(\beta l_{oc})}{\omega Z_0} \quad (7.13)$$

$$C_{oc} = C_{oc(air)} \epsilon_{eff} \quad (7.14)$$

$$\text{where } \epsilon_{eff} = 1 + \frac{(\epsilon_r - 1) K(k_1) K(k_0)}{2 K(k'_1) K(k'_0)} \quad (7.15)$$

$$\text{and } C_{oc(air)} = \frac{2\epsilon_0}{\pi} \left\{ (S + W) \left[ \frac{\ln(\eta + \sqrt{1 + \eta^2})}{\eta} + \ln \left( \frac{\sqrt{1 + \eta^2} + 1}{\eta} \right) - \frac{1}{3} \left( \frac{1}{1 + \sqrt{1 + \eta^2}} + \frac{1}{\eta + \sqrt{1 + \eta^2}} \right) \right] - (S + 2/3W) \right\} \quad (7.16)$$

$$\text{where } \eta = \frac{g_1}{S + W} \quad (7.17)$$

where  $S$  is equal to the signal track width,  $W$  is equal to the gap between the signal track and the ground plane along the length of the stub and  $g_1$  is equal to the gap between the signal track and the ground plane at the end of the stub. For this work,  $W$  is equal to  $g_1$  which is 1 mm.

Once the open circuit capacitance was calculated the additional stub length due to fringing could be determined. The values for  $Z$  and  $\beta$  were taken from transmission line data with the same track width at the resonant frequency. The resulting changes in length due to fringing for each of the four stubs are summarised in Table 7.2. The theoretical resonant frequency, accounting for the additional stub length, is also listed.

**Table 7.2:** Measured resonant frequencies ( $f_r$ ) for four stub geometries compared to analytically calculated resonant frequencies for the same stubs with the effect of fringing accounted for.

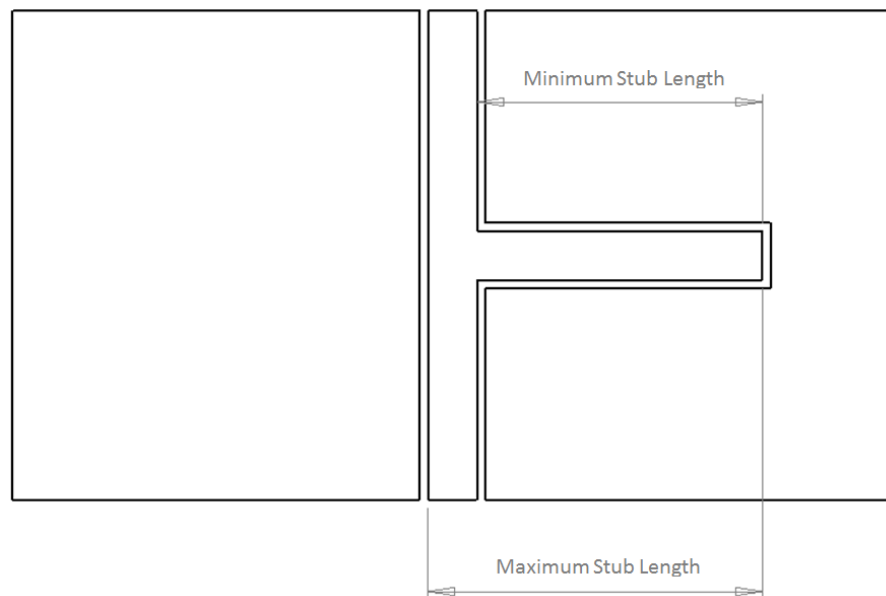
Stub	Measured $f_r$ (GHz)	$l_{oc}$ at $f_r$ (mm)	Theoretical $f_r$ accounting for $l_{oc}$ (GHz)
1	1.95	2.04	2.46
2	1.63	2.28	1.86
3	2.02	0.703	2.56
4	1.71	0.697	1.94

The resonant frequency was shown to reduce from the values quoted in Table 7.1, but the theoretical values were still approximately 0.5 GHz higher for stubs 1 and 3 and approximately 0.2 GHz higher for stubs 2 and 4 when compared to the measured values. Changing the length of the stub was shown to alter the resonant frequency as expected; however, the change in stub length due to fringing was not

sufficient to explain the difference in resonant frequency when comparing theoretical and measured data.

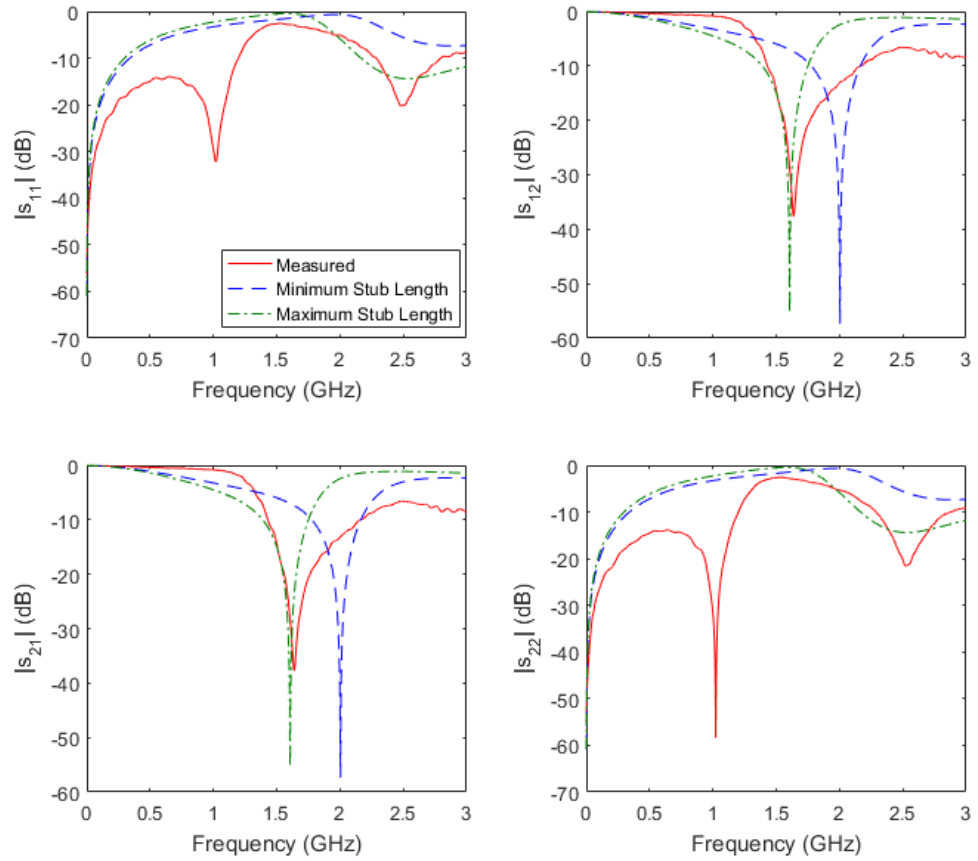
### Accounting for the Finite Transmission Line Width

The length of the stub can be taken from several positions. Changing the length of the stub has been shown to alter the resonant frequency. Previous results took the stub length as being from the edge of the signal track to the end of the stub; the effect of fringing and the resulting increase in stub length has been shown to reduce the theoretical resonant frequency. The measurement for stub length used to this point was considered the minimum stub length and the maximum physical stub length was considered to be from the end of the stub to the opposite end of the signal track, as shown in Figure 7.14.



**Figure 7.14:** Illustration of the minimum and maximum stub length dimensions.

The maximum electrical stub length can be considered as the maximum physical stub length, plus the additional length due to fringing. This was the value used to produce the results in Figure 7.15, which were created using the cascading method and varying the stub length. These results were for an example of stub design 2 where the minimum length is 35 mm and the maximum length was a total of 43.28 mm (41 mm physical length plus 2.28 mm additional length due to fringing).



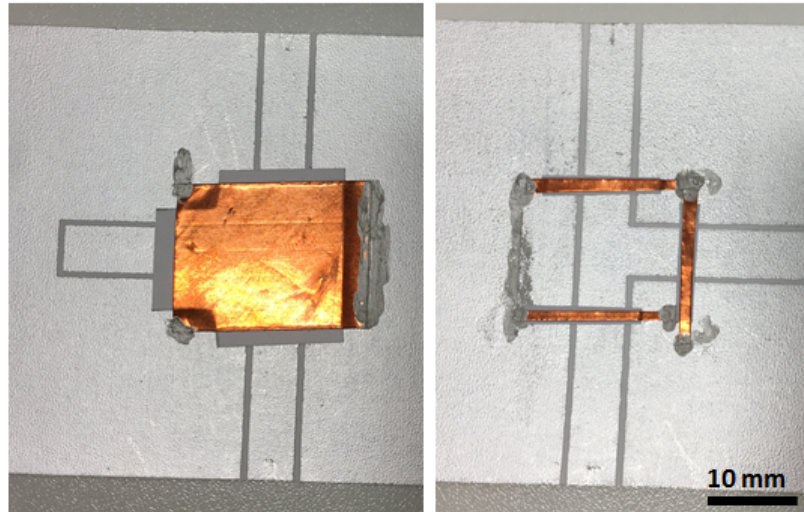
**Figure 7.15:** Comparison of measured scattering parameters for stub 2 design with those calculated analytically using the minimum stub length and the maximum stub length with the effect of fringing also accounted for.

Considering the maximum stub length, including the effect of fringing, was shown to account for the difference in resonant frequency between the measured and theoretical data. Considering the maximum stub length and the additional length due to the effect of fringing, the theoretical resonant frequency was then within 5% of the measured resonant frequency. The shape of the measured plot when compared to the theoretical one was still not a perfect fit but this could be explained by the effect of the transmission lines on the scattering parameters and the effect of the mismatch between the ports and the transmission line.

### Accounting for the Transmission Line Discontinuity

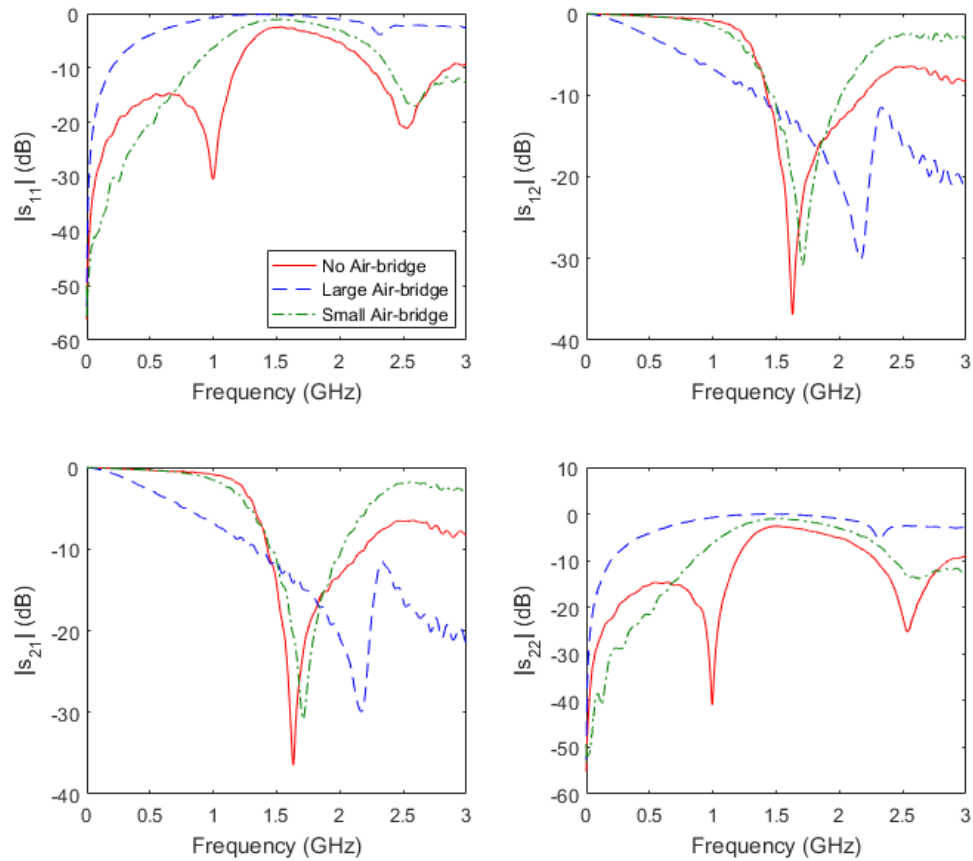
Discontinuities are often found in microwave networks and circuits, either by design or necessity; an example of a discontinuity is the junction where the transmission line and the stub meet. Several modes propagate along the transmission line, for example the design in this work supports full slab modes due to the large area of substrate material exposed with no metallisation [8]. When a discontinuity is included in the transmission line, further modes can be injected which interfere with the original ones and lead to radiation losses. In order to reduce this effect, air-bridges can be added to the device

between the ground planes. Air bridges are typically used in coplanar waveguide design, they short the ground planes and prevent spurious modes. In reality, more uniform connections would be used and the conductive sections would be made from the same material as the signal and ground tracks. However for this work copper tape and silver dag have been used as a proof of concept. Air-bridges were added to the stubs to improve the resonant response with the designs shown in Figure 7.16 and their resulting scattering parameters shown in Figure 7.17.



**Figure 7.16:** Examples of air-bridges created using copper tape, made to counteract the effect of discontinuities along the transmission line.





**Figure 7.17:** Measured scattering parameters for stub 2 design with: no air-bridge; a large air-bridge where the discontinuity is fully covered; and a small air-bridge where the ground planes were connected with minimal copper tape.

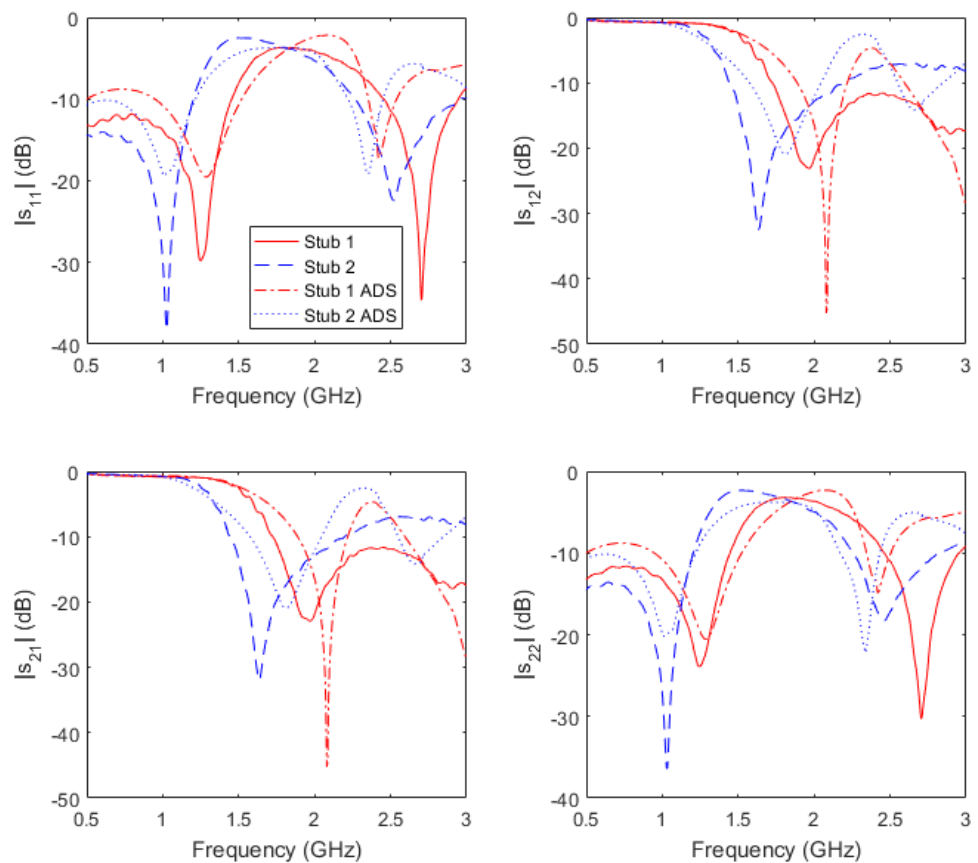
Both air-bridges were created using copper tape with paper between the tape and the ground plane to prevent connection between the signal and ground tracks. The larger air-bridge on the left of Figure 7.16 covers the entire join between the stub and the main transmission line. This was shown to largely affect the resonant frequency and prevented the stub from operating as it should. The smaller, separate air-bridges shown on the right of Figure 7.16 had little effect on the resonance of the device but removed the minima in  $s_{11}$  and  $s_{22}$ . The scattering parameters  $s_{12}$  and  $s_{21}$  showed lower losses at higher frequencies when the air-bridges were added. These air-bridges could be improved further and have less effect on the resonance of the stub, but for this work the theory has been verified suitably.

The measured scattering parameters for the stubs were compared to theory and it were shown that the difference in resonant frequency was mainly due to the measured length of the stub and fringing effects. The differences in  $s_{11}$  and  $s_{22}$  could be explained by a combination of port impedance mismatch, the effect of the transmission lines either side of the stub and also the modes injected due to the stub discontinuity. Each of these factors were investigated and the discrepancies between the measured and theoretical scattering parameters explained. The difference in resonant frequency between the measured and analytical data is due to the difference in measured length of the stub

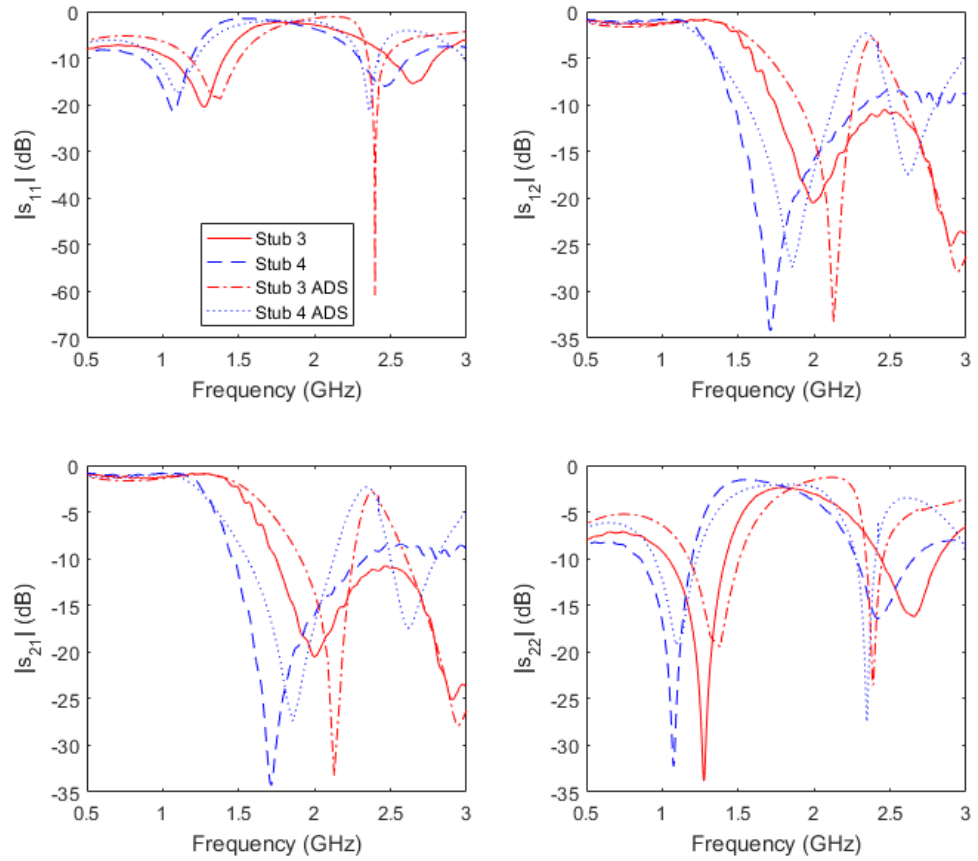
and the effect of fringing at the end of the stub. The difference in reflection between the measured and analytical data is due to the addition of the transmission lines and corresponding mismatch of impedance between the port and the line. This will cause the minima in the reflection as seen for the transmission line data in the previous chapter.

### 7.3.3 Simulations of Transmission Line Stubs

The stubs were simulated using Agilent Advanced Design Systems (ADS) software as in Chapter 6, using the same parameters for the substrate and metal layers. The results for the simulations are compared to the measured scattering parameters of the stubs in Figures 7.18 and 7.19 for stub designs 1 and 2 and then 3 and 4 respectively.



**Figure 7.18:** Measured and simulated scattering parameters for stub designs 1 and 2.

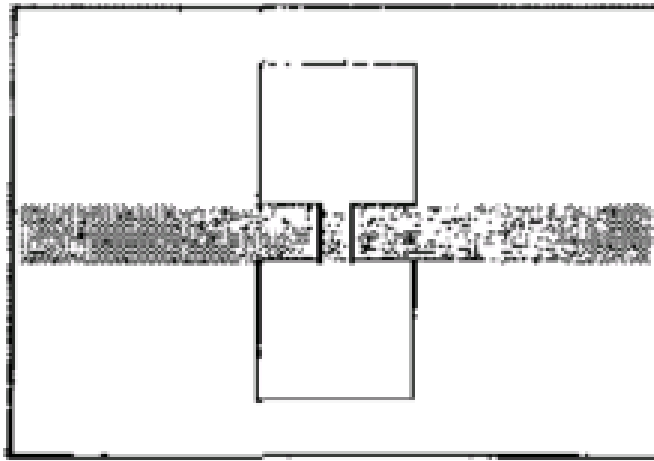


**Figure 7.19:** Measured and simulated scattering parameters for stub designs 3 and 4.

These simulations were shown to be in agreement with the measured scattering parameters. The measured resonant frequency of the spirals was consistently lower than the simulated values by  $0.15 \pm 0.03$  GHz. This was good agreement and the lower value could be attributed to a longer stub length due to variation in the fabrication process. All screen-printed devices show features larger than those designed.

## 7.4 Defected Ground Structure Resonators

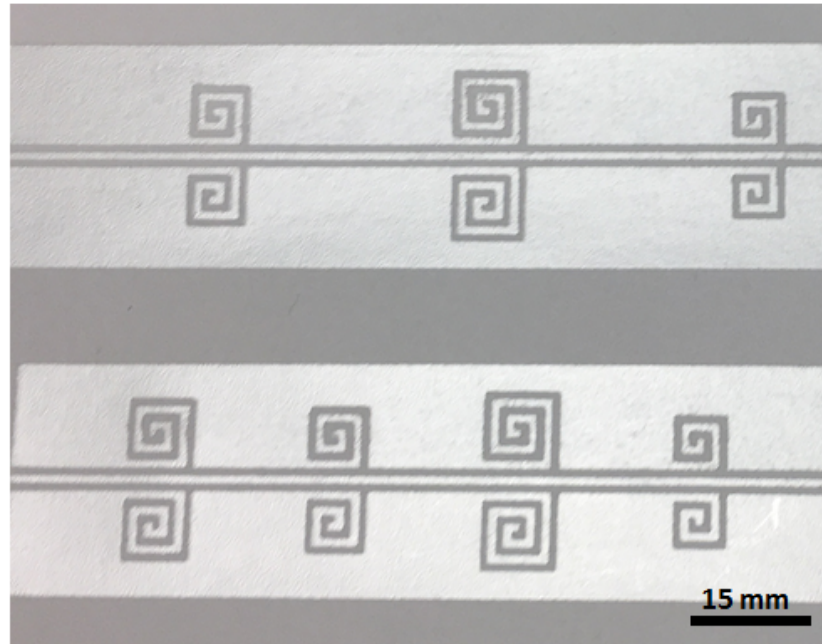
A defected ground structure (DGS) can be used to create a resonator coupled to a coplanar waveguide or micro-strip [9–19]. Defected ground structures have an absence of conductor in the ground plane which results in a change in the behaviour of the waveguide and often a resonance. The first example of a DGS was by Jong et al. in 1999 who used the design shown in Figure 7.20, which is the etched ‘photonic bandgap structure’ in the ground plane of a microstrip, known as DGS. This shape is called a dumbbell DGS and is common for both microstrip [20] and CPW [21] designs.



**Figure 7.20:** The first example of defected ground structure, taken from [22].

Building on the dumbbell design, groups have created square-shaped designs and also used shorts in these squares to create tunable resonators [21, 23, 24]. The substrate can also be altered in addition to DGS to create resonators and are named ‘substrate integrated waveguides’ [25, 26]. Filters are a common application for the DGS resonators [27–31].

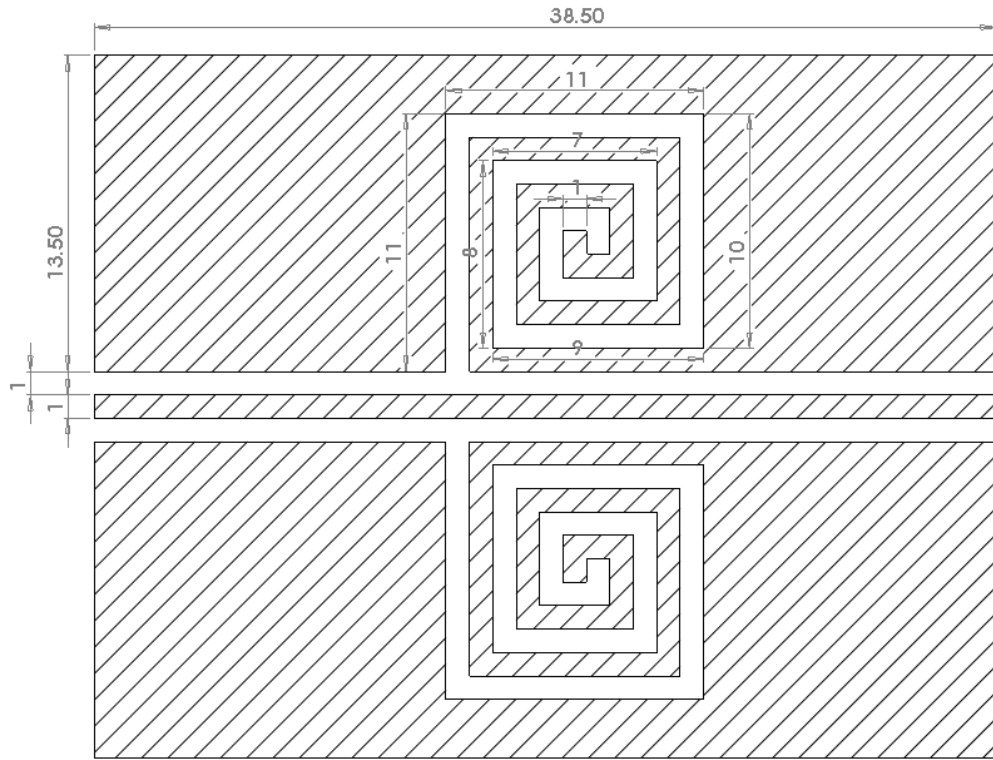
This work investigates a spiral defected ground structure, with screen-printed examples shown in Figure 7.21. The resonant frequency was determined by the size of the spiral, taking into account the number of turns and the length/width of the spiral. Spiral resonators have been created by other groups using microstrip designs for touch pad and humidity sensor applications [32–35]. Choi et al. compared simulated results for measurements of microstrip-based spiral resonators for use as touch pads [32]. The spirals are of approximately 3.5 and 5 mm in size and the microstrips are inkjet printed onto photo paper, resulting in resonances of 1.83 and 0.94 GHz respectively. Preradovic et al. produce spiral resonators of less than 1 cm in dimensions using copper etching with resulting resonant frequencies between 2.5 and 3 GHz. Similar spiral DGS resonators have been fabricated for CPW and grounded CPW, however not on paper substrates [36, 37].



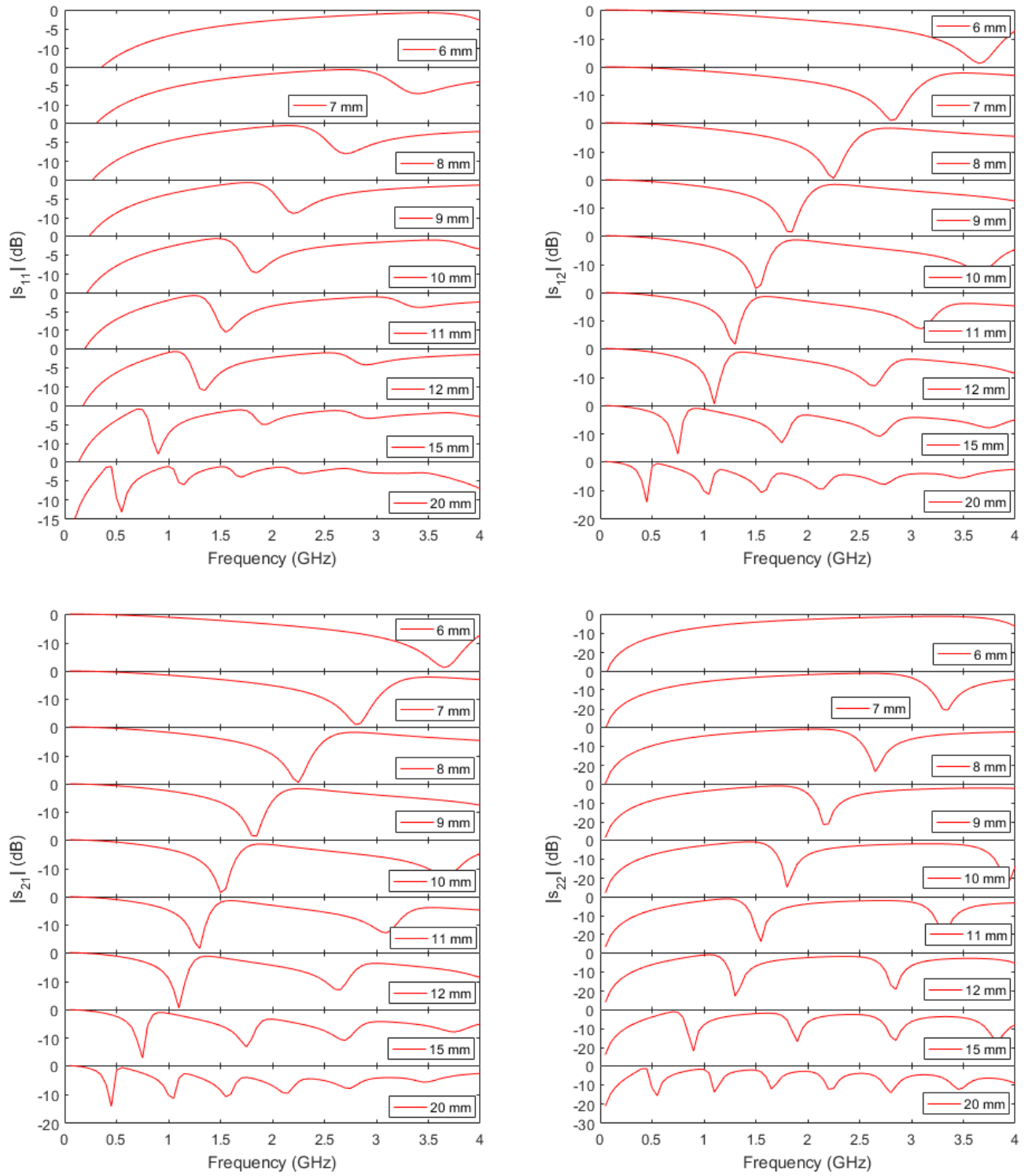
**Figure 7.21:** Example spiral defected ground structure resonators fabricated using screen printing on paper.

#### 7.4.1 Design of Spiral Defected Ground Structure Resonators

For this work, the resonant frequency of the spiral resonators was determined using ADS simulations prior to fabrication. The simulations were conducted using ADS with the same parameters as detailed for simulation of the transmission lines. The longest length of the spiral, as shown in Figure 7.22, was increased from 6 mm to 20 mm to determine the resulting resonant frequency. Results for these simulations are shown in Figure 7.23. These dimensions were chosen as work from Lim et al. showed that spirals up to 6 mm large produced resonant frequencies approximately 5 GHz [37].



**Figure 7.22:** Schematic diagram of an example spiral defected ground structure resonator. Units for all dimensions are in mm.



**Figure 7.23:** Simulated scattering parameters for spiral defected ground structure resonators with varying dimensions with the largest spiral edge ranging from 6 mm to 20 mm.

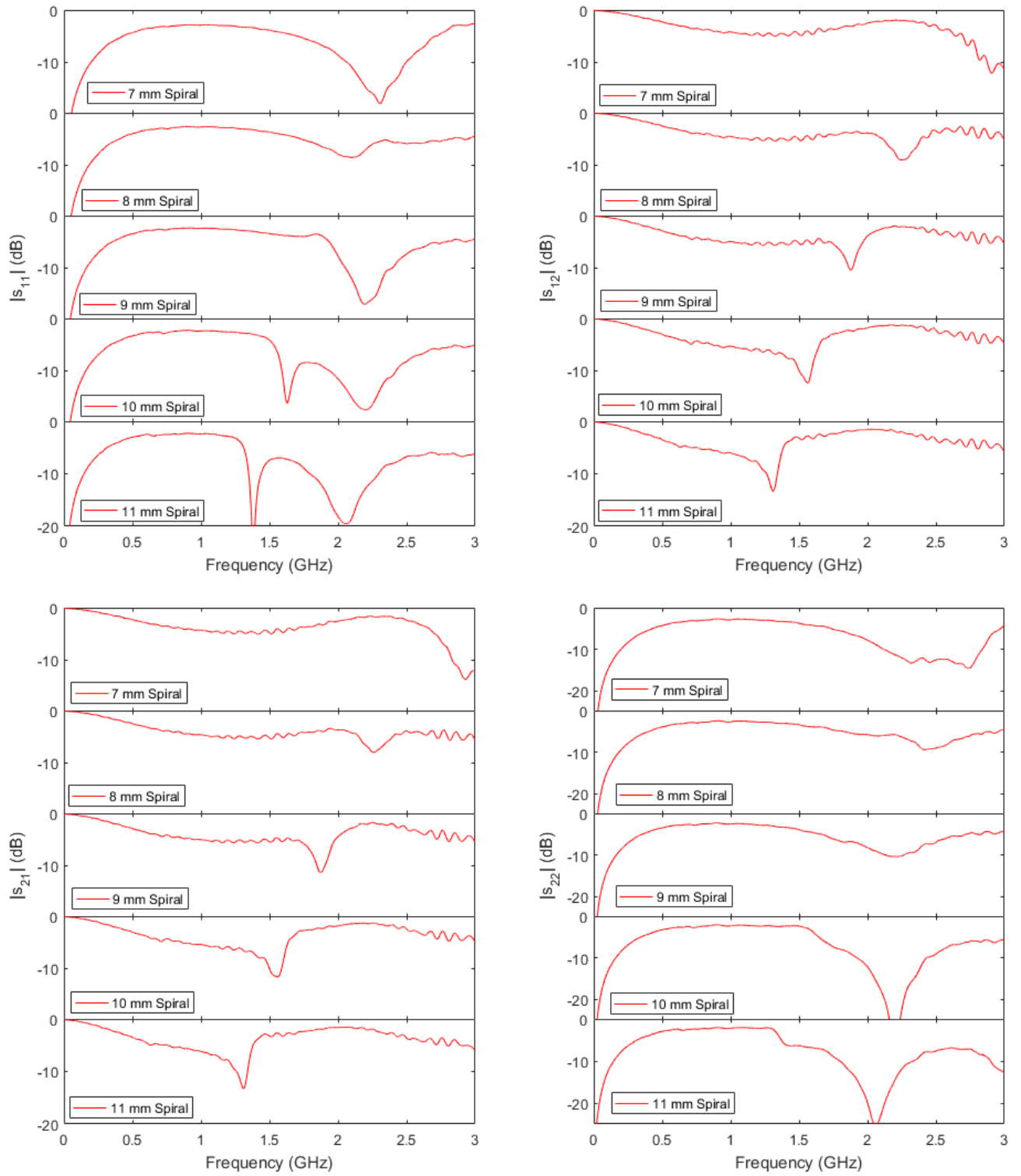
The maximum measurable frequency in this work was 3 GHz and so it could be seen that a spiral with 6 mm maximum length was not suitable. Spirals with maximum lengths longer than 11 mm have multiple resonances within the measurable range of the VNA and so were also not suitable as this could lead to errors within the measurements. Spirals with maximum lengths between 7 mm and 11 mm were considered in this work as they have single resonant peaks within the range 1 - 3 GHz.

The differences in  $s_{11}$  and  $s_{22}$  were due to the asymmetry of the device, the connection between the DGS and the transmission line was at one side of spiral. However, the minima were below  $-10$  dB and clear peaks at 0 dB could be seen.

#### **7.4.2 Measurement of Spiral Defected Ground Structure Resonators**

Defected ground structures were made using the screen-printing method detailed in Chapter 4. Spirals with maximum lengths of 7-11 mm were printed along a continuous transmission line with spacings of 15 mm and 30 mm. Devices with identical spirals printed on either side of the signal track were printed with examples shown in Figure 7.21. Examples where the spirals were not identical on either side of the signal track were also fabricated. Results for single pairs of identical spirals are shown in Figure 7.24.





**Figure 7.24:** Measured scattering parameters for spiral defected ground structure resonators with varying dimensions with the largest spiral edge ranging from 7 mm to 11 mm.

These results were comparable with the simulated results shown in Figure 7.23. The resonant frequency (the minima in  $s_{12}$ ) were within 0.1GHz for all spiral resonators. The transmission at resonance for the simulated results was lower than the measured; this was as expected as the dimensions will vary slightly and the simulations are often subject to lower losses. The measured data had a drop in able transmission at lower frequencies due to additional losses which were not

accounted for in the simulations, and there were oscillations due to the calibration non-idealities as the calibration did not account for the connectors.

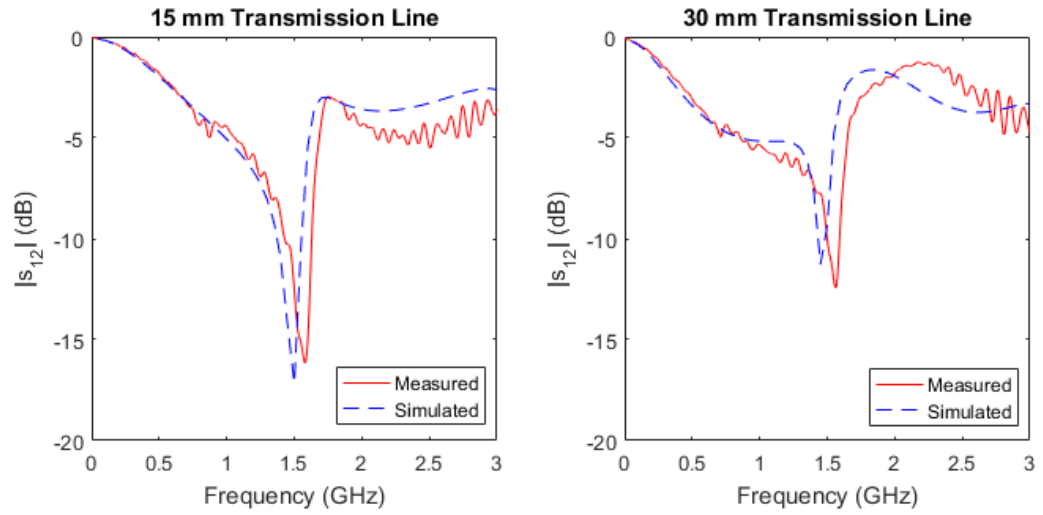
The quality factor was calculated for each of the resonators using Equation (7.3) and the measured resonant frequency taken from scattering parameter  $s_{12}$  from Figure 7.24. The bandwidth and quality factor are listed in Table 7.3 for five examples of each of the measured spirals. The bandwidth was taken at the point 3 dB above the minima and the resonant frequency was at the point of the minima. The bandwidth and quality factor of the 7 mm spiral could not be determined as the resonant frequency was higher than what can be measured with the VNA. The values presented were based on maximum and minimum measured data.

**Table 7.3:** Measured resonant frequencies for four spiral DGS resonators and their respective bandwidth and quality factors.

<b>Spiral longest length (mm)</b>	<b>Resonant Frequency (GHz)</b>	<b>Bandwidth (GHz)</b>	<b>Quality Factor</b>
8	$2.25 \pm 0.03$	$0.16 \pm 0.04$	$15.4 \pm 4$
9	$1.88 \pm 0.02$	$0.09 \pm 0.01$	$21.6 \pm 2$
10	$1.56 \pm 0.02$	$0.095 \pm 0.01$	$16.7 \pm 2$
11	$1.32 \pm 0.02$	$0.078 \pm 0.01$	$17.2 \pm 3$

The resonant frequency and the bandwidth were seen to be highly repeatable with low variation. The variation in the quality factor was higher but only approximately 10% of the average values. Although the quality factor of the 9 mm spiral was higher than that of the 10 and 11 mm ones, they were still within the variation of each other. The quality factor will be highly dependent on the fabrication method and so the change in quality factor was likely to be due to this. The quality factor for the 8 mm and 7 mm was likely to be lower as the minima in  $s_{12}$  were consistently broader.

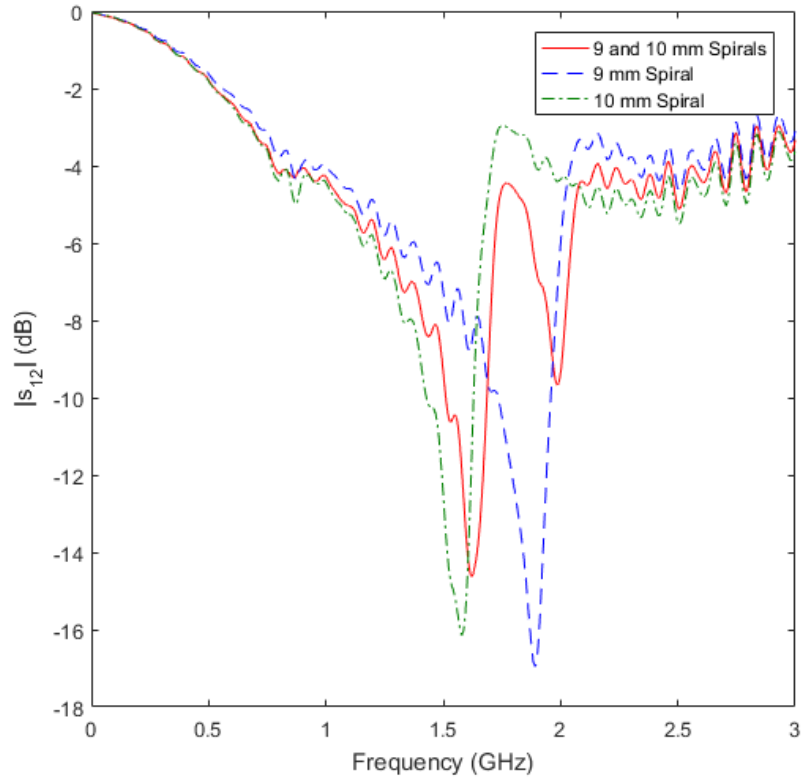
The effect of the transmission line length on either side of the spiral was considered and examples of this for both measured and simulated data are shown in Figure 7.25. Only  $s_{12}$  or  $s_{21}$  are considered for further results, as these showed the resonance of the device and this could be used in any application.



**Figure 7.25:** Measured and simulated scattering parameter  $s_{12}$  for an example spiral defected ground structure resonator with 15 (left) and 30 mm (right) transmission lines on either side of the resonator to determine the effect of transmission line length.

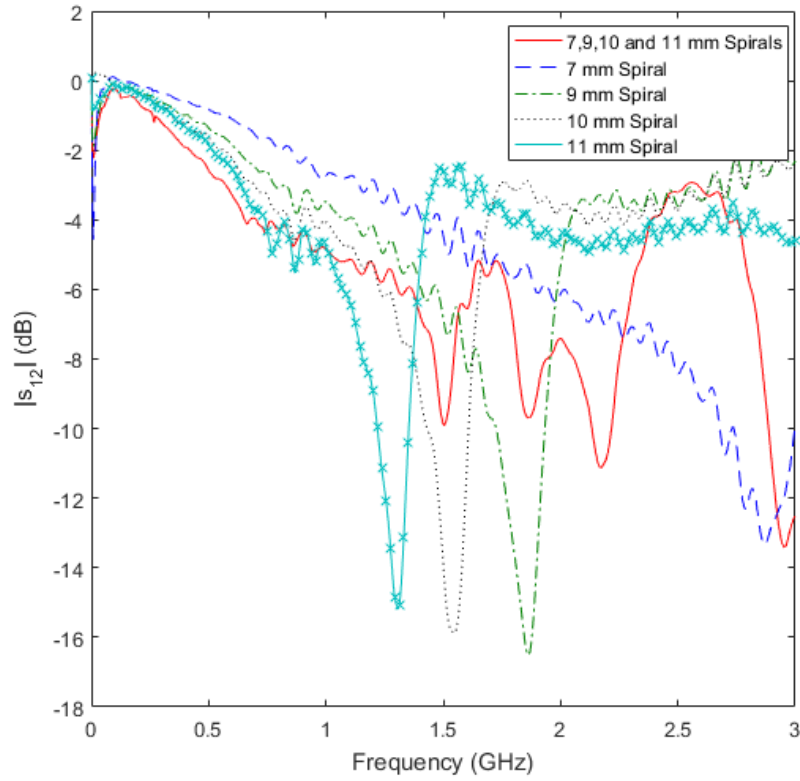
The shorter transmission line results in a lower transmission at resonance as there were lower losses in the line. Owing to this, it was decided that the transmission line length on either side of the spirals would be limited to 15 mm, any smaller than this and there would be interference between the connectors.

Examples of resonators with different sized spirals on either side of the transmission line were considered, with an example shown in Figure 7.26. This example shows data for three devices: one with two identical 9 mm spirals either side of the transmission line; one with two identical 10 mm spirals either side of the transmission line; and another with one 9 mm and one 10 mm spiral opposite each other.



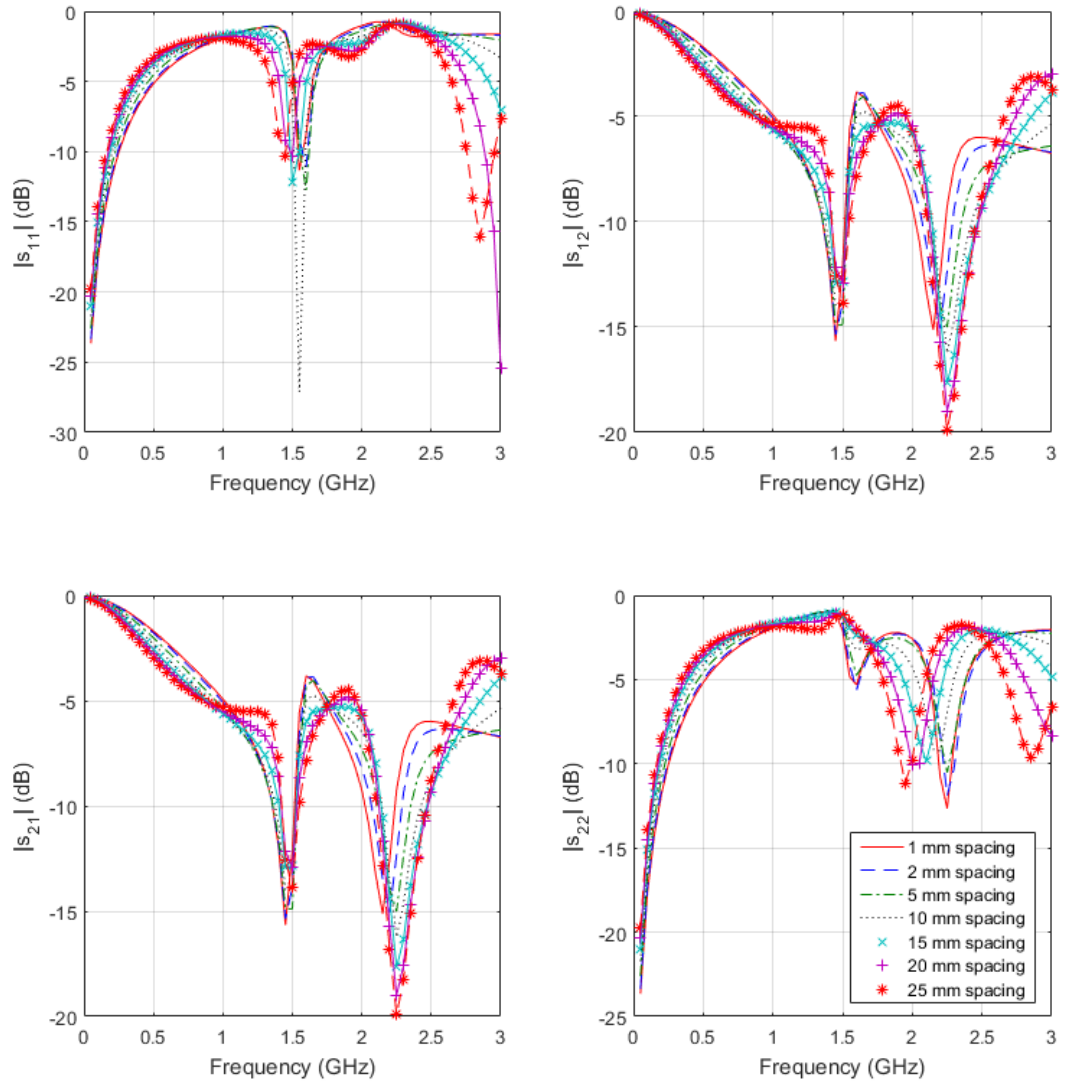
**Figure 7.26:** Measured scattering parameter  $s_{12}$  for three spiral resonators. One with two identical 9 mm spirals on either side of the transmission line, one with two identical 10 mm spirals on either side of the transmission line and a third with two different spirals on either side of the transmission line, one of 9 mm and one of 10 mm.

Using two spiral DGSs of different sizes leads to two defined minima in  $s_{12}$ . The locations of the minima of the combined resonator agreed with the results obtained when two individual, identical spirals were used. This meant that multiple resonances could be produced using non-identical spirals on either side of the transmission line. A further example of multiple resonances is shown in Figure 7.27 where four sets of two identical sized spirals were measured along one transmission line. The examples shown in Figure 7.21 show this with three spirals and then four spirals.



**Figure 7.27:** Measured scattering parameter  $s_{12}$  for five devices. Four with one identical spiral on either side of the transmission line of sizes 7, 9, 10 and 11 mm and another device with four different pairs of spirals connected along one transmission line.

The individual resonator plots can then be considered. The trace with all four resonators can be seen to have four distinct minima; however, these were shifted to a higher frequency than the individual resonators. The transmission at this point was also lower, showing that the resonances were not as well defined. This was due to loading between the resonators; when the resonators are in close proximity with one another, coupling between them occurs. This was confirmed by ADS simulations with varying spacing between two sets of identical spirals, with results shown in Figure 7.28.



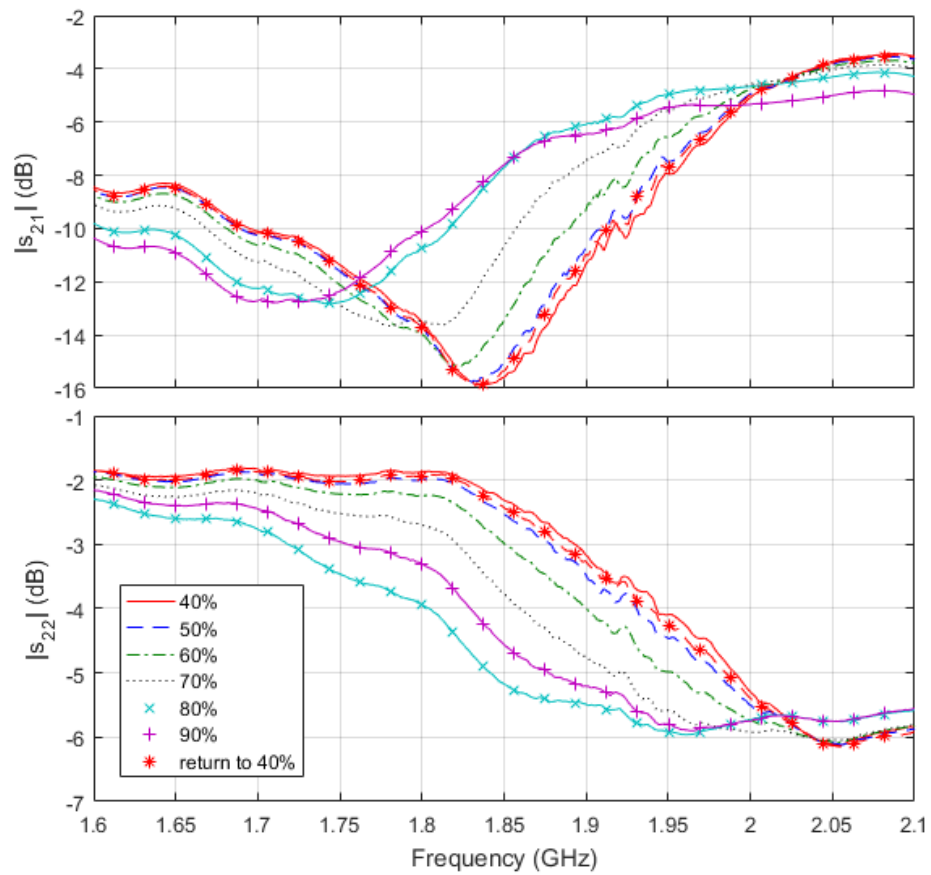
**Figure 7.28:** Simulated scattering parameters for two pairs of identical spirals, one with a longest length of 8 mm and one with a longest length of 10 mm, when the spacing between them was increased from 1 mm to 25 mm.

As the spacing between the spirals was increased, the transmission at the resonance due to the 8 mm spiral decreased and the transmission at the point of the 10 mm spiral increased. Therefore, the smaller spiral was a better resonator as there was less transmission at resonance. This was likely due to the size of the spiral; the smaller spiral was closer to the transmission line and therefore had stronger coupling. The minima for the resonance of the smaller spiral had a lower transmission but a broader peak, which was consistent with stronger coupling.

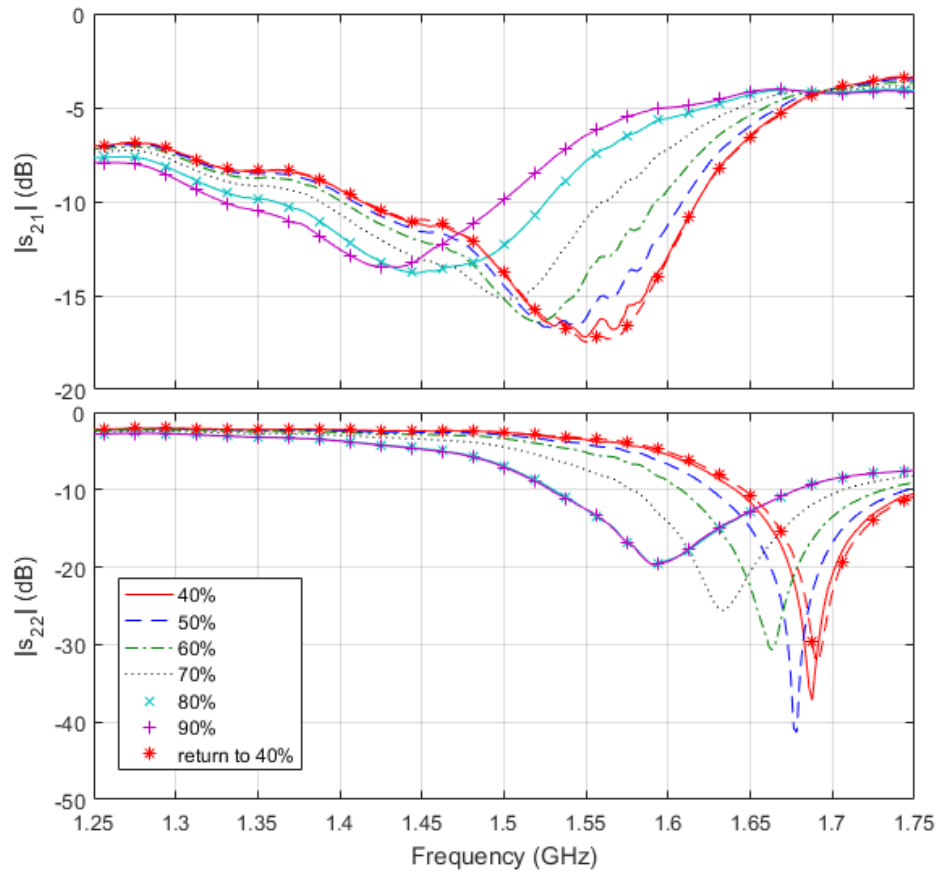
The results for multiple, different-sized spirals show the tunability of the resonators for a possible application. Spirals of different sizes can be utilised to alter the position of the resonances. The use of the resonators for possible applications including humidity and touch sensing is presented next.

### 7.4.3 Effect of Humidity on Spiral Defected Ground Structure Resonators

As with the transmission lines in Chapter 6, the spiral DGS structures were characterised with varying relative humidity. The humidity was increased from 40 to 90% over an eight-hour period and then reduced back to 40% for one hour. Three types of resonators were considered, all with two identical sized spirals either side of the transmission line. 9, 10 and 11 mm examples were considered, with results shown in Figures 7.29 to 7.31 respectively. As the full response has been shown previously, the x-axis here has been modified to show the region with the major changes. For this work, the temperature was kept constant at 30 °C.

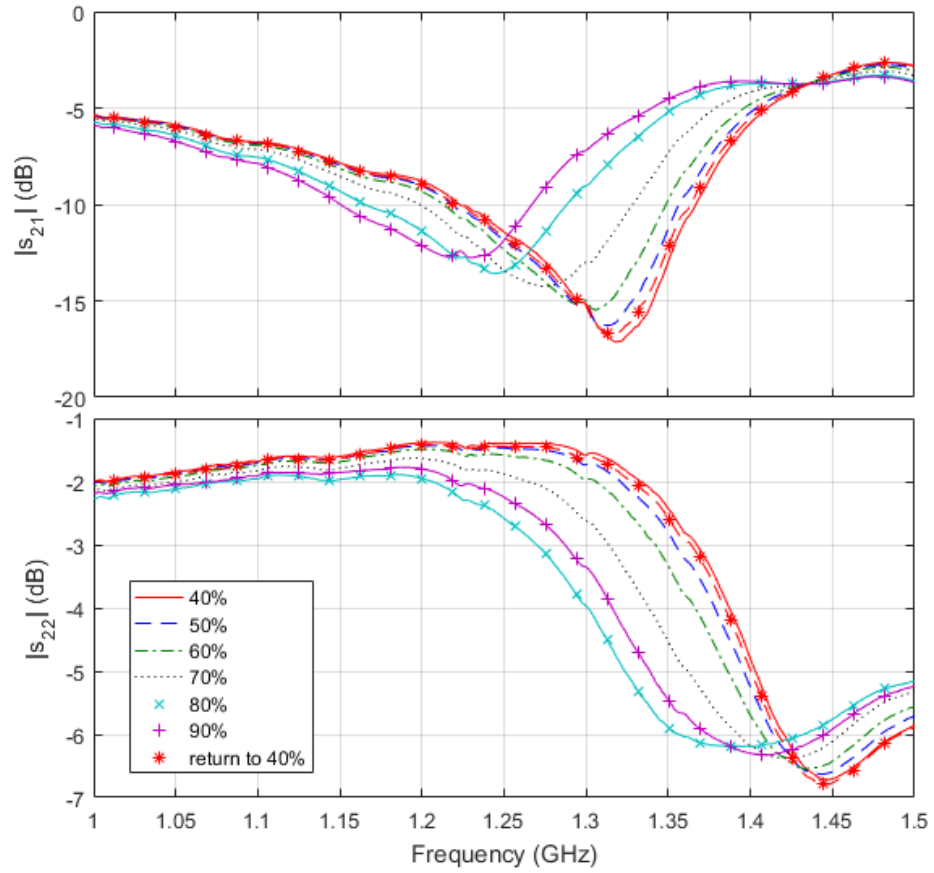


**Figure 7.29:** Measured scattering parameters  $s_{21}$  and  $s_{22}$  for an example 9 mm spiral resonator with humidity increased from 40% to 90% and then returned to 40%.



**Figure 7.30:** Measured scattering parameters  $s_{21}$  and  $s_{22}$  for an example 10 mm spiral resonator with humidity increased from 40% to 90% and then returned to 40%.





**Figure 7.31:** Measured scattering parameters  $s_{21}$  and  $s_{22}$  for an example 11 mm spiral resonator with humidity increased from 40% to 90% and then returned to 40%.

Chapter 6 determined that the increase in water content with relative humidity and the corresponding change in permittivity was the reason for the shift in scattering parameters with frequency. These results showed the same behaviour for all three resonators, i.e. the resonant frequency decreased with relative humidity. The response was not permanent and if returned to, and left at 40% for a longer period of time (six hours), the response would return to its original value.

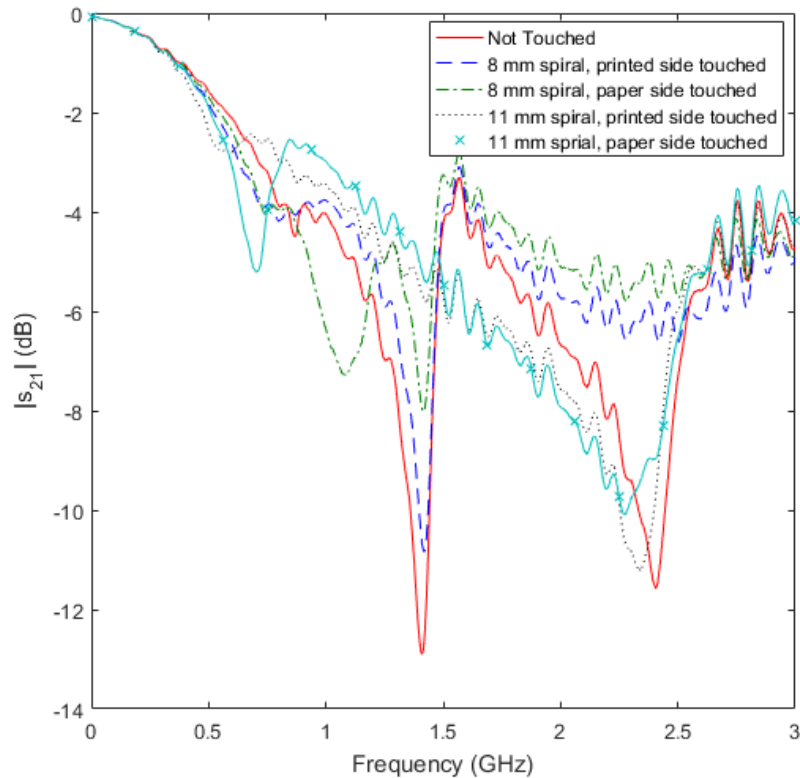
For all three examples, the response was seen to have a higher change at higher relative humidity except at 90%, where the change was much less than that at 80%. As this was not the case with transmission lines (results presented in Chapter 6), it was speculated that the reason for this smaller change at 90% was due to the difference in geometries of the printed structures. The substrate and the metal layer were the same in both.

As the spiral DGS resonators are paper-based, they are lightweight, flexible, cheap and easily disposable. The characterisation has shown that the resonators were sensitive to humidity and so could be utilised as sensors. 9 and 10 mm sized spirals were shown to have a shift of 0.13 GHz between 40 and 90% relative humidity, and 11 mm spirals a change of 0.10 GHz. This was a measurable change which could be calibrated to measure a change in humidity for a given environment. As this was not a

permanent change, the sensors could be used repeatedly and not just to determine a rise above some threshold.

#### 7.4.4 Spiral Defected Ground Structure Resonators as Touch Pads

Chapter 5 presented results for interdigitated capacitive touch sensors which could be used with a custom measurement system. Here, the resonators could be combined with antennas to create wireless touch sensors where all aspects are screen printed. The response to touch for an example resonator with one 8 mm and one 11 mm spiral is shown in Figure 7.32.



**Figure 7.32:** Measured scattering parameters for a spiral resonator with a 8 mm spiral and a 11 mm spiral when it is not touched, and when the spirals are touched independently on the printed and non-printed side of the device.

When one of the spirals was touched, the resonance for that spiral was shifted owing to the large change in effective permittivity of the finger. It was shown in Chapter 5 that the relative permittivity of the skin is 540, which is vastly different to that of air. As with devices in Chapter 5, touching the device on the printed side produced sub-optimal results. If the device was touched in such a way that both the signal track and the ground plane were touched, the device no longer acted as intended and could lead to false data. When the devices were touched on the paper side where the spirals were, the resonance was shifted to a lower frequency by approximately 1 GHz. This is a repeatable and predictable response and so can be taken into account in any measurement system.

## 7.5 Conclusion

The theory of microwave resonators has been presented, beginning with RLC resonators and including transmission line stubs and defected ground structures. Transmission line stubs have been fabricated and their measured scattering parameters compared to analytical modelling. Due to the differences in these scattering parameters, the effects of several non-idealities were considered to determine the source of these differences including: the impedance mismatch between the ports and the transmission line; the effect of the transmission line either side of the stub; fringing effects; the uncertainty in length of the stub; and the effects from additional modes being injected into the system. It was determined that the measurement of the stub length was important in obtaining the correct resonant frequency and also the additional electrical length of the stub due to fringing.

Spiral defected ground structure resonators were fabricated and it was shown to be possible to create more than one resonance by adding different sized spirals along the same transmission line. The spacing between spirals was shown to have an effect on the response and that there is a trade off between the size of the device and the interference between resonators. The use of the resonators as sensors for both humidity and touch was demonstrated with predictable and recoverable changes in the frequency response.

## References

- [1] Q. Simon, Y. Corredores, X. Castel, R. Benzerga, R. Sauleau, K. Mahdjoubi, A. Le Febvrier, S. Deputier, M. Guilloux-Viry, L. Zhang, P. Laurent, and G. Tanne, "Highly tunable microwave stub resonator on ferroelectric  $\text{KTa}_{0.5}\text{Nb}_{0.5}\text{O}_3$  thin film," *Applied Physics Letters*, vol. 99, no. 9, p. 92904, 2011.
- [2] M. R. Khan, G. J. Hayes, S. Zhang, M. D. Dickey, and G. Lazzi, "A pressure responsive fluidic microstrip open stub resonator using a liquid metal alloy," *IEEE Microwave and Wireless Components Letters*, vol. 22, no. 11, p. 577, 2012.
- [3] C. Quendo, E. Rius, and C. Person, "Narrow bandpass filters using dual-behavior resonators based on stepped-impedance stubs and different-length stubs," *IEEE Transactions on Microwave Theory and Techniques*, vol. 52, no. 3, p. 1034, 2004.
- [4] P. Heymann, H. Prinzler, and F. Schnieder, "De-embedding of MMIC transmission-line measurements," *IEEE Microwave Theory and Techniques Society, International Microwave Symposium Digest*, p. 1045, 1994.
- [5] D. Pozar, *Microwave Engineering Fourth Edition*. Wiley Global Education, 2005.
- [6] D. A. Frickey, "Conversions between S, Z, Y, h, ABCD, and T parameters which are valid for complex source and load impedances," *IEEE Transactions on Microwave Theory and Techniques*, vol. 42, no. 2, p. 205, 1994.
- [7] R. N. Simons, *Coplanar Waveguide Discontinuities and Circuit Elements*, vol. 7. John Wiley and Sons, 2001.
- [8] M. Riaziat, R. Majidi-Ahy, and I.-J. Feng, "Propagation modes and dispersion characteristics of CPW," *IEEE Transactions on Microwave Theory and Techniques*, vol. 38, no. 3, p. 245, 1990.
- [9] M. K. Khandelwal, B. K. Kanaujia, and S. Kumar, "Defected ground structure: Fundamentals, analysis, and applications in modern wireless trends," *International Journal of Antennas and Propagation*, 2017.
- [10] J. S. Hong and B. M. Karyapudi, "A general circuit model for defected ground structures in planar transmission lines," *IEEE Microwave and Wireless Components Letters*, vol. 15, no. 10, p. 706, 2005.
- [11] L. H. Weng, Y. C. Guo, X. W. Shi, and X. Q. Chen, "An overview of defected ground structures," *Progress In Electromagnetics Research*, vol. 7, p. 173, 2008.
- [12] M. Rezaee and M. Joodaki, "Two-dimensional displacement sensor based on CPW line loaded by defected ground structure with two separated transmission zeroes," *IEEE Sensors Journal*, vol. 17, no. 4, p. 994, 2017.

- [13] F. Y. Zulkifli, E. T. Rahardjo, and D. Hartanto, "Radiation properties enhancement of triangular patch microstrip antenna array using hexagonal defected ground structure," *Progress in Electromagnetic Research Letters*, vol. 5, p. 101, 2008.
- [14] J.-S. Lim, C.-S. Kim, J.-S. Park, D. Ahn, and S. Nam, "Design of a 10 dB branch line coupler using microstrip line with defected ground structure," *IET Electronics Letters*, vol. 36, p. 1784, 2000.
- [15] R. Dua, H. Singh, and N. Gambhir, "2.45 GHz microstrip patch antenna with defected ground structure for Bluetooth," *Journal of Soft Computing and Engineering*, no. 6, p. 262, 2012.
- [16] S. Hekal, A. B. Abdel-Rahman, H. Jia, A. Allam, A. Barakat, and R. K. Pokharel, "A novel technique for compact size wireless power transfer applications using defected ground structures," *IEEE Transactions on Microwave Theory and Techniques*, vol. 65, no. 2, p. 591, 2016.
- [17] H. Oraizi and M. S. Esfahlan, "Miniaturization of Wilkinson power dividers by using defected ground structures," *Progress In Electromagnetics Research Letters*, vol. 4, p. 113, 2008.
- [18] P. Bhakhar, V. Dwivedi, and P. Prajapati, "Directivity enhancement of miniaturized directional coupler using defected ground structure," *Advances in Intelligent Systems Research*, vol. 137, p. 739, 2017.
- [19] M. Ramesh, V. Lakshmi, and P. Mallikarjunarao, "Investigation on UWB kite shape textile antenna with defective ground structure," *3rd International Conference on Advances in Electrical, Electronics, Information, Communication and Bio-Informatics*, p. 15, 2017.
- [20] Y. Chung, S. S. Jeon, S. Kim, D. Ahn, J. I. Choi, and T. Itoh, "Multifunctional microstrip transmission lines integrated with defected ground structure for RF front-end application," *IEEE Transactions on Microwave Theory and Techniques*, vol. 52, no. 5, p. 1425, 2004.
- [21] A. M. Safwat, F. Podevin, P. Ferrari, and A. Vilcot, "Tunable bandstop defected ground structure resonator using reconfigurable dumbbell-shaped coplanar waveguide," *IEEE Transactions on Microwave Theory and Techniques*, vol. 54, no. 9, p. 3559, 2006.
- [22] J.-I. Park, C.-S. Kim, J. Kim, J.-S. Park, Y. Qian, D. Ahm, and T. Itoh, "Modelling of a photonic bandgap and its application for the low-pass filter design," *IEEE Microwave Conference, Asia Pacific*, 1999.
- [23] J. Wang, H. Ning, and L. Mao, "A compact reconfigurable bandstop resonator using defected ground structure on coplanar waveguide," *IEEE Antennas and Wireless Propagation Letters*, vol. 11, p. 457, 2012.
- [24] H. B. El-Shaarawy, F. Coccetti, R. Plana, M. El-Said, and E. A. Hashish, "Novel reconfigurable defected ground structure resonator on coplanar waveguide," *IEEE Transactions on Antennas and Propagation*, vol. 58, no. 11, p. 3622, 2010.
- [25] Y. L. Zhang, W. Hong, K. Wu, J. X. Chen, and H. J. Tang, "Novel substrate integrated waveguide cavity filter with defected ground structure," *IEEE Transactions on Microwave Theory and Techniques*, vol. 53, no. 4, p. 1280, 2005.
- [26] W. Li, Z. Tang, and X. Cao, "Design of a SIW bandpass filter using defected ground structure with CSRRs," *Active and Passive Electronic Components*, 2017.
- [27] W. Shen, W.-Y. Yin, S. Member, and X.-W. Sun, "Compact substrate integrated waveguide (SIW) filter with defected ground structure," *IEEE Microwave and Wireless Components Letters*, vol. 21, no. 2, p. 83, 2011.
- [28] F. Martin, F. Falcone, J. Bonache, T. Lopetegi, M. A. G. Laso, and M. Sorolla, "Dual electromagnetic bandgap CPW structures for filter applications," *IEEE Microwave and Wireless Components Letters*, vol. 13, no. 9, p. 393, 2003.
- [29] J.-S. Lim, C.-S. Kim, Y.-T. Lee, D. Ahn, and S. Nam, "Design of lowpass filters using defected ground structure and compensated microstrip line," *Electronics Letters*, vol. 38, no. 22, p. 1357, 2005.
- [30] A. Abdel-Rahman, A. R. Ali, S. Amari, and A. S. Omar, "Compact bandpass filters using Defected Ground Structure (DGS) coupled resonators," *IEEE Microwave Theory and Techniques Society, International Microwave Symposium Digest*, p. 1479, 2005.
- [31] A. Danideh and R. A. Sadeghzadeh, "Defected ground structure based wideband microstrip low-pass filter for wireless communication," *Microwave and Optical Technology Letters*, vol. 59, no. 5, p. 993, 2016.
- [32] S. Choi, S. Eom, M. M. Tentzeris, and S. Lim, "Inkjet-printed electromagnet-based touchpad using spiral resonators," *Journal of Microelectromechanical Systems*, vol. 25, no. 5, p. 947, 2016.
- [33] S. Preradovic and A. Menicanin, "Chipless wireless sensor node," *Proceedings of the 35th International Convention MIPRO*, p. 179, 2012.
- [34] E. M. Amin, N. Karmakar, and S. Preradovic, "Towards an intelligent em barcode," *Proceedings of the 7th International Conference on Electrical and Computer Engineering*, p. 826, 2012.
- [35] S. Preradovic, N. Kamakar, and E. M. Amin, "Chipless RFID tag with integrated resistive and capacitive sensors," *Asia-Pacific Microwave Conference Proceedings*, p. 1354, 2011.
- [36] D. Schlieter and R. Henderson, "High Q defected ground structures in grounded coplanar waveguide," *Electronics Letters*, vol. 48, no. 11, p. 635, 2012.
- [37] J. Lim, C. Kim, and Y. Lee, "A spiral-shaped defected ground structure for coplanar waveguide," *Microwave and Wireless Components Letters*, vol. 12, no. 9, p. 330, 2002.

## Chapter 8

# Conclusions and Outlook

This thesis has assessed the feasibility of screen printing paper-based passive components up to microwave frequencies. One of the key achievements of this work has been the creation of two decision matrices to determine the optimum substrate and fabrication method. Screen printing on Neenah paper was judged to be optimum for this work and was then developed further. Touch pads, microwave transmission lines and resonators were fabricated as demonstrators of the screen-printing process developed, with measured results supported by numerical analysis.

The two decision matrices determined both optimum substrate and fabrication method for a given application. Substrates were compared in terms of surface roughness, cost, weight, thickness, water and heat resilience. Fabrication methods were compared in terms of available materials, minimum feature size, process repeatability and ease of use. The fabrication method and paper were then considered together in terms of compatibility, sheet resistance and adhesion of deposited conductive layers. The method and substrate must be considered in parallel as it has been shown they may not be well suited to each other.

This work has shown the vast variety in the term ‘paper’ as a substrate. Surface imaging and topography measurements of a range of papers have provided information on the differences in paper structures, with matt papers consisting simply of bare cellulose fibres and coated papers having a smoother surface on top of this cellulose fibre structure. These images and measurements can be used to explain why matt papers have a lower cost, weight and thickness, also why they are more susceptible to water when compared to glossy papers. Papers were compared to silicon, glass and PET to highlight paper as having a lower cost and being easier to handle.

The results presented in this thesis only include those for thermal evaporation and screen printing, the investigation was not limited to these but they were the most scalable and provided acceptable

results in the preliminary stages. Screen printing was determined to be the preferred fabrication method for this work as it is cost effective, fast and large areas can be patterned. Neenah paper was selected as the optimum substrate for use with screen printing as rougher papers lead to a thicker layer of ink deposited, resulting in a higher conductivity.

The screen-printing process was optimised and ultimately produced minimum repeatable features of 500  $\mu\text{m}$ . The screen properties, printing parameters and ink curing were all considered and it was determined, when considering the mesh, that there was a trade off between ink thickness (and resulting conductivity) and minimum feature size. Although carbon and nickel inks were considered, a silver flake ink was determined to be better suited to this work for its high conductivity. A sheet resistance of 15  $\text{m}\Omega/\square$  was achieved when the ink was cured at 125  $^{\circ}\text{C}$ . Coalescing of the ink did not occur as this required temperatures of above 250  $^{\circ}\text{C}$ , which was proved to discolour and curl paper substrates.

To demonstrate the capabilities of the optimised screen-printing process, passive devices were fabricated including resistors, capacitors and inductors. Due to the high conductivity of the silver ink, this was not suited to resistors, however inductors which were directly comparable to state-of-the-art inductors screen printed on PET were produced. Both parallel plate and interdigitated capacitors were also fabricated and the use of the interdigitated structures as touch pads was demonstrated.

Although parallel plate structures have a higher capacitance, the change in capacitance with touch is greater for interdigitated designs. The touch pads were shown to perform well for a wide variety of users and the measured results were supported by COMSOL modelling, which also provided further detail on the device operation. The change in capacitance with touch was shown to increase with force of touch and contact area and the touch pads were also shown to be proximity sensitive.

Screen-printed paper-based passive devices have been considered so that the use of plastics can be avoided. It was identified early in this thesis that paper is more recycled and environmentally friendly than plastics. There are high requirements for cost effective, disposable substrates for use in the 'Internet of Things', especially in the ISM band for sensing and communications applications. This work has included an investigation into the behaviour of paper and silver ink at microwave frequencies using transmission line structures illustrating that changing the substrate and metal layer properties have an effect on the line parameters.

A simple circuit using the transmission lines was created and a transmission line stub, which creates a resonance, was investigated at microwave frequencies. The resulting measurements were compared to both numerical and analytical modelling, which highlighted the effect of stub length, fringing and injection modes at discontinuities. Based on these findings, spiral resonators were used

to create multiple resonances which were sensitive to both touch and humidity.

A key result in this thesis has been determining the effect of humidity on paper-based devices due to the hygroscopic nature of paper. The effect of humidity on the touch pads, the transmission lines and the microwave resonators has been identified and shown not to be negligible. Paper and water have three main bonding mechanisms and this work has suggested that the effect of loosely bound water in the cellulose structure is the main cause in increased effective permittivity and resulting change in response of the devices at higher humidities.

Overall, this work suggests that screen printing conductive ink on paper is a viable alternative to current fabrication methods on flexible plastic substrates. The large amounts of plastic waste have seen a drive towards paper-based electronics. This thesis provides a method to determine an optimum fabrication technique and substrate and also highlights the possible effects of humidity which must be considered for all devices using paper.

## 8.1 Suggestions for Further Work

This thesis has covered a wide range of topics within the title ‘Paper-based Electronics’ and for this reason, there is a large range of further work that could take place based on this.

The screen-printing method could be used to create multiple layers of conductive and insulating materials. Increasing the number of layers of conductive ink would increase conductivity, leading to lower losses for the microwave devices presented in Chapters 6 and 7. Multiple layers of differing metals can lead to the production of more complex devices, for example thermoelectric generators. Examples of these have been fabricated in Durham using a syringe pump deposition method and both silver and nickel inks.

Multiple layers of differing materials would allow the fabrication of devices which incorporate both metals and insulators. Work is on going investigating the printing of silver ink and PVA using a syringe pump method. The curing of multiple layers may be an issue, however the temperatures required for both silver and PVA are lower than those which would deteriorate the substrate. The main concern when screen printing multiple layers is the alignment, which is less of a concern with syringe printing. Although the alignment would be difficult with the in-house system developed in this work, it would not be an issue with an automated system.

The ability to screen print multiple layers leads to the possibility of producing active devices such as transistors. These active devices could then be integrated into a larger system which includes

sensors, batteries and inputs which have already successfully been printed on paper. Although some groups have printed complete systems on paper, this is still in its early stages and further development could lead to commercial applications.

The foldability of paper has been discussed in this work and could be considered for further work. Foldable devices reduce the area and can also alter the operation of devices. Antennas are a device which may likely be considered in an extension of this work and foldable antennas can provide multiple transmitting and receiving frequencies.

Altering the chemical structure of the paper itself was not considered in this work, however this has been considered by others and could be further explored. The porous structure of matt papers especially makes it an ideal substrate for functionalisation, which can be utilised to create sensors. The option of alternate substrates similar to paper substrates should also be considered, for example textiles. Electronics on textiles would likely become a popular commercial area due to the novelty of electronics embedded in clothing and footwear.